Star Formation in Merging Galaxies

MIAH, JUNAD,ALAM

University of Durham

Doctoral Thesis

Star Formation in Merging Galaxies

Author: Junayd Alam Miah *Supervisor: Prof. Ray Martin Sharples*

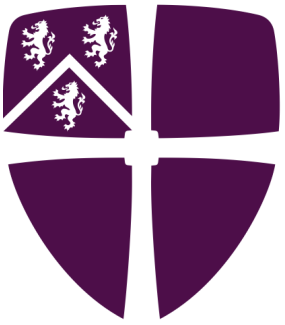

A thesis submitted to the University of Durham in accordance with the regulations for admittance to the Degree of Doctor of Philosophy in the

Extragalactic & Cosmology Group
Department of Physics

November 2014

Abstract

Star formation is detected in any galaxy with an appreciable amount of gas and the vast majority of stars form in embedded clusters. However, very few bound star clusters are detected in the Milky Way, which has led to the hypothesis that as many as 90% of these clusters are disrupted during the early stages of their evolution. Many of those that do survive are likely to be progenitors of globular clusters that are observed in elliptical galaxies, and in the bulge and halo regions of spiral galaxies. In order to understand how star clusters form and evolve, and the disruption mechanisms they encounter, it is necessary to observe star clusters during their earliest evolutionary stages. This is difficult to observe in quiescent galaxies like the Milky Way where only a few newly formed star clusters have currently been detected. Gas-rich interacting and merging galaxies however, host thousands of newly formed star clusters and are ideal targets to observe the evolution of star clusters.

In this thesis star clusters are observed in galaxy mergers for a range of evolutionary states using both photometric and spectroscopic data. We find evidence that tidal interactions have produced new cluster populations in two separate galaxy mergers. Analysis of the cluster populations in these mergers also suggest that tidal interactions do not destroy more clusters than they produce, in disagreement with simulations in the literature. Furthermore, we observe several star clusters that may be the product of merging between multiple clusters. These star clusters show spectral features consistent with multiple episodes of star formation. If these clusters remain bound for the next few Gyrs, they could explain the multiple stellar population feature observed in globular clusters in the Galaxy. We also explore the possibility of star clusters evolving to form the halo cluster population of their host merger before the progenitor disks coalesce. Star clusters are generally found in the halo population of a galaxy merger once the progenitor nuclei coalesce. However, some galaxy mergers like the Antennae harbour star clusters that may be forming their halo cluster population before their progenitor nuclei merge. This suggests that star clusters begin to form the halo cluster population of a galaxy merger before the progenitor nuclei coalesce. We recommend future surveys of gas-rich major galaxy mergers to study young ($\sim$ few hundred Myr) star clusters in dense and quiescent regions to further support our findings.

Contents

List of Figures

List of Tables

Declaration of Authorship

I, Junayd Alam Miah, declare that this thesis titled, 'Star Formation in Merging Galaxies' and the work presented in it are my own. I confirm that:

- This work was done wholly or mainly while in candidature for a research degree at this University.
- Where any part of this thesis has previously been submitted for a degree or any other qualification at this University or any other institution, this has been clearly stated.
- Where I have consulted the published work of others, this is always clearly attributed.
- Where I have quoted from the work of others, the source is always given. With the exception of such quotations, this thesis is entirely my own work.
- I have acknowledged all main sources of help.
- Where the thesis is based on work done by myself jointly with others, I have made clear exactly what was done by others and what I have contributed myself.

Signed: _____

Date: _____

Acknowledgements

The acknowledgements section can be as much of a burden to write as it is a joy, particularly because of the shear number of people I'm indebted to at the end of this lengthy Ph.D. project. A complete show of gratitude to all those who supported me during my Ph.D. research could easily be a chapter of its own. In short, I can make my first conclusion here by realising that not all those who helped me throughout my course can be given my full gratitude in these few pages. Nevertheless, the following paragraphs will represent my best attempt.

Naturally the first people I thank are my parents, Khalique Miah and Rahela Parvin. Their love and affection has always been a driving force throughout the most difficult periods of my research. The same can be said of my siblings and extended family who have always been supporting and have shown pride in whatever goal I have endeavoured. This thesis is as much of their work as it is mine.

A considerable number of friends will undoubtedly demand my gratitude so here it is. Firstly, I thank my dearest friend Suzie Qassim, who has consistently supported me throughout my eight years of academia. They say that time flies when you're having fun, well these years have definitely flown by for me because of the countless enjoyable moments we've shared. I hope to see you soon after you complete your doctoral research and keep the fun times rolling.

I thank my good friends Han Goksel (aka Lord Salerne) and Fabio Pintore for being great house mates and providing constant comedy in our home throughout these past few years. Whether it was relaxing in front of the Playstation (while I served humiliating defeats to both of you) or racing around places like Padova (humiliating defeats again), it's all been great fun. And yes, even the infamous 'I' word moment from Mr Goksel, was a great experience. Teşekkür ederim e grazie mille my friends, I wish you well for the future and hope to see both of you soon!

Thanks to Peter Runge, Natasha Cooper, Sneha Singh and Sigit Wibowo for their continual support throughout my research. I will make sure I visit all of you in Berlin, Bombay and Jakarta soon! I do expect some gulab jamun ready for me in Bombay when I visit, however a biryani would suffice. Nothing too spicy in Jakarta please! Thanks to Jamil Mahmood for all the discussions and advice on my Ph.D. research. I will miss our conversations and I hope your research progresses well. Thanks to Saleh Al-Luqmani for always providing a helping hand during my

frequent travels up and down the country, particularly those back home. I hope to visit you and your family some day soon in Mecca. Thanks to Mohammed Al-Muzaini for all the crazy visits. I'll try to visit you in Kuwait soon.

From the physics department I thank my office mates of past and present Adlyka Annuar, Emma Gardner, James Collinson and Mari Kolehmainen. I will miss the random discussions that took place in our office, which were generally unrelated to physics and often concluded with the use of a super-slow motion camera or a Simpsons quote. Honestly, we could form a successful think tank if we dare to try. I also thank Andy Sutton, Agnese Del-Moro, Ben Chehade and Ton Luangtip, all of whom have always contributed to the friendly atmosphere of the X-ray corridor, albeit with the occasional sarcastic banter and verbal abuse (Andy and Ben respectively).

Outside of Durham Physics, I thank Dr Ben Davies for his contributions to my study of star clusters in the Antennae galaxies. Last but not least, I am greatly indebted to my supervisor, Professor Ray Sharples. His vast knowledge of my research field and continual guidance has been invaluable.

Dedicated to my family, whose continual support has made this work possible

Chapter 1

Introduction

1.1 Prologue

A quick glance at a clear night sky away from city lights show the heavens filled with an almost uncountable number of stars. Since the dawn of mankind these stars have played a pivotal role in our development as a civilization. During the course of our existence they have been used for navigation, religion, mathematics and science to name a few. Our galaxy, the Milky Way, consists of over a 100 billion stars distributed mainly in the bulge and disk of the galaxy (Freedman et al., 2010). Almost all galaxies in the known universe share this feature. Our understanding of how stars form and evolve has greatly increased in the past century but there are still questions about the formation and evolution process that remain unknown.

It has been understood for some time that the majority of star formation occurs in clusters and associations (Blaauw 1964; Lada 1987), with only a few individual stars forming in relative isolation (Krumholz et al., 2009). Evidence for this can be seen in our own Milky Way. Studies of hot O-type stars have shown a global clustering of these stellar types (Parker and Goodwin, 2007), where $\sim 70\%$ reside in young clusters or associations (Gies, 1987). Almost half of the remaining field population have been identified as runaway stars, and a remaining $\sim 4\%$ are considered as having formed outside of clustered environments (de Wit et al., 2005).

Cluster Type	Age [Gyr]	M_{tot} [$\mathcal{M}_\odot$]	ρ_c [$\mathcal{M}_\odot$/pc^3]	Z_c [$Z_\odot$]	Location in galaxy	t_{dyn} [Myr]	t_{rlx} [Myr]
OC	$\lesssim 0.3$	$\lesssim 10^3$	$\lesssim 10^3$	~ 1	disk	~ 1	$\lesssim 100$
GC	$\gtrsim 1$	$\sim 10^5$	$\gtrsim 10^3$	< 1	halo	$\gtrsim 1$	$\gtrsim 1000$
YMC	$\lesssim 0.1$	$\gtrsim 10^5$	$\gtrsim 10^3$	$\gtrsim 1$	disk	$\lesssim 1$	$\lesssim 100$

TABLE 1.1: Comparison between the fundamental parameters of the different types of star clusters: open cluster (OC), globular cluster (GC), and young massive cluster (YMC). The columns provide cluster age, followed by the total cluster mass (in $\mathcal{M}_\odot$), the core density, the metallicity, the typical cluster location within a galaxy, and the dynamical and relaxation time scales. The dynamical time scale refers to the typical time for a star to cross the system, and the relaxation time scale refers to the energy transfer between individual stars via two-body encounters that cause the system to reach thermal equilibrium. The relaxation time is typically much longer than the dynamical time in all of the cluster types. The values provided are results from a number of observations and are very general but can be used as vague guidelines for the different cluster types.

There are three types of star clusters currently accepted by the scientific community: open clusters (OCs), globular clusters (GCs), and young massive clusters (YMCs). Table 1.1 lists a comparison between the physical parameters of the different cluster types. The focus of this thesis will be on YMCs and GCs. The following subsections will elaborate into these two cluster types, but for now it can be said that YMCs are nurseries to star formation and harbour the brightest and youngest stars ($\sim$ 1 - 100 Myrs), while GCs consist of stars considerably older ($\sim$ 1 Gyr or more). An example of a GC and YMC is shown in Figure 1.1 and 1.2, respectively.

1.2 Star Clusters in the Milky Way

The Milky Way is considered as a quiescent galaxy with a low star formation rate (SFR) of $\sim 1.9 \pm 0.4\ \mathcal{M}_\odot\ \mathrm{yr}^{-1}$, although this is poorly constrained (Chomiuk and Povich, 2011). Assuming this SFR, Longmore et al. (2012) determine that $\sim$ 10 star clusters of masses greater than $10^4\ \mathcal{M}_\odot$ and ages less than 10 Myrs are expected within the Galaxy. Indeed, around ten YMCs have been observed in the Galaxy so far, the most famous of which being Westerlund 1 (see Figure 1.3). Discovered in the 1960s (Westerlund, 1961), photometric observations (Borgman et al. 1970; Lockwood 1974) along with spectroscopic surveys (Westerlund, 1987) suggested the presence of a population of highly luminous early and late type

FIGURE 1.1: The above HST/WFPC2 image shows M80, one of the densest globular clusters in the Galaxy. The cluster has the typical traits of GCs: a population of old, metal-poor stars clustered around a dense centre. Stars within GCs are all thought to have the same age, which makes GCs particularly useful for studying stellar evolution. The Milky Way has 147 known GCs, located in either the halo or bulge, which is the typical amount expected for a spiral galaxy (Harris and van den Bergh 1981; van den Bergh and Harris 1982; Harris 1991; West et al. 1995). GCs are devoid of gas, and so show no signs of current star formation.

supergiants in a compact region. Despite these observations, the significant reddening of Westerland 1 (Av $\sim$ 12.9 mag. Piatti et al. 1998) stagnated any further investigations, leaving the cluster in relative obscurity for the following few decades after its discovery.

It was not until the beginning of the 21st century that interest was re-ignited in this cluster. Extensive photometric and spectroscopic surveys were undertaken between 2001 and 2002, primarily motivated by the unusual radio and infrared properties of two cluster members in Westerlund 1 (Clark et al., 1998). This investigation led to the finding of a compact group of unambiguously post-main

FIGURE 1.2: Composite colour HST/ACS image of NGC 3603, a YMC located in the Carina spiral arm and approximately $2{\times}10^5$ light-years from the solar system. The numbers of stars inhabiting the cluster are similar to those expected from GCs, however their ages are considerably younger with ages ranging in Myrs rather than Gyrs. The existence of massive Wolf-Rayet stars has been well documented in this cluster (de Pree et al., 1999). Stellar winds from these stars, along with stellar winds from OB type stars, have removed gas (orange-red clouds) from the cluster centre, giving an unobscured view of the cluster (Brandner et al., 2000).

sequence objects, consisting of rich populations of Wolf-Rayet stars, OB supergiants and short lived transitional objects such as luminous blue variables (LBVs) and red supergiants (RSGs). Westerlund 1 is thought to have an age ranging between $\sim$ 3.5 - 5.0 Myrs with an upper mass limit of $\sim 10^5 \mathcal{M}_{\odot}$. However, this mass limit does not account for incompleteness (Clark et al., 2005).

Other YMCs exist within the Galaxy, such as NGC 3606 (Figure 1.2), a cluster $\sim$ 6 kpc away and located in the Carina spiral arm (de Pree et al. 1999; Pandey et al. 2001), which is thought to be younger than Westerlund 1 given its Wolf-Rayet stars are still on the main sequence (Walborn et al., 2002). Furthermore, there remains

FIGURE 1.3: The above ESO optical image of Westerlund 1 shows how significantly reddening can limit observation. This cluster has a reddening of Av $\sim$ 12.9. The stars in this image are of OB type, which primarily emit at shorter wavelengths and appear blue in the absence of extinction. However, the heavy optical extinction around Westerlund 1 causes these stars to appear red at visible wavelengths. This reddening effect restricts observations on other massive clusters in the Galaxy such as the Arches and Quintuplet clusters, both of which are near the Galactic centre which has an extinction of Av $\simeq$ 30 (Figer et al., 1999, 2002).

the massive Arches and Quintuplet clusters (each with mass $\sim 10^4 \mathcal{M}_\odot$). Unfortunately, these clusters are close to the Galactic centre which prevents detailed investigations due to the extreme reddening present (Figer, 2004).

One of the most striking findings in the study of star clusters in the Milky Way was the sharp decline in the number of young and embedded star clusters at an age of a few Myrs. Indeed, even though the majority of star formation occurs in clusters and associations, only a small fraction of stars in the Galactic disk currently reside in bound star clusters. The process responsible for the decline is often referred to as "infant mortality" and is thought to be due to interactions between clusters and giant molecular clouds (GMCs) during the early stages of

YMC evolution (Lada and Lada 2003; Gieles et al. 2006c; Kruijssen et al. 2011). Section § 1.4 and § 1.5 further elaborate on this phenomenon.

1.3 Extragalactic Star Clusters

1.3.1 Surveys of Galaxy Mergers

Galaxies throughout the universe show similar star cluster populations to those of the Milky Way. The most massive star forming regions are known as super star clusters (SSCs) and are generally found in galactic mergers, where two or more galaxies are in the process of merging (Barnes and Hernquist, 1992). More specifically, SSCs are particularly abundant in merging between gas-rich galaxies such as spirals, where a larger supply of gas is available for star cluster formation than in gas-poor mergers. These gas-rich mergers are given the term 'wet-mergers' (Faber et al. 2007; Lin 2010). These SSCs are thought to resemble a mode of star formation that was ubiquitous in the early universe (Leitherer, 2001). Observations of SSCs were very limited prior to the launch of the Hubble Space Telescope (HST), with only bluish knots being observed in merger remnants such as NGC 7252 (Schweizer, 1982). These knots were thought to be clumps of star clusters produced from the merger process which could not be resolved by ground based instruments available at the time.

Since the commissioning of HST, observations of star clusters have been in abundance. HST observations were used to detect $\sim$ 500 star clusters in NGC 7252, with ages spreading over three distinct groups ($<$ 10 Myrs, $\sim$ 650 Myrs, and a population older than 650 Myrs that originate from the progenitor galaxies prior to merging). Zepf et al. (1999) detected $\sim$ 1000 star clusters in NGC 3256, a merger in an advanced stage of merging but less complete than NGC 7252 (i.e., the progenitor nuclei in NGC 3256 have yet to coalesce). These clusters show a variety of ages, from a few Myrs to 150 Myrs (Trancho et al., 2007a,b). The Antennae galaxies, an intermediate-age merger (Barnes, 1988) consisting of two spiral galaxies (NGC 4038/39) have also been studied in great detail, with as many as 8000 star clusters distributed throughout the merger (Whitmore et al., 1999). Multiple cluster age populations have been observed ($<$ 20 Myr, 100 Myr, 500 Myr, and a population of progenitor clusters) indicating multiple periods of star formation

since the merging process began (Whitmore et al. 1999; Renaud 2010). In all of these systems the youngest and most massive star clusters are generally found in the overlapping regions of the merging galaxies (Zhang et al. 2001; Gilbert and Graham 2007).

Studies of these extragalactic star cluster populations have shown several differences to the YMC population of the Milky Way. One obvious difference is the large number of YMCs observed in merging systems, which easily accumulate to a few hundred, compared to only a dozen YMCs that have so far been observed in the Milky Way. Also, the mass of clusters observed in these mergers are up to $10^7 \mathcal{M}_\odot$ which easily exceeds the masses determined for YMCs in the Milky Way (Clark et al. 1998; de Pree et al. 1999). However, there are some common characteristics between extragalactic and Galactic YMCs. One notable similarity is the effect of "infant mortality". Much like the Milky Way, studies of mergers have suggested up to 90% of clusters formed may be tidally disrupted within 10 Myrs (Mengel et al. 2005; Gilbert and Graham 2007). However cluster observations in M83 show that, if the population and mass of YMCs are dependent on environment (i.e., location within the galaxy), the level of disruption also varies with environment (Bastian et al., 2012). Section § 1.4 continues further on the mechanisms responsible for star cluster disruption.

1.3.2 Observed Parameters of YMCs

A significant advantage of studying these extragalactic star clusters is the ability to observe a galaxy in its entirety. This provides a 'complete' census of the star cluster population and the environments in which they form and evolve. However, some young ($<$ 4 Myrs) star clusters can still be obscured due to the effects of extinction, such as those in the overlapping region of the Antennae (e.g., Gilbert and Graham 2007).

Nonetheless, the study of YMCs in other galaxies has allowed many of their physical parameters to be constrained. Their luminosity function (LF), defined as the number of clusters per unit luminosity ($\mathrm{d}N/\mathrm{d}L$), is well described by a power-law function of the form $\mathrm{d}N/\mathrm{d}L \sim L^\alpha$ where $\alpha \approx$ -2 (Miller et al. 1997; Whitmore et al. 1999; Larsen 2002). The mass function (MF) is not as trivial to determine as the LF. One cannot simply interpret the LF as the underlying MF since the LF

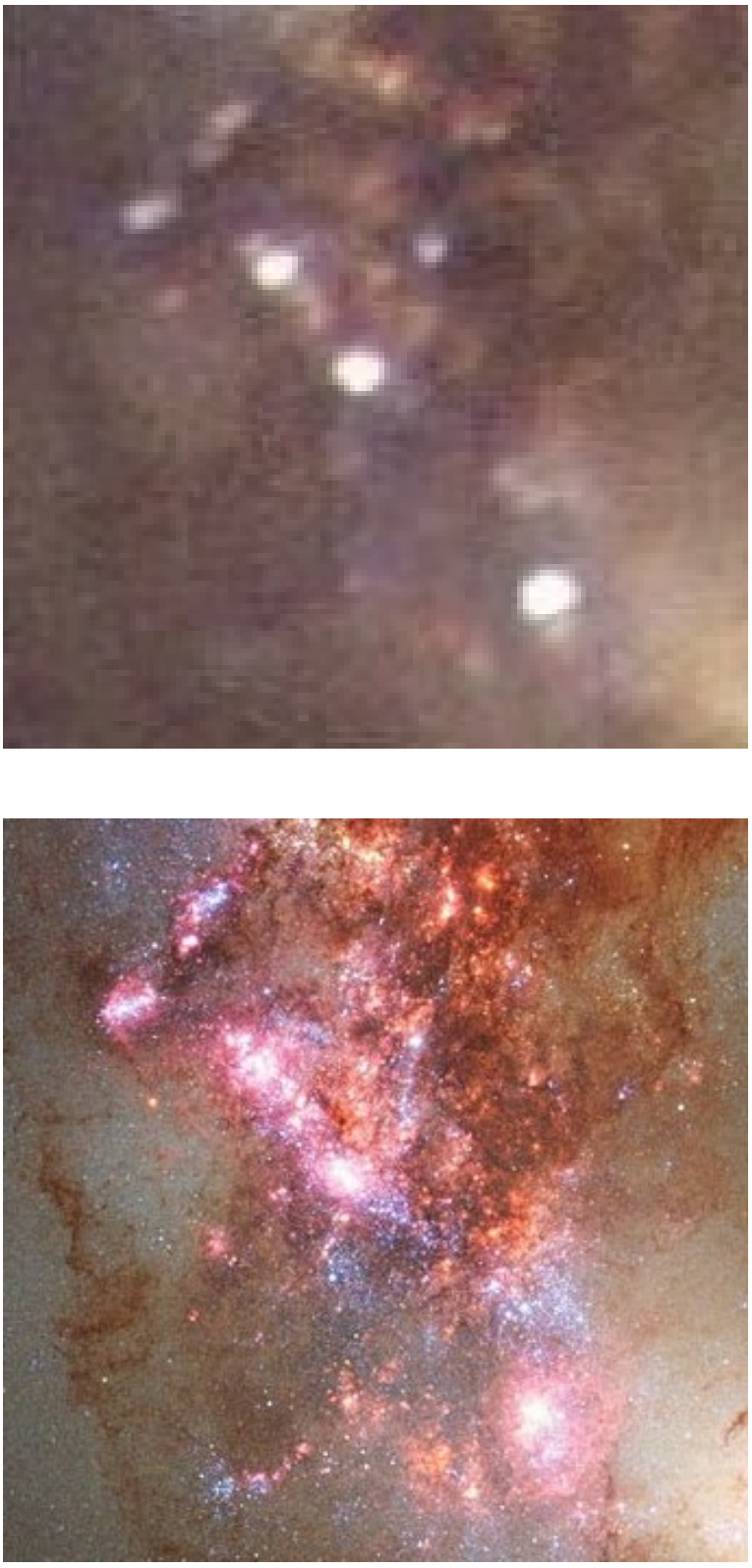

FIGURE 1.4: Comparison between the spatial resolution of ground-based telescopes (*top*) and the Hubble Space Telescope (*bottom*) for a section of the overlap region in the Antennae galaxies (NGC 4038 and NGC 4039). The high angular resolution of 0.05"/pix provided by HST/ACS allows star clusters to be better resolved (Whitmore et al., 1999).

consists of star clusters of a variety of ages, and also star clusters fade dramatically within the first Gyr of their lifetime due to stellar evolution. However, thus far the MF has been well represented by a power-law of the form $\mathrm{d}N/\mathrm{d}M \sim M^{\beta}$ where $\beta \approx$ -2 (Zhang and Fall 1999; Bik et al. 2003), with other studies showing a truncation of the power-law at the high mass end (Gieles et al. 2006b; Bastian 2008; Larsen 2009). Section § 1.4 elaborates more on the MF for clusters.

Star cluster sizes have also been determined in a number of merging and quiescent galaxies, with many showing an effective radius ranging between $\mathrm{r}_{eff} \approx 0.5$ - 10 pc, which is similar to the sizes of YMCs observed in the Milky Way (Larsen 2004a; Lee et al. 2005). Interestingly though, star clusters in the Milky Way have shown a trend for r_{eff} to increase with age (Brandner et al., 2008). A similar increase with age has been observed for the cluster core radius, r_c (Elson et al. 1989; de Grijs et al. 2002). A promising explanation for this observation is that, as a star cluster evolves, a change in the gravitational potential within the cluster causes the cluster to expand and leave its embedded phase (Bastian et al., 2008).

1.4 Formation & Evolution of Star Clusters

1.4.1 Birth of a Star Cluster

It is currently understood that star clusters form when gas clouds condense into stars. Based on the Salpeter IMF, O stars should inhabit star clusters with masses exceeding 10^3 $\mathcal{M}_{\odot}$. Stellar winds from these O stars are expected to expel the vast majority of the remaining gas within a crossing time, and halt further star formation, thereby establishing an upper cluster mass limit of $\sim 10^3$ $\mathcal{M}_{\odot}$ (Hills 1980; Scoville et al. 2001). However, this theoretical mass limit is not observed, with YMCs often found in the mass range of 10^4 - 10^7 $\mathcal{M}_{\odot}$ (e.g., Mengel et al. 2008). Moreover, GCs observed in the Milky Way and other galaxies have masses that exceed 10^4 $\mathcal{M}_{\odot}$ (Rejkuba et al., 2008). Thus, clusters with masses exceeding the theoretical limit are not only created but also survive for billions of years.

There are a few theories that explain the origin of star clusters with masses exceeding 10^3 $\mathcal{M}_{\odot}$. One is simply that the lower-mass star clusters merge to form more massive clusters (Tan and McKee, 2001). Another possibility is the existence of high gas pressures around the proto-cluster. Sufficient external pressure would

increase the difficulty for gas to disperse from within a cluster, and produce clusters with masses exceeding 10^4 $\mathcal{M}_\odot$ and star formation efficiencies between 20% - 50%, which is typically observed in extragalactic star clusters (Jog and Solomon 1992; McLaughlin 1999). These high pressures may not be exclusive to the high velocity impacts of galaxy mergers, and may naturally occur in quiescent disk galaxies (Irwin 1994; Jog and Solomon 1992; Schweizer et al. 1996).

1.4.2 Cluster Evolution

The evolution of YMCs can be split into three phases: (1) A period where gas condense to form stars from a hierarchically structured ISM (Kruijssen, 2012), (2) A period where most of the gas has been exhausted via star formation, and whatever gas remains is expelled from a cluster primarily via stellar winds and supernovae, (3) A later stage where only stellar dynamical processes, such as two body relaxation, dominate the long-term evolution of a cluster. The transition from phase (1) to phase (2) ranges between $\sim$ 1 - 7 Myrs after cluster formation. The dividing line between phase (2) and phase (3) can be anywhere between 100 Myrs and 1 Gyr, depending on properties such as the initial mass, radius, and density profile of a cluster as well as the stellar mass function (Eggleton, 2006).

Phase (1) is the most poorly understood of the three phases, mainly due to the short time-scale and extreme reddening of this phase (Elmegreen 2007; Price and Bate 2009). Phase (1) consists of a complex mix of gas dynamics, stellar dynamics, stellar evolution, and radiative transfer, all of which set up the initial conditions for the later phases. Hence, the poorly constrained parameters of phase (1) lead to uncertainties in the results derived from simulations for phase (2) and phase (3).

Setting aside the uncertainties in phase (1), the latter phases can be studied using N-body simulations. As mentioned, phase (2) occurs around $\sim$ 1 Myr after cluster formation, and represents a period where most to all of the gas within a star cluster has been exhausted via star formation. Whatever gas remaining in the cluster is expelled after the onset of the first supernovae, $\sim$ 3 Myrs after cluster formation (Kruijssen, 2012). Stellar winds from massive stars such as OB types and Wolf-Rayet stars also contribute to gas expulsion (Boily and Kroupa, 2003). The division between gas exhaustion and gas expulsion depends on the gas density within a star cluster. If the density is high enough to lead to gas exhaustion, then

gas expulsion cannot influence the dynamical state of the stars within a cluster. However, a low gas density implies that the stars within a cluster are only held together by the gravitational potential of the gas, and therefore will disperse when the gas is expelled. Young ($<$ 3 Myrs) clusters in the Galaxy and lower mass ($< 10^3$ $\mathcal{M}_\odot$) clusters in the Large Magellanic Cloud (LMC) are generally devoid of gas before the onset of the first supernovae (Seale et al., 2012), suggesting that gas expulsion has no significant contribution to the dynamical stability of a cluster.

Phase (3) commences after this turbulent period. The surviving clusters from phase (2) will now be affected mainly by two body relaxation and tidal stripping. Two body relaxation occurs when stars gravitationally interact within pairs, leading to a redistribution of stars within a star cluster as well as a redistribution of their energies and velocities (Meylan, 2000). This redistribution leads to a mass segregation of stars in a cluster, where the heavier stars settle in the cluster centre, increasing their negative binding energy, while the lighter stars populate the cluster halo and have reduced binding energy. This results in the core of a star cluster shrinking in size and becoming denser, and leads to an accelerating collapse on a time scale of the order of the Hubble time (Spitzer and Shull, 1975). The mechanism is referred to as core collapse (Cohn and Hut 1984; Makino 1996). Tidal stripping is the removal of stars in a star cluster halo due to changes in the external tidal field, which is expected as a star cluster travels around its parent galaxy, particularly when it encounters giant molecular clouds (GMCs) (Spitzer 1958; Kruijssen et al. 2012). The combination of these two mechanisms further removes stars from a cluster and leads to the cluster becoming spherical in appearance as it evolves (Chattopadhyay et al., 2009).

1.4.3 Cluster Initial Mass Function

The history of a star is primarily predetermined by one physical parameter: its birth mass. Hence, knowledge of the initial distribution of mass, or the initial mass function (IMF), and how it varies with time and space is vital in predicting the evolution of stellar systems such as star clusters. Whether the cluster initial mass function (CIMF) is universal or varies between galaxy types had sparked some debate in recent years. Gallagher and Smith (2004) suggest that the high pressures in the interstellar medium (ISM) are responsible for more massive cluster production in mergers and starbursts, whereas the less massive clusters in

quiescent galaxies are just a product of the normal star formation process. This implies that the CIMF is dependent on host galaxy. However, Elmegreen and Efremov (1997) and Larsen (2002) have argued for a universal CIMF based on observations of the luminosity function (LF) of star clusters, which can be taken as an approximate mass function (MF) provided the clusters are all the same age. They found a consistency of the LF in both mergers and quiescent galaxies, and a correlation between the most luminous star cluster in a galaxy and the number of star clusters present, $L_{max} \propto N_{cl}^{\eta}$ where $\eta \approx 0.75$. Indeed, this implies that the more luminous and hence more massive star clusters present in galaxy mergers are simply a statistical effect due to the presence of more star clusters inhabiting a merger and not because of different initial mass functions.

The luminosity function observed in both Galactic and extragalactic surveys is well fit by a power-law of the form $dN/dL \sim L^{\alpha}$ where $\alpha \approx$ -2 (see Figure 1.5). It is tempting to interpret this LF as the underlying cluster mass function, and it was initially thought that the mass function was also a power-law function of the form $dN/dM \sim M^{\beta}$ where $\beta \approx$ -2. However, a power-law CIMF cannot explain the observed mass function in several galaxies. For example, in mergers like the Antennae, the high-mass end of the cluster MF is found to fall more rapidly than a power-law with an exponent of $\beta \approx$ -2 (Gieles et al. 2006b; Bastian 2008). Furthermore, if one assumes a power-law CIMF for star clusters in the Milky Way then star clusters of mass $\sim 10^7 \mathcal{M}_{\odot}$ should statistically exist within 8 kpc from the Sun (Portegies Zwart et al., 2010). A star cluster of such mass would have already been discovered unless it was disrupted, which seems unlikely. A Schechter function (Schechter 1976; see Equation 1.1) was proposed as a solution to these problems and provides a good fit to observational data (Larsen 2009; Gieles 2009).

$$\Psi(M) \equiv \frac{dN}{dM} = M^{\beta} \exp\Big(-\frac{M}{M_c}\Big) \tag{1.1}$$

Here $\beta \simeq$ -2, which is the usual slope of a power-law CIMF, and M_c represents the exponential drop of the mass function (i.e., truncation). The latter is dependent on environment such that quiescent galaxies like the Milky Way have $M_c \approx 2{\times}10^5$ $\mathcal{M}_{\odot}$ while interacting galaxies and mergers show higher values of $M_c \gtrsim 10^6$ $\mathcal{M}_{\odot}$ (Bastian, 2008). Hence, it is possible for mergers to form more massive star clusters than quiescent galaxies. Figure 1.6 shows how well a Schechter function fits the observed mass functions of star clusters from several galaxies.

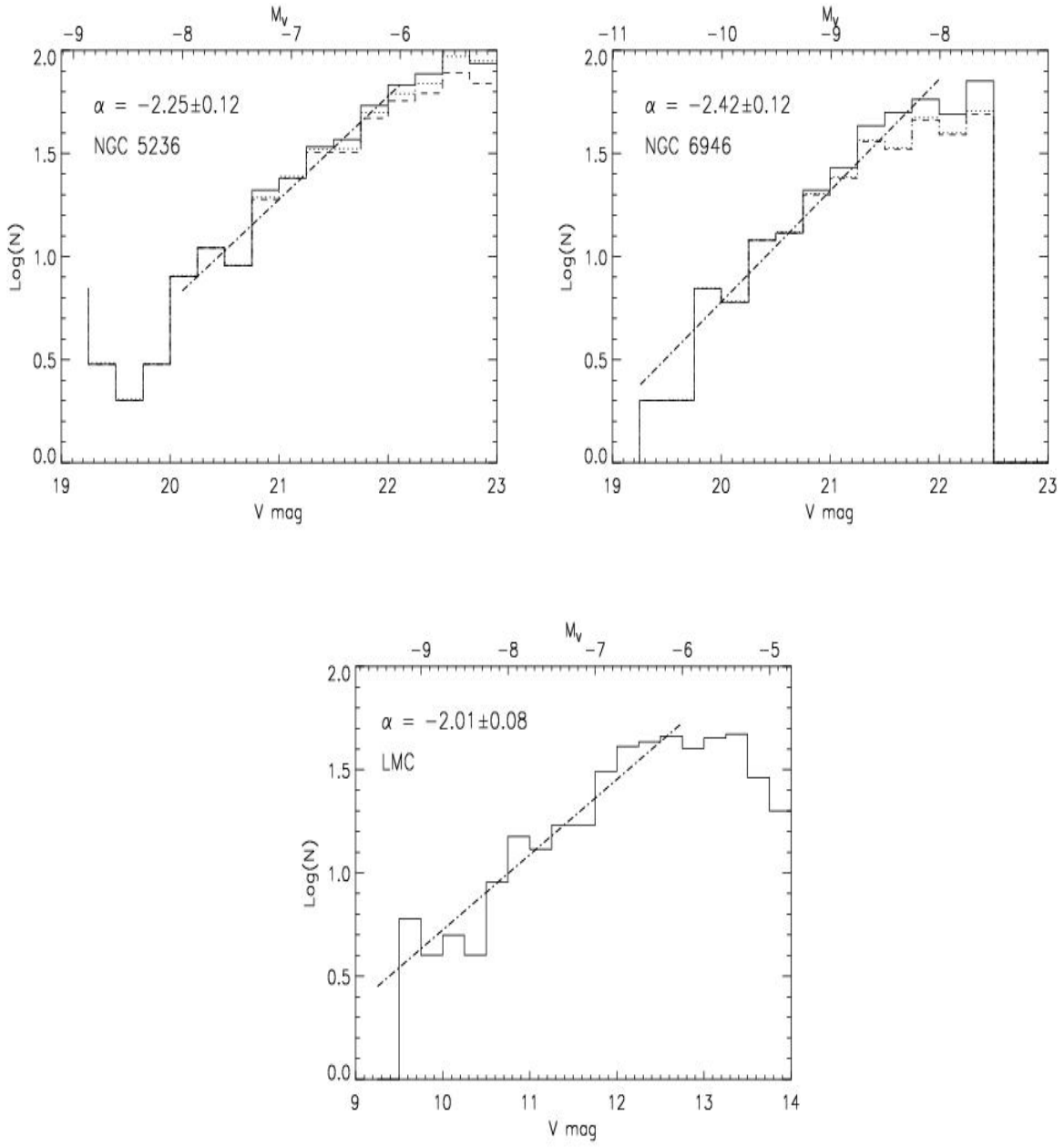

FIGURE 1.5: These plots, produced by Larsen (2002), show the V band luminosity function for star cluster candidates in two spiral galaxies and the Large Magellanic Cloud (LMC). Histograms with dashed lines show the luminosity functions after removal of potential contaminants and corrected for incompleteness while histograms with solid lines represent uncorrected LFs. The dotted-dashed lines represent power-law fits of the form $\mathrm{d}N/\mathrm{d}L \sim L^{\alpha}$ to the uncorrected LFs, where the values of α are shown in each plot.

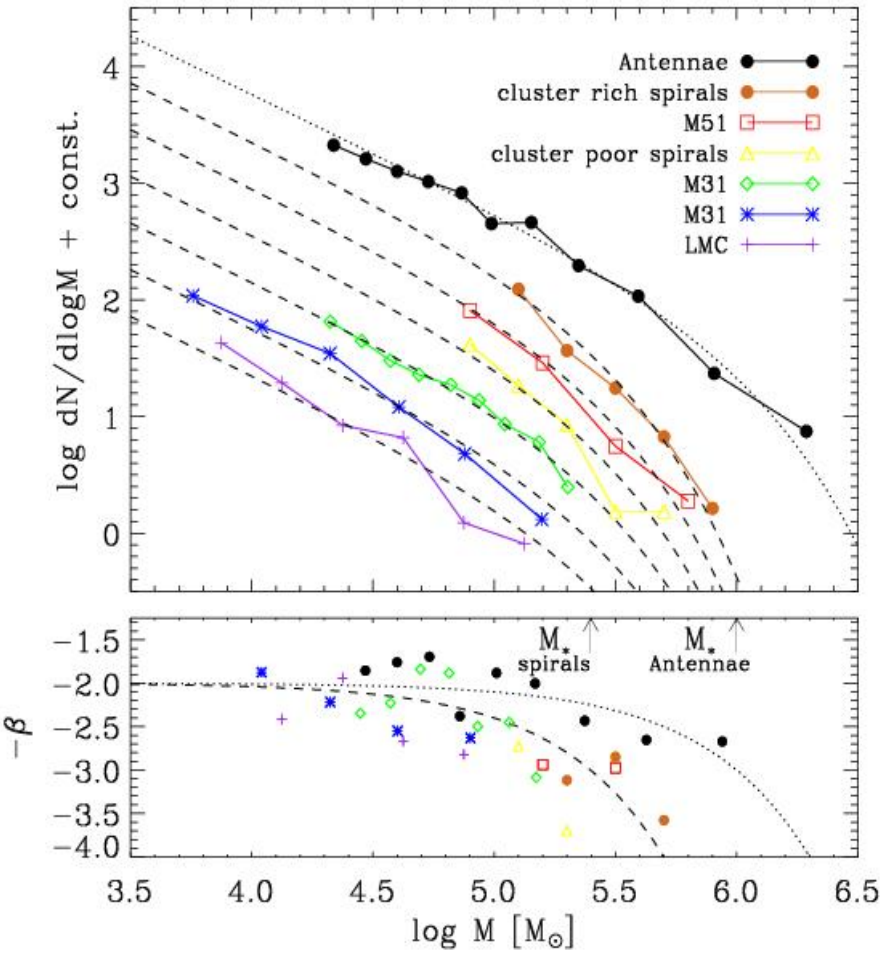

FIGURE 1.6: *Top*: A comparison of star cluster mass functions in several different galaxies. These star clusters are less than a Gyr in age. Results are taken from Zhang and Fall (1999), Gieles (2009), Larsen (2009), and Vansevičius et al. (2009). The 'cluster rich spirals' contain more than 100 star clusters, and the 'cluster poor spirals' have less than 40 star clusters. The plot shows how well a Schechter function with $M_c = 2.5{\times}10^5\ \mathcal{M}_\odot$ (dashed curves) fits to the MF from star clusters in spirals. A comparison between the Antennae cluster MF and a Schechter function with $M_c = 1{\times}10^6\ \mathcal{M}_\odot$ (dotted curve) is also shown. *Bottom*: corresponding logarithmic slopes of these mass functions. The dotted and dashed curves are the logarithmic slopes of the functions shown in the *top* panel. This figure was taken from Portegies Zwart et al. (2010).

1.5 Survival of YMCs and Relationship to Young Globular Clusters

1.5.1 Observations of Globular Clusters

Globular clusters (GCs) are defined as spherical collections of old (> few Gyrs), metal-poor stars, and are intrinsically luminous and present over most of the galaxy mass range (e.g., Peng et al. 2008). These properties have allowed GCs to be used to map galactic structures and trace galaxy formation and evolution (Harris, 1991; Harris and van den Bergh, 1981).

A significant discovery was made from these investigations before the turn of the century from GC surveys in elliptical galaxies. GCs were observed to have a bimodal colour distribution (Zepf and Ashman 1993; Ostrov et al. 1993; Kundu and Whitmore 2001), which indicates that elliptical galaxies harbour two GC populations of different metallicities where the blue population is metal-poor and the red population is metal-rich (Brodie and Strader, 2006). This changed our understanding of galaxy formation. Theories predicting only unimodal GC distributions, such as the Monolithic Collapse model (Larson 1975; Carlberg 1984; Arimoto and Yoshii 1987), were rejected. Instead, theories such as the Major Merger model were used to explain observations. In this model, ellipticals formed via the merger of two or more disk galaxies (Toomre 1977; Ashman and Zepf 1992; Zepf et al. 2000). This resulted in young GCs forming from shocked gas in the disk, giving rise to the red, metal-rich GC population. The blue, metal-poor population of GCs came from the progenitor galaxies. The metal-rich clusters would mainly be located in the inner regions of the elliptical galaxy while the metal-poor clusters harboured the outer regions.

Although the Major Merger model has become a very popular theory for explaining the bimodality of GCs, other plausible theories, such as multiphase dissipational collapse, can also explain bimodality (see Forbes et al. 1997; Cote et al. 1998). Another, more recent finding, is the observation of some GCs that contain stars with different metallicities, which implies that GCs cannot all be treated as simple stellar populations (Renzini 2008; Milone et al. 2009; Conroy and Spergel 2011).

1.5.2 Evolution of YMCs to YGCs

The proposal that YMCs evolve to become young globular clusters (YGCs) has been one of great debate in recent years (Portegies Zwart et al. 2010; Longmore et al. 2014). Essentially GCs are objects which are thought to be the fossils of an ancient period of star formation, hence the inclination to believe they are the descendants of bound YMCs. The scenario is supported by similarities observed in the sizes and masses of YMCs and GCs (e.g., Schweizer et al. 1996; Miller et al. 1997; Whitmore 2003). However, problems arise when comparing their luminosity and mass functions. As shown in § 1.4.3, YMCs have a power-law luminosity function and a mass function well described by a Schechter function (Larsen, 2002, 2009). GCs on the other hand have luminosity and mass functions that are well fit by a Gaussian or log-normal distribution with peak turnovers of $M_V = -7.4$ and $M_{TO} = 2 \times 10^5\ \mathcal{M}_\odot$ for luminosity and mass, respectively (Harris, 1991, 2001). If YMCs are indeed the progenitors of GCs, then their observed luminosity and mass functions must evolve to the log-normal functions observed for GCs.

Many models have been proposed that show the evolution of YMCs to YGCs, the most popular being that of Fall and Zhang (2001). Their models show the plausibility of YMCs evolving to YGCs within a reasonable time period of 12 Gyrs. Through a combination of disruption processes such as stellar evolution (stellar winds, supernovae, etc.), two body relaxation, and tidal stripping of star clusters passing near the disk or bulge of the parent galaxy, their simulations have shown the removal of the low-mass end of YMCs and the production of the familiar bell-shaped turnover observed for GCs (Vesperini 2001; Fall and Zhang 2001; Elmegreen and Hunter 2010). Gaussian mass functions have been produced for both power-law and Schechter CIMFs (with β = -2 and $M_c = 5{\times}10^6\ \mathcal{M}_\odot$).

1.6 Structure of the Thesis

The main goal of the research described in this thesis is to integrate information of the formation of star clusters in galaxy mergers in a range of evolutionary states using both photometric and spectroscopic observations.

Chapter 2 introduces the compact galaxy triplet HCG 90, which consists of two elliptical galaxies of similar mass and size, and a spiral galaxy (Plana et al., 1998).

There is a clear interaction taking place between the spiral NGC 7174 and one elliptical NGC 7176. The purpose of investigating this group is to see whether the interaction between the spiral and elliptical galaxies have caused the production of star clusters. Colour-magnitude diagrams of observed star clusters are presented in this chapter along with their observed luminosity functions.

Chapter 3 presents results from a photometric study of the large elliptical NGC 5128 and a dwarf irregular galaxy (or similar sized gas fragment) which is in the process of merging with the former. A tidally triggered burst of star formation is thought to have occurred in the merger $\sim$ 300 Myrs ago as the dwarf irregular galaxy fell into NGC 5128 and became disrupted (Peng et al., 2002), hence this galaxy merger is likely to have produced a new generation of star clusters. The type of merging taking place here is known as a minor merger or galactic cannibalism (Hopkins et al., 2009), with the much larger NGC 5128 feeding on the dwarf galaxy. Colour-magnitude diagrams of star clusters near the centre of NGC 5128 are presented. Similarities and differences between the physical parameters of star clusters with different observed ages are also presented.

Chapter 4 presents results from a spectroscopic survey of young massive clusters in the Antennae galaxies, a well known major merger that is $\sim$ 400 Myrs old (Mihos et al., 1993) and consists of a pair of spiral galaxies. The merger is relatively close ($\sim$ 20 Mpc away) and has a star formation rate of $\sim$ 20 $\mathcal{M}_{\odot}$ yr^{-1} (Zhang et al., 2001), making it a likely place to find YMCs. Our sample of star clusters was observed with KMOS, a recently commissioned near-infrared spectrograph. Spectra for 47 star clusters were obtained in the YJ, H, K and HK observing mode. Stellar population and environment parameters were derived from absorption and emission line measurements, and were compared to optical and near-infrared measurements in the literature.

Chapter 5 continues with results from further KMOS observations of a smaller, albeit much closer major merger ($\sim$ 10 Mpc), NGC 1487 (Lee and Lee, 2005). HK spectra of nine star clusters are presented. The main conclusions from all these surveys are summarized in Chapter 6.

Chapter 2

Galaxy Interactions in HCG 90

2.1 Introduction

HCG 90 has received limited observational attention partly due to it being only accessible from the southern hemisphere. The group was initially observed by Rose (1977) before being catalogued by Hickson (1982). HCG 90 consists of 19 members with a mean recession velocity of ~ 2600 kms^{-1} and a velocity dispersion ~ 190 kms^{-1} (Zabludoff and Mulchaey, 1998). However it is the core of this group that provides the most interest. The core consists of two bright ellipticals (NGC 7173 and NGC 7176) and an extremely disturbed disk galaxy (NGC 7174), all contained within a $3' \times 3'$ area and surrounded by an extended loose group with a diameter of $\sim 30'$ (de Carvalho et al. 1997; Ribeiro et al. 1998b). Figure 2.1 shows a HST ACS/WFC image of these three galaxies. The galaxies in the core of HCG 90 are all infrared emitters, detected both at 60 and 100 μm (Allam et al., 1996). X-ray observations show strong emission centred on the interacting pair NGC 7174/76 which may follow the spatial distribution of the extended diffuse light component (Ponman et al. 1996; White et al. 2003; Osmond and Ponman 2004; Treister et al. 2005).

While an interaction is obviously occurring between NGC 7174 and NGC 7176, HI observations have also shown a weak interaction taking place between the elliptical galaxy NGC 7173 and NGC 7174 (Oosterloo and Iovino, 1997). The effects of the interaction can still be seen in the morphology of the two galaxies and their stellar kinematics. Plana et al. (1998) studied into the kinematics of the core of HCG

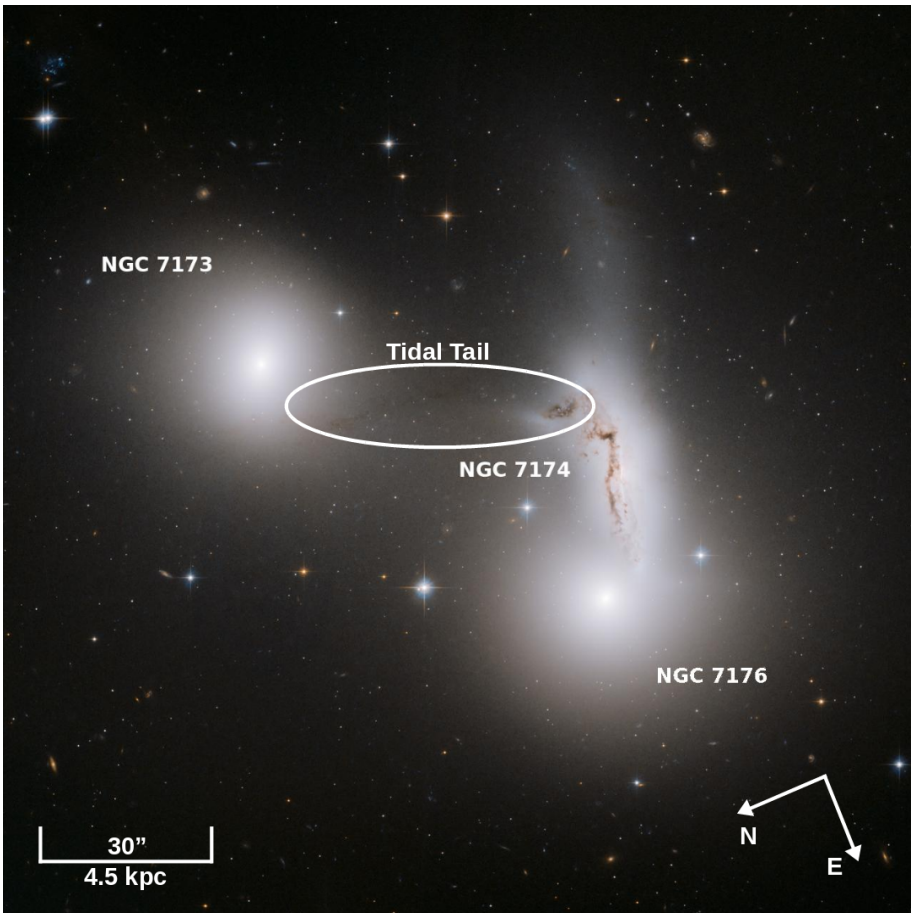

FIGURE 2.1: HST ACS/WFC image of the three tidally interacting galaxies at the centre of HCG 90 using F475W and F850LP filters. The morphology of NGC 7174 is clearly disturbed, likely due to the tidal effects of the two ellipticals. Also, Plana et al. (1998) suggest that the bulk of gas in the elliptical NGC 7176 is concentrated in the region closest to the irregular NGC 7174, suggesting that the latter galaxy is being used as a ‘gas reservoir’ to fuel star formation in the former. Moreover, tidal interactions between NGC 7173 and NGC 7174 has produced a tidal tail extending outward from NGC 7174 towards NGC 7173, as highlighted by the white oval.

90 using Hα emission and detected very disturbed velocity fields which suggests: (1) the three galaxies may be in the process of merging and (2) the emission-line gas associated with NGC 7176 may have an external origin with the disturbed disk galaxy NGC 7174 acting as a gas reservoir. This suggests that the core of the group may also have undergone some relatively recent star formation. In particular, the mixing of gas between NGC 7174 and NGC 7176 makes it a likely place for the formation of new star clusters, and this region was the focal point of the current investigation. It is difficult to precisely estimate the age of the merger. However, merger simulations by Barnes (1988) and Mihos et al. (1993) along with

Parameter	NGC 7174	NGC 7176
Other names[a]	HCG90b	HCG90d
Morphological type[b]	Sab pec	E pec
$\alpha_{\rm J2000}$[b]	$22^{\rm h}02^{\rm m}06\overset{\rm s}{.}8$	$22^{\rm h}02^{\rm m}08\overset{\rm s}{.}5$
$\delta_{\rm J2000}$[b]	$-31°59'36''$	$-31°59'29''$
$b_{\rm J2000}$[b]	-53.1°	-53.1°
M_B[c]	-20.2	-20.4
D (Mpc)[d]	31.3 ± 2.9	31.3 ± 2.9
Systemic heliocentric velocity (kms^{-1})[a]	2525 ± 30	2778 ± 30

TABLE 2.1: Basic parameters for NGC 7174 and NGC 7176 taken from the literature. [a] Hickson et al. (1992), [b] White et al. (2003), [c] Lauberts and Valentijn (1989), [d] Plana et al. (1998). Different values of distance have been used in other studies (e.g., Barkhouse et al. 2001).

observations of merging galaxies in their final stage of merging (e.g., Schweizer and Seitzer 1998) have shown that galaxies typically require $\sim$ 1 Gyr to completely merge. Since NGC 7174 and NGC 7176 are still in the process of merging, we estimate that the merger event began $<$ 1 Gyr ago. Basic parameters for NGC 7174 and NGC 7176 are listed in Table 2.1.

HST ACS/WFC images were acquired in 2006 as part of program GO-10554. The observations consist of one pointing centred between the two most luminous galaxies (NGC 7173 and NGC 7176) at $\alpha_{\rm J2000} = 22^{\rm h}02^{\rm m}03\overset{\rm s}{.}94$, $\delta_{\rm J2000} = -31°59'34''$. Four sub-exposure images were taken in F475W (1×340, 3×345 seconds) and F850LP (1×639, 1×774 and 2×831 seconds) which were then combined and geometrically corrected using the *Multidrizzle* package from the ACS pipeline, giving total integration times of 1375 and 3075 seconds for the F475W and F850LP filter, respectively. The final drizzled images consist of a 4096×4096 pixel science image in units of electrons/s and an error map in the second extension that contains all error sources such as readout noise, dark current, and photon noise. ACS/WFC has a pixel scale of $0\overset{''}{.}05$ per pixel which corresponds to $\sim$ 8 parsecs at the adopted distance for HCG 90. Galactic reddening values of $A_{F475W} = 0.087$ mag and $A_{F850LP} = 0.033$ mag are used throughout this investigation (Schlafly and Finkbeiner, 2011).

The structure of this chapter is as follows: Section § 2.2 summarizes the data analysis and reduction procedures, photometry results are presented in section § 2.3 and discussed in section § 2.4. Our conclusions are summarised in § 2.5.

2.2 Data Reduction

2.2.1 Galaxy Light Subtraction

As discussed in § 2.1, the interacting galaxies NGC 7174 and NGC 7176 are observed to have an irregular and elliptical morphology, respectively. Moreover, the brightness of the two galaxies along with any diffuse light limits the ability to detect star clusters at fainter magnitudes. Thus, it was decided to subtract the background light from each galaxy individually in order to improve the detectability of cluster candidates.

In the case of NCG 7176 the smooth galaxy light was fitted with elliptical isophotes using the *IRAF/ELLIPSE* routine. NGC 7174 was completely masked before running this routine. This ensured that starlight from NGC 7174 did not affect or distort the modelling of NGC 7176. Fitted ellipse parameter tables were then used to build galaxy model images using the task *IRAF/BMODEL* which were then subtracted from the original images.

Removing the galaxy light from NGC 7174 proved less trivial since there are no analytic models that can fit such a disturbed galaxy. Therefore, images with the NGC 7176 galaxy light subtracted were first smoothed using the task *IRAF/F-MEDIAN*. This routine found the median pixel counts in 7×7 pixel boxes for both g band and z band images. The smoothed frames were then subtracted from the input frames (frames already subtracted for NGC 7176 galaxy light), giving frames with galaxy light from both NGC 7174 and NGC 7176 subtracted. Figure 2.2 shows different stages of the galaxy light subtraction methods.

The combination of the two subtraction methods provided images that were well subtracted for galaxy continuum light, and improved the efficiency of detecting clusters near the central regions of the two galaxies. However, the varying brightness of the dust lane proved difficult to subtract and could not be removed perfectly. This area was therefore eliminated from the cluster detection procedure (see § 2.2.2).

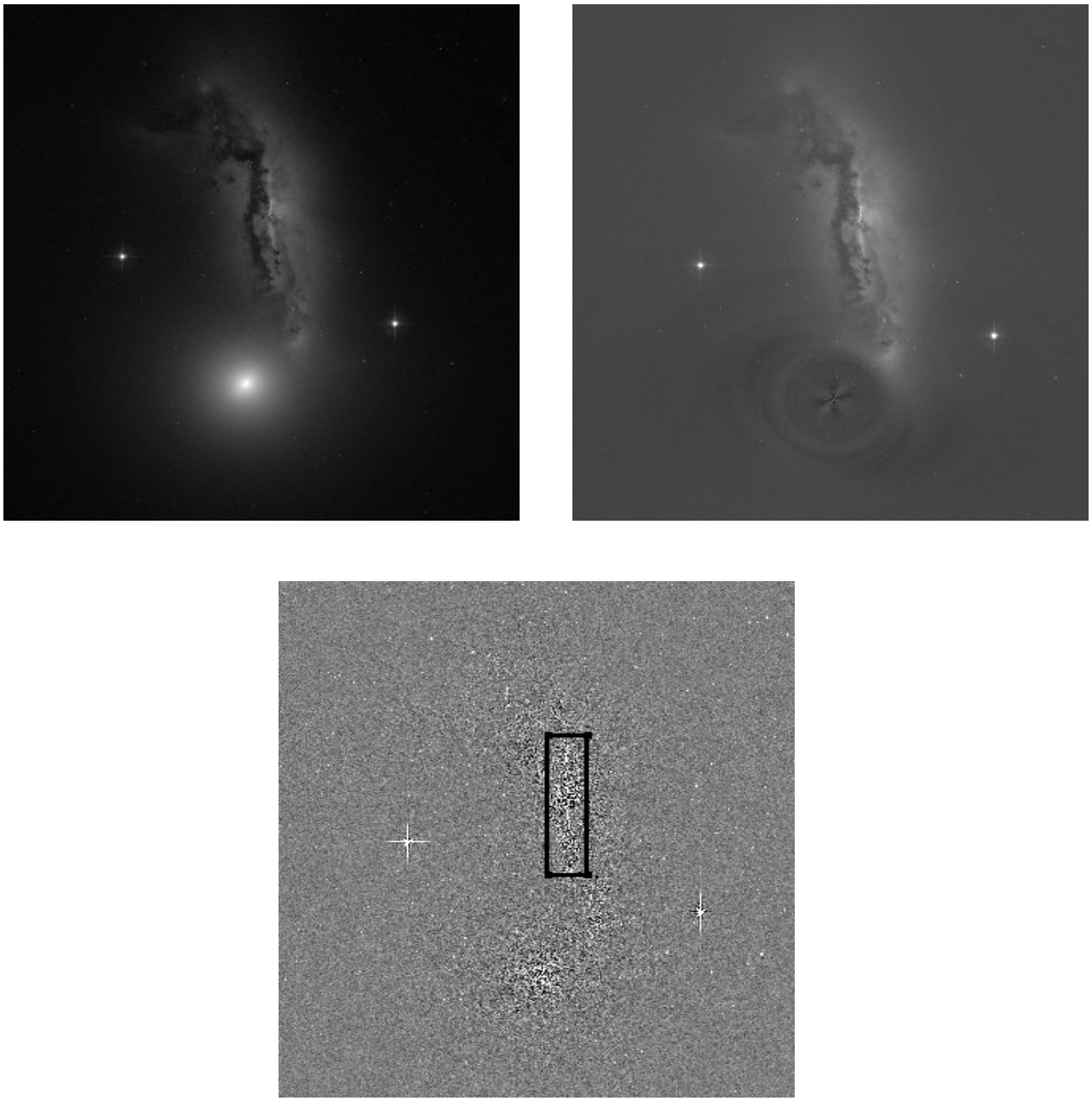

FIGURE 2.2: Results from galaxy light subtraction performed on the F475W frame for NGC 7174 and NGC 7176. *Top-Left*: original HST/ACS image of NGC 7174/76. *Top-Right*: result of galaxy light subtraction for NGC 7176. *Bottom*: galaxy light subtracted for NGC 7174 and NGC 7176. The black box represents an area of very distorted isophotes where sporadic fluctuations of the galaxy light became difficult to subtract. Many of the objects detected within this box were found to be false detections. Thus, all detections within the black box were rejected.

2.2.2 Cluster Detection and Selection

SExtractor (Bertin and Arnouts, 1996) was run on the galaxy light subtracted images in order to detect star cluster candidates with an isophotal detection threshold, `DETECT_THRESH` $> 3\sigma$ above the background. Among the detected objects, those with `ELONGATION` > 2 in either the F475W or F850LP band were rejected. Empirical data show that star clusters have ellipticities corresponding to `ELONGATION` < 2 (Harris et al., 2012). Also, any objects with `CLASS_STAR` < 0.9 and `MAG_BEST` < 20 in the F475W band were rejected. The former criterion successfully retrieved GCs in the neighbouring galaxy NGC 7173 (Cho et al., 2012), and the magnitude limit is based on the luminosity of the brightest observed Super Star Clusters (SSCs) in the Antennae galaxies (Gilbert and Graham, 2007). Some bad pixels found at the edges of both frames managed to pass this stage of the selection criteria. These were manually removed.

The galaxy light subtracted images also had some distortion around the central region of the irregular galaxy NGC 7174 where fluctuations of galaxy light became very sporadic. Many of the objects detected in this region were found to be false detections produced from over-subtracting parts of the dust lane during the galaxy light subtraction procedure. Thus, objects detected within a $10'' \times 40''$ box centred on NGC 7174 in both F475W and F850LP images were rejected (see Figure 2.2). Objects were matched within a 2 pixel radial separation across the two bands.

The selection criteria reduced an initial sample of 1000 detected objects to a sample of 160 star cluster candidates detected in both bands that have image parameters similar to those expected for star clusters at the distance of NGC 7174/76.

2.2.3 Cluster Photometry

Aperture photometry was performed using the *IRAF/PHOT* package on the galaxy light subtracted images for objects that passed the selection criteria given in § 2.2.2. The FWHM results for cluster candidates from the *SExtractor* routine were inspected and used to determine a suitable aperture radius for photometry. An aperture radius of 6 pixels and a sky annulus of 2 pixels were adopted for all cluster candidates. Background measurements were taken at a distance of 8 pixels from the centre of each cluster candidate, ensuring good estimates of the local background.

Zeropoints were adopted from the latest and improved photometric calibration of the ACS listed on the STScI website[1], which supersedes the previous values given by Sirianni et al. (2005). ACS/WFC zeropoints at −81°C were adopted since ACS frames used in this study were acquired in May 2007 (i.e., after July 2006 when the temperature of the WFC detector was lowered from −77°C following the recovery of the ACS).

A correction for Galactic extinction was also added using the Schlafly and Finkbeiner (2011) recalibration of the Schlegel et al. (1998) extinction map values, giving extinction values of $A_{F475W} = 0.087$ mag and $A_{F850LP} = 0.033$ mag. Hereafter, g and z magnitudes refer to the F475W and F850LP extinction-corrected AB magnitudes. A colour-magnitude diagram of the star cluster candidates is shown in Figure 2.4.

2.2.4 Completeness Tests

Completeness tests were made to evaluate the effectiveness of the proposed cluster detection and selection method. A sample of 1000 artificial clusters with a uniform luminosity function, AB magnitudes ranging from 20 to 28, and a uniform spatial distribution was generated using the *IRAF/STARLIST* routine. *IRAF/MKOBJECTS* was then used to add these artificial clusters to the galaxy light subtracted images produced in § 2.2.1. This ensured the artificial clusters were subject to the same noise sources such as crowding and background fluctuations as the original star cluster candidates. The artificial clusters were then run through the same detection algorithms used in § 2.2.2 and the initial coordinates of the artificial clusters were matched with those of the recovered clusters. Artificial clusters within 2 pixels of their initial coordinates were accepted while those exceeding this limit were rejected. The fraction of recovered clusters were calculated for a given magnitude bin and are plotted in Figure 2.3.

The results were then fitted with a completeness curve of the form:

$$f = \frac{1}{2}\left(1 - \frac{a(m - m_0)}{\sqrt{1 + a^2(m - m_0)^2}}\right) \tag{2.1}$$

[1]Zeropoints and details on the new calibrations can be found on http://www.stsci.edu/hst/acs/analysis/zeropoints

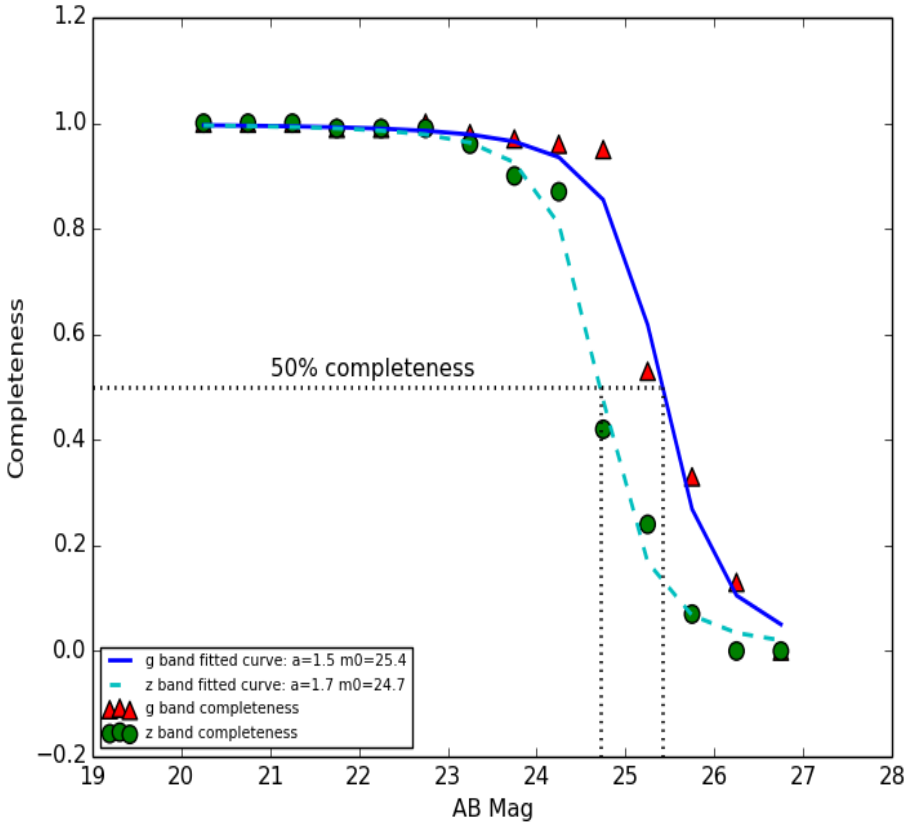

FIGURE 2.3: The completeness of star cluster detections in NGC 7174 and NGC 7176. The red triangles and green circles denote the completeness of the g and z bands respectively. The blue and cyan lines are the fitted curves from Equation 2.1 for the g and z bands respectively. 50% completeness limit is marked with the black dashed lines, providing values of $g = 25.4$ and $z = 24.7$ for the two respective bands.

where m_0 is the magnitude when f is 0.5 and a controls how quickly f declines (the larger the value of a, the steeper the transformation from 1 to 0) (Fleming et al., 1995). Figure 2.3 shows the resultant completeness curves for the two bands. One can see the completeness levels in z decline at a brighter magnitude than in g. This is primarily due to the difference in zeropoints of the two frames, with the z frame using a brighter zeropoint magnitude than the g frame.

2.2.5 Contaminating Sources

Finally, the images were corrected for contamination by background galaxies. Contamination by foreground stars is small at magnitudes greater than the limit specified in the selection criteria (see § 2.2.2). Although it is impossible to completely

α_{J2000}	δ_{J2000}	b_{J2000}	No: exposures per filter	Exposure time(secs) F475W/F850LP
$12^h22^m54^s.9$	$-72°23'25''$	-09.6°	6	3600/3407
$10^h34^m04^s.1$	$58°58'02''$	50.3°	6	4201/4921
$14^h18^m29^s.7$	$24°59'18''$	70.4°	5	3000/2942
$12^h10^m54^s.9$	$39°13'59''$	75.2°	4	2400/2400
$11^h13^m32^s.7$	$22°15'53''$	67.2°	3	1577/1800
$12^h43^m29^s.1$	$11°49'24''$	74.6°	3	1601/1800

TABLE 2.2: Co-ordinates and exposure times of blank fields used in § 2.2.5.

remove individual background galaxies, it is possible to statistically correct for their presence using 'blank' comparison fields. The ACS archive was searched for high Galactic latitude blank fields that were observed with the same filters and similar exposure times to the HCG 90 frames used above. In total 6 blank fields were retrieved (proposal ID: 9488). Their exposure times along with the RA and Dec of the field centres are listed in Table 2.2. Each field was run through the same cluster detection and selection procedures as discussed in § 2.2.2.

One out of every six objects that passed the selection criteria were then randomly selected and added to the colour distribution and luminosity function plots shown in Figure 2.5 and Figure 2.6, respectively. Since the blank fields selected are deeper than those used for the HCG 90 observations, the completeness limits obtained for both g and z bands (see § 2.2.4) were also applied. These contamination estimates were then used in the subsequent analysis presented below.

2.3 Results

2.3.1 Colour Distribution

Colour and magnitude cuts were then applied to the remaining star cluster candidates. A colour cut of $0.6 < (g-z)_0 < 1.7$ was used by Cho et al. (2012) and Jordán et al. (2007) during their studies of old (> 2 Gyr) GCs in elliptical galaxies. A similar red limit was applied in the analysis presented here. However, as discussed in § 2.1, NGC 7174/76 are likely to host a new population of star clusters that show bluer colours than GCs observed in passive or isolated ellipticals. Therefore the lower limit for the colour cut used by Cho et al. (2012) and Jordán

et al. (2007) requires adjustment in order to include these younger star clusters. The $g-z$ colours from stellar population synthesis (SPS) models for a metallicity range of -1.35 < [Fe/H] < +0.35 were investigated to determine this lower limit (Maraston, 2007). A lower limit of $(g-z)_0 = -1.2$ was adopted from this investigation, resulting in a final colour cut of $-1.2 < (g-z)_0 < 1.7$. This colour cut corresponds to ages between 0 - 14 Gyrs for stellar populations in the range of -1.35 < [Fe/H] < +0.35. In addition to this lower limit, the models showed colours of $(g-z)_0 > 0.6$ for all populations exceeding 1 Gyr in age. Based on galaxy merger models (Barnes 1988; Mihos et al. 1993), the interaction between NGC 7174 and NGC 7176 is unlikely to be older than 1 Gyr in age, hence any new populations of star clusters will have ages < 1 Gyr. This age constraint provides a colour range of $-1.2 < (g-z)_0 < 0.6$ for these new star clusters.

It is worth noting that colours measured from our star cluster candidate sample may be affected by internal extinction. Based on Galactic reddening values for the g and z bands ($A_{F475W} = 0.087$ mag and $A_{F850LP} = 0.033$ mag, respectively), an extinction of $A_V = 1$ mag will result in a colour reddening of $g-z = 0.47$ and an extinction of $A_V = 2$ mag will have a colour reddening of $g-z = 0.94$. However, our candidate cluster sample is generally located away from the dust lane area in NGC 7174/76 and therefore may suffer from low internal extinction.

The lower magnitude limit cut was set to $g < 25.5$, which corresponds to a completeness of $\sim 50\%$ (see Figure 2.3). Combining this with the upper magnitude limit discussed in § 2.2.2 gives a magnitude range of $20.0 < g < 25.5$. The adopted colour and magnitude cuts further refined our sample to 140 star cluster candidates. Figure 2.4 shows the final sample of star cluster candidates and the applied colour and magnitude limits.

Figure 2.5 shows the spread in colour over the applied limits. The raw distribution, corrected for incompleteness, is drawn with a green histogram. In § 2.2.5, it was noted that the raw distribution will contain some background galaxies. However, as can be seen from the red histogram, the contribution from background galaxy contamination is quite small ($\sim 5\%$). For each colour bin, the number of contaminating objects were removed from the raw distribution. The resultant background contamination-corrected colour distribution is displayed as the blue histogram. For comparison, the colour distribution recorded for globular clusters in NGC 7173 by Cho et al. (2012) is overplotted in orange.

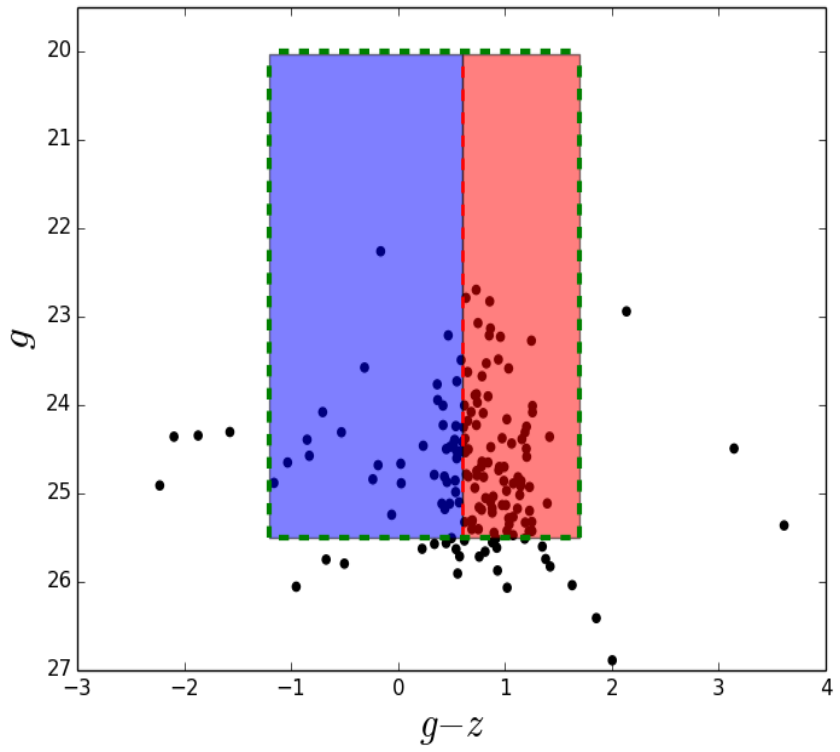

FIGURE 2.4: Colour-magnitude diagram of star cluster candidates. The dashed green box indicates the applied colour and magnitude cuts. The red region represents star cluster candidates exceeding 1 Gyr in age for a metallicity ranging between -1.35 < [Fe/H] < +0.35. The bulk of the candidates show colours in the range $0.6 < (g-z)_0 < 1.7$, typical for old extragalactic GCs (Jordán et al. 2007; Cho et al. 2012). The blue region represents star cluster candidates with $(g-z)_0 < 0.6$ which correspond to ages less than 400 Myrs (Maraston, 2007). The dashed red line represents a colour of $(g-z)_0 = 0.6$, which corresponds to an age of 400 Myrs at [Fe/H] $= -1.35$.

The GC population in NGC 7173 has a bimodal colour distribution with peaks at $g-z = 0.98$ and 1.38 respectively, and a mean value of $\langle (g-z)_0 \rangle = 1.13 \pm 0.02$. NGC 7174/76 shows a peak colour value of $g-z = 0.62$ and a mean colour of $\langle (g-z)_0 \rangle = 0.71 \pm 0.04$. Thus, the colour distribution of star cluster candidates observed in the NGC 7174/76 pair is bluer than that of its near neighbour. This bluer colour distribution is likely the result of tidal interactions taking place between NGC 7174 and NGC 7176, since tidal interactions are expected to produce high gas pressures which lead to the formation of massive star clusters with very blue colours (Jog and Solomon 1992; Elmegreen and Efremov 1998; Ashman and Zepf 2001). Indeed, 30% of star cluster candidates in NGC 7174/76 have very blue colours ($g-z < 0.6$) corresponding to ages < 400 Myrs for a metallicity ranging

between -1.35 < [Fe/H] < +0.35 (Maraston, 2007), whereas the remaining population in our sample have $g-z$ colours corresponding to ages of $\sim$ 6 Gyrs, typical for old GCs. Given that the merger is unlikely to be older than 1 Gyr (Barnes 1988; Mihos et al. 1993), these colours indicate that tidal interactions in NGC 7174/76 may have produced a moderate population of new star clusters. Moreover, the colours derived for our candidate sample may be affected by internal extinction. Therefore, the blue cluster candidates in our sample may be younger than determined from SPS models.

Previous work by Longo et al. (1995) also found an excess of blue star clusters in the core of HCG 90. The authors found a mean $B-R$ colour index of $\langle B-R\rangle = 0.8 \pm 0.1$, and a peak value of $B-R = 0.5$. Using the SPS models, and assuming a metallicity range of -1.35 < [Fe/H] < +0.35, provides an age ranging between 300 - 500 Myrs for their cluster sample. This age range is in agreement with ages obtained for the bluest candidates in our sample.

2.3.2 Luminosity Function

From the final sample of 140 star cluster candidates, 70% of the star cluster population in NGC 7174/76 show colours ranging between $0.6 < (g-z)_0 < 1.7$ and are likely to be old GCs. Several studies have shown that the luminosity functions of extragalactic GCs can be used as a distance indicator (e.g., Villegas et al. 2010; Rejkuba 2012). This method of determining distance has also been performed on the neighbouring NGC 7173 by Cho et al. (2012). Generally, elliptical galaxies have been used for this method since they harbour a large population of old ($\sim$ several Gyrs) GCs and no young star clusters. Hence, it is interesting to see whether this method of determining distance can still provide reliable results when applied to a star cluster population which may contain a mixture of young and old star clusters.

The globular cluster luminosity function $\phi(m)$ can be fitted using the well known Gaussian distribution shown by Equation 2.2. Here, A is a constant related to the total globular cluster population, m is the apparent magnitude of individual globular clusters, m_o is the magnitude of the turnover, and σ is the dispersion (Harris, 1991). A value of $\sigma = 1.3$ is often applied, based on globular cluster luminosity functions observed from several galaxies (Harris, 1991, 2001).

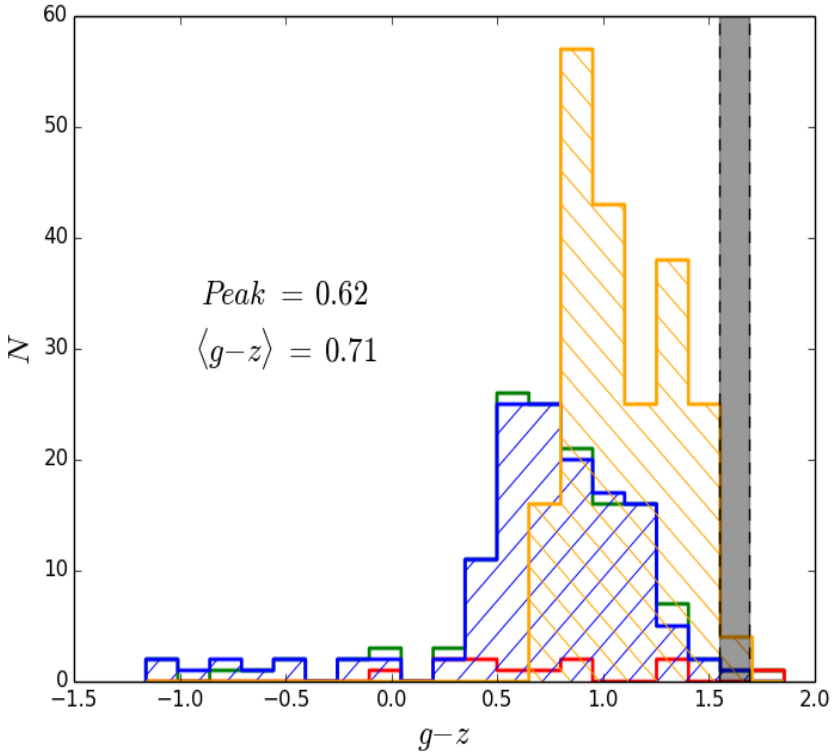

FIGURE 2.5: Colour histograms for compact objects observed in the core of HCG 90: The blue histogram represents the colour distributions of star cluster candidates in NGC 7174/76 after correction for background contamination. The green and red histograms represent the colour distribution of the raw data and the contamination estimates, respectively. The contamination-corrected colour distribution of globular clusters from the neighbouring elliptical galaxy NGC 7173 is shown as the orange histogram (Cho et al., 2012). Lastly, the black filled region represents the range of colours observed for the diffuse intracluster light (White et al., 2003).

$$\phi(m) = A\ exp\left[\frac{-(m-m_o)^2}{2\sigma^2}\right] \tag{2.2}$$

Figure 2.6 shows Gaussian fits to g and z band magnitudes for our star cluster candidate sample, which have colours ranging between $-1.2 < (g-z)_0 < 1.7$. The green histograms represent the magnitude distribution of our star cluster candidate sample, corrected for incompleteness and background galaxy contamination. These were fitted with a Gaussian function up to the 50% completeness limits of $g = 25.4$ and $z = 24.7$. The calculated peak magnitudes are also labelled in Figure 2.6. These peak magnitudes can be used as a secondary distance indicator if a large population of GCs exist in the host galaxy. Hence, the turnover magnitudes from these plots were used with the peak absolute magnitude values of $\mu_g = -7.2 \pm 0.2$

and $\mu_z = -8.4 \pm 0.2$ from the GCLF obtained by Jordán et al. (2007) to determine the distance modulus of NGC 7174 and NGC 7176. Based on the fitting parameters shown in Figure 2.6, distance moduli of $(m - M)_g = 32.3 \pm 0.2$ and $(m - M)_z = 32.7 \pm 0.2$ were obtained for the g and z bands, respectively. These result in distances of $d_g = 28.8 \pm 2.6$ Mpc and $d_z = 34.7 \pm 3.1$ Mpc, respectively.

Cho et al. (2012) observed the GC population in the neighbouring, more isolated elliptical galaxy NGC 7173 and also used the GCLF as a distance indicator. Their sample consisted of 208 GCs and observations were made with the same ACS filters used in the survey presented here (F475W and F850LP), which allows a direct comparison between both studies. They determine distance moduli of $(m-M)_g = 32.5 \pm 0.3$ and $(m - M)_z = 32.8 \pm 0.3$ for NGC 7173 in the g and z bands respectively, which correspond to distances of $d_g = 33.1$ Mpc and $d_z = 31.3$ Mpc. The distances obtained by Cho et al. (2012) are therefore in good agreement with the distances obtained for NGC 7174 and NGC 7176 from our analysis. Moreover, our distance measurements are in agreement with Faber et al. (1989), who determined a distance of 31.3 ± 2.9 Mpc to NGC 7174/76 using a $D_n - \sigma$ relation for their galaxy sample.

2.3.3 Ellipticity & Half-Light Radii

Numerical simulations have shown the half-light radius (or effective radius) r_e of old globular clusters to be fairly constant throughout their dynamical evolution (Spitzer and Thuan 1972; Murphy et al. 1990; Aarseth and Heggie 1998). However, surveys of GCs in external galaxies have shown that the median half-light radii can vary between metal-poor and metal-rich GC populations (e.g., Kundu et al. 1999; Larsen et al. 2001). These studies found that metal-rich GCs in early-type galaxies have $\sim 20\%$ smaller half-light radii than metal-poor GCs. Portegies Zwart et al. (2010) also found that the half-light radii of star clusters may increase during their first 100 Myrs due to gas expulsion by supernovae. In addition, observations of star clusters in the Large Magellanic Clouds (LMC) show a weak trend for the ellipticity to decrease with age (Kontizas et al., 1989). If the blue cluster candidates in our sample are indeed a new population of star clusters, it would be interesting to see if they show smaller half-light radii or appear more elliptical than the red cluster candidate population.

Ellipticities and half-light radii for the star cluster cluster candidates were determined using the *ISHAPE* routine, which is implemented in the data reduction package *BAOLAB* (Larsen, 1999). *ISHAPE* convolves a user provided PSF with an analytic elliptical profile for a range of sizes until the best fit between the observed light profile and model profile is obtained. A King profile (King, 1962) with a concentration parameter of 30 has been used for several cluster surveys and was adopted here (e.g., Mengel et al. 2008; Bastian et al. 2009).

Figure 2.7 shows histograms for the ellipticity and half-light radii (r_e) measured in the g band for each star cluster candidate, in addition to ellipticity *vs* colour and half-light radii *vs* colour diagrams. The colour scheme used in the figure separates the candidates based on the colour cuts presented in § 2.3.1. The red histogram represents clusters with colour values between $0.6 < (g-z)_0 < 1.7$ and the blue histogram represents clusters with colours between $-1.2 < (g-z)_0 < 0.6$. Likewise, the red circles represent red cluster candidates and the blue circles represent blue cluster candidates.

In general, the ellipticity peaks around $\epsilon_{peak} = 0.08$ with a mean value of $\langle\epsilon\rangle = 0.11 \pm 0.01$. Separating the cluster candidates into blue and red groups does provide some correlation between ellipticity and $g-z$ colour. Blue clusters have a mean value of $\langle\epsilon_{blue}\rangle = 0.14 \pm 0.02$ while red clusters have a value of $\langle\epsilon_{red}\rangle = 0.09 \pm 0.01$ for the ellipticity. However, this is almost entirely due to a few outlying blue cluster candidates which are more flatter than their red counterparts, as would be expected if these bluer objects are indeed a population of very young star clusters (Kontizas et al., 1989).

The bottom-right panel of Figure 2.7 shows the colour *vs* half-light radii distribution of the star cluster candidates. No significant correlation between colour and half-light radii is observed for these star cluster candidates, as both red and blue star cluster populations have a mean value of $\langle r_e\rangle = 2.5 \pm 0.2$ parsecs. The observed sizes fall within the range expected from young star clusters and old GCs (Chies-Santos et al. 2006; Woodley and Gómez 2010). Hence, under the assumption that the blue ($g-z < 0.6$) population of star clusters presented in this survey were formed from tidal interactions around NGC 7174/76, any trend of young star clusters showing smaller half-light radii than old GCs is not observed in NGC 7174 and NGC 7176.

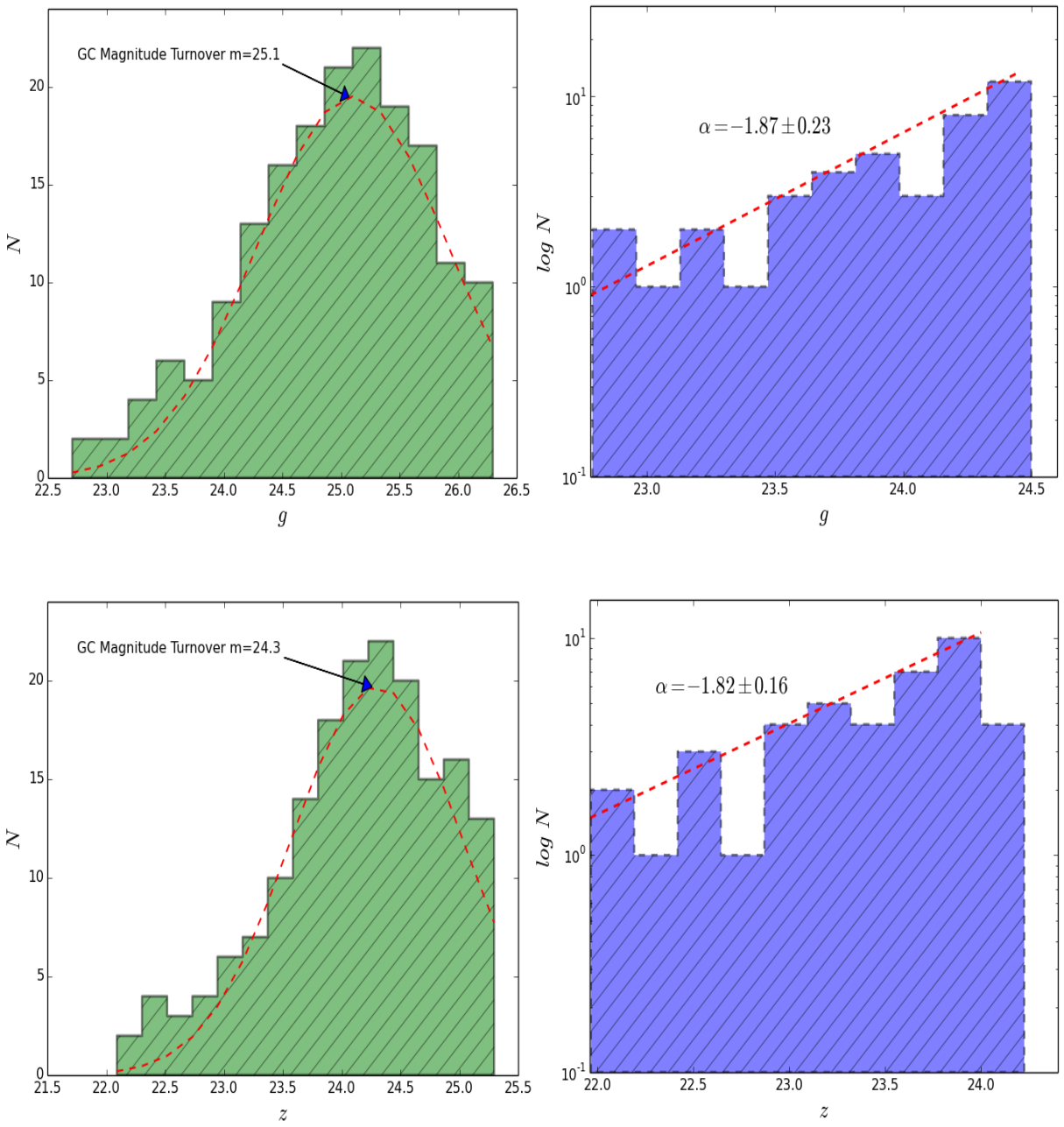

FIGURE 2.6: Luminosity functions of our star cluster candidates. *Top-left*: Magnitude distribution of our entire star cluster candidate sample in the g band fitted with a Gaussian luminosity function (Equation 2.2) with a magnitude turnover of $g = 25.1$ and dispersion of $\sigma = 1.2$. *Bottom-left*: Same as *top-left* but for the z band and a Gaussian fit with a magnitude turnover of $z = 24.3$ and dispersion of $\sigma = 1.2$. *Top-right*: Magnitude distribution of blue ($g - z < 0.6$) cluster candidates in our sample in the g band fitted with a power-law function of the form $\mathrm{d}N/\mathrm{d}L \sim L^{\alpha}$ where $\alpha = -1.87 \pm 0.23$. *Bottom-right*: Same as *top-right* but for the z band and a power-law fit where $\alpha = -1.82 \pm 0.16$. It is worth noting that the distribution in these plots is dependent on the binning choice. A coarse binning approach will not give much information on the shape of the cluster distribution, while more frequent binning will produce empty bins and a noisy histogram.

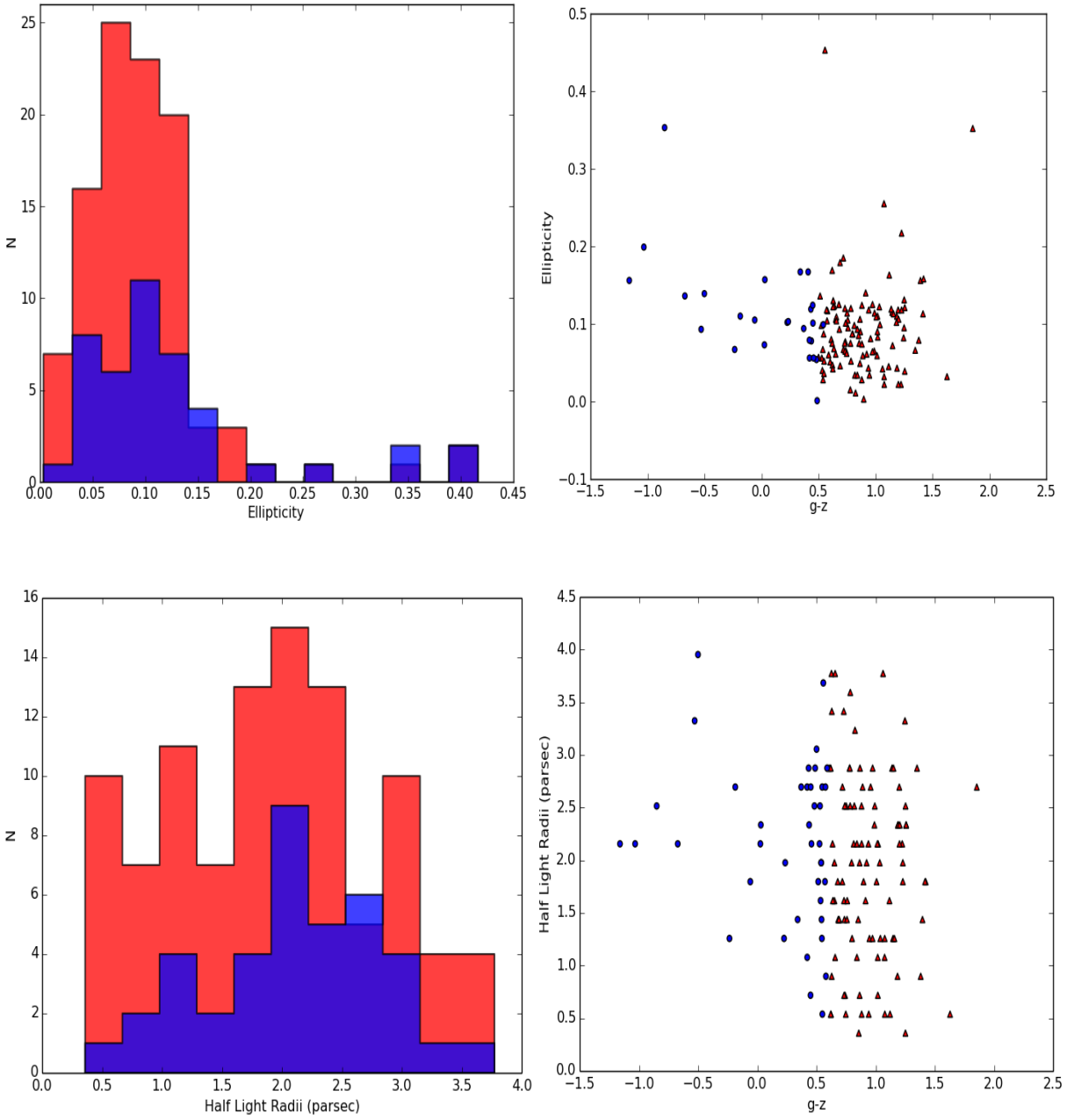

FIGURE 2.7: Physical properties of star cluster candidates. Distribution of ellipticity (*top-left*) and half-light radii (*bottom-left*); Variation of colour with ellipticity (*top-right*) and half-light radii (*bottom-right*). Blue cluster candidates are represented by blue histograms while red cluster candidates are represented by red histograms. Both cluster populations have a mean half-light radii value of 2.5 ± 0.2 parsecs. The blue cluster candidates have a larger mean ellipticity value of $\langle \epsilon_{blue} \rangle = 0.14 \pm 0.02$ compared to the red cluster candidates, which have a mean value of $\langle \epsilon_{red} \rangle = 0.09 \pm 0.01$. However, the larger mean ellipticity of the blue population is almost entirely due to a few outlying blue cluster candidates as can be seen in the ellipticity distribution plot of our cluster candidate sample.

2.3.4 Specific Frequency

A useful parameter for quantifying the richness of a cluster population is the specific frequency S_N, which is the total number of clusters per unit galaxy luminosity, normalized to a galaxy luminosity of $M_V = -15$ (Harris and van den Bergh, 1981).

$$S_N = N_{GC} \times 10^{0.4(M_V+15)} \tag{2.3}$$

where N_{GC} is the total number of clusters and M_V is the absolute magnitude of a galaxy in the V band. An interesting question is whether the formation of any star clusters produced by the interaction between NGC 7174 and NGC 7176 has changed the cluster specific frequency. Previous studies have shown that globular cluster populations vary systematically with galaxy type and environment (Harris 1991; West et al. 1995). Characteristic values of S_N range from $S_N \leq 1$ for field spiral galaxies (van den Bergh and Harris, 1982), to $S_N \simeq 2-4$ for field ellipticals, or $S_N \simeq 5-7$ for ellipticals in dense environments (Harris and van den Bergh 1981; Miller et al. 1998; Chapelon et al. 1999).

The first step in calculating S_N for NGC 7174/76 is to determine the total number of globular clusters N_{GC}. An observed population of $N_{GC}^{obs} = 140$ star clusters has been identified. However, these observations were restricted to a photometric limit of $g = 25.5$. At this photometric limit, GCs at the faint end of the standard globular cluster luminosity function were not observed. Therefore, the incomplete coverage of the luminosity function must be accounted for in order to determine the total GC population. Since the globular cluster luminosity function is well fit by a Gaussian (see Figure 2.6), it is trivial to determine the percentage of GCs observed in our survey. Integrating this Gaussian function to the photometric limit of the data indicates that 66% of the total GC population was observed to $g = 25.5$. Correcting N_{GC}^{obs} for the unobserved part of the luminosity function gives a total GC population of $N_{GC}^{tot} \simeq 212 \pm 10$. Using a total V band absolute magnitude of $M_V = -21.3$ for NGC 7174/76 gives a value of $S_N \sim 0.6 \pm 0.1$.

A comparison can be made with the specific frequency of the nearby neighbouring elliptical galaxy NGC 7173. Barkhouse et al. (2001) and Cho et al. (2012) made separate studies of the globular cluster population of NGC 7173 and found specific frequency values of $S_N \sim 3.4 \pm 1.1$ and $S_N \sim 1.6 \pm 0.1$, respectively. For consistency, we also observed the globular cluster population in NGC 7173 and obtained a

specific frequency of $S_N \sim 1.5 \pm 0.1$, in agreement with Cho et al. (2012). These values are larger than that obtained in this analysis of NGC 7174/76, which has a S_N value below the expected range for elliptical galaxies, but within the range expected for spiral galaxies. We discuss this point further in § 2.4.

2.4 Discussion

Results from analysis of the colour distribution in § 2.3.1 suggest that $\sim 30\%$ of our cluster candidates are less than 400 Myrs old and may have formed from tidal interactions from the merger of NGC 7174 and NGC 7176. As shown in Figure 2.8, there is no correlation between $g-z$ colour and location around these merging galaxies. However, as marked by the dashed box in Figure 2.8, there is a pocket of blue cluster candidates in the north-west region of NGC 7174. These blue clusters may have formed from tidal interactions between NGC 7174 and the neighbouring elliptical NGC 7173. Evidence for an interaction between these two galaxies comes from observations of a tidal tail extending northward from NGC 7174 toward NGC 7173 (White et al. 2003; see Figure 2.1). These cluster candidates are the bluest objects in our sample, with an average colour of $\langle g-z \rangle = -0.65$. Based on these colours, SPS models suggest these cluster candidates have ages less than 20 Myrs (assuming a metallicity ranging between -1.35 < [Fe/H] < +0.35). More star clusters may have formed in the dust lane around NGC 7174 due to tidal interactions with NGC 7173 and NGC 7176. However, challenges faced when subtracting galaxy light from this region prevented any star cluster candidates around the dust lane being observed in our survey.

The luminosity function of blue ($g - z < 0.6$) candidates in our sample also provides indirect evidence that a new population of star clusters may have formed around the merger. In § 2.3.2, our entire cluster candidate sample was fitted with a Gaussian function, which well describes the luminosity function of old ($\sim$ few Gyrs) GCs (Harris, 1991, 2001). However, young ($<$ Gyr) populations of star clusters formed in other interacting galaxies typically have luminosity functions that are well fit by a power-law function of the form $\mathrm{d}N/\mathrm{d}L \sim L^{\alpha}$ where $\alpha \approx$ -2 (Whitmore et al. 1999; Larsen 2002). A similar luminosity function is observed for the blue cluster candidates in this study. Fitting a power-law function to the g and z band magnitudes of star cluster candidates with colours ranging between $-1.2 < (g-z)_0 < 0.6$ provides an average slope of $\alpha = -1.85 \pm 0.28$ (see Figure 2.6).

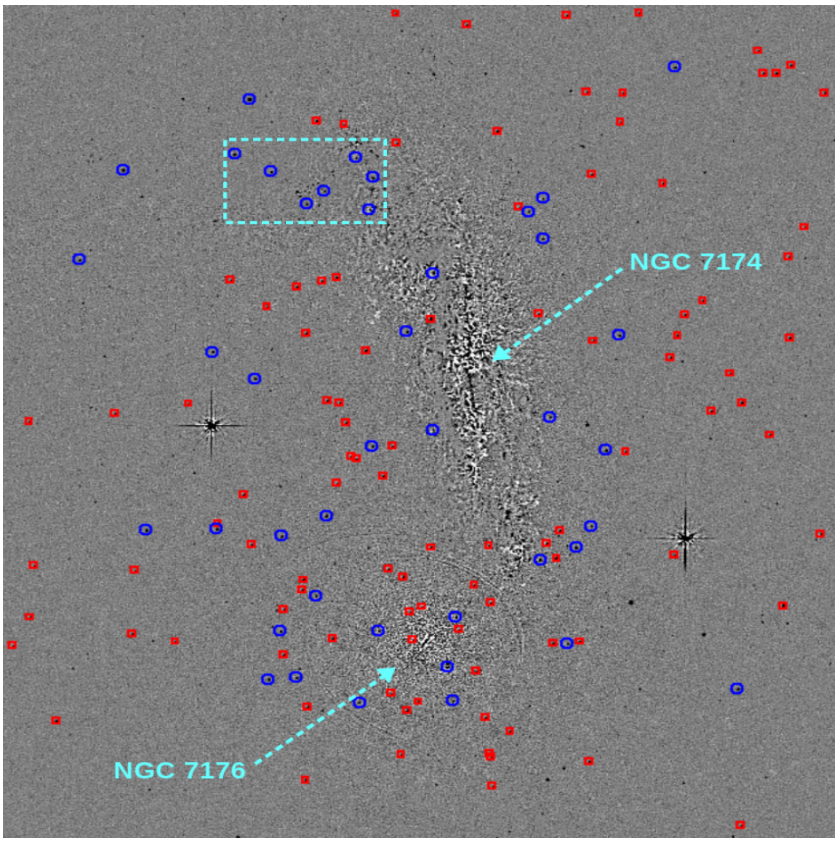

FIGURE 2.8: Distribution of cluster candidates after selection procedures, overlaid on the g band frame. Blue circles represent candidates with colours between $-1.2 < (g-z)_0 < 0.6$ and are potentially relatively young (< 400 Myr) star clusters, whereas red squares represent candidates with colours between $0.6 < (g-z)_0 < 1.7$ and are likely to be intermediate/old (> 1 Gyr) GCs. The dashed cyan box contains the bluest star cluster candidates in our sample, with an average colour of $\langle g-z \rangle = -0.65$. This colour corresponds to an average age less than 20 Myrs for these cluster candidates, assuming a metallicity ranging between -1.35 < [Fe/H] < +0.35.

The slope of our blue cluster candidates is in general agreement to the luminosity functions obtained from star clusters in several interacting and starburst galaxies, which generally show slopes ranging between -1.7 and -2.1 (Whitmore, 2000).

The colour distribution of the star cluster candidates in NGC 7174/76 can be compared with the diffuse light observed from all three galaxies at the core of HCG 90. White et al. (2003) determined that $\sim 45\% \pm 5\%$ of the total light from the core of the group belongs to this diffuse light component, and this diffuse light has a very narrow colour distribution with a mean value of $V-R = 0.7$ and dispersion of 0.1 mag. Using SPS models from Maraston (2007) and adopting a solar metallicity for the diffuse light gives a corresponding $g-z$ value of 1.6 and dispersion of 0.1

mag. The shaded grey area in Figure 2.5 shows the colour range of the diffuse light. This colour range is quite consistent with an old stellar population, and much redder than the vast majority of star clusters observed in NGC 7174 and NGC 7176. Thus, the diffuse light may have originated from a stellar population that existed before the merger. The colour of the diffuse light corresponds to an age of $\sim$ 13 Gyrs (assuming solar metallicity). This is considerably older than the 1 Gyr timescale estimated for galaxy mergers to complete based on dynamical models (Barnes 1988; Mihos et al. 1993).

A rather low specific frequency of $S_N \sim 0.6 \pm 0.1$ was determined for NGC 7174/76. This value can be compared to the typical combined S_N for these galaxy types. The typical specific frequencies for a spiral galaxy and an elliptical galaxy are $S_N \sim 0.5$ and $S_N \sim 3$, respectively (Harris and van den Bergh 1981; van den Bergh and Harris 1982). A combined specific frequency from these galaxy types yields a value of $S_N \sim 1.8$. Thus, the specific frequency observed from NGC 7174/76 is lower than expected. A higher specific frequency is also expected if one adopts the specific frequency obtained by Cho et al. (2012) for NGC 7173 as the typical S_N for an elliptical galaxy in a compact group. Low specific frequencies for interacting galaxies are not uncommon as seen in the cases of M32 and NGC 4478 (van den Bergh 1995; Neilsen et al. 1997). Both M32 and NGC 4478 are near a much larger companion (M31 and M87, respectively), hence it is thought that their GCs have been stripped away by tidal forces from their larger companions (Ribeiro et al., 1998a). In the case of HCG 90, both NGC 7173 and NGC 7176 are of similar size and luminosity. However, there is a large amount of diffuse light found in the core of the HCG 90 group (White et al., 2003) accounting for almost 50% of the total light from all three core galaxies combined. It is likely that this intragroup light is the product of tidal stripping from the extended halos of these three interacting galaxies. Given that GCs typically have spatially extended distributions around these galaxy types (Brodie and Strader, 2006), it is possible that many GCs were also stripped from their parent galaxies to form the intragroup light. This would then result in parent galaxies with low specific frequencies, as is observed for NGC 7174/76, and an intragroup light with a high specific frequency.

The expected cluster population for NGC 7174/76 can be used to determine the specific frequency of the intragroup light. Assuming a typical combined specific frequency of $S_N = 1.8$ for NGC 7174/76 provides a total expected GC population

of $N_{expected} \sim 450$. However, only 140 clusters were observed in our survey. Therefore, 310 clusters may now be part of the intragroup light. Using this population and a V band absolute magnitude of $M_{intragroup} = -20.7$ (White et al., 2003) provides a specific frequency of $S_N = 1.6$ for the intragroup light. Therefore, the intragroup light has a higher specific frequency than NGC 7174/76. These intragroup GCs are likely difficult to identify due to their low surface density of 0.03 GCs per arcsec^2 on the sky.

Some clusters may also have been disrupted due to tidal effects from this triple-galaxy interaction. Galaxy merger simulations by Kruijssen et al. (2012) have shown that this is possible. However, these simulations invoke strong tidal interactions and high gas densities, typically observed in gas-rich major mergers like the Antennae, to produce a high cluster disruption rate. Similar tidal shocks to the Antennae are unlikely to occur in NGC 7174/76, which consists of tidal interactions with a clumpy interstellar medium.

2.5 Conclusion

High spatial resolution images of HCG 90 were obtained in both F475W and F850LP bands using the ACS Wide Field Camera (WFC) on board the HST. Star cluster candidates in NGC 7174 (Sab) and NGC 7176 (E) were investigated to determine whether the ongoing interaction between these two galaxies had produced any new populations of star clusters. Objects were selected based on magnitude cuts of $20.0 < m_g < 25.5$ and colour cuts of $-1.2 < (g-z)_0 < 1.7$ as well as *SExtractor* parameters `ELONGATION` < 2 and `CLASS_STAR` > 0.9. A sample of 140 star cluster candidates was assembled using this selection criteria.

- Based on SPS models, $\sim 30\%$ of our cluster candidates have $g-z$ colours corresponding to ages less than 400 Myrs for a metallicity ranging between -1.35 < [Fe/H] < +0.35. Longo et al. (1995) also observed an excess of blue star clusters in the HCG 90 group, which have ages less than 500 Myrs. Given that these star clusters may have formed from tidal interactions around the galaxy merger, their ages could be used to constrain the merger age to $\sim$ 500 Myrs, consistent with dynamical ages of merging systems.

- The youngest star cluster candidates are located in the north-west region of NGC 7174. These candidates may be less than 20 Myrs old and may have formed from a more recent tidal interaction between NGC 7174 and another neighbouring elliptical galaxy NGC 7173. These objects are promising targets for future surveys of young star clusters in the HCG 90 group. More star clusters of similar age may be embedded in the dust lane around NGC 7174, however this region proved inaccessible to the HST/ACS images available. Near-infrared photometry may be able to penetrate the dust lane and detect more star cluster candidates in this region.

- The low cluster specific frequency of $S_N \sim 0.6 \pm 0.1$ for NGC 7174/76 is an unexpected result. However, this could be explained by the diffuse light present in the core of HCG 90. Our findings suggest that tidal interactions between NGC 7174 and NGC 7176 have stripped many progenitor globular clusters as well as a large amount of stellar light from their host galaxies to form this diffuse light. This stripping process would have left NGC 7174/76 with a low specific frequency, and a diffuse light with a high specific frequency. A specific frequency of $S_N = 1.6$ was determined for the diffuse light, which agrees with this scenario. Clusters in the diffuse light are difficult to identify due to their low surface density. Future surveys of the cluster population in the diffuse light are required to determine whether this has occurred.

Chapter 3

NGC 5128

3.1 Introduction

With an apparent magnitude of $m_V = 6.84$, NGC 5128 is the 5th brightest galaxy in the sky. It is also the only massive elliptical galaxy in a group of 25 galaxies known as the Centaurus Group (Cote et al., 1997). The distance modulus for NGC 5128 is $(m-M)_o = 27.92 \pm 0.08$, giving a distance of $d = 3.8 \pm 0.1$ Mpc (McLaughlin et al. 2008; Harris et al. 2010). It is located at $\alpha_{\rm J2000} = 13^{\rm h}25^{\rm m}27\overset{\rm s}{.}6$, $\delta_{\rm J2000} = -43°01'09$, and has an absolute magnitude of $M_V = -21.08$ which is typical for elliptical galaxies (Gil de Paz et al., 2007). Deep optical images reveal numerous shells and filaments, in addition to kinematic and globular cluster surveys (Malin et al. 1983; Quillen et al. 1992). These give indirect evidence that NGC 5128 is a post-merger elliptical (Israel, 1998).

Figure 3.1 shows a BVR and H_α mosaic of NGC 5128 taken using the Wide Field Imager (WFI) affixed to the MPG/ESO 2.2-metre telescope at La Silla. Although most of its properties are fairly normal for an elliptical galaxy, NGC 5128 hosts two remarkable features: large radio lobes extending out to 250 kpc from the centre, and a prominent warped dust lane projected across the galactic centre that extends out to a radius of 4 kpc, both of which suggest past merger activity (Israel, 1998). The dust and gas in the dust lane have masses of $M_d \sim 1.5 \times 10^6 \mathcal{M}_\odot$ and $M_g \sim 1.3 \times 10^9 \mathcal{M}_\odot$, respectively (Eckart et al. 1990; Israel 1998). Considering that dwarf irregular (dI) galaxies are plentiful in the Centaurus Group, Peng et al. (2002) speculate that this dust lane is actually the remnant of a dwarf irregular

galaxy that collided with the elliptical galaxy somewhere between $2-6\times10^8$ years ago as the likely scenario for its unusual appearance. However, the gas mass of the dust lane suggests that a late-type galaxy rather than a dwarf irregular merged with NGC 5128 (Malin et al. 1983; Quillen et al. 1993). The age estimate by Peng et al. (2002) is in agreement with dynamical models and other estimates which give an age estimate of $2-8\times10^8$ years for the merger (Malin et al. 1983; Sparke 1996).

The short distance to NGC 5128 has made it a prime target for a multitude of scientific surveys. The interstellar medium, planetary nebulae, and dark matter content of NGC 5128 are examples of topics that have been documented in recent years (e.g., Samurovic 2006; Kainulainen et al. 2009; Morganti 2010). In addition, several surveys have observed the many globular clusters (GCs) associated with this galaxy. Currently, 564 GCs have been observed using spectroscopy, 605 have been studied photometrically, and $\sim$ 2000 GCs are expected to be associated with NGC 5128 (Harris et al. 2010; Woodley et al. 2010). Spectroscopic surveys by Woodley et al. (2009) show that 68% of GCs in NGC 5128 have ages exceeding 8 Gyrs, 14% have intermediate ages between 5 - 8 Gyrs, and the remaining 18% have ages less than 5 Gyrs. The metallicities of GCs studied thus far have a mean value of [Fe/H] $\sim$ -0.33 (Peng et al. 2002; Woodley et al. 2005; Rejkuba et al. 2011). The globular cluster luminosity function (GCLF) in NGC 5128 resembles a Gaussian function, with a peak at $M_V \simeq$ -7.4 mag and dispersion of $\sigma \simeq 1.3$, typical for old ($\sim$ few Gyrs) GCs (Harris, 1991). The GC population has a variety of masses ranging from $1.2\times10^5\mathcal{M}_\odot$, typical of Galactic globular clusters, up to $1.4\times10^7\mathcal{M}_\odot$. The high-mass end of this GC population is similar to masses observed for ultra compact dwarfs (UCDs) and to nuclei of nucleated dE galaxies, indicating that some GCs in NGC 5128 may be related to these larger objects Rejkuba et al. (2008).

Although there are many studies of the star cluster population in NGC 5128, the majority of these surveys commence around $5'$ from the galaxy centre and beyond (e.g., Harris et al. 2006; Geisler et al. 2008; Harris et al. 2010) and generally avoid the central region of NGC 5128 due to extinction from the dust lane, which causes difficulty in subtracting the background galaxy light from the centre. However, tidal interactions between the elliptical galaxy and the dust lane may have produced a new population of star clusters in the central region of this merger. Surveys of star cluster formation in mergers such as the Antennae galaxies and NGC 3256

show evidence that tidal interactions are likely to form populations of new star clusters (Whitmore et al. 1999; Trancho et al. 2007b). Indeed, star formation around the dust lane is in abundance. Colour images show concentrations of very blue stellar populations at the northwestern and southeastern edges of the dust lane, and a substantial number of HII regions embedded in the dust lane (Dufour et al. 1979; Hodge and Kennicutt 1983). Furthermore, Minniti et al. (2004) and Villegas et al. (2005) report the discovery of two young star clusters in Sersic 13, a HII region $\sim 0.5'$ north of the centre of NGC 5128. Emission line features from these clusters suggest the presence of Wolf-Rayet stars, and an age of ~ 5 Myrs. Peng et al. (2002) also find young star clusters in their sample, albeit at a larger distance of $\sim 6'$ from the centre. Their survey discovered a blue arc consisting of bright star clusters with young ages of ~ 350 Myrs, which they attribute to the interactions between the dust lane and elliptical galaxy. These studies suggest that the ongoing tidal interactions in NGC 5128 have probably formed numerous star clusters in the past few hundred Myrs, and a promising location to find these relatively new star clusters is the central region of NGC 5128 where tidal interactions with the dust lane are at their strongest. Thus, this region will be the focal point of the following study in an attempt to discover newly formed star clusters.

HST Wide Field Camera 3 (WFC3) images of the central $3'$ region of NGC 5128 were acquired in 2010 as part of program GO-11360 (PI: R. Connell). Observations were taken with both UVIS and IR detectors, which have a spatial resolution of $0.04''$/pixel and $0.13''$/pixel, respectively. From the available WFC3 images the UVIS F814W band and the IR F160W band frames were least affected by extinction from the dust lane and so were selected for this analysis. However, given the dust lane has an extinction of $A_V \sim 3$ (Simpson and Meadows, 1998), these filters are still greatly influenced by extinction. Section § 3.2.2 discusses this issue further.

The F814W frame is centred at $\alpha_{\rm J2000} = 13^{\rm h}25^{\rm m}22\overset{\rm s}{.}5$, $\delta_{\rm J2000} = -43°00'23''$ and the F160W frame is centred at $\alpha_{\rm J2000} = 13^{\rm h}25^{\rm m}24\overset{\rm s}{.}1$, $\delta_{\rm J2000} = -43°00'35''$. The total integration times are 1240 and 1806 seconds for the F814W and F160W frames, respectively. At the adopted distance of 3.8 Mpc for NGC 5128, 1 parsec corresponds to an angular size of $0''\!.05$. Galactic reddening values of $A_{F814W} = 0.176$ mag and $A_{F160W} = 0.059$ mag were used throughout this investigation (Schlafly and Finkbeiner, 2011). Hereafter the F814W band and F160W band will be referred to as I band and H band, respectively.

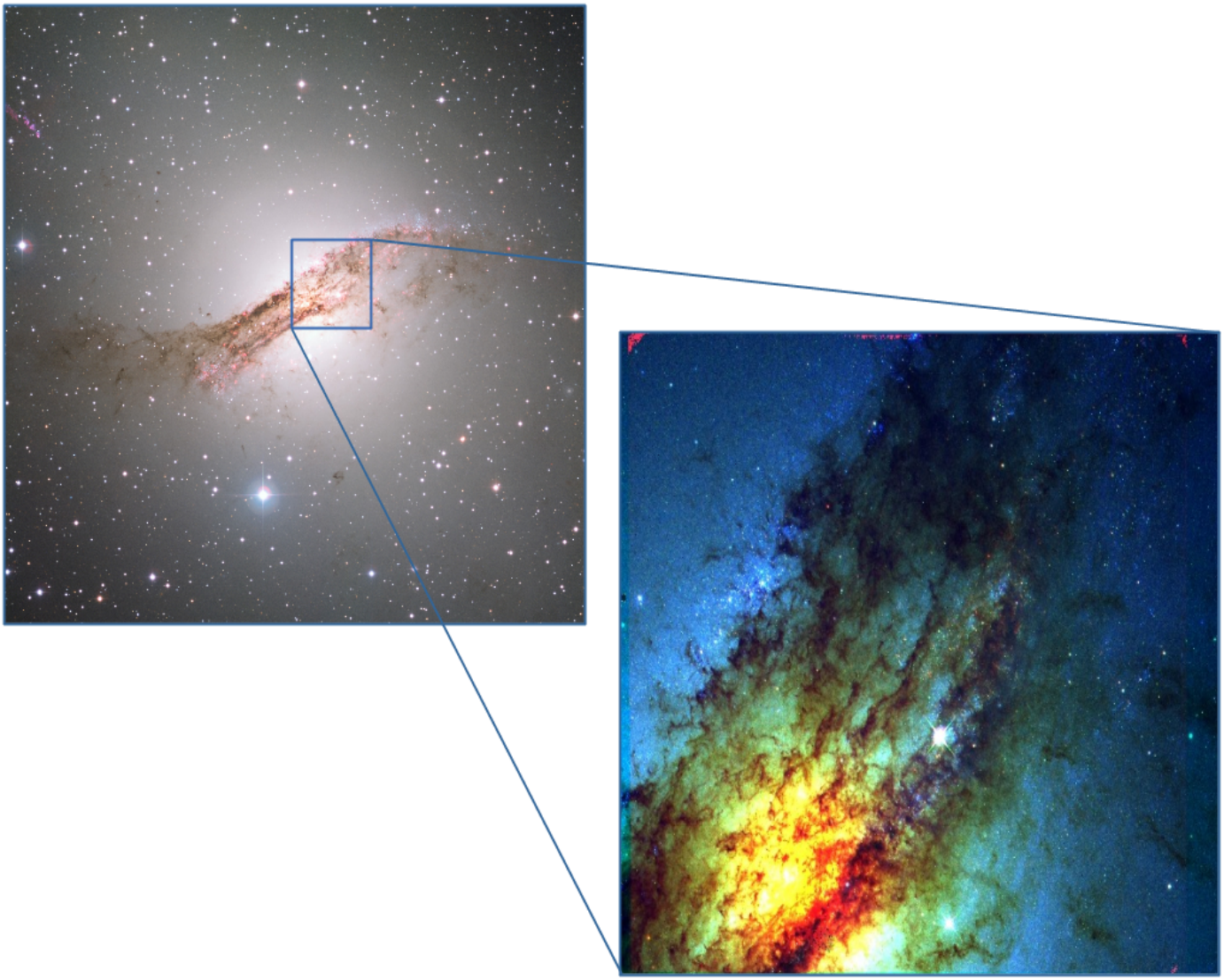

FIGURE 3.1: *Left*: BVR and H_α mosaic of NGC 5128 with the Wide Field Imager (WFI) attached to the MPG/ESO 2.2-metre telescope at La Silla. The blue box represents the $3' \times 3'$ area covered by the HST frames that were analysed in our study. *Right*: HST UVIS mosaic showing the central region of NGC 5128. It is likely that tidal interactions between the elliptical galaxy and the dust lane have formed of a new population of star clusters in this region.

The structure of this chapter is as follows. Section § 3.2 summarizes the data selection and reduction procedures used to obtain a sample of star cluster candidates. Section § 3.3 presents the properties of these star cluster candidates. The results are discussed and concluded in sections § 3.4 and § 3.5, respectively.

3.2 Data Reduction

The close proximity of NGC 5128 has its obvious observational advantages. However, analysing any object within NGC 5128 has several major disadvantages as well. Firstly, the large dust lane overlapping this elliptical galaxy is likely obscuring many stars and potentially star clusters. Secondly, NGC 5128 occupies a relatively large area of the sky, $2^\circ \times 2^\circ$ (Harris et al., 2010). Such a large area suffers significant contamination from foreground stars as well as distant galaxies. Thirdly, the low galactic latitude of NGC 5128 ($b = 19^\circ$) increases the level of contamination expected from foreground stars. These problems must be either removed or dramatically reduced before any star clusters can be analysed.

3.2.1 Background Galaxy Light Subtraction

Apart from the dust lane overlapping the galaxy, NGC 5128 is thought to be a typical elliptical galaxy (Dufour et al. 1979; Harris 2010). Subtracting the galaxy light from ellipticals is relatively straight forward and can be easily performed using tools such as *IRAF/ELLIPSE* and other elliptical modelling applications. However, the dust lane complicates the subtraction of galaxy light. A simple elliptical model subtraction procedure will not successfully remove galaxy light from the dust lane, and there are no models available for the unique galaxy morphology seen here.

Instead of trying to model the dust lane, the task *IRAF/FMEDIAN* was applied to smooth the galaxy light and subtract it from the original frame. This routine was applied only to the *H* band frame as it is the least affected by extinction due to the dust lane of the two bands. *IRAF/FMEDIAN* was set to find the median pixel counts in 7×7 pixel boxes across the image. This smoothed frame was then subtracted from the original frame, resulting in a background galaxy light subtracted frame ready for cluster detection and selection. A larger pixel box for the *IRAF/FMEDIAN* was unable to take into account the fluctuating background light in the dust lane region, while a smaller pixel box resulted in the production of false artificial objects.

However, the central 20″ region of NGC 5128 proved difficult to subtract due to sporadic fluctuations of the galaxy light. Many of the objects within this region

were found to be false artificial objects, hence this central 20″ region was avoided during the star cluster selection procedure described in § 3.2.2. Figure 3.3 shows the results of the *IRAF/FMEDIAN* routine.

3.2.2 Cluster Detection and Selection

SExtractor (Bertin and Arnouts, 1996) was used to detect objects in the galaxy light subtracted H band frame, finding a total of $\sim$ 2000 objects in NGC 5128. Unfortunately, many of these objects are likely due to contamination, primarily from foreground stars as NGC 5128 lies at a low galactic latitude of $b = 19°$ and covers a very large area in the sky ($2° \times 2°$). Although there is no way to completely remove the effects of contamination, there are methods to statistically reduce its impact.

Previous GC surveys in the literature used the mean stellar FWHM and typical GC ellipticity values as criteria for selection (Staneva et al. 1996; Rejkuba 2001; Harris et al. 2006). Hence, a constraint of FWHM $>$ 1.4 pixels and ellipticity $<$ 0.4 was applied to all detected objects. The FWHM constraint was deduced after observing FWHM values from foreground stars in the WFC3 frames, which showed FWHM values less than 1.4 pixels.

Another useful selection criterion is the globular cluster luminosity function (GCLF), in particular the magnitude turnover. It has been recognized that the differential magnitude distribution of old GCs throughout a range of host galaxies is well fit by a Gaussian function, and provides a peak magnitude (or magnitude turnover) of $M_V \simeq -7.4$ mag with a dispersion $\sigma = 1.3$ (Harris 1991; Jordán et al. 2007; Rejkuba 2012). Stellar population synthesis (SPS) models from Maraston (2007) were used to convert these values to the H band. The models provide a 3σ apparent magnitude range of $14.5 < m_H < 22.5$ expected from the star cluster population, where the magnitude turnover occurs at $m_H = 18.6$ (or $M_H = -9.3$). This range can be used as a magnitude constraint for the detected objects. However, this magnitude range will include many old and faint GCs in addition to bright young star clusters. The upper limit of this magnitude range can be amended to exclude most of these old GCs, since the purpose of this survey is to investigate newly formed star clusters. A suitable magnitude cutoff can be determined by observing the magnitude distribution of newly formed star clusters in other mergers that are of similar age to NGC 5128, such as NGC 3921 and NGC 7252 (Schweizer et al.

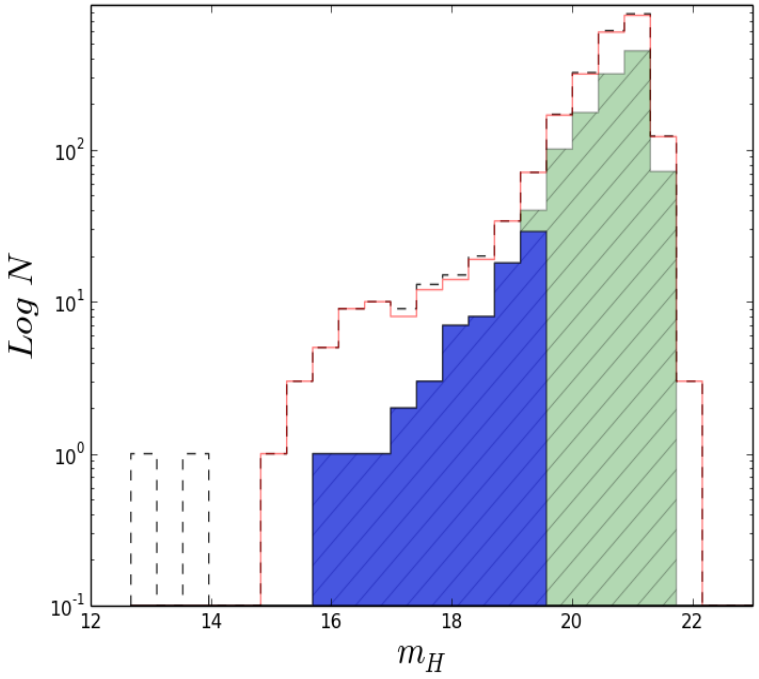

FIGURE 3.2: Affects of selection procedure on initial sample of detected objects. The black dashed line represents the initial detected sample consisting of $\sim$ 1800 objects. The red histogram represents objects that have FWHM > 1.4. The green hatched histogram represents objects from the red histogram with ellipticity $\epsilon < 0.4$ and located at least $20''$ from the galactic centre. The blue histogram represents objects from the green histogram with magnitudes between $14.5 < m_H < 19.5$ and colours ranging between $-0.6 < (I - H) < 3.1$. This selection criteria refined the initial sample to 160 star cluster candidates.

1996; Schweizer and Seitzer 1998). Results from these star clusters recommend an apparent magnitude constraint of $14.5 < m_H < 19.5$ for this analysis.

Exploiting the parameters of GCs further, Jordán et al. (2005) have shown that old ($\sim$ few Gyrs) GCs tend to fall within a certain colour range. Earlier studies by Rejkuba (2001) and Harris et al. (2004) have already used the colour parameter as a selection criterion for GCs in NGC 5128. However, any new star clusters produced from the tidal interaction will generally have bluer colours than the old ($\sim$ several Gyr) globular clusters present in NGC 5128. SPS models from Maraston (2007) were investigated to determine a suitable colour range that includes both the colours expected from new star clusters and the colours expected from old globular clusters.

As discussed in § 3.1, GCs close to the dust lane have a mean metallicity value of

[Fe/H]= −0.33 (Woodley et al. 2005; Rejkuba et al. 2011). Furthermore, metallicity values measured from nebulae and clouds in the dust lane show solar metallicities (Dufour et al. 1979; Eckart et al. 1990). Applying both metallicities to the models provide a colour range of $-0.6 < (I - H) < 2.0$ expected from all star clusters, which corresponds to an age range of 0 - 14 Gyrs. The upper colour limit reduces the presence of galaxies in the sample as distant galaxies often have redder colours than globular clusters (Cho et al., 2012). A similar colour range was observed for star clusters in M87 (Kundu and Zepf, 2007). However, any star clusters observed in our survey are likely to suffer from high extinction values due to the dust lane, which may have a varying extinction ranging between $A_V = 0$ - 3 mag (Simpson and Meadows, 1998). Based on Galactic reddening values for the I and H bands ($A_{F814W} = 0.176$ mag and $A_{F160W} = 0.059$ mag, respectively), an extinction of $A_V = 3$ mag will result in a colour reddening of $I - H = 1.08$. Therefore, in order to account for reddening effects of the dust lane, a colour range of $-0.6 < (I - H) < 3.1$ is adopted for this survey.

Applying the FWHM and ellipticity selection criteria reduced the sample from ∼ 1800 objects to ∼ 1100 objects. Aperture photometry was then applied to the remaining objects to determine I and H band magnitudes. The magnitude and colour constraints mentioned earlier were then applied to the sample (see § 3.2.3).

3.2.3 Cluster Photometry

The task *IRAF/PHOT* was used to perform aperture photometry on the original I band and H band frames for the sample of objects that passed the FWHM and ellipticity constraints set in § 3.2.2. An aperture radius of 0.4″ (∼ 8 parsec) and a sky annulus of 0.1″ were adopted for all objects in the sample. Background measurements were taken at a distance of 0.5″ from the centre of each object, ensuring good estimates of the local background.

Zeropoints were adopted from the latest and improved photometric calibration for WFC3, which can be found on the STScI website[1]. The magnitudes obtained using *IRAF/PHOT* were also corrected for Galactic reddening using the Schlafly and Finkbeiner (2011) extinction map values of $A_{F814W} = 0.176$ and $A_{F160W} = 0.059$.

[1]Zeropoints and details on the new calibrations can be found on http://www.stsci.edu/hst/wfc3/phot_zp_lbn

After performing aperture photometry, objects were matched within a 2 pixel radial separation across the two bands. The H band magnitude constraints and $I - H$ colour constraints presented in § 3.2.2 were then applied to the sample of objects. These selection criteria refined the initial sample of $\sim$ 1800 objects to a sample of 160 star cluster candidates. Figure 3.2 shows how the various stages of the selection procedure refined the initial sample of detected objects. Table 3.1 provides basic parameters for the sample of star cluster candidates.

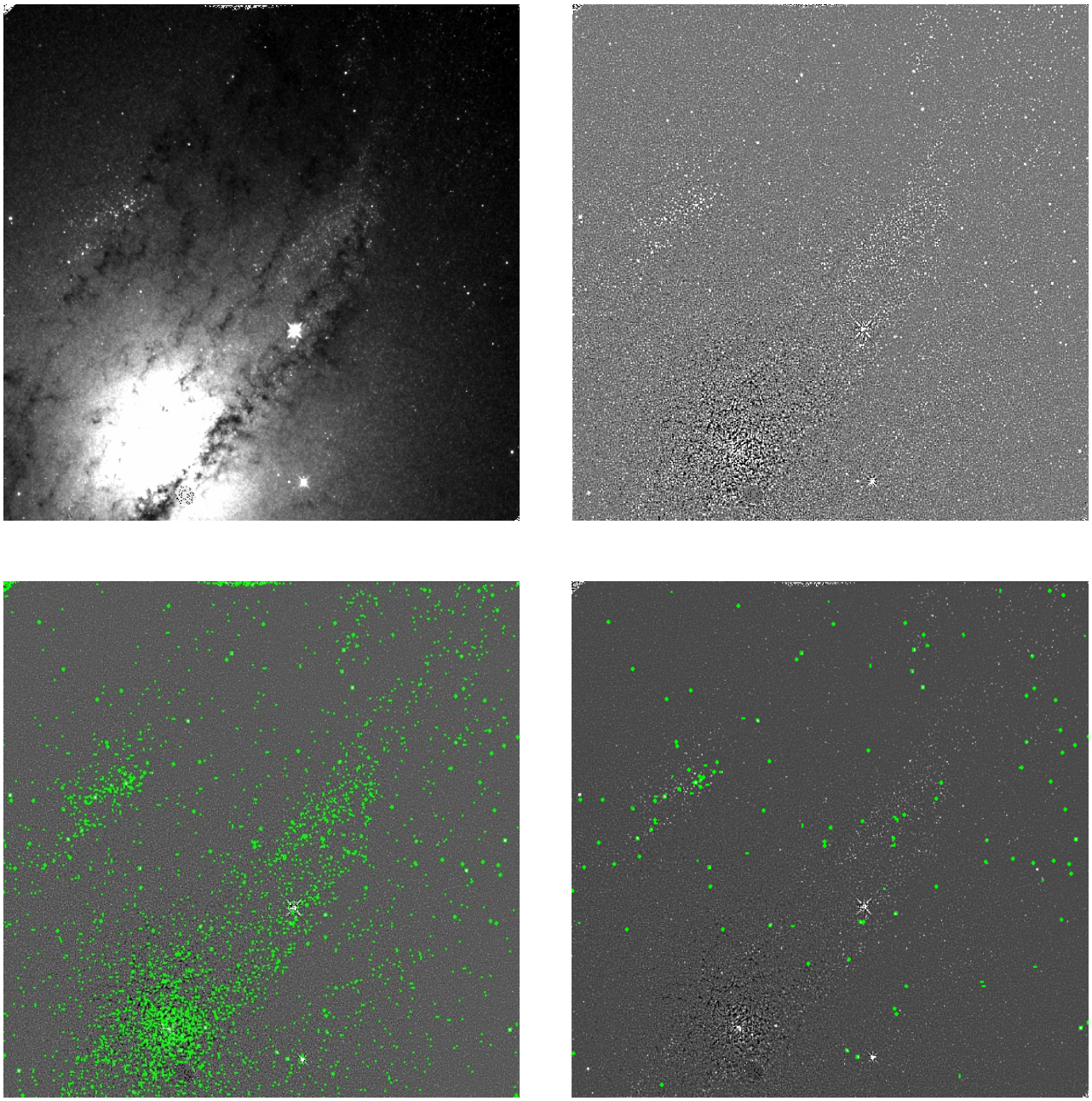

FIGURE 3.3: *Top-Left*: original H band frame of NGC 5128. *Top-Right*: galaxy light subtracted image of NGC 5128. The galaxy light and the dust lane has been removed, allowing star clusters to be detected and analysed. *Bottom-Left*: initial object detection results from *SExtractor*. Approximately 1800 objects were detected, of which only $\sim$ 2% are star clusters (Harris, 2010). *Bottom-Right*: final star cluster candidate sample in NGC 5128. The selection criteria discussed in § 3.2.2 reduced the initial sample of $\sim$ 1800 objects to 160 star cluster candidates, shown here in green.

TABLE 3.1: Basic parameters for star clusters candidates in NGC 5128

ID	$\alpha_{\rm J2000}$	$\delta_{\rm J2000}$	m_H	m_I	$(I-H)$	ϵ	r_e
1	$13^h25^m24^s.3$	$-42°59'34.39$	18.76 ± 0.04	19.09 ± 0.06	0.33 ± 0.10	0.012	2.7
2	$13^h25^m27^s.7$	$-43°00'09.92$	18.90 ± 0.05	19.82 ± 0.09	0.92 ± 0.14	0.019	2.8
3	$13^h25^m18^s.7$	$-43°00'43.36$	18.21 ± 0.02	18.88 ± 0.06	0.67 ± 0.08	0.026	2.6
4	$13^h25^m27^s.2$	$-42°59'38.37$	19.16 ± 0.05	19.13 ± 0.06	-0.03 ± 0.11	0.027	2.6
5	$13^h25^m19^s.5$	$-43°01'15.13$	17.87 ± 0.02	17.62 ± 0.03	-0.25 ± 0.05	0.028	2.8
6	$13^h25^m19^s.2$	$-43°00'37.44$	19.36 ± 0.05	20.04 ± 0.09	0.68 ± 0.14	0.030	2.8
7	$13^h25^m26^s.5$	$-43°00'09.37$	18.93 ± 0.04	19.80 ± 0.09	0.87 ± 0.13	0.031	2.6
8	$13^h25^m22^s.3$	$-42°59'47.50$	18.81 ± 0.03	19.85 ± 0.09	1.04 ± 0.12	0.034	2.4
9	$13^h25^m22^s.7$	$-43°01'05.53$	19.46 ± 0.07	21.82 ± 0.25	2.37 ± 0.32	0.035	2.7
10	$13^h25^m24^s.8$	$-43°00'12.02$	18.84 ± 0.04	19.34 ± 0.07	0.50 ± 0.11	0.036	3.2
11	$13^h25^m22^s.5$	$-43°00'18.89$	19.15 ± 0.04	19.38 ± 0.07	0.23 ± 0.11	0.038	3.1
12	$13^h25^m19^s.7$	$-43°00'59.73$	18.27 ± 0.02	18.29 ± 0.04	0.02 ± 0.06	0.039	3.1
13	$13^h25^m20^s.7$	$-43°00'00.87$	16.68 ± 0.01	16.61 ± 0.02	-0.07 ± 0.03	0.042	3.0
14	$13^h25^m23^s.2$	$-43°00'34.27$	18.83 ± 0.06	19.60 ± 0.08	0.77 ± 0.14	0.044	2.8
15	$13^h25^m23^s.4$	$-42°59'51.94$	18.66 ± 0.03	19.97 ± 0.09	1.31 ± 0.12	0.049	2.5
16	$13^h25^m30^s.4$	$-43°00'30.21$	19.31 ± 0.08	20.12 ± 0.10	0.81 ± 0.18	0.050	2.8
17	$13^h25^m16^s.9$	$-43°00'02.65$	19.40 ± 0.04	21.21 ± 0.16	1.81 ± 0.20	0.051	3.1
18	$13^h25^m25^s.7$	$-42°59'24.92$	19.32 ± 0.05	19.49 ± 0.07	0.17 ± 0.12	0.056	3.0
19	$13^h25^m20^s.9$	$-43°00'05.53$	18.30 ± 0.02	19.14 ± 0.06	0.84 ± 0.08	0.058	3.2
20	$13^h25^m26^s.2$	$-43°00'09.18$	18.92 ± 0.05	19.81 ± 0.09	0.89 ± 0.14	0.058	2.8
21	$13^h25^m18^s.5$	$-43°00'58.46$	17.21 ± 0.01	17.40 ± 0.03	0.19 ± 0.04	0.058	3.1
22	$13^h25^m20^s.4$	$-42°59'58.31$	19.44 ± 0.04	21.14 ± 0.16	1.70 ± 0.20	0.058	3.1
23	$13^h25^m20^s.4$	$-43°00'01.25$	19.43 ± 0.05	20.74 ± 0.13	1.31 ± 0.18	0.058	2.6
24	$13^h25^m21^s.4$	$-43°00'36.17$	18.67 ± 0.04	18.41 ± 0.04	-0.26 ± 0.08	0.060	2.7
25	$13^h25^m28^s.6$	$-43°00'15.84$	19.36 ± 0.09	20.30 ± 0.12	0.94 ± 0.21	0.060	2.9
26	$13^h25^m29^s.1$	$-43°00'20.35$	19.24 ± 0.07	20.17 ± 0.10	0.93 ± 0.17	0.060	2.8
27	$13^h25^m17^s.5$	$-43°00'36.67$	18.73 ± 0.03	18.41 ± 0.04	-0.32 ± 0.07	0.061	3.0
28	$13^h25^m16^s.6$	$-43°00'14.00$	19.47 ± 0.05	20.19 ± 0.10	0.72 ± 0.15	0.061	2.7
29	$13^h25^m20^s.8$	$-43°00'10.11$	16.75 ± 0.01	17.27 ± 0.03	0.52 ± 0.04	0.064	3.0
30	$13^h25^m29^s.4$	$-43°00'36.05$	19.17 ± 0.05	20.17 ± 0.11	1.00 ± 0.16	0.064	3.1
31	$13^h25^m27^s.2$	$-43°00'30.15$	17.50 ± 0.02	18.61 ± 0.05	1.11 ± 0.07	0.065	3.0
32	$13^h25^m25^s.4$	$-43°01'23.94$	17.72 ± 0.02	17.77 ± 0.03	0.05 ± 0.05	0.067	2.7
33	$13^h25^m25^s.2$	$-43°01'26.53$	17.70 ± 0.03	18.33 ± 0.04	0.63 ± 0.07	0.067	3.2
34	$13^h25^m31^s.3$	$-43°01'03.51$	17.45 ± 0.02	20.09 ± 0.10	2.64 ± 0.12	0.067	3.6
35	$13^h25^m19^s.5$	$-43°00'02.25$	19.11 ± 0.04	20.92 ± 0.14	1.81 ± 0.18	0.067	2.8
36	$13^h25^m26^s.8$	$-42°59'59.88$	19.45 ± 0.06	20.69 ± 0.13	1.24 ± 0.19	0.068	3.1
37	$13^h25^m20^s.5$	$-43°01'23.18$	19.11 ± 0.04	20.48 ± 0.12	1.37 ± 0.16	0.068	2.8
38	$13^h25^m21^s.8$	$-43°00'00.40$	19.46 ± 0.04	21.05 ± 0.15	1.59 ± 0.19	0.070	2.9
39	$13^h25^m26^s.7$	$-43°00'09.46$	18.78 ± 0.09	19.67 ± 0.09	0.89 ± 0.18	0.071	2.4
40	$13^h25^m16^s.9$	$-43°00'06.55$	19.31 ± 0.04	21.29 ± 0.17	1.98 ± 0.21	0.072	2.6
41	$13^h25^m20^s.1$	$-43°00'57.07$	18.83 ± 0.04	18.97 ± 0.06	0.14 ± 0.10	0.073	2.9

Table 3.1 – *Continued*

ID	$\alpha_{\rm J2000}$	$\delta_{\rm J2000}$	m_H	m_I	$(I-H)$	ϵ	r_e
42	$13^{\rm h}25^{\rm m}18\overset{\rm s}{.}9$	$-43°01'03.39$	19.27 ± 0.04	20.04 ± 0.09	0.77 ± 0.13	0.074	3.3
43	$13^{\rm h}25^{\rm m}18\overset{\rm s}{.}5$	$-43°00'21.73$	17.99 ± 0.03	18.53 ± 0.05	0.54 ± 0.08	0.075	2.9
44	$13^{\rm h}25^{\rm m}19\overset{\rm s}{.}2$	$-43°01'01.13$	18.27 ± 0.03	19.48 ± 0.07	1.21 ± 0.10	0.075	3.0
45	$13^{\rm h}25^{\rm m}18\overset{\rm s}{.}5$	$-43°00'50.79$	19.10 ± 0.04	20.12 ± 0.10	1.02 ± 0.14	0.077	2.6
46	$13^{\rm h}25^{\rm m}19\overset{\rm s}{.}7$	$-43°01'40.62$	19.32 ± 0.06	19.54 ± 0.08	0.22 ± 0.14	0.077	2.7
47	$13^{\rm h}25^{\rm m}27\overset{\rm s}{.}4$	$-42°59'25.79$	18.99 ± 0.05	19.34 ± 0.07	0.35 ± 0.12	0.078	3.8
48	$13^{\rm h}25^{\rm m}27\overset{\rm s}{.}1$	$-43°00'06.20$	19.49 ± 0.08	20.03 ± 0.10	0.54 ± 0.18	0.080	2.6
49	$13^{\rm h}25^{\rm m}24\overset{\rm s}{.}2$	$-43°00'36.26$	18.66 ± 0.06	19.87 ± 0.09	1.21 ± 0.15	0.082	2.8
50	$13^{\rm h}25^{\rm m}18\overset{\rm s}{.}3$	$-43°00'20.82$	18.97 ± 0.03	19.66 ± 0.08	0.69 ± 0.11	0.083	3.2
51	$13^{\rm h}25^{\rm m}23\overset{\rm s}{.}8$	$-43°01'02.94$	19.33 ± 0.05	21.54 ± 0.19	2.21 ± 0.24	0.083	3.3
52	$13^{\rm h}25^{\rm m}18\overset{\rm s}{.}3$	$-42°59'55.86$	19.29 ± 0.04	21.20 ± 0.16	1.91 ± 0.20	0.085	2.7
53	$13^{\rm h}25^{\rm m}26\overset{\rm s}{.}7$	$-42°59'48.37$	19.23 ± 0.05	19.18 ± 0.06	-0.05 ± 0.11	0.087	3.0
54	$13^{\rm h}25^{\rm m}26\overset{\rm s}{.}8$	$-42°59'58.91$	19.16 ± 0.04	20.38 ± 0.11	1.22 ± 0.15	0.088	2.7
55	$13^{\rm h}25^{\rm m}26\overset{\rm s}{.}3$	$-43°00'01.74$	19.36 ± 0.05	21.04 ± 0.16	1.68 ± 0.21	0.089	2.6
56	$13^{\rm h}25^{\rm m}27\overset{\rm s}{.}7$	$-43°00'09.12$	19.33 ± 0.05	20.42 ± 0.12	1.09 ± 0.17	0.090	2.7
57	$13^{\rm h}25^{\rm m}30\overset{\rm s}{.}3$	$-43°00'22.44$	18.78 ± 0.04	19.59 ± 0.08	0.81 ± 0.12	0.090	2.9
58	$13^{\rm h}25^{\rm m}17\overset{\rm s}{.}2$	$-43°00'00.53$	19.30 ± 0.04	21.14 ± 0.16	1.84 ± 0.20	0.091	2.5
59	$13^{\rm h}25^{\rm m}29\overset{\rm s}{.}4$	$-43°00'02.62$	18.48 ± 0.04	18.19 ± 0.04	-0.29 ± 0.08	0.093	2.7
60	$13^{\rm h}25^{\rm m}20\overset{\rm s}{.}9$	$-43°00'27.23$	19.19 ± 0.04	21.33 ± 0.17	2.14 ± 0.22	0.094	2.6
61	$13^{\rm h}25^{\rm m}22\overset{\rm s}{.}6$	$-43°00'41.17$	18.37 ± 0.03	18.75 ± 0.05	0.38 ± 0.08	0.095	2.5
62	$13^{\rm h}25^{\rm m}26\overset{\rm s}{.}3$	$-43°00'11.37$	19.01 ± 0.06	20.89 ± 0.17	1.88 ± 0.23	0.096	2.6
63	$13^{\rm h}25^{\rm m}20\overset{\rm s}{.}8$	$-43°00'40.35$	18.80 ± 0.05	21.28 ± 0.17	2.47 ± 0.21	0.096	2.9
64	$13^{\rm h}25^{\rm m}22\overset{\rm s}{.}1$	$-43°00'55.75$	19.11 ± 0.04	20.84 ± 0.14	1.73 ± 0.18	0.096	3.3
65	$13^{\rm h}25^{\rm m}28\overset{\rm s}{.}9$	$-43°00'04.91$	19.34 ± 0.05	20.62 ± 0.13	1.28 ± 0.18	0.097	3.1
66	$13^{\rm h}25^{\rm m}25\overset{\rm s}{.}4$	$-43°00'22.58$	18.67 ± 0.04	18.66 ± 0.05	-0.01 ± 0.09	0.099	3.0
67	$13^{\rm h}25^{\rm m}29\overset{\rm s}{.}9$	$-43°01'06.18$	18.92 ± 0.06	20.93 ± 0.18	2.00 ± 0.24	0.104	2.9
68	$13^{\rm h}25^{\rm m}18\overset{\rm s}{.}9$	$-43°01'05.85$	19.16 ± 0.05	20.26 ± 0.11	1.10 ± 0.16	0.105	3.0
69	$13^{\rm h}25^{\rm m}26\overset{\rm s}{.}8$	$-43°00'11.96$	19.46 ± 0.07	20.58 ± 0.13	1.12 ± 0.20	0.106	2.7
70	$13^{\rm h}25^{\rm m}31\overset{\rm s}{.}5$	$-43°00'58.81$	19.27 ± 0.04	20.48 ± 0.12	1.21 ± 0.16	0.106	2.9
71	$13^{\rm h}25^{\rm m}27\overset{\rm s}{.}2$	$-43°00'45.18$	18.41 ± 0.07	20.15 ± 0.11	1.74 ± 0.18	0.107	3.3
72	$13^{\rm h}25^{\rm m}23\overset{\rm s}{.}9$	$-43°01'19.12$	19.30 ± 0.05	20.56 ± 0.12	1.26 ± 0.17	0.107	3.1
73	$13^{\rm h}25^{\rm m}26\overset{\rm s}{.}1$	$-43°00'30.48$	19.06 ± 0.09	19.92 ± 0.10	0.86 ± 0.19	0.111	2.7
74	$13^{\rm h}25^{\rm m}26\overset{\rm s}{.}3$	$-43°00'04.17$	19.30 ± 0.06	20.98 ± 0.15	1.67 ± 0.21	0.114	2.5
75	$13^{\rm h}25^{\rm m}26\overset{\rm s}{.}7$	$-43°00'09.95$	16.57 ± 0.01	16.61 ± 0.02	0.04 ± 0.03	0.112	3.2
76	$13^{\rm h}25^{\rm m}24\overset{\rm s}{.}8$	$-43°00'01.90$	17.75 ± 0.02	19.56 ± 0.08	1.80 ± 0.10	0.116	3.1
77	$13^{\rm h}25^{\rm m}26\overset{\rm s}{.}9$	$-43°00'10.43$	19.20 ± 0.10	21.55 ± 0.27	2.34 ± 0.36	0.116	2.4
78	$13^{\rm h}25^{\rm m}24\overset{\rm s}{.}6$	$-43°00'29.57$	19.19 ± 0.05	20.51 ± 0.12	1.32 ± 0.17	0.117	2.7
79	$13^{\rm h}25^{\rm m}20\overset{\rm s}{.}7$	$-42°59'53.97$	18.75 ± 0.03	20.47 ± 0.11	1.72 ± 0.14	0.119	3.3
80	$13^{\rm h}25^{\rm m}26\overset{\rm s}{.}5$	$-43°00'08.88$	18.64 ± 0.06	19.07 ± 0.06	0.43 ± 0.12	0.121	2.6
81	$13^{\rm h}25^{\rm m}24\overset{\rm s}{.}7$	$-43°01'01.09$	19.10 ± 0.12	20.57 ± 0.13	1.47 ± 0.25	0.122	2.8
82	$13^{\rm h}25^{\rm m}26\overset{\rm s}{.}0$	$-42°59'48.74$	18.59 ± 0.03	18.17 ± 0.04	-0.42 ± 0.07	0.123	3.0
83	$13^{\rm h}25^{\rm m}29\overset{\rm s}{.}8$	$-43°00'18.15$	19.28 ± 0.05	19.79 ± 0.09	0.51 ± 0.14	0.131	3.4

Table 3.1 – *Continued*

ID	$\alpha_{\rm J2000}$	$\delta_{\rm J2000}$	m_H	m_I	$(I-H)$	ϵ	r_e
84	$13^{\rm h}25^{\rm m}27\overset{\rm s}{.}2$	$-43°00'27.47$	19.42 ± 0.08	19.48 ± 0.07	0.06 ± 0.15	0.133	2.8
85	$13^{\rm h}25^{\rm m}29\overset{\rm s}{.}8$	$-43°01'14.21$	18.65 ± 0.06	19.89 ± 0.10	1.24 ± 0.15	0.135	2.9
86	$13^{\rm h}25^{\rm m}25\overset{\rm s}{.}1$	$-43°00'00.10$	19.29 ± 0.04	20.81 ± 0.14	1.52 ± 0.18	0.135	3.0
87	$13^{\rm h}25^{\rm m}28\overset{\rm s}{.}3$	$-43°00'09.60$	18.47 ± 0.03	19.37 ± 0.07	0.90 ± 0.10	0.138	2.8
88	$13^{\rm h}25^{\rm m}29\overset{\rm s}{.}3$	$-43°00'13.94$	19.20 ± 0.04	19.80 ± 0.09	0.60 ± 0.13	0.138	3.1
89	$13^{\rm h}25^{\rm m}24\overset{\rm s}{.}6$	$-43°01'03.92$	18.60 ± 0.10	19.74 ± 0.09	1.13 ± 0.19	0.138	2.8
90	$13^{\rm h}25^{\rm m}18\overset{\rm s}{.}2$	$-43°00'37.92$	19.38 ± 0.04	19.67 ± 0.08	0.29 ± 0.12	0.140	3.2
91	$13^{\rm h}25^{\rm m}22\overset{\rm s}{.}7$	$-43°00'42.48$	19.05 ± 0.07	20.23 ± 0.11	1.18 ± 0.18	0.140	2.6
92	$13^{\rm h}25^{\rm m}22\overset{\rm s}{.}7$	$-43°00'42.58$	19.41 ± 0.08	21.79 ± 0.25	2.38 ± 0.33	0.140	2.8
93	$13^{\rm h}25^{\rm m}22\overset{\rm s}{.}7$	$-43°00'42.56$	19.00 ± 0.06	20.38 ± 0.12	1.38 ± 0.18	0.141	2.7
94	$13^{\rm h}25^{\rm m}17\overset{\rm s}{.}6$	$-43°00'31.16$	19.37 ± 0.05	21.87 ± 0.23	2.50 ± 0.28	0.142	3.2
95	$13^{\rm h}25^{\rm m}24\overset{\rm s}{.}2$	$-43°00'35.17$	18.84 ± 0.04	20.30 ± 0.11	1.46 ± 0.15	0.142	3.0
96	$13^{\rm h}25^{\rm m}19\overset{\rm s}{.}3$	$-43°00'37.16$	19.32 ± 0.04	19.62 ± 0.08	0.30 ± 0.12	0.143	2.2
97	$13^{\rm h}25^{\rm m}26\overset{\rm s}{.}7$	$-43°00'06.24$	18.87 ± 0.04	19.11 ± 0.06	0.24 ± 0.10	0.144	3.1
98	$13^{\rm h}25^{\rm m}21\overset{\rm s}{.}8$	$-43°01'22.55$	19.47 ± 0.06	20.76 ± 0.14	1.29 ± 0.20	0.146	2.7
99	$13^{\rm h}25^{\rm m}23\overset{\rm s}{.}4$	$-43°00'36.53$	19.31 ± 0.09	20.46 ± 0.12	1.15 ± 0.21	0.147	2.6
100	$13^{\rm h}25^{\rm m}17\overset{\rm s}{.}8$	$-43°00'37.47$	19.32 ± 0.05	19.78 ± 0.08	0.46 ± 0.13	0.151	2.8
101	$13^{\rm h}25^{\rm m}18\overset{\rm s}{.}9$	$-43°00'11.96$	18.91 ± 0.04	20.94 ± 0.14	2.03 ± 0.19	0.154	2.7
102	$13^{\rm h}25^{\rm m}27\overset{\rm s}{.}2$	$-43°00'09.64$	19.38 ± 0.10	20.54 ± 0.13	1.17 ± 0.23	0.155	3.0
103	$13^{\rm h}25^{\rm m}17\overset{\rm s}{.}9$	$-43°00'25.54$	19.29 ± 0.05	20.54 ± 0.12	1.25 ± 0.17	0.157	3.0
104	$13^{\rm h}25^{\rm m}24\overset{\rm s}{.}6$	$-43°00'17.17$	19.22 ± 0.05	22.11 ± 0.28	2.89 ± 0.33	0.157	3.2
105	$13^{\rm h}25^{\rm m}25\overset{\rm s}{.}6$	$-43°01'01.03$	18.93 ± 0.09	19.65 ± 0.09	0.72 ± 0.18	0.157	3.0
106	$13^{\rm h}25^{\rm m}25\overset{\rm s}{.}6$	$-43°00'51.04$	18.87 ± 0.08	20.12 ± 0.11	1.25 ± 0.19	0.158	2.7
107	$13^{\rm h}25^{\rm m}22\overset{\rm s}{.}5$	$-43°00'36.95$	19.32 ± 0.11	19.63 ± 0.08	0.31 ± 0.19	0.159	2.2
108	$13^{\rm h}25^{\rm m}20\overset{\rm s}{.}6$	$-43°00'50.26$	18.62 ± 0.03	19.31 ± 0.07	0.69 ± 0.10	0.159	3.9
109	$13^{\rm h}25^{\rm m}21\overset{\rm s}{.}2$	$-43°00'35.41$	16.57 ± 0.01	16.61 ± 0.02	0.04 ± 0.03	0.162	3.2
110	$13^{\rm h}25^{\rm m}21\overset{\rm s}{.}2$	$-43°00'35.41$	19.10 ± 0.08	21.40 ± 0.19	2.30 ± 0.27	0.162	3.2
111	$13^{\rm h}25^{\rm m}22\overset{\rm s}{.}6$	$-43°00'45.90$	19.35 ± 0.06	22.24 ± 0.27	2.89 ± 0.34	0.164	2.8
112	$13^{\rm h}25^{\rm m}27\overset{\rm s}{.}5$	$-43°00'10.01$	17.16 ± 0.02	17.40 ± 0.03	0.24 ± 0.04	0.165	3.4
113	$13^{\rm h}25^{\rm m}27\overset{\rm s}{.}5$	$-43°00'09.98$	17.67 ± 0.03	19.33 ± 0.07	1.66 ± 0.10	0.165	3.5
114	$13^{\rm h}25^{\rm m}27\overset{\rm s}{.}7$	$-43°00'16.06$	19.17 ± 0.09	20.67 ± 0.14	1.50 ± 0.23	0.166	2.7
115	$13^{\rm h}25^{\rm m}24\overset{\rm s}{.}3$	$-43°01'34.12$	19.19 ± 0.06	20.84 ± 0.15	1.66 ± 0.21	0.171	2.8
116	$13^{\rm h}25^{\rm m}21\overset{\rm s}{.}1$	$-43°00'33.08$	18.55 ± 0.04	19.33 ± 0.07	0.78 ± 0.11	0.173	3.3
117	$13^{\rm h}25^{\rm m}26\overset{\rm s}{.}0$	$-43°00'07.42$	19.22 ± 0.07	20.35 ± 0.11	1.13 ± 0.18	0.176	2.9
118	$13^{\rm h}25^{\rm m}25\overset{\rm s}{.}3$	$-43°00'32.76$	19.19 ± 0.07	20.70 ± 0.13	1.54 ± 0.20	0.178	3.1
119	$13^{\rm h}25^{\rm m}23\overset{\rm s}{.}9$	$-43°01'20.54$	18.97 ± 0.05	19.88 ± 0.09	0.91 ± 0.14	0.179	2.7
120	$13^{\rm h}25^{\rm m}26\overset{\rm s}{.}1$	$-43°00'48.84$	17.98 ± 0.02	17.79 ± 0.03	-0.19 ± 0.05	0.180	3.1
121	$13^{\rm h}25^{\rm m}21\overset{\rm s}{.}4$	$-43°00'40.75$	18.96 ± 0.05	21.70 ± 0.22	2.71 ± 0.27	0.185	2.7
122	$13^{\rm h}25^{\rm m}27\overset{\rm s}{.}9$	$-43°00'14.50$	18.43 ± 0.03	19.34 ± 0.07	0.91 ± 0.10	0.189	3.3
123	$13^{\rm h}25^{\rm m}20\overset{\rm s}{.}7$	$-43°00'55.10$	18.50 ± 0.03	19.45 ± 0.07	0.95 ± 0.10	0.193	3.2
124	$13^{\rm h}25^{\rm m}26\overset{\rm s}{.}4$	$-43°00'11.35$	19.13 ± 0.05	20.16 ± 0.10	1.03 ± 0.15	0.204	3.1
125	$13^{\rm h}25^{\rm m}28\overset{\rm s}{.}5$	$-43°00'20.94$	19.01 ± 0.07	20.02 ± 0.11	1.01 ± 0.18	0.204	3.2

Table 3.1 – *Continued*

ID	$\alpha_{\rm J2000}$	$\delta_{\rm J2000}$	m_H	m_I	$(I-H)$	ϵ	r_e
126	$13^{\rm h}25^{\rm m}24\overset{\rm s}{.}1$	$-43°00'36.37$	19.36 ± 0.05	21.05 ± 0.17	1.69 ± 0.22	0.214	3.2
127	$13^{\rm h}25^{\rm m}26\overset{\rm s}{.}6$	$-43°00'11.22$	19.06 ± 0.07	20.06 ± 0.11	1.00 ± 0.18	0.221	3.1
128	$13^{\rm h}25^{\rm m}23\overset{\rm s}{.}5$	$-43°01'15.40$	18.99 ± 0.05	19.88 ± 0.09	0.89 ± 0.14	0.222	3.3
129	$13^{\rm h}25^{\rm m}21\overset{\rm s}{.}8$	$-43°01'21.44$	19.30 ± 0.09	20.06 ± 0.10	0.76 ± 0.19	0.223	2.8
130	$13^{\rm h}25^{\rm m}26\overset{\rm s}{.}0$	$-43°00'09.99$	19.32 ± 0.05	20.87 ± 0.15	1.55 ± 0.20	0.224	2.6
131	$13^{\rm h}25^{\rm m}28\overset{\rm s}{.}3$	$-43°00'38.07$	19.18 ± 0.08	21.17 ± 0.17	1.99 ± 0.24	0.224	3.1
132	$13^{\rm h}25^{\rm m}24\overset{\rm s}{.}6$	$-43°00'57.14$	18.95 ± 0.08	20.75 ± 0.14	1.80 ± 0.22	0.224	2.6
133	$13^{\rm h}25^{\rm m}26\overset{\rm s}{.}3$	$-43°00'07.03$	19.46 ± 0.08	20.44 ± 0.12	0.98 ± 0.20	0.225	2.8
134	$13^{\rm h}25^{\rm m}27\overset{\rm s}{.}1$	$-43°00'34.31$	18.79 ± 0.06	19.03 ± 0.06	0.24 ± 0.12	0.225	2.9
135	$13^{\rm h}25^{\rm m}17\overset{\rm s}{.}0$	$-42°59'59.93$	19.36 ± 0.05	21.34 ± 0.17	1.98 ± 0.22	0.225	2.4
136	$13^{\rm h}25^{\rm m}27\overset{\rm s}{.}1$	$-43°00'09.63$	18.72 ± 0.06	19.53 ± 0.08	0.81 ± 0.14	0.229	2.9
137	$13^{\rm h}25^{\rm m}18\overset{\rm s}{.}9$	$-43°00'32.11$	18.97 ± 0.04	20.05 ± 0.10	1.08 ± 0.14	0.236	3.2
138	$13^{\rm h}25^{\rm m}26\overset{\rm s}{.}6$	$-43°00'07.65$	18.03 ± 0.03	17.54 ± 0.03	-0.49 ± 0.06	0.237	3.6
139	$13^{\rm h}25^{\rm m}25\overset{\rm s}{.}4$	$-43°00'50.53$	19.24 ± 0.17	21.07 ± 0.20	1.84 ± 0.37	0.248	3.5
140	$13^{\rm h}25^{\rm m}26\overset{\rm s}{.}7$	$-43°00'12.39$	19.07 ± 0.11	21.11 ± 0.20	2.04 ± 0.31	0.253	2.8
141	$13^{\rm h}25^{\rm m}22\overset{\rm s}{.}5$	$-43°00'36.30$	18.92 ± 0.04	20.55 ± 0.12	1.63 ± 0.16	0.253	2.6
142	$13^{\rm h}25^{\rm m}23\overset{\rm s}{.}2$	$-43°00'16.35$	19.49 ± 0.07	21.09 ± 0.16	1.61 ± 0.23	0.262	2.8
143	$13^{\rm h}25^{\rm m}20\overset{\rm s}{.}8$	$-43°00'28.98$	19.25 ± 0.06	22.01 ± 0.26	2.76 ± 0.32	0.263	3.4
144	$13^{\rm h}25^{\rm m}21\overset{\rm s}{.}8$	$-43°00'43.96$	19.40 ± 0.07	22.27 ± 0.28	2.86 ± 0.35	0.267	3.7
145	$13^{\rm h}25^{\rm m}23\overset{\rm s}{.}9$	$-43°00'32.69$	18.52 ± 0.03	19.52 ± 0.08	1.00 ± 0.11	0.272	2.8
146	$13^{\rm h}25^{\rm m}23\overset{\rm s}{.}2$	$-43°00'58.07$	17.52 ± 0.02	18.23 ± 0.04	0.71 ± 0.06	0.272	2.8
147	$13^{\rm h}25^{\rm m}28\overset{\rm s}{.}4$	$-43°00'16.72$	17.24 ± 0.02	18.01 ± 0.04	0.77 ± 0.06	0.273	3.4
148	$13^{\rm h}25^{\rm m}18\overset{\rm s}{.}1$	$-43°00'13.36$	18.68 ± 0.04	20.18 ± 0.10	1.50 ± 0.14	0.275	3.0
149	$13^{\rm h}25^{\rm m}26\overset{\rm s}{.}5$	$-43°00'09.72$	18.37 ± 0.05	19.28 ± 0.07	0.91 ± 0.12	0.289	3.2
150	$13^{\rm h}25^{\rm m}24\overset{\rm s}{.}3$	$-43°00'34.88$	18.96 ± 0.08	20.57 ± 0.12	1.61 ± 0.20	0.297	3.1
151	$13^{\rm h}25^{\rm m}23\overset{\rm s}{.}0$	$-43°00'38.72$	19.14 ± 0.11	21.05 ± 0.16	1.91 ± 0.27	0.305	3.1
152	$13^{\rm h}25^{\rm m}28\overset{\rm s}{.}1$	$-43°00'04.73$	19.21 ± 0.10	20.33 ± 0.11	1.12 ± 0.21	0.306	3.4
153	$13^{\rm h}25^{\rm m}22\overset{\rm s}{.}2$	$-43°00'36.76$	18.86 ± 0.06	19.92 ± 0.09	1.06 ± 0.15	0.317	2.7
154	$13^{\rm h}25^{\rm m}28\overset{\rm s}{.}0$	$-43°00'16.17$	17.99 ± 0.03	18.46 ± 0.05	0.47 ± 0.08	0.325	3.5
155	$13^{\rm h}25^{\rm m}24\overset{\rm s}{.}3$	$-43°01'02.98$	19.14 ± 0.09	20.41 ± 0.12	1.27 ± 0.21	0.326	2.8
156	$13^{\rm h}25^{\rm m}26\overset{\rm s}{.}0$	$-43°00'54.80$	18.85 ± 0.14	19.98 ± 0.11	1.13 ± 0.24	0.337	3.1
157	$13^{\rm h}25^{\rm m}22\overset{\rm s}{.}9$	$-43°00'33.23$	19.40 ± 0.06	21.01 ± 0.15	1.61 ± 0.22	0.342	3.3
158	$13^{\rm h}25^{\rm m}22\overset{\rm s}{.}4$	$-43°00'37.48$	18.98 ± 0.06	20.59 ± 0.13	1.61 ± 0.19	0.354	2.9
159	$13^{\rm h}25^{\rm m}22\overset{\rm s}{.}3$	$-43°00'30.92$	19.18 ± 0.11	21.58 ± 0.21	2.40 ± 0.31	0.391	3.3
160	$13^{\rm h}25^{\rm m}27\overset{\rm s}{.}9$	$-43°00'15.19$	18.31 ± 0.05	18.97 ± 0.06	0.66 ± 0.11	0.396	2.9

Cluster ID: 75 and 138 are known star clusters Sersic 13-S and Sersic 13-N, respectively.

3.3 Results

3.3.1 Colour Distribution

The detection and selection procedure described in § 3.2 yield a sample of 160 star cluster candidates. However, it is unknown whether any of the star clusters in this sample have formed from tidal interactions occurring at the centre of NGC 5128 or if they are pre-existing GCs with ages of a few billion years. Fortunately, the use of SPS models along with information from earlier studies in the literature can help constrain the age of these star cluster candidates.

Earlier surveys suggest that GCs approximately $5'$ away from the centre and nebulae in the dust lane have metallicities ranging between $-0.33 \leq [Fe/H] \leq 0$ (Eckart et al. 1990; Peng et al. 2002; Woodley et al. 2005). Furthermore, studies by Quillen et al. (1993) and Peng et al. (2002) suggest the merger event commenced between 200 - 300 Myrs ago. This age range can be used as an upper limit for the ages of any newly formed star clusters, and the metallicity range can be used to contain its chemical abundance. These two parameters can be used as constraints in SPS models to provide a colour range expected from star clusters formed from the merger.

Applying these metallicity values and upper age limit to SPS models produced by Maraston (2007) gave $I - H$ colours < 1.2 for star clusters younger than 250 Myrs. Moreover, both metallicity values have the same $I - H$ colour for an age of 250 Myrs, and show little variation at younger ages (see Figure 3.4). Figure 3.5 shows a colour-magnitude diagram (CMD) and colour distribution of the star cluster candidates. The blue and red shaded regions represent candidates with ages younger and older than 250 Myrs, respectively. The blue candidates have a mean colour $\langle I - H \rangle = 0.6 \pm 0.1$ and the red candidates have $\langle I - H \rangle = 1.8 \pm 0.1$. The total candidate sample has a mean $\langle I - H \rangle = 1.2 \pm 0.1$, corresponding to an age of $\sim$ 250 Myrs.

However, it is important to note the affects of extinction on these observed colours. As discussed in § 3.2.2, the extinction due to the dust lane can redden cluster candidate colours by $I - H = 1.08$. Therefore, cluster candidates in our sample may be bluer than observed. This implies that red cluster candidates in our

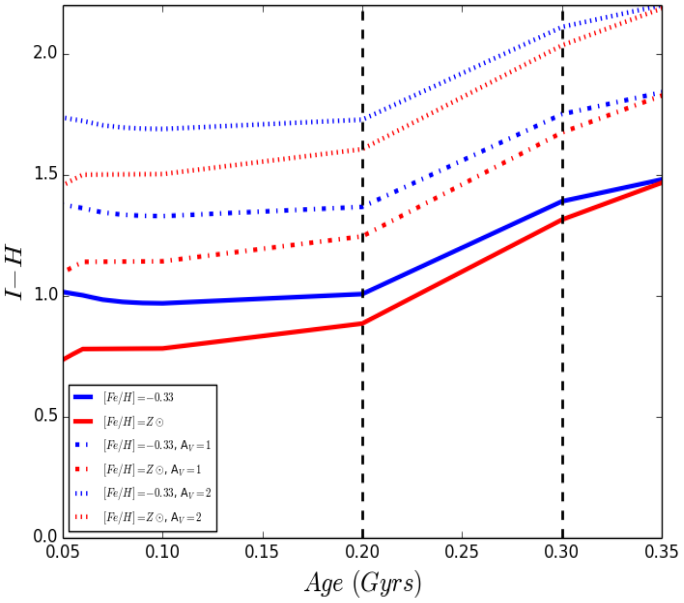

FIGURE 3.4: Variation of $I-H$ colour for $Fe/H = -0.33$ and $Fe/H = Z_{\odot}$. SPS models by Maraston (2007) were adopted for this study. An upper age limit of 250 Myrs was adopted for newly formed star clusters based on the merger time of NGC 5128. Both metallicities have an $I-H$ colour ~ 1.2 at this upper age limit. However, $I-H$ colours obtained from our cluster candidates may also suffer from extinction due to the dust lane. As an example, $I-H$ colours at $A_V = 1$ and $A_V = 2$ for these two metallicities are plotted to show the affects of extinction.

sample may be younger than observed due to high levels of extinction. The affects of extinction by the dust lane will be discussed further in § 3.4.

It is worth noting that, based on the non-linearity of the model colours as a function of age, star clusters with colours of $I-H \geq 1.3$ can have several ages. However, the models show that only star clusters younger than 250 Myrs can produce colours of $I-H < 1.2$. From the sample of 160 star cluster candidates 56% showed colours corresponding to ages $<$ 250 Myrs.

3.3.2 Luminosity Function

The luminosity function varies for star clusters as they evolve, with newly formed star clusters in mergers and starburst galaxies showing a magnitude distribution well fit by a power-law function of $\mathrm{d}N/\mathrm{d}L \sim L^{\alpha}$ where $\alpha \approx$ -2 (Whitmore et al. 1999; Larsen 2002), while old globular clusters have a luminosity function well described by a Gaussian function with a peak magnitude of $\mathrm{M}_V = -7.4$ and

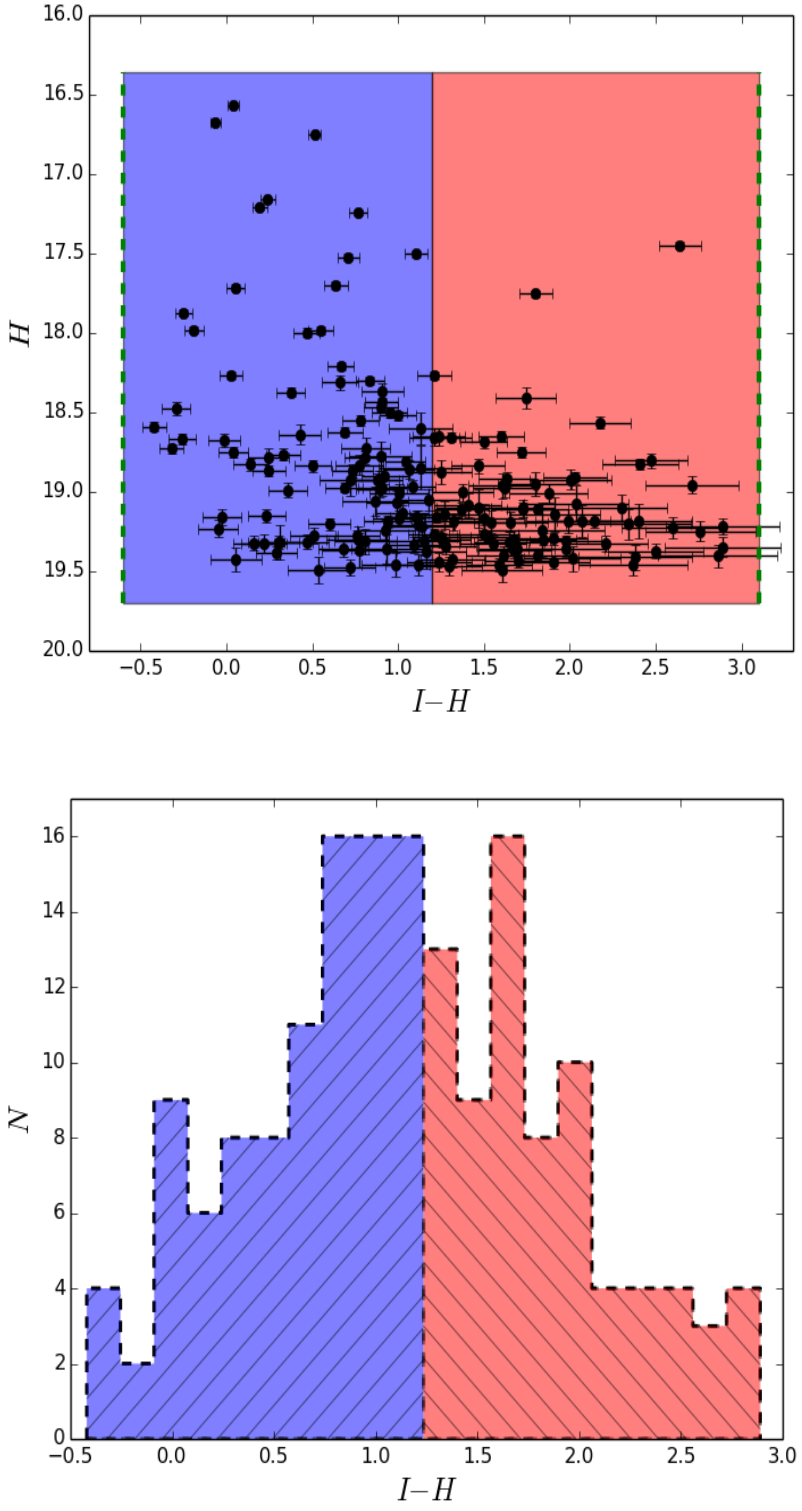

FIGURE 3.5: Colours of star cluster candidates in NGC 5128. *Top*: Colour-magnitude diagram of star cluster candidates. The dashed green lines indicate the applied colour cuts of $-0.6 < (I-H)_0 < 3.1$. Cluster candidates with colours of $I-H < 1.2$ are shown in blue, while the red region represents cluster candidates with colours exceeding $I-H > 1.2$. From the total cluster sample, 90 cluster candidates have colours corresponding to ages < 250 Myrs. *Bottom*: Colour distribution of star cluster candidates using the same colour scheme as the above diagram. Blue candidates have a mean $\langle I-H \rangle = 0.6 \pm 0.1$ and the red candidates have $\langle I-H \rangle = 1.8 \pm 0.1$. The total candidate sample has a mean $\langle I-H \rangle = 1.2 \pm 0.1$.

$\sigma = 1.3$ mag (Harris, 1991). It is interesting to see how the luminosity function of our star cluster candidate sample in NGC 5128 behaves. SPS models have shown that 56% of candidates in our sample are relatively young with ages less than 250 Myrs. Hence, this sample of cluster candidates should show a luminosity function similar to a power-law function if they are truly young star clusters similar to those found in other merging galaxies.

The luminosity function for the entire star cluster sample obtained in this study is shown in Figure 3.6. The distribution of these star clusters is similar to that of a power-law distribution. Fitting this sample to a single power-law function yields a slope of $\alpha = -2.04 \pm 0.15$. However, since this sample consists of newly formed star clusters as well as progenitor clusters with ages greater than the merger time, this power-law fit does not give a true representation of just the luminosity function for the newly formed star clusters. Removing red cluster candidates from the sample and refitting to a power-law provides a slope of $\alpha = -1.94 \pm 0.15$. Both slopes are identical within errors.

These slopes are in agreement to those observed from star cluster populations in other galaxy mergers. While the population of super star clusters in the Antennae galaxies has a steeper slope of $\alpha = -2.35 \pm 0.03$ (Whitmore et al., 2010), other star cluster populations from older galaxy mergers such as NGC 3256 and NGC 7252 have shallower slopes of $\alpha \approx -1.8$ (Zepf et al. 1999; Miller et al. 1997). In general, star cluster populations in galaxy mergers and starburst galaxies cover a broad range of slopes, usually lying between -1.7 and -2.4 (Whitmore, 2003, 2000), in agreement with the slopes provided here.

Figure 3.6 also shows a Gaussian fit to the red ($I - H > 1.3$) cluster candidate population. A mean apparent magnitude of $\mu = 19.0 \pm 0.1$ and dispersion $\sigma = 0.4$ is derived from the Gaussian fit. A magnitude turnover of $m_H = 19.0$ provides a distance modulus of $m - M = 28.3$, which is in general agreement with other moduli values determined for NGC 5128 (e.g., Harris et al. 2010). The total GC population can be determined using the Gaussian nature of the GCLF. An upper magnitude limit of $m_H = 19.5$ only includes 82% of the total GC population. Under the assumption that the 70 red cluster candidates in our sample with colours corresponding to ages exceeding 250 Myrs represent this percentage, the total GC population in the WFC3 frames is $N_{GC}^{Tot} = 85$.

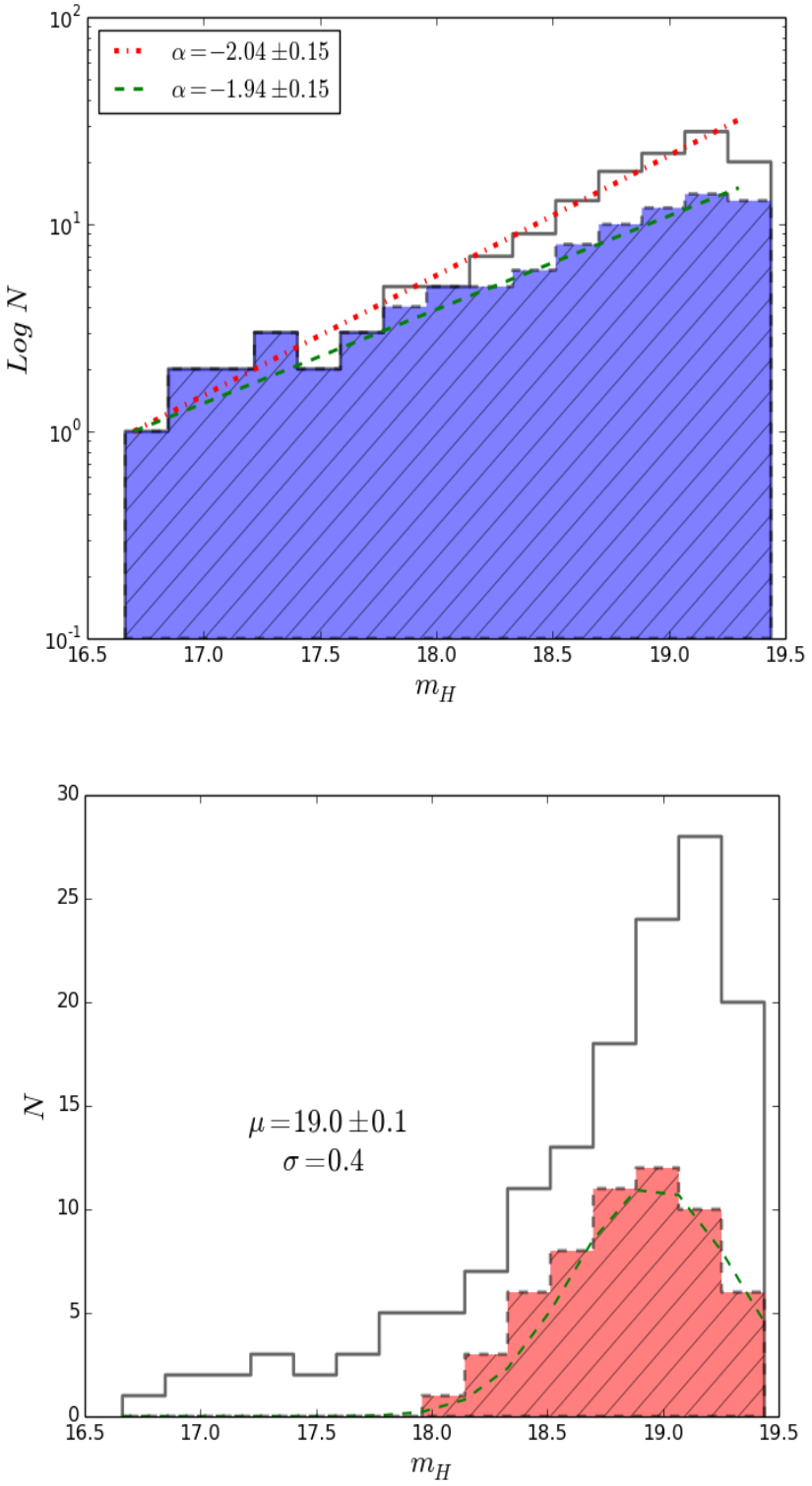

FIGURE 3.6: Luminosity function of star cluster candidates in the central 3′ region of NGC 5128. *Top*: Best fit power-law plots of the total candidate sample (black histogram) and newly formed star cluster candidates (blue hatched histogram). Both histograms were fit with a power-law of the form $\mathrm{d}N/\mathrm{d}L \sim L^{\alpha}$. The total candidate population is best fit with a slope of $\alpha = -2.04 \pm 0.15$ (red dot-dashed line), and the younger candidate population is best fit with $\alpha = -1.94 \pm 0.15$ (green dashed line). *Bottom*: magnitude distribution of the older candidate population (red hatched histogram) and the total candidate population (black histogram). A gaussian fit to the older candidate population provides a mean apparent magnitude of $\mu = 19.0 \pm 0.1$ and $\sigma = 0.4$ (green dashed line).

3.3.3 Half-Light Radii of Young and Old Candidates

Sizes of GCs in NGC 5128 has been studied extensively. Of note, Harris et al. (2006) and Gómez and Woodley (2007) found that GCs with smaller diameters tend to be found closer to the galactic centre, and these smaller clusters are redder in appearance and more metal-rich than the larger GCs (Geisler et al., 2008). Furthermore, van den Bergh (2008) suggest there is a week trend for brighter GCs to be rounder than fainter ones. Many of these studies were taken at distances of $R_{gal} > 5'$ from the centre of NGC 5128 in order to avoid the difficulty of subtracting the background galaxy light from the centre due to the complexity of the dust lane. Therefore, it is interesting to see if the same trends can be observed for GCs in the inner $3'$ region of NGC 5128.

Half-light radii for our star cluster candidates were determined using the *ISHAPE* routine, which is implemented in the data reduction package *BAOLAB* (Larsen, 1999). *ISHAPE* convolves a user provided PSF with an analytic elliptical profile for a range of sizes until the best fit between the observed light profile and model profile is obtained. Standard PSF files were generated using the *PSF* task in the *DAOPHOT* package and stellar objects in the WFC3 frames. A King profile (King, 1962) with a concentration parameter of 30 has been used for several cluster surveys and was adopted here (e.g., Mengel et al. 2008; Bastian et al. 2009).

Figure 3.7 shows the distribution of ellipticity ϵ, and half-light radii r_e, for the candidate sample obtained in § 3.3.1 and how these parameters vary with magnitude and galactocentric distance. The colour scheme in this figure separates the candidates based on their $I - H$ colour. Red denotes candidates with colours of $I - H > 1.3$ and blue denotes candidates with colours of $I - H < 1.2$. The relationships observed by Gómez and Woodley (2007) and van den Bergh (2008) for r_e and ϵ are also plotted in Figure 3.7.

The red clusters and blue clusters show an average size of $\langle r_e \rangle = 3.0 \pm 0.3$ pc, slightly smaller than the average GC radii of 4 pc observed at $R_{gal} > 5'$ by Harris et al. (2006) and Geisler et al. (2007) but in agreement with their findings that smaller clusters are located closer to the galactic centre. Both red and blue populations have an average ellipticity of $\langle \epsilon \rangle = 0.12 \pm 0.01$. These candidates are flatter than GCs observed by Rejkuba (2001) and Harris et al. (2006) which have a mean value of $\langle \epsilon \rangle = 0.07 \pm 0.01$ and $\langle \epsilon \rangle = 0.08 \pm 0.01$, respectively. Simulations by Akiyama (1991) have shown that star clusters become rounder with age due

to gravothermal contraction in the inner regions of these clusters and the tidal stripping of stars in the outer regions. Therefore, since the young (< 250 Myr) clusters in our sample have not evolved as much as the old (3 - 5 Gyr) GCs observed by Rejkuba (2001) and Harris et al. (2006), they are expected to be flatter. This may also explain the high ϵ values of the red cluster population. Many of these red cluster candidates may be young blue star clusters suffering from high extinction. A significant presence of young star clusters will result in a higher average ellipticity for the red cluster population.

The travelling median plots in Figure 3.7 show no correlation of the ellipticity of blue and red clusters to increase with either magnitude or galactocentric distance. There is a weak trend of cluster size to increase with H band apparent magnitude, more so for the red candidate population. However, neither population show any correlation between size and galactocentric distance.

The lack of correlation between ellipticity and magnitude/galactocentric distance could be due to three reasons: (1) removal of some progenitor GCs after subtraction of galaxy light from the H band frame, (2) tidal interactions due to the merger that may have disrupted some progenitor GCs, (3) There was no initial intrinsic correlation between these parameters in the central region of NGC 5128.

To test if progenitor GCs were removed during the galaxy light subtraction procedure, the task *IRAF/MKOBJECTS* was used to apply 100 artificial star clusters of varying magnitudes, ellipticities and distances from the galactic centre to the H band frame before the galaxy light subtraction procedure described in § 3.2.1. A magnitude range of $14.5 < m_H < 19.5$ was applied to these artificial star clusters. Ellipticities ranged between $\epsilon = 0$ - 0.3, as observed by van den Bergh (2008), and galactocentric distances ranged between 0 - $2'$. Artificial GCs were distributed to increase in ellipticity with decreasing magnitude and increasing galactocentric distance. Galaxy light was then subtracted using the procedure described in § 3.2.1, and artificial GCs were detected using the selection procedure described in § 3.2.2.

A total of 92 artificial star clusters were retrieved from our selection procedure. Moreover, these artificial clusters retained the input distribution of increasing ellipticity with increasing magnitude/galactocentric distance. This result suggests the lack of correlation between ellipticity and magnitude/galactocentric distance in our sample of star cluster candidates is not due to the galaxy light subtraction procedure applied in § 3.2.1. Instead the lack of correlation suggests there was

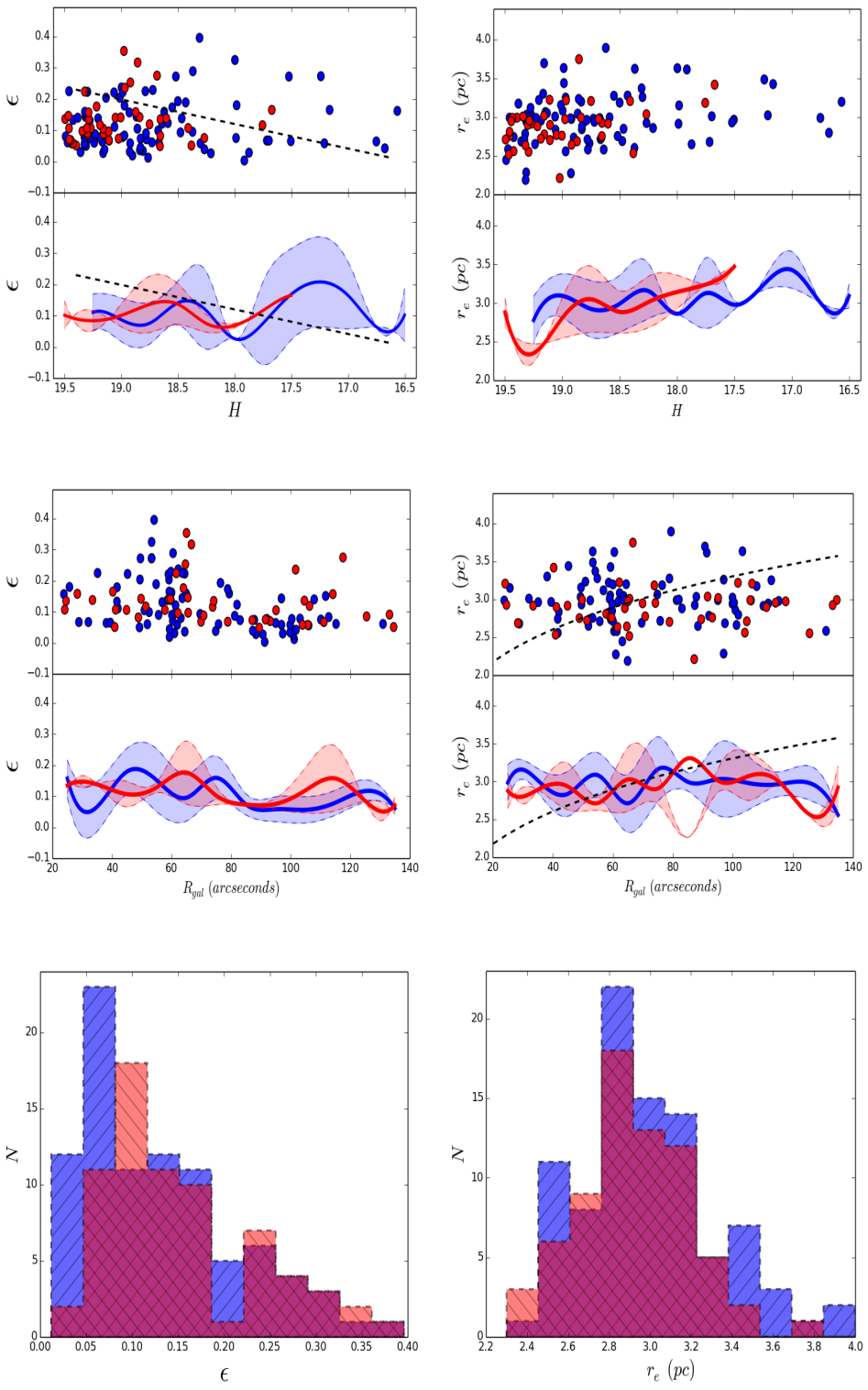

FIGURE 3.7: Physical properties of star cluster candidates. *Top*: Variation of apparent magnitude with star cluster ϵ (*left*) and r_e (*right*). Blue circles/lines represent candidates with ages < 250 Myrs, while red circles/lines represent ages > 250 Myrs for *all* panels. The lower line plots show the travelling median values for ϵ and r_e. Shaded blue and red regions mark $\pm 1\sigma$ error of the mean. The black dashed line represents the best-line fit by van den Bergh (2008) to their GC sample. *Middle*: Same as *top* but now showing how the galactocentric distance of these candidates vary with their ϵ and r_e. The black dashed line represents a power-law of the form $r_e = c(R_{gal})^{\alpha}$ derived by Gómez and Woodley (2007), where $c = 2.76$ and $\alpha = 0.26$. *Bottom*: Distribution of ϵ and r_e values plotted as histograms.

no initial correlation between these parameters or tidal interactions around NGC 5128 have distrupted this correlation.

It is difficult to distinguish between these two scenarios. If tidal interactions between the elliptical galaxy and the dust lane are responsible for the lack of correlation between ellipticity and magnitude/galactocentric distance, then pockets of star forming regions may have been produced throughout the central region of NGC 5128. Tidal interactions may have also altered the location of some of the initial population of GCs in the centre. Hence, any initial relationship between star cluster size and galactocentric distance would have been disrupted. Furthermore, a new population of star clusters are likely to be brighter than the progenitor GCs and be of similar size (Gilbert and Graham 2007; Whitmore et al. 2010). Hence, any initial correlation between magnitude and galactocentric distance will also have been disrupted.

3.4 Discussion

Analysis of the central $3'$ region of NGC 5128 has yielded a population of 160 star cluster candidates, defined using colour and magnitude cuts, and ellipticity and FWHM constraints. Under the assumption that cluster metallicities range between $-0.33 \leq [Fe/H] \leq 0$, SPS models were used to determine ages of individual star clusters in the sample based on their $I - H$ colour. These models indicate that star clusters with colours of $I - H < 1.2$ have ages less than 250 Myrs, and could have been formed from the tidal interactions taking place at the centre of NGC 5128 due to the recent merger event, which is estimated to have an age between 2 - $8{\times}10^8$ years (Malin et al. 1983; Sparke 1996; Peng et al. 2002).

Approximately 56% of the candidates in this sample show bluer colours than $I - H = 1.2$, and therefore could be newly formed star clusters produced by the tidal interactions. Furthermore, 63 candidates showed colours corresponding to ages greater than 200 Myrs. If these blue candidates are indeed star clusters then they have likely survived the early stages of cluster evolution, where stellar winds and tidal shocks play a pivotal role in star cluster disruption, and may evolve into bound GCs (Lada and Lada 2003; Kruijssen 2012). However, our sample of cluster candidates may be heavily reddened due to the dust lane, which has an extinction ranging between $A_V = 0$ - 3 mag (Simpson and Meadows, 1998). Therefore bluer

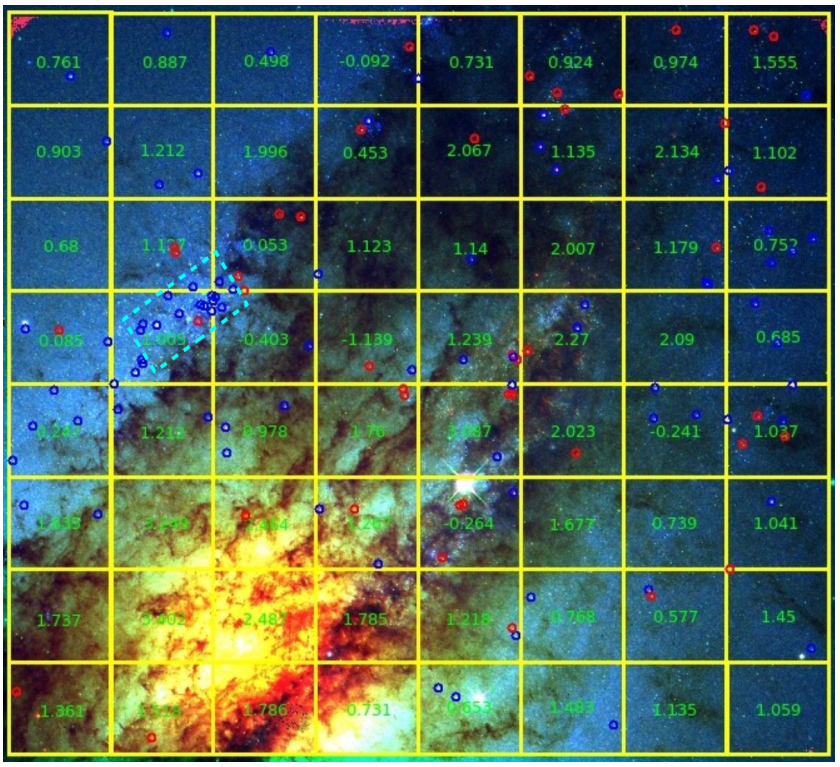

FIGURE 3.8: Distribution of star cluster candidates in NGC 5128. Our cluster sample is overlaid on a HST/WFC3 mosaic. Blue circles represent star clusters with colours of $I - H < 1.2$ and red circles represent star clusters with colours of $I - H > 1.3$. The cyan dashed box covers a region abundant in young star clusters. This region is already known to contain two very young (< 6 Myr) star clusters, Sersic 13-N and Sersic 13-S, both of which formed from a large HII region known as Sersic 13 (Villegas et al., 2005). The yellow grid represents $I-H$ colours in different regions of the dust lane, measured using *IRAF/POLYPHOT*. Redder regions in the grid may represent areas of high extinction. Cluster candidates in red dust lane regions often have red ($I-H > 1.3$) colours. Hence, these cluster candidates may be bluer than observed. There are also red regions of the dust lane that contain blue ($I - H < 1.2$) cluster candidates. Both cluster populations in these regions may be younger than observed due to the high extinction levels present.

cluster candidates may represent low extinction windows in the dust lane, while red cluster candidates may appear red due to high extinction.

In order to determine how extinction affects cluster candidate colours, the task *IRAF/POLYPHOT* was used to measure $I - H$ colours for different regions of the dust lane. Redder regions in the dust lane will likely represent higher levels of extinction. These colours were then compared to cluster candidate colours in the same region to determine if a correlation exists. Figure 3.8 shows the distribution of our cluster candidates and the varying colours of the dust lane. $I - H$ colours

obtained for different regions of the dust lane are labelled in green. There are several red cluster candidates in our sample that are in regions of high extinction. Hence, these candidates may be bluer and younger than observed in this survey. However, this also applies to several blue cluster candidates that are also located in regions of high extinction. Therefore, the ages derived in our survey can be taken as upper limits for our cluster candidate sample.

The luminosity function of these bluer candidates provides indirect evidence for the presence of newly formed star clusters in NGC 5128. Young ($\lesssim$ 500 Myr) star clusters in other galaxy mergers have luminosity functions well fit by a power-law of the form $\mathrm{d}N/\mathrm{d}L \sim L^{\alpha}$ where $\alpha \approx$ -2 (Goudfrooij et al. 2001b; Larsen 2002; Mengel et al. 2005). Both the bluer candidate population and total sample luminosity functions are well fit by this power-law and have slopes of $\alpha \approx$ -2. However, neither the bluer candidate population or the total candidate sample show a bend in their luminosity function, a feature that has been observed by Gieles et al. (2006a) for young star clusters in M51, NGC 6946 and the Antennae. Gieles et al. (2006a) conclude a break should appear in the power-law luminosity function of young star clusters due to their truncating mass function. Furthermore, they find the cluster luminosity function is better described by a double power-law fit or Schechter function. A possible reason to explain why this bend is not observed from the star cluster sample presented here is likely due to statistics. The bend observed by Gieles et al. (2006a) occurs at $M_V \approx -10$, which corresponds to a H band apparent magnitude of $m_H \sim 15$. None of the candidates in the NGC 5128 cluster sample extend to this bright magnitude, hence no bend is observed (see Figure 3.6). Gieles et al. (2006a) find a similar reason for the absence of this bend in the luminosity function from star clusters in the Magellanic Clouds and NGC 5236, which are better described by a single power-law fit.

Many of the blue star cluster candidates appear $\sim$ 600 parsecs north of the centre of NGC 5128 (see Figure 3.8). These star clusters may have formed from the giant HII cloud inhabiting that region, known as Sersic 13. Two of these star cluster candidates have already been confirmed as bona fide star clusters and are located in the northern and southern region of Sersic 13, respectively (Minniti et al. 2004; Villegas et al. 2005). Known as Sersic 13-N and Sersic 13-S, spectral surveys of these two star clusters by Minniti et al. (2004) have shown the presence of Wolf-Rayet stars in both clusters, indicating a young age of a few Myrs. Photometric analysis by Villegas et al. (2005) suggest these star clusters have ages between 3.9

Target	Our Survey			Villegas et al. (2005)	
	$I-H$	ϵ	r_e (pc)	ϵ	r_e (pc)
Sersic 13-N	-0.49 ± 0.06	0.24 ± 0.01	3.2 ± 0.3	0.23	3.5
Sersic 13-S	0.04 ± 0.03	0.11 ± 0.01	3.6 ± 0.3	0.09	3.9
Blue sample	0.52 ± 0.14	0.12 ± 0.01	3.0 ± 0.3		

TABLE 3.2: Comparison between star cluster properties from this survey and those obtained by Villegas et al. (2005).

- 5.9 Myrs. Both surveys report Sersic 13-S to be older than Sersic 13-N, with the latter showing bluer colours and the presence of nebular emission lines.

The $I-H$ colours obtained from these two star clusters provide an age of less than 1 Myr for Sersic 13-N and $\sim$ 2 Myrs the Sersic 13-S cluster. However, the SPS models used in this survey do not include nebular emission, which is important at very young ages. Therefore, the ages derived in our study for Sersic 13-N and Sersic 13-S can only be taken as estimates. Sersic 13-N is the bluest cluster in the candidate sample with a colour of $I-H = -0.49 \pm 0.06$ while Sersic 13-S has a redder colour of $I-H = 0.04 \pm 0.03$, appearing slightly brighter in the H band. Villegas et al. (2005) suggest that Sersic 13-S has a redder appearance possibly because it is further away from us than Sersic 13-N and its light is passing through a larger amount of gas and is more significantly scattered. While it is possible for Sersic 13-S to be further away than Sersic 13-N, neither I band or H band frames show any dust regions obscuring the light from either of these star clusters. Furthermore, Minniti et al. (2004) observe stronger Wolf-Rayet features in Sersic 13-S compared to Sersic 13-N, suggesting a larger number of Wolf-Rayet stars in Sersic 13-S than Sersic 13-N. Stellar winds from these massive stars will have likely expelled any gas from Sersic 13-S that was unresolved in the I and H band frames (Boily and Kroupa, 2003).

The presence of two bona fide star clusters in the sample presented here allow comparisons to be made with the remaining star cluster candidates. Table 3.2 lists the parameters determined for the Sersic star clusters in the literature compared to the values derived for them from our investigation, and values derived for the remaining candidate sample.

Slightly smaller values for size were obtained in this survey compared to those by Villegas et al. (2005). The difference in size is possibly due to their frames having a slightly better spatial resolution of 0.1″/pixel compared to the 0.13″/pixel H band frame used in our survey. Ellipticities of $\epsilon_{S13N} = 0.24 \pm 0.01$ and $\epsilon_{S13S} =$

0.11 ± 0.01 were also obtained in our study and are in agreement with those from Villegas et al. (2005). The other blue star cluster candidates have a mean size of $\langle r_e \rangle = 3.0 \pm 0.3$ pc and mean ellipticity $\langle \epsilon \rangle = 0.12 \pm 0.01$, although peaking at $\epsilon = 0.06$. The difference in mean and peak ellipticity values suggest that while the majority of objects are quite round, there are a number of elongated star clusters in the candidate sample. There is no correlation between cluster age and ellipticity however, as the values listed in Table 3.1 show the candidate $I - H$ colour varies randomly with ϵ.

The sizes of the blue candidates are somewhat smaller than those observed from young star clusters in other mergers of similar age such as NGC 3921 and NGC 7252, both of which have star clusters with average sizes $\sim$ 5 - 7 pc (Schweizer et al. 1996; Bastian et al. 2013c). However, the sizes of these blue candidates are in good agreement with the average size of GCs in the Galaxy, which have a mean value of $\langle r_e \rangle = 3$ pc (Djorgovski, 1993). In essence, any star cluster with $\geq 10^4$ stars, and $r_e \leq 10$ pc is likely to be bound if it has an age 10 - 20 core-crossing times, t_{cr} (Schweizer et al., 2004). Given that the blue candidate sample have sizes similar to GCs in the Galaxy, one can assume that they have similar crossing times of $t_{cr} \sim$ few Myrs (Meylan and Heggie, 1997). As mentioned earlier, 63 blue candidates show colours corresponding to ages greater than 200 Myrs and so have ages exceeding 50 t_{cr}. Hence, these candidates are likely bound.

3.4.1 Formation *vs* Destruction of Star Clusters

An important open question in the evolution of star cluster populations is whether tidal interactions between merging galaxies destroy more star clusters than are formed. Simulations by Kruijssen et al. (2012) show that the dynamical heating of star clusters by tidal shocks, which are about an order of magnitude stronger in merging galaxies than in isolated galaxies, is sufficient to destroy star clusters at a higher rate than new clusters are being formed. Thus, the total number of star clusters in a galaxy merger may actually decrease due to the merging process.

Tidal shocks in high gas density environments are known to have a disruptive effect on star clusters (e.g., Gieles et al. 2006c). However, the destruction rate of star clusters decreases with increasing cluster mass and density (Spitzer 1987; Lamers et al. 2005), hence low-mass star clusters are preferentially disrupted while the brightest and therefore most massive star clusters are least affected by disruption.

This implies that the effects of star cluster disruption may largely go unnoticed in observations due to observational selection effects which tend to sample the brightest star clusters.

The star cluster sample presented here can be used to determine a very crude estimate of how disruptive tidal interactions in NGC 5128 may have been to the progenitor GC population at the centre. By comparing the number of detected star clusters to those expected from an extrapolation of the old GC cluster population at larger galactocentric radii, one can determine whether the effect of tidal shocks due to the merger in NGC 5128 has destroyed more star clusters than it has formed.

The radial distribution of GCs in isolated galaxies approximately follow a power-law profile of the form $n \sim R^{-\alpha}$, where n is the number of GCs at a radius R from the galactic centre (Harris et al., 2004). The value of α roughly correlates with galaxy luminosity in the sense that luminous elliptical galaxies show shallower values of α than spirals (Harris 1993; Kaisler et al. 1996; Woodworth and Harris 2000). Photometric studies of GCs in NGC 5128 by Harris et al. (2004) and Harris et al. (2006) found the radial distribution to follow a power-law with $\alpha \sim 2$.

Harris et al. (2006) used this trend to determine a crude estimate of the GC population within $3'$ of the centre of NGC 5128 in their HST/ACS V band frame, finding a population of 190±14 GCs. Unlike the survey presented here, Harris et al. (2006) observed GCs to the faint end of the standard GCLF. They also applied similar selection criteria to those presented in § 3.2.2, with the exception of a colour constraint of $-0.6 < (I - H) < 3.1$. This colour constraint had little affect on our candidate sample once they passed the other selection criteria, removing only 2 objects from the candidate sample. Hence, a GC value of $N_{exp} = 190 \pm 14$ can be adopted as the number of GCs expected in the WFC3 frames used here.

From the sample of star cluster candidates obtained in § 3.2.2, 90 showed colours corresponding to ages younger than the estimated merger time, while the remaining 70 candidates may be progenitor GCs. However, as shown in § 3.3.2, the applied magnitude constraint did not sample old GCs at the faint end of the GCLF, and detected only 82% of the total GC population. The total old GC population in the WFC3 frames is $N_{GC}^{Tot} = 85$, giving a total sample of $N_{obs} = 175 \pm 14$ star clusters present at the centre of NGC 5128. Hence, the observed population accounts for 90% of the expected population.

It is possible that some star clusters were also subtracted with the galaxy light due to over subtraction. To test the plausibility of this query, 190 artificial clusters with similar parameters to the detected cluster sample were randomly distributed on the raw H band frame. The galaxy light subtraction method from § 3.2.1 was then performed on this frame, and the detection and selection methods discussed in § 3.2.2 were then applied. 176 artificial clusters were retrieved from the galaxy light subtracted H band frame. Hence, 14 star clusters are added to the observed sample to account for loss due to the applied galaxy light subtraction method, giving a total observed sample of 189 ± 14. This suggests our observed cluster population can account for the expected cluster population. Therefore, in contrast to simulations by Kruijssen et al. (2012), our results suggest that tidal interactions do not destroy more star clusters than they produce. Furthermore, given that the extinction in some parts of the dust lane may be as high as $A_V = 7$ (Schreier et al., 1996), the centre of NGC 5128 may harbour more star clusters than were observed in our survey.

3.5 Conclusion

High spatial resolution images of the central $3'$ region of NGC 5128 were obtained using the Wide Field Camera 3 (WFC3) on board the HST to investigate whether the tidal interactions due to the merger have produced a new population of star clusters. A sample of 160 star cluster candidates were detected based on magnitude and colour cuts, and physical parameters expected from star clusters.

- SPS models indicate that 56% of these star cluster candidates are younger than 250 Myrs, based on their $I - H$ colours. The youngest of these blue candidates have ages between 1 - 10 Myrs, and are found around Sersic 13, a giant HII cloud known for producing at least 2 young (1 - 6 Myr) star clusters (Minniti et al., 2004). The abundance of these blue candidates supports the possibility that tidal interactions from the merger may have produced an array of new star clusters. Indirect evidence further supporting this possibility comes from the power-law luminosity function of these blue candidates, which is typically observed from young star cluster populations.
- These star cluster candidates are not as large as young star clusters in other mergers of similar age, such as NGC 3921 and NGC 7252, which have average

sizes between 5 - 7 pc (i.e., twice as large as seen in NGC 5128). It is possible that the smaller sizes observed here are due to lower gas pressures involved.

- Our observed cluster population is in rough agreement with the total GC population expected at the centre of NGC 5128. We suspect more star clusters may be present at the centre but were not observed in our survey due to the high extinction affects of the dust lane. Our findings are in disagreement with simulations by Kruijssen et al. (2012) which show that tidal shocks in mergers destroy more star clusters than they form. A comparison between observed and expected star cluster populations in other galaxy mergers are required to shed light on this debate.

Chapter 4

The Antennae: NGC 4038/4039

4.1 Introduction

The Antennae (Figure 4.1) consists of two disturbed spiral galaxies (NGC 4038 / NGC 4039) and is one of the youngest and closest examples of a pair of merging disk galaxies in the Toomre (1977) sequence. Dynamical models estimate a time lapse of roughly 200 Myrs since the last pericentre passage (Barnes, 1988), which is also when the tidal tails formed (Whitmore et al., 1999). Models suggest that the merger will be complete within $\sim$ 100 Myrs (Mihos et al., 1993). The merging process has produced a high global star formation rate for the Antennae, estimated to be 20 $\mathcal{M}_{\odot}$ yr^{-1} (Zhang et al., 2001).

HST observations of the Antennae by Whitmore and Schweizer (1995) and Whitmore et al. (1999) led to the discovery of a large population of compact star clusters, often referred to as super star clusters (SSCs), with a variety of ages. Since then the Antennae has been observed in virtually all bands (e.g., Wilson et al. 2000; Mengel et al. 2005; Hibbard et al. 2005; Fabbiano et al. 2003). Nearly 8000 star clusters were identified by Whitmore and Schweizer (1995) using HST/WFPC2, the faintest and reddest of which were revealed to be bright near-infrared and mid-infrared emitters, and contain the youngest stars (Wang et al. 2004; Brandl et al. 2005; Snijders et al. 2006). Indeed, many of the star clusters are embedded in dust/gas clouds, making near-infrared observations particularly powerful. Near-infrared broad-band imaging by Mengel et al. (2005) identified over a thousand young star clusters.

The age distribution of the star cluster population in the Antennae can be loosely divided into four groups: $<$ 20 Myr, $\sim$ 100 Myr, $\sim$ 500 Myr, and a population of possible progenitor globular clusters exceeding ages of 1 Gyr, indicating multiple periods of star formation since the merging process began (Whitmore et al., 1999). Furthermore, the clusters formed recently from the merger are seen to follow a power-law luminosity function of the form $\mathrm{d}N/\mathrm{d}L \sim L^{\alpha}$ where $\alpha \approx$ -2 and have a truncated power-law mass function of the form $\mathrm{d}N/\mathrm{d}M \sim M^{\beta} \exp\left(-\frac{M}{M_c}\right)$ where $\beta \approx$ -2 and $\mathrm{M}_c \gtrsim 10^6\ \mathcal{M}_{\odot}$ (Gieles et al. 2006b; Bastian 2008; Whitmore et al. 2010).

Many of the above studies relied on photometric data, with relatively few using spectroscopic analysis. While observationally time intensive, spectroscopic surveys are extremely powerful as they provide far more information about the properties of a star cluster than photometric data can provide. Hence, the survey presented in this chapter uses near-infrared spectroscopic data from the recently commissioned KMOS Multi-object Integral Field Spectrometer at the ESO Very Large Telescope (VLT) (Sharples et al., 2010, 2013). This instrument comprises of 24 arms which can be positioned so as to cover almost any combination of objects within a 7.2′ patrol field. Each arm is an integral field unit (IFU) with a field of view of $2.8'' \times 2.8''$ and a sampling of 0.2″/pixel. KMOS is designed so that 8 IFU arms are fed into a single spectrograph and have their light dispersed onto a single detector. Thus, in total KMOS consists of 3 spectrographs and 3 detectors. KMOS observes a wavelength range of 0.8 - 2.5μm, which is divided into 5 gratings: IZ, YJ, H, K, and HK. The spectral resolution provided by KMOS is $\sim$ 3000 depending on the grating being observed. Table 4.2 provides further information of the capabilities of KMOS. The multiple IFUs of KMOS enable many star clusters to be observed simultaneously, thus improving the efficiency of the spectroscopic survey. Observations in the near-infrared also permit coverage of areas of high extinction in the Antennae, which are obscured in the optical.

A spectroscopic survey of a sample of 47 star clusters was taken over a 12 night period during the commissioning phase of KMOS between January and April 2013. Spectra were taken in the YJ, H, K, and HK bands with intermediate spectral resolution ($\sim$ 2000 - 3800; see Table 4.2 for further information). Whitmore et al. (2010) divided the Antennae galaxies into 18 star-forming knots, of which 16 were observed in the study presented here.

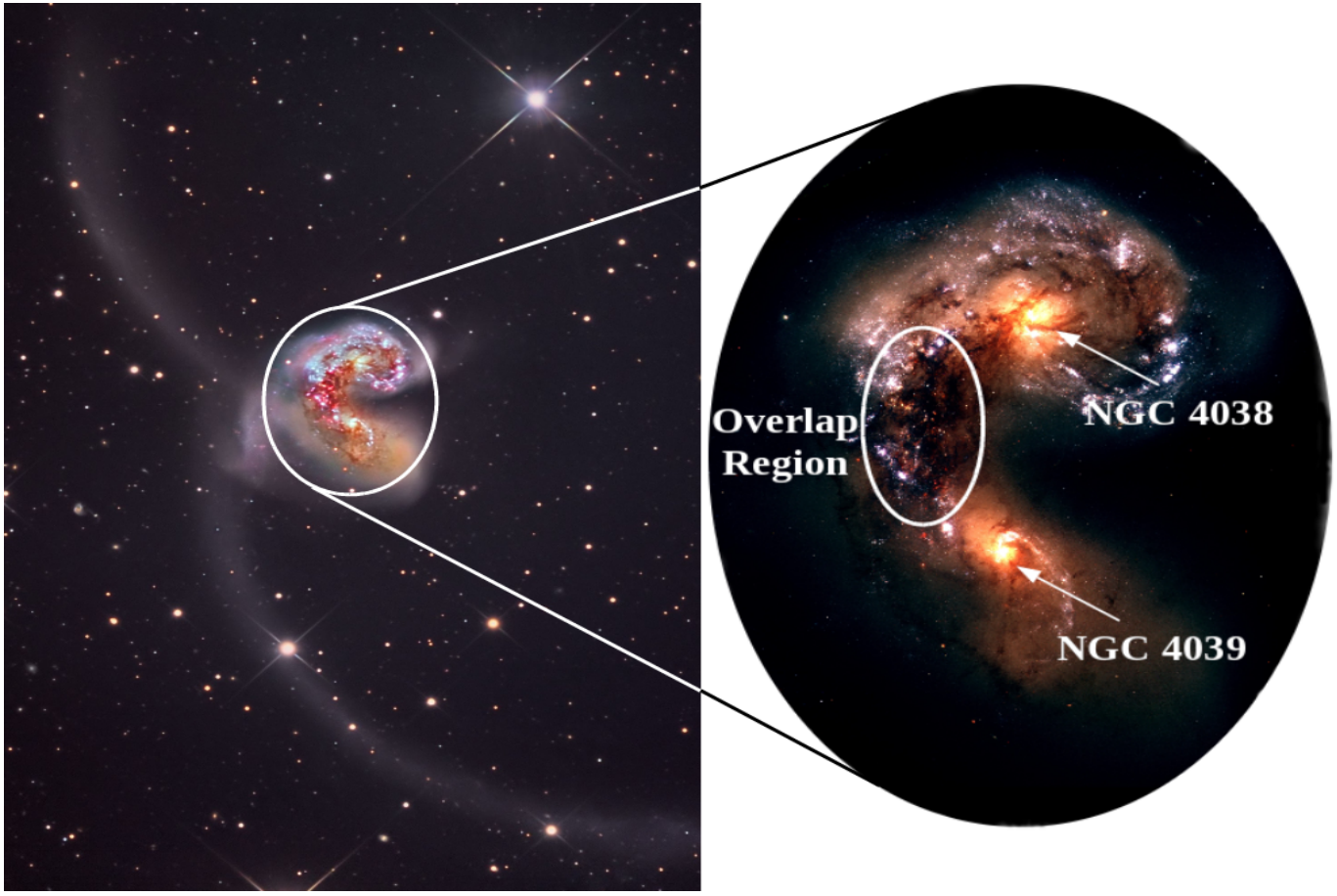

FIGURE 4.1: *Left:* RGB image from the Cerro Tololo Inter-American Observatory (CTIO) of the Antennae. The bulges of the two progenitor galaxies can be seen here as well as the tidal tails produced from the merging process. The area observed in this survey is highlighted by the white circle. *Right:* Closer inspection of the central region of the Antennae. The overlapping region between the two progenitor galaxies is highlighted.

There has been some debate in the literature about the distance to the Antennae. Under the assumption that $H_o = 72$ kms^{-1}Mpc^{-1}, the recession velocity of the merger provides a distance of 19.2 Mpc (Whitmore et al., 1999). However, distance measurements using the tip of the red giant branch have suggested a much closer distance of 13.3 Mpc (Saviane et al., 2008), while measurements using the Type Ia supernova 2007sr have given a distance of 22.3 Mpc (Schweizer et al., 2008). A distance of 19.2 Mpc is adopted for the work presented here as it is the most commonly used distance in the literature and provides a direct comparison between results.

The star cluster sample and data reduction procedures are introduced in § 4.2. Stellar population synthesis models used for analysis and derived cluster properties are presented in § 4.3. Implications from these derived properties are discussed in § 4.4, and conclusions follow in § 4.5.

4.2 Data Reduction

4.2.1 Cluster Catalogue

The star clusters studied in this survey were selected from catalogues produced from earlier near-infrared spectral observations of star clusters in the Antennae (Gilbert and Graham 2007; Christopher 2008; Greissl et al. 2010), as well as optical spectral observations (Bastian et al., 2009) and optical photometric observations (Whitmore et al., 1999, 2010). Previous spectroscopic surveys of Antennae star clusters have generally focused on small samples of only a few clusters observed with high ($\lambda/\delta\lambda > 7500$) spectral resolution, or low ($\lambda/\delta\lambda \sim 1500$) resolution observations of many (> 20) clusters. While high resolution spectroscopy of several star clusters provides detailed spectra, it does not provide a complete census of the star-forming regions in the Antennae. This is critical for understanding the formation and evolution of young massive star clusters in galaxy mergers. Observations of a large sample of star clusters throughout the star-forming regions of the Antennae will give a better insight into their properties, such as age, mass, metallicity, and how they vary with location. The work presented here consists of medium ($\lambda/\delta\lambda \sim 2000$ - 3800) resolution spectroscopy of a large sample of star clusters located throughout the major star-forming regions in the Antennae. This

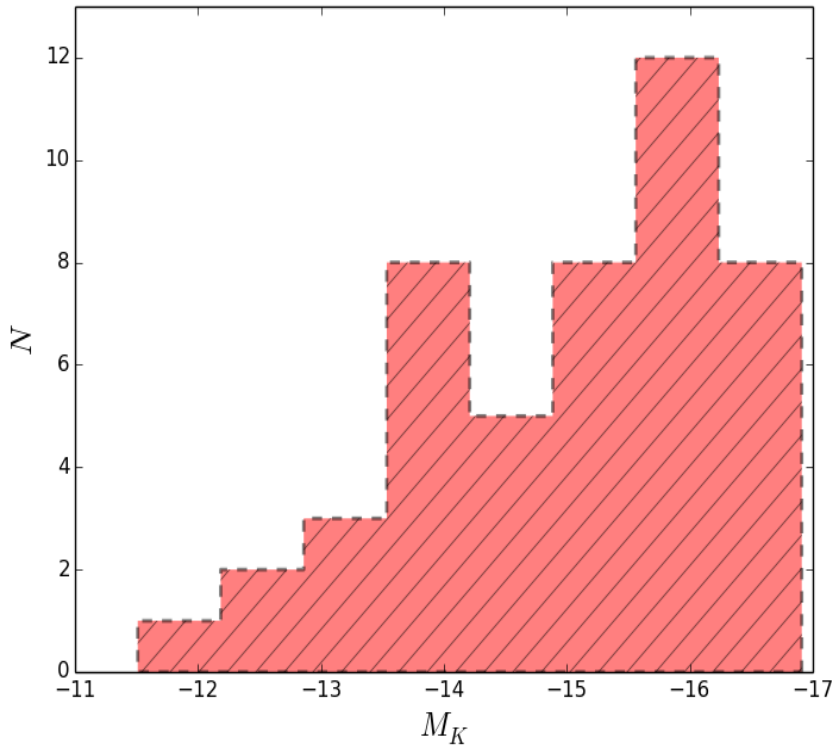

FIGURE 4.2: Absolute K band magnitude distribution of star cluster targets in the Antennae. The average magnitude of our sample is $M_K = -15$ mag.

sample will give a direct comparison between variation in cluster properties with environment, and therefore help evaluate how star clusters form and evolve within a galaxy merger.

An initial sample of 84 star cluster candidates was compiled from the literature. For the sake of comparison, star clusters previously observed with NIR spectroscopy were then prioritised. Star clusters with optical spectra were given medium priority, while those with only photometric data were given lowest priority. The KMOS arms were then allocated using this prioritised catalogue and evenly distributed throughout the star-forming regions in the Antennae. This selection criteria produced a final sample of 47 star clusters for which near-infrared spectra were obtained. 26 star clusters were observed in the H, K and HK gratings, and 30 were observed in the YJ grating. 9 star clusters were observed in all these gratings. Target IDs and their basic parameters are given in Table 4.1.

Figure 4.3 shows the pointings of each of the 47 clusters in the sample overlaid on top of a HST/WFC3 frame of the Antennae in the F110W and F160W bands (Whitmore et al., 2010). Star clusters are colour-coded based on the bands in

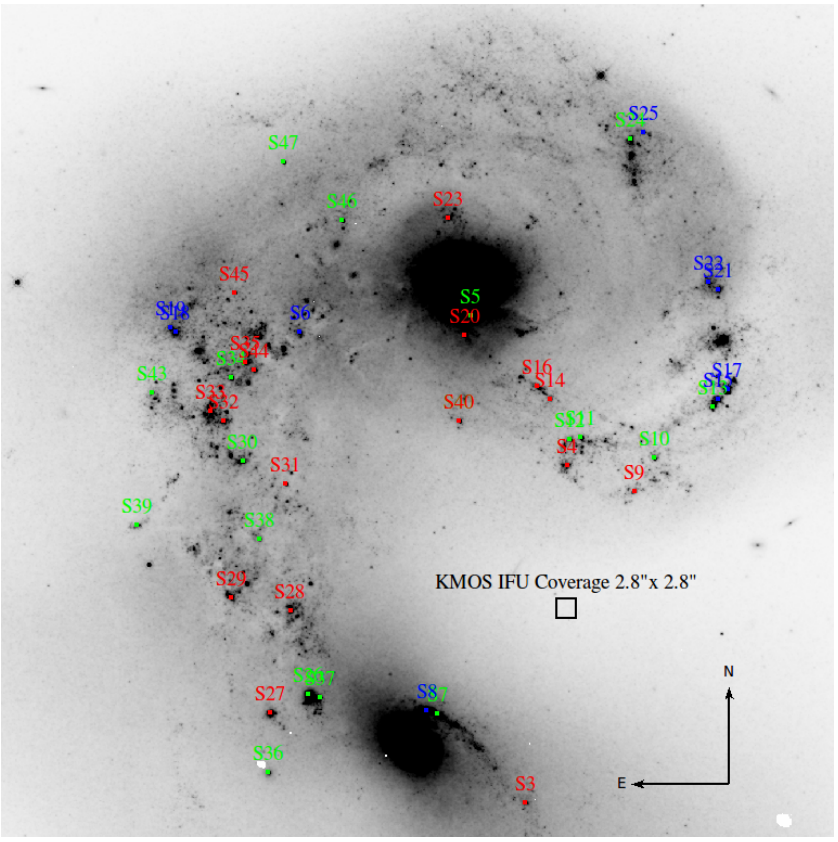

FIGURE 4.3: KMOS cluster targets in the Antennae. A total of 47 clusters were observed using KMOS. 26 star clusters were observed in the H, K and HK gratings, and 30 were observed in the YJ grating. The green circles in this figure represent star clusters observed with the YJ grating, and the red circles represent those observed with the H, K, and HK gratings. 9 star clusters were observed in all these gratings and are shown as the blue circles. A single KMOS IFU coverage is shown by the black box.

which they were observed. Green clusters have been observed in the YJ band, and red clusters have been in the H and K bands. The blue clusters have been observed in both bands. The spatial coverage of a single KMOS IFU ($2.8'' \times 2.8''$) is also shown in this figure, represented by the black box. As shown in Figure 4.3, the cluster sample is well distributed throughout the Antennae.

Target	Other names	α_{J2000}	δ_{J2000}	m_K	Observation band
Antennae		$12^h01^m53^s.40$	$-18°52'25''$	7.2	
S1	B111	$12^h01^m53^s.27$	$-18°51'37''.46$	19.9*	H,K,HK
S2	B130	$12^h01^m55^s.27$	$-18°51'37''.07$	19.1*	H,K,HK
S3	B299	$12^h01^m52^s.35$	$-18°53'18''.70$	18.4*	YJ
S4	B324	$12^h01^m51^s.93$	$-18°52'30''.40$	18.6*	H,K,HK
S5	B352	$12^h01^m52^s.91$	$-18°52'08''.92$	17.2*	YJ
S6	B367	$12^h01^m54^s.63$	$-18°52'11''.32$	18.4*	YJ,H,K,HK
S7	C14, B270	$12^h01^m53^s.24$	$-18°53'06''.09$	16.0	YJ
S8	C17	$12^h01^m53^s.35$	$-18°53'05''.51$	16.1	YJ,H,K,HK
S9	C41	$12^h01^m51^s.25$	$-18°52'34''.08$	16.1	H,K,HK
S10	C49	$12^h01^m51^s.06$	$-18°52'29''.34$	15.5	YJ
S11	C54	$12^h01^m51^s.79$	$-18°52'26''.43$	15.8	YJ
S12	C55	$12^h01^m51^s.90$	$-18°52'26''.71$	15.8	YJ
S13	C61	$12^h01^m50^s.46$	$-18°52'21''.98$	15.0	YJ
S14	C62	$12^h01^m52^s.10$	$-18°52'20''.88$	16.0	H,K,HK
S15	C63	$12^h01^m50^s.41$	$-18°52'20''.86$	15.1	YJ,H,K,HK
S16	C65	$12^h01^m52^s.24$	$-18°52'19''.04$	16.0	H,K,HK
S17	C68	$12^h01^m50^s.31$	$-18°52'19''.56$	16.1	YJ,H,K,HK
S18	C82, W36731	$12^h01^m55^s.89$	$-18°52'11''.41$	14.9	YJ,H,K,HK
S19	C85	$12^h01^m55^s.94$	$-18°52'10''.72$	14.9	YJ,H,K,HK
S20	C87	$12^h01^m52^s.97$	$-18°52'11''.71$	15.1	H,K,HK
S21	C88, B343	$12^h01^m50^s.40$	$-18°52'05''.27$	15.5	YJ,H,K,HK
S22	C90	$12^h01^m50^s.50$	$-18°52'04''.17$	15.7	YJ,H,K,HK
S23	C97, W46102	$12^h01^m53^s.14$	$-18°51'54''.93$	15.5	H,K,HK
S24	C108	$12^h01^m51^s.29$	$-18°51'43''.61$	14.7	YJ
S25	C109	$12^h01^m51^s.16$	$-18°51'42''.64$	16.3	YJ,H,K,HK
S26	GB, C19, W15466, G89/90	$12^h01^m54^s.54$	$-18°53'03''.21$	14.5	YJ
S27	GB1, C15, W14612	$12^h01^m54^s.93$	$-18°53'05''.83$	14.7	H,K,HK
S28	GC, C26, W18848	$12^h01^m54^s.73$	$-18°52'51''.31$	15.2	H,K,HK
S29	GD, C29, W19330	$12^h01^m55^s.32$	$-18°52'49''.33$	15.4	H,K,HK
S30	GE2, C48, W25439	$12^h01^m55^s.21$	$-18°52'29''.77$	15.6	YJ
S31	GE3, C42, W24126	$12^h01^m54^s.78$	$-18°52'33''.07$	17.1	H,K,HK
S32	GE4, W28435	$12^h01^m55^s.40$	$-18°52'24''.24$	15.7	H,K,HK
S33	GE5, W29516	$12^h01^m55^s.53$	$-18°52'22''.56$	15.3	H,K,HK
S34	GF	$12^h01^m55^s.33$	$-18°52'17''.87$	15.9	YJ
S35	GF1	$12^h01^m55^s.19$	$-18°52'15''.80$	15.7	H,K,HK
S36	W11721	$12^h01^m54^s.95$	$-18°53'14''.48$	17.0	YJ
S37	W15398	$12^h01^m54^s.43$	$-18°53'03''.62$	16.8	YJ
S38	W21464	$12^h01^m55^s.04$	$-18°52'41''.00$	17.7	YJ
S39	W22079	$12^h01^m56^s.28$	$-18°52'39''.02$	17.7	YJ
S40	W28556	$12^h01^m53^s.02$	$-18°52'24''.07$	16.8	H,K,HK
S41	W29090	$12^h01^m55^s.53$	$-18°52'22''.23$	17.5	YJ
S42	W30673	$12^h01^m56^s.10$	$-18°52'20''.81$	17.8	YJ
S43	W31216	$12^h01^m56^s.13$	$-18°52'19''.97$	17.9	YJ
S44	W33331	$12^h01^m55^s.09$	$-18°52'16''.78$	16.7	YJ
S45	W40436	$12^h01^m55^s.29$	$-18°52'05''.65$	17.8	H,K,HK
S46	W45889	$12^h01^m54^s.20$	$-18°51'55''.30$	17.3	YJ
S47	W50277	$12^h01^m54^s.80$	$-18°51'46''.92$	17.2	YJ

TABLE 4.1: Basic parameters for Antennae star clusters. Targets were selected from the literature. Target names beginning with 'B' are from Bastian et al. (2009), those beginning with 'C' are from Christopher (2008), 'G' are from Gilbert and Graham (2007), and 'W' are from Whitmore et al. (2010). Target GB, also known as G89/90, was observed by Greissl et al. (2010). Cluster coordinates are taken from the HST/WFC3 world coordinate system. The fifth column gives the apparent K band magnitudes for these clusters which were also taken from the aforementioned literature. However, apparent magnitudes with an asterisk superscript were converted from the I band using spectral model fits from *Starburst99* stellar population synthesis models. The last column presents the wavebands each cluster was observed in.

4.2.2 Spectral Observations

Spectra were obtained at medium ($\sim$ 3400 - 3800) resolution for the H, K, and YJ gratings provided by KMOS. Spectra were also taken in the HK observing mode, which has a lower spectral resolution of $\lambda/\delta\lambda \sim 2000$. 26 star clusters were observed in the H, K, and HK bands, and 30 clusters in the YJ observing band (1.03 - 1.34μm). Table 4.2 provides a summary of the observation dates and exposure times.

The KMOS Arm Allocator software (*KARMA*) was used to allocate arms to individual targets (Wegner and Muschielok, 2008). Cluster coordinates were uploaded to the software and arms were assigned using a combination of built-in allocation algorithms and manual allocation to star cluster targets. Figure 4.4 shows an example of the *KARMA* graphical interface during arm allocation for the H, K and HK observations. The observation mode for all bands was set to *Free-dither*, which moved the telescope between two positions while keeping the arm positions fixed. This allowed the arms to switch between star cluster targets and a nearby sky background position (typically 20″ away from cluster targets). The switch between cluster target and sky positions typically occurred after 5 - 20 minutes of target observation. This ensured that reliable sky background measurements were available for data reduction. In addition, the *Free-dither* mode moved the IFUs around the cluster targets and background positions in a pre-defined dither pattern. These small offsets (2.7″) ensured different pixels on the IFU array were used for the same target, which is particularly useful for improving flat fielding of faint sources.

Of the 24 available KMOS IFUs, arms 11, 13 and 22 were fixed on regions devoid of star clusters and bright objects for the H, K and HK observations. Arms 1, 11, 20 and 23 were also fixed at similar positions for YJ observations. These arms were used to improve sky subtraction by making simultaneous observations of the local background.

Band	Date	Exposure Time (secs)	$\lambda/\delta\lambda$	λ Range	Airmass	Seeing FWHM	Spectral features
YJ	29/03/2013	4800	3400	1.15-1.32μm	1.010	0.70	Paβ, HeI
	30/03/2013	4800			1.068	0.65	
	29/01/2013	3600			1.034	1.28	
H	30/01/2013	2400	3800	1.54-1.79μm	1.020	2.20	FeII, CO 6-3
	24/03/2013	1200			1.023	0.90	
	26/03/2013	1500			1.801	0.60	
	23/01/2013	3600			1.375	0.71	
	27/01/2013	5400			1.016	0.99	
K	28/01/2013	3600	3800	2.03-2.29μm	1.022	1.45	Brγ, CO 2-0
	24/03/2013	1200			1.006	1.52	
	25/03/2013	1200			1.208	0.64	
	27/03/2013	2800			1.347	0.84	
	24/03/2013	1200			1.012	0.95	
HK	25/03/2013	1200	2000	1.54-2.29μm	1.122	1.13	FeII, Brγ
	26/03/2013	1500			2.367	0.73	
	27/03/2013	2800			1.130	0.74	

TABLE 4.2: Summary of KMOS observations of star clusters in the Antennae. The first column represents the observing modes used by KMOS for star cluster observations. The last column gives some example features observed at these wavelengths from star clusters.

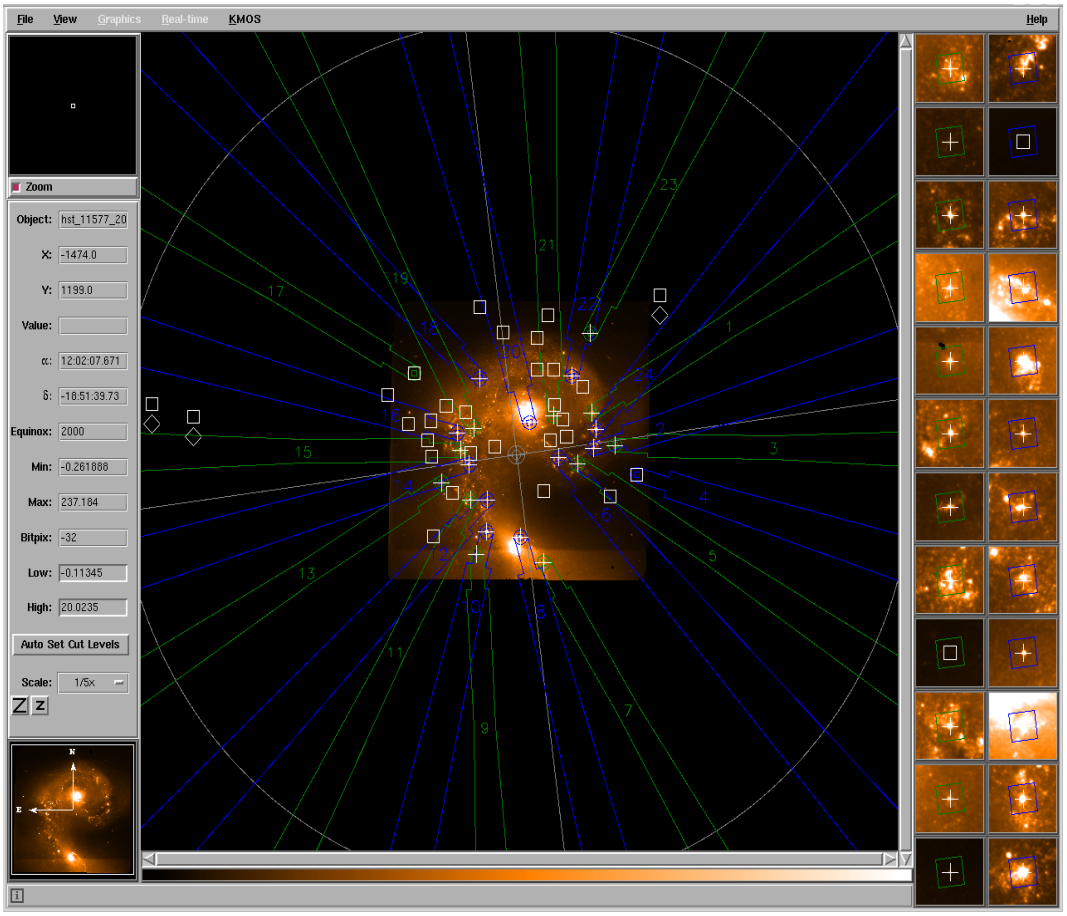

FIGURE 4.4: Selecting star clusters in the Antennae galaxies using KARMA for H, K and HK observing modes. Crosses represent star clusters targeted for these observations, diamonds represent reference stars used to align the telescope and instrument, and squares represent all sky observations. The blue and green arms represent the top and bottom layers of the KMOS IFUs, respectively. Each IFU has a spatial coverage of $2.8'' \times 2.8''$, which corresponds to an area of ~ 0.07 kpc^2 at the distance of the Antennae. The 24 small images on the right show the coverage of each IFU. The background image is a HST/WFC3 F110W/F160W image with a spatial resolution of $0''.1$. The smaller images on the right are therefore not representative of the typical VLT near-infrared seeing of FWHM $\sim 0''.7$.

4.2.3 Processing KMOS Datasets

A single KMOS integration produces three data frames stacked in three extensions of a single file, each of which are 2048×2048 pixels in size. Each frame/extension represents data recorded from one near-infrared detector. KMOS consists of three detectors, with 8 IFUs assigned to each detector. Each IFU consists of 14 slices, with approximately 14 detector pixels across each slice. Figure 4.5 shows the typical appearance of one of these raw datasets.

Each observation night in Table 4.2 typically consists of half a dozen KMOS integrations as the *Free-dither* mode switched the IFUs between object and sky positions multiple times throughout a single night. Calibration frames, namely dark, flatfield, arc and standard star frames, were taken before and after each science observation. These also consisted of several KMOS integrations at different instrument rotator angles to minimise flexure effects.

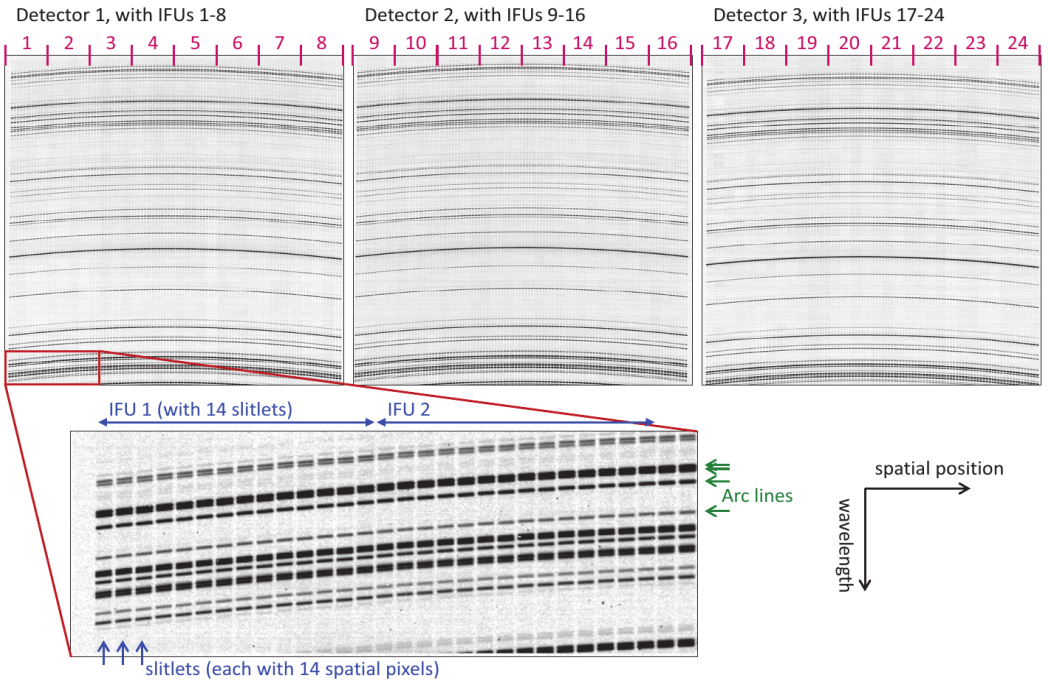

FIGURE 4.5: Illustrative layout of KMOS raw dataset. *Top*: H band images of arc lines from all three detectors, illustrating how data are arranged on the detectors. The curved black lines across each detector are the arc lines. There are 8 IFUs across each detector or 112 slices. The wavelength axis is in the vertical direction, with longer wavelengths at the top and shorter wavelengths at the bottom. The horizontal axis denotes spatial position. *Bottom*: Closer inspection of a section of one image. Each IFU is divided into 14 slitlets across the spatial axis. Each slitlet covers approximately 14 pixels.

4.2.3.1 Processing Calibration Frames

Recipes from the ESO *SPARK* data reduction package (Davies et al., 2013) were used to process these raw frames. Calibration of the KMOS datasets can be summarized as three procedures: (1) correct variations in pixel gain on each detector and spatial variations in throughput of the instrument (i.e., flat-fielding); (2) map each measured value on the detector to a spatial/spectral location in a reconstructed cube; (3) correct for spectral variations in atmospheric and instrument transmission, and apply a flux calibration.

Flat-fielding is a two-step procedure. First, raw dark frames were used to identify hot pixels. This was achieved using the *kmo_dark* recipe, which outputs a bad pixel mask for any flagged bad pixels and a mean dark frame and noise map. The second phase utilised the *kmo_flat* recipe to identify cold pixels in the raw flatfield frames based on their low flux. This recipe output a bad pixel mask combining the bad pixels identified from both dark and flatfield frames, as well as a mean flatfield frame and noise map.

In addition to the bad pixels file and mean flatfield frames, the *kmo_flat* recipe produced a set of x and y calibration frames. These are used to assign a spatial location to each measured value on the detector, and are used in conjunction with raw arc frames and a reference arc lines file to produce a spectral calibration frame using the recipe *kmo_wave_cal*. Arc frames are obtained using observations of Argon or Neon wavelength calibration lamps. *kmo_wave_cal* produces a spectral calibration frame by first searching for known emission lines from these elements using the list of reference arc lines already provided, and then fitting a polynomial function to these lines along the dispersion direction. During this calibration stage, *kmo_wave_cal* treats each slitlet independently in order to limit the order of the fit along the spatial axis and to avoid problems that may arise due to possible discrete shifts between the slitlets.

The final calibration requirements for data reduction were to correct for absorption in the spectra due to the Earth's atmosphere and apply a flux calibration. As is common for near-infrared spectroscopy, the same standard stars are used for both telluric correction and flux calibration. Standard star frames are processed by *kmo_std_star* until a reconstructed cube is available. The spatial/spectral calibration frames produced earlier are used here to produce a reconstructed cube. A 1D integrated spectrum is then extracted from this cube and corrected for stellar

features, either by using a solar spectrum or fitting out the most common lines, in order to produce a telluric spectrum. An atmospheric model is used to guide the line fitting, since some stellar lines are blended with atmospheric lines. The telluric spectrum is then divided by the effective temperature of the standard star and normalised, yielding a telluric correction frame. The *kmo_std_star* routine also applies flux calibration by determining a zeropoint for each IFU using the magnitude of the standard star and the total flux within the field of view of each IFU. The zeropoint, which is written into the header of the processed files, is defined as $magnitude = zeropoint - 2.5log_{10}(counts/second)$.

4.2.3.2 Processing Science Frames

The standard monolithic pipeline recipe *kmo_sci_red* was called to process all science frames for a given night in Table 4.2. This recipe intakes a set of science frames (frames that observed objects and frames that observed the sky) together with calibration frames produced from the procedure described in § 4.2.3.1. The *kmo_sci_red* recipe first selects a calibration angle that best matches the dataset. It then identifies which IFUs observed an object and which IFUs observed the sky. For each object frame, *kmo_sci_red* then assigns a sky frame that is taken closest in time to that object frame. Depending on the observing sequence during observation, some nights in Table 4.2 consist of more object frames than sky frames. For these cases, a single sky frame is assigned to multiple object frames.

Once a calibration angle is selected and object-sky pairings assigned, *kmo_sci_red* begins processing the science frames. This recipe applies the following procedure to reduce the data: subtract the sky frame from the object frame, divide the result by the flatfield, reconstruct the cubes, divide out the telluric spectrum, align the cubes, and finally combine them. However, because each IFU may have to be treated differently, the recipe processes one IFU at a time. The resulting output from *kmo_sci_red* is a set of combined data cubes, one for each IFU, and an associated noise cube. Figure 4.6 shows a typical data cube and extracted spectrum from the YJ band.

4.2.3.3 Enhanced OH Subtraction

Due to the significant presence of OH night sky emission lines in the near-infrared, an additional subtraction step was performed following the recipe of Davies (2007). The *kmo_sci_red* routine extracted a 1D spectrum for each target and sky cube and determined the location of bright OH lines using a reference OH line file. It then scaled the OH lines in the sky spectrum to match the object spectrum and subtracted them. The resulting target cube showed reduced OH line contamination. Figure 4.7 shows the spectrum for a typical star cluster before and after sky subtraction, and then after this enhanced OH subtraction procedure.

4.2.4 Quality of Output Data Cubes

A concern when combining all the science frames from an observation night is whether there will be any deterioration in quality of the output spectra due to instrumental shifts. This can be tested by comparing the combined data cubes to a single cube from one science frame. Figure 4.8 shows a comparison between the spectra obtained from a single data cube and combined data cube in the K band from night 27-03-2013. Data from this night is particularly interesting because the observation consists of six object frames and only one sky frame. The time between an object frame and sky frame is up to 25 minutes for this night. Therefore, the sky subtraction procedure may not have worked as well for these frames. If this is the case, the resultant combined data cube may have a lower signal-to-noise ratio than a single cube produced from an object frame taken at a closer time to the sky frame.

Inspecting the two spectra in Figure 4.8, one can see the single cube spectrum contains several P-Cygni residuals that are absent in the combined cube spectra. These are likely due to a combination of cosmic rays and instrumental flexure, and have been removed during the combining procedure. A comparison between the S/N of the two spectra show an average increase of $\sim$ 10% for the combined data cube. S/N values were estimated by measuring the strength of the brightest emission lines in both spectra relative to their continua. A 10% - 20% increase in S/N is typically what is observed from all the combined cubes.

A common result when combining object cubes is that they are not perfectly stacked on top of each other. This is due to subtle changes in the positions of the

targets on the IFUs between each KMOS integration. The variation in the spatial positions of each object is at most 2 pixels, and causes minimal ($\sim 5\%$) loss in S/N for the combined cubes. Figure 4.9 shows a combined cube that is not perfectly stacked.

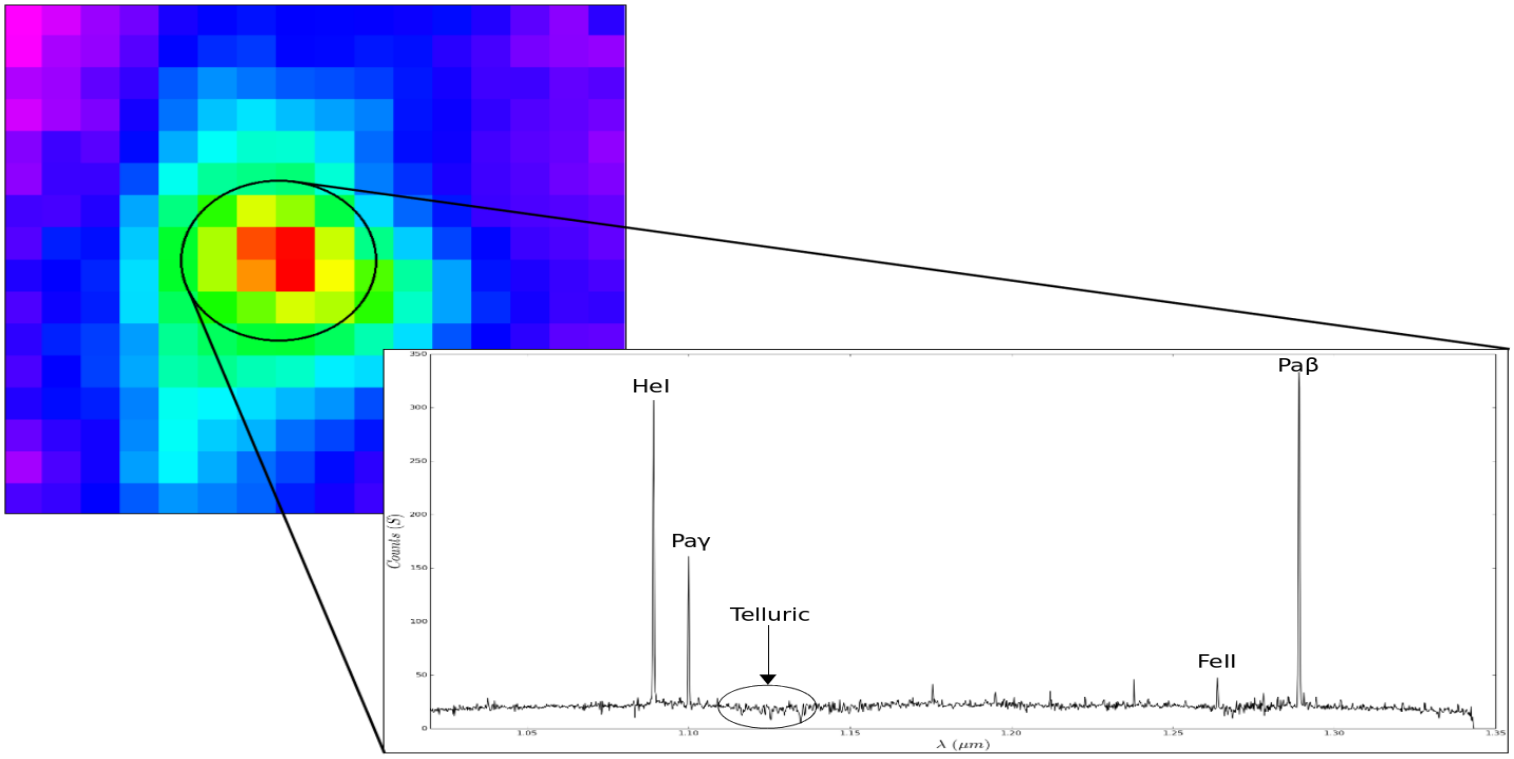

FIGURE 4.6: Example of KMOS YJ band data after processing through the SPARK pipeline. *Left*: Combined cube for cluster S6 collapsed along the wavelength axis. Each raw output frame from the two observation nights was processed using *SPARK* recipes. Output cubes for each night were then combined to give the $14 \times 14 \times 2048$ pixel cube shown here. *Right*: Extracted spectrum from a $0.5''$ radius aperture centred on S6.

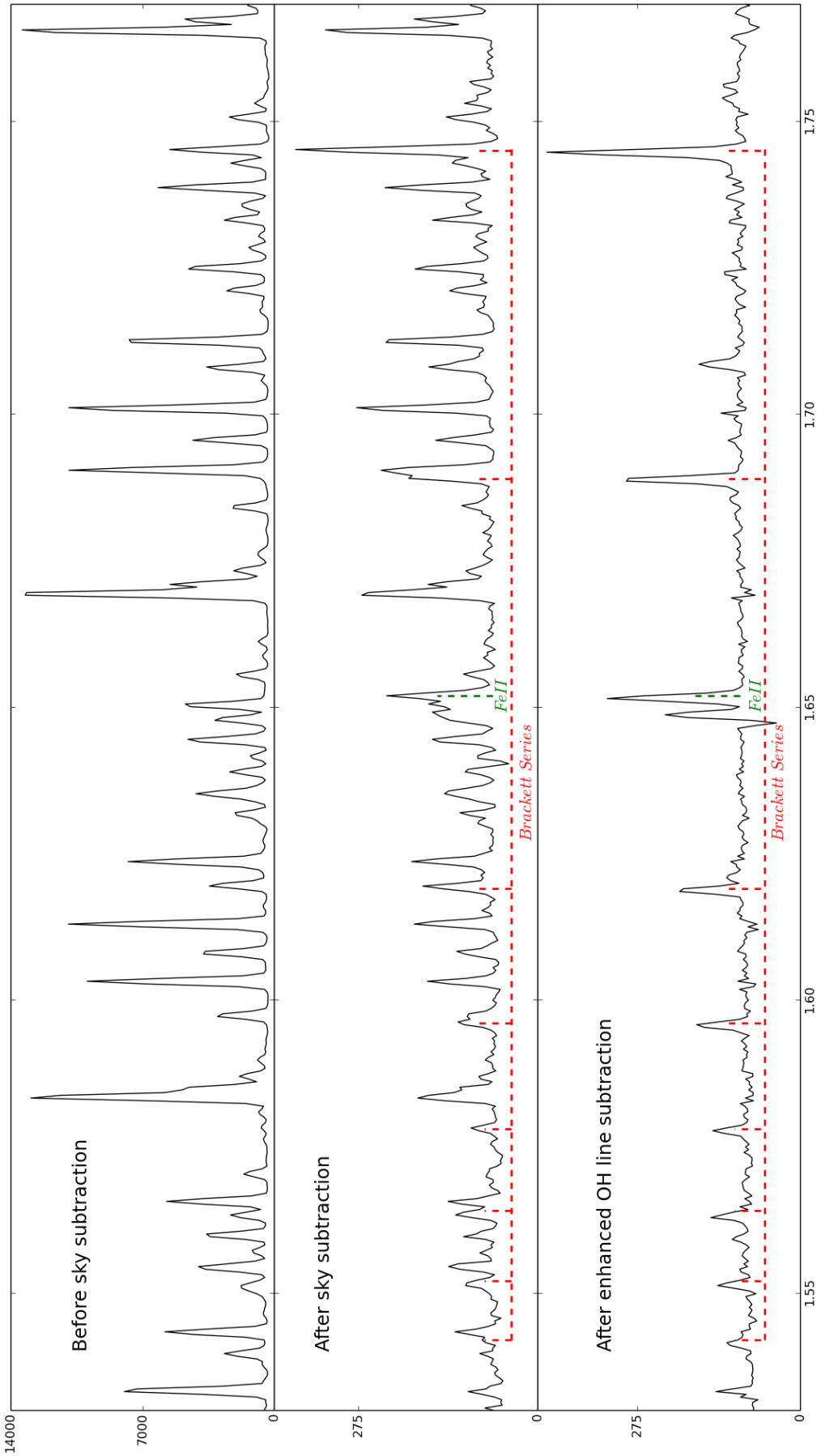

FIGURE 4.7: H band spectra of cluster S29 before sky subtraction (*top*), after sky subtraction (*middle*), and after enhanced OH line subtraction (*bottom*); note the change in Y-axis scales. The positions of the brackett lines series and FeII emission at 1.65μm are also labelled here.

4.2.5 Combining Datasets from Different Nights

Given the results from *kmo_sci_red*, which combined data for each target IFU from all KMOS integrations for a given night, the next task was to combine all target data across the different nights to improve S/N. However, similar concerns raised when combining frames from a single observation night are also valid here, particularly will combining different sets of data cubes improve the S/N to the level expected and not deteriorate the quality of the output spectra. In some cases the data cubes were taken 2 months apart, therefore obtaining a lower observed S/N than expected when combining cubes is a valid concern. An additional problem when combining cubes from different nights is the shifts in the spatial position of each cube. As shown in Figure 4.9 combining data cubes from a single night does not produce perfectly stacked cubes. This is due to subtle changes in IFU position during each KMOS integration. While there was minimal ($\sim 5\%$) loss in S/N when combining data cubes from a single night, the S/N in the spectra may be much lower than expected when combining target cubes from different nights.

Thus, to check for quality loss, S/N values obtained from spectra of combined nights were compared to expected S/N values and to S/N values of spectra from single nights. Furthermore, two methods were adopted to combine spectra from different nights. The first method was to combine individual data cubes using

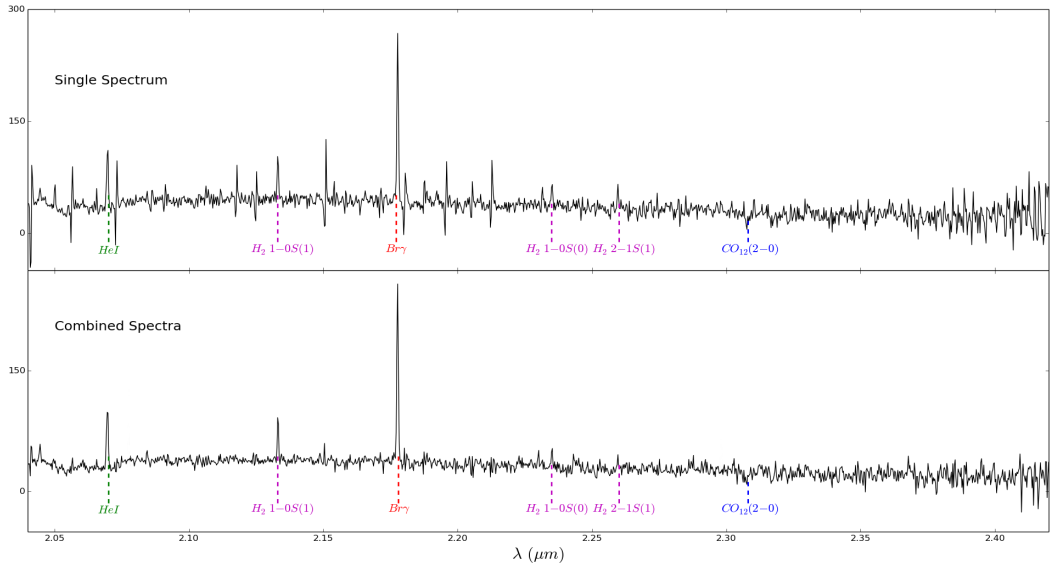

FIGURE 4.8: Comparison between spectra from single and combined data cubes. Combining the spectra for one night produced a spectra that typically had a 10% - 20% increase in S/N compared to the individual spectra.

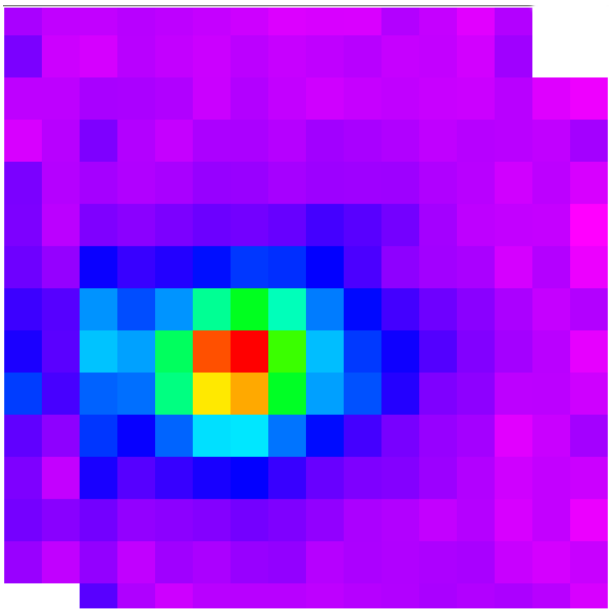

FIGURE 4.9: The above image shows a result often seen when combining cubes. Due to subtle changes in the IFU positions when moving between object and sky coordinates, the *kmo_sci_red* routine is unable to stack data cubes perfectly on top of each other.

the task *IRAF/IMCOMBINE* and extract the spectrum from the combined cube. The second method was to extract the spectrum from each individual target cube and combine the spectra. Both methods used a median routine to combine data. Products from both methods were compared with each other for loss in S/N as well as to spectra from single observation nights and the expected S/N.

As an example, comparative results from combining target data for the K band are shown in Figure 4.10. This example shows the combined spectra for nights 23/01/2013, 25/03/2013 and 27/03/2013, using the two methods mentioned. In addition, the spectra from each night are plotted. Combining the spectra using either method was seen to increase the S/N of the spectra by $\sim 20\%$ compared to the S/N of spectra from individual nights. The difference between the observed and expected S/N is $\sim 5\%$. Furthermore, lines produced from dormant pixels (e.g., cosmic rays) in the spectrum of individual nights were removed in the combined spectra due to the median routine. There is no difference in the S/N between the combined data cubes method and the combined spectra method. The spectra from both methods are identical, therefore either method can be used to combine the data from different observation nights.

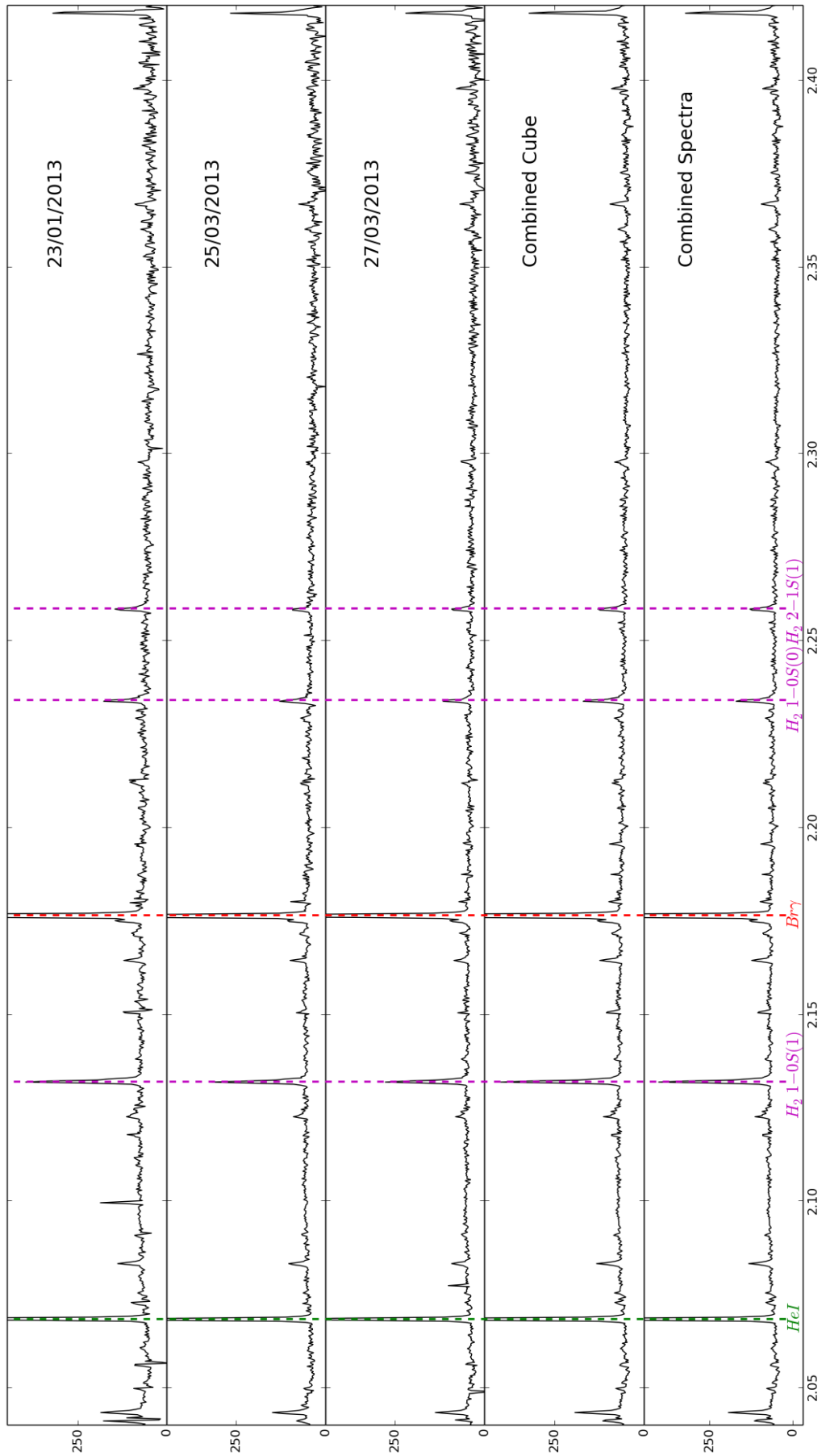

FIGURE 4.10: Comparison between spectra before and after combining. The three top plots are the spectra from individual nights, and the bottom two plots are results from combining data from each night. The fourth plot is the result of combining data cubes, and the fifth plot is the result of combining the spectra from individual nights. Both combining methods used a median routine to combine the data.

4.3 Results

4.3.1 Stellar Population Synthesis

Our sample is composed of bright ($M_K < -12$) near-infrared star clusters across the Antennae that have already been identified as bona fide star clusters from earlier surveys in the literature. The spectra obtained for the sample of star clusters in Table 4.1 contain numerous absorption and emission lines that give insight into their physical properties. Stellar population synthesis (SPS) models are commonly used to help determine these properties. SPS models simulate the temporal evolution of star clusters by using assumptions about their age, chemical composition, star formation history and initial mass function (IMF). Synthetic spectra from these models can be compared to measurements of the observed spectra of star clusters to determine their physical properties. The following sections will discuss the SPS models used in this study, lines measured from observed spectra, and properties derived for each of the star clusters in Table 4.1.

4.3.1.1 Starburst99

A number of SPS models can be found in the literature (e.g., Leitherer et al. 1999; Bruzual and Charlot 2003; Maraston 2007). *Starburst99*[1] (Leitherer et al., 1999) is adopted for this study primarily because of its widespread use in the study of star clusters, particularly for those in the Antennae (e.g., Christopher 2008; Bastian et al. 2009).

Starburst99 uses stellar evolutionary models from the Geneva and Padova groups (Schaerer et al. 1993; Vázquez and Leitherer 2005), and model atmospheres from Lejeune et al. (1997). Padova tracks were adopted for this study as they provide more accurate models for clusters older than 10^8 years, which may exist in our star cluster sample (Whitmore et al., 1999). *Starburst99* provides models for a range of metallicities, initial mass functions (IMF), and star formation modes.

Christopher (2008) and Bastian et al. (2009) have measured metallicities for 133 star clusters with ages ranging between 3 - 630 Myrs around the Antennae using several line indices. As listed in Table 4.1, 31 star clusters in our sample have been

[1] http://www.stsci.edu/science/starburst99/docs/default.htm

previously analysed in their work. From their metallicity measurements, Christopher (2008) and Bastian et al. (2009) conclude that the Antennae star clusters have an average metallicity that is approximately solar. Therefore, solar metallicity is adopted for our SPS models. Furthermore, earlier work in the literature assumes a Kroupa IMF for modelling the Antennae star clusters (Larsen 2004b; Mengel et al. 2008; Bastian et al. 2009), hence a Kroupa IMF is adopted. However, utilising either a Salpeter IMF or Kroupa IMF causes no discernible difference in modelling star clusters in this survey as both IMFs are nearly identical in their distributions of high mass stars, which contribute the most light observed from young star clusters in the Antennae galaxies (Mengel et al. 2005; Kornei and McCrady 2009).

Starburst99 offers two star formation profiles: an instantaneous burst of star formation and a continuous star formation at a fixed rate. Several studies in the literature suggest an instantaneous burst provides a more accurate profile of the Antennae star clusters, notably because star clusters are typically very small ($R_{eff} \sim$ few parsec) and very concentrated, hence star formation is effectively instantaneous across a star cluster (Mengel et al. 2005; Bastian et al. 2009). Therefore, an instantaneous burst is adopted for this study. Lastly, an upper age limit for the models was set to 500 Myrs as previous work on ages for star clusters in the Antennae merger show ages less than 500 Myrs (Whitmore et al. 1999; Christopher 2008).

4.3.2 Equivalent Widths

Several diagnostic lines are used in this study to derive physical parameters for the Antennae star clusters. Equivalent width (EW) measurements of two hydrogen recombination lines (Paβ and Brγ) and two CO bandheads (CO 2-0 at 2.29μm and CO 6-3 at 1.62μm) from star cluster targets were compared with *Starburst99* model results to derive ages and masses for our star cluster sample. EWs from molecular hydrogen and iron emission lines were also measured to derive line ratios and supernova rates. The following subsections describe each of the diagnostic lines used in this survey and results obtained from their measurements.

Target	Paβ (Å)	Paγ (Å)	Brγ (Å)	HeI$_{1.08}$ (Å)	HeI$_{2.06}$ (Å)	FeII$_{1.26}$ (Å)	FeII$_{1.64}$ (Å)	H_2 1-0S(1) (Å)	CO 2-0 (Å)	CO 6-3 (Å)
S1										
S2										
S3										
S4			13.2±2.1				4.9±0.9	4.8±0.9	4.1±1.4	
S5	38.8±3.0	17.5±2.1		20.0±3.3		3.5±1.6				
S6	79.4±5.2	35.2±5.3	20.7±4.1	67.6±6.6	4.7±2.1	4.5±1.4	6.2±1.0	6.5±1.2		
S7	14.3±3.3	8.3±1.5		8.7±2.0		4.7±1.2				
S8	14.7±2.4	8.7±1.3	7.9±1.4	10.2±2.4		5.5±1.4	5.3±1.2	5.3±1.0	9.6±2.4	
S9			4.7±1.7							
S10	14.3±3.0	8.2±2.2		15.8±3.1		4.1±1.2				
S11	8.5±3.2	4.7±1.0		5.7±1.4						
S12	121.2±10.3	56.6±5.0		55.1±4.9		10.7±1.5				
S13	77.0±7.3	35.9±3.2		53.2±4.9		3.1±1.2				
S14			15.8±2.1				7.7±1.0	4.2±0.8		
S15	65.6±7.0	28.1±3.6		37.4±4.0		6.0±1.0				
S16			15.1±2.2					5.5±1.0		
S17	27.9±5.1	13.9±2.1	9.6±2.2	19.5±2.3					14.7±4.1	3.6±1.7
S18									11.5±3.2	6.3±1.3
S19									12.6±1.4	
S20			3.7±1.8						7.2±2.6	
S21	21.0±3.3	10.0±2.0	11.7±2.1 & 13.0±2.0			7.4±1.2	5.1±1.0			
S22	25.0±3.6	12.0±2.8	16.1±2.1	17.0±2.0		5.4±1.1	11.1±2.1			
S23									9.3±6.7	5.6±1.7
S24	6.9±1.1	3.3±1.2		4.8±1.2						
S25	14.3±2.2	6.2±1.2	6.4±1.2	8.2±2.1			4.4±1.8	2.8±1.0	6.7±3.9	5.2±1.7
S26	101.3±8.1	42.3±4.4		111.0±11.5		5.5±1.0				
S27			313.3±16.1		147.4±12.1		72.6±4.5	30.4±3.5		
S28			47.5±8.1		14.6±3.9		22.1±3.0	22.1±3.2	9.4±2.9	
S29			163.0±10.1		76.8±13.2		40.3±6.2	44.8±6.3		
S30	12.5±2.4	6.0±1.8		10.4±1.7						
S31			24.2±4.0		10.5±2.3			11.1±2.1		
S32			47.1±7.1		14.4±3.1		17.2±3.2	9.2±2.5	8.6±2.5	
S33			45.9±7.1		16.1±2.9			8.7±1.8		
S34	3.9±1.2	1.5±1.0		2.9±1.3						
S35									15.7±2.4	4.9±1.9
S36										
S37	28.6±3.0	15.0±2.5		32.9±3.8		6.0±1.1				
S38	182.0±9.5	72.3±6.2		116.7±1.2		15.2±2.5				
S39	29.6±4.4	14.4±2.4		21.7±3.7		3.8±1.0				
S40									9.2±2.4	
S41										
S42										
S43										
S44									12.8±4.4	5.4±2.1
S45									8.7±2.7	
S46										
S47										

TABLE 4.3: Equivalent width measurements of absorption and emission lines from Antennae star clusters. Equivalent widths from Paβ, Brγ, CO 2-0 and CO 6-3 were compared with *Starburst99* values to determine cluster ages and masses.

4.3.2.1 Hydrogen Emission Lines

Hydrogen recombination lines are formed in ionized gas associated with sources having strong Lyman continuum, such as HII regions created by young, hot O- and B-type stars (de Grijs et al., 2004). Due to the rapid evolution of these massive stars, star clusters with these recombination lines are likely to have ages of < 6 Myrs (de Grijs et al. 2004; Kornei and McCrady 2009). 18 star clusters in this survey show Brγ emission in their K band spectra, and 21 star clusters show Paβ and Paγ emission lines in their YJ band spectra. These indicate the presence of young, massive stellar populations in these star clusters. Since high-mass stars evolve more rapidly than low-mass stars the strength of the Brγ line will vary over time as the output of UV photons from O- and B-type stars declines sharply after 5 Myrs (Leitherer et al., 1999). Therefore, the strength of the Brγ emission line, quantified by its EW, is a powerful indicator of cluster age. Furthermore, since both the Brγ line flux and continuum level increase with cluster mass, the EW is relatively insensitive to mass. Using EWs also has the advantage of being relatively insensitive to reddening. Paschen emission lines are also useful probes of cluster age and are generally stronger than Brackett emission lines (Sellgren and Smith, 1992). The only other notable difference between these lines is that the Paschen series are less sensitive to temperature changes than the Brackett series (Cidale et al., 2000).

EWs were extracted for all emission and absorption lines in the observed spectra using the *SPLAT-VO*[2] spectral analysis tool (Castro-Neves and Draper, 2014). Table 4.3 lists the measured EWs.

4.3.2.2 Helium Emission Lines

HeI (1.08μm) emission is detected in 20 star clusters in the YJ band. It is often used as a probe for dense star forming regions such as HII regions and young star clusters, and also coincides with CO clouds around young star clusters (Lumsden and Puxley 1996; Clark et al. 2013). Temperatures in excess of $\sim 10^4$ K are required to produce this emission line, hence it is thought to be the product of massive O- and B-type stars, possibly due to UV photoionisation (Kwan and

[2]http://star-www.dur.ac.uk/ pdraper/splat/sun243.htx/sun243.html

Fischer 2011; Clark et al. 2013). HeI emission is comparable in strength to hydrogen recombination lines in the YJ band for massive stars, hence it is very bright and easy to identify in our star cluster sample. Moreover, the YJ band spectral resolution of $\lambda/\delta\lambda = 3400$ ensures that the HeI emission line in the YJ band is not blended with the nearby Paγ emission line in the spectra of the star clusters observed.

HeI (2.06μm) emission is also detected from 7 star clusters. This line is often associated with stellar winds from Wolf-Rayet stars as well as O- and B-type stars, and requires similar temperatures to the HeI (1.08μm) emission line for production Figer et al. 1997; Homeier et al. 2003). Measurements of HeI (2.06μm) emission is usually subject to large errors due to its close coincidence with an atmospheric line within the strong telluric CO_2 band falling in this spectral range (Armand et al., 1996). Fortunately, the spectral resolution in the K band ($\lambda/\delta\lambda = 3800$) is sufficient to separate these two lines and allow accurate measurements of the HeI (2.06μm) line. As with the hydrogen recombination lines, HeI EWs were extracted using *SPLAT-VO* and measurements are listed in Table 4.3.

4.3.2.3 Molecular Hydrogen Emission Lines

The H_2 1–0S(1) emission line at 2.12μm is observed in the spectra of 13 star clusters. H_2 emission lines are often used as tracers for star cluster outflows (Hodapp and Davis 2002; Eislöffel et al. 2003). These emission lines can be excited by either thermal shocks or UV photoionisation, and trace energy that is being dissipated and radiated away from cloud complexes associated with star clusters (Hanson et al. 2002; Herrera et al. 2012). H_2 emission is generally observed away from the brightest regions of star clusters, where hydrogen recombination lines such as Brγ are located (Dale et al., 2004). Table 4.3 lists line strengths measured from H_2 1–0S(1) for the 13 star clusters.

4.3.2.4 Iron Emission Lines

FeII emission is detected in the spectra of 21 star clusters. Of these, 13 show FeII (1.26μm) emission in the YJ band, and 11 show FeII (1.64μm) emission in the H band. Of the 9 star clusters that were observed in all four bands, S6, S8 and S22 showed both FeII (1.26μm) and FeII (1.64μm) in their spectra. 5 of the remaining

6 star clusters showed neither emission line in their spectra. S21 showed only FeII (1.64μm).

Both emission lines share the same upper atomic level and have an intrinsic line ratio of FeII $\lambda 1.26/\lambda 1.64 = 1.36$ (Nussbaumer and Storey, 1988). FeII line emission originates through two different mechanisms: (1) strong, compact FeII emission originates in partially ionized zones or shock-excited gas produced by supernovae (SNe); (2) diffuse, spatially extended FeII emission is associated with galactic super winds from active galactic nuclei (AGNs; Thompson 1995; Baldwin et al. 2004). Strong FeII emission requires both the destruction of dust grains, which contain a large fraction of interstellar iron, and large transition zones between HII regions and HI regions (Oliva et al., 1989). Hence, FeII emission is thought to be produced from thermal shock excitation (Vanzi and Rieke 1997; Alonso-Herrero et al. 2003). FeII emission reaches maximum luminosity when the expansion of a supernova remnant (SNR) becomes radiative after its initial adiabatic phase (Lumsden and Puxley 1995; Morel et al. 2002). This occurs $\sim 10^4$ years after a supernova explosion, when radiative cooling occurs on shorter timescales than the dynamical timescale. Hence, strong FeII emission lines are not only useful tracers of SNRs but can also help set constraints on the star formation history of a galaxy (e.g., de Grijs et al. 2004).

Furthermore, strong FeII emission can be used to classify two groups of SNRs: a young core-collapse SNR in dense circumstellar medium and a middle-aged SNR interacting with molecular clouds (Koo, 2014). SNRs from the latter group show bright H_2 1-0S(1) emission at 2.12μm, suggesting that both atomic and molecular shocks are prevalent in these SNRs. In our sample, 10 of the 11 star clusters that show FeII emission in the H band also show H_2 emission in their spectra. Table 4.3 lists EWs measured from both FeII emission lines for 21 star clusters.

4.3.2.5 CO Absorption Bandheads

CO absorption bandheads in the near-infrared are common features in the spectra of red supergiants, which first appear in star clusters with ages exceeding ~ 7 Myrs (Davies et al. 2010; Gazak et al. 2013). The strength of these bandheads tend to increase with reduced effective temperature, such that they only appear in stars cooler than early K giants, and reach maximum strength in mid-late M supergiants (Kleinmann and Hall 1986; Origlia et al. 1993). Instantaneous burst models from

Starburst99 show the strength of CO bandheads in star clusters gradually declines over 100 Myrs after reaching peak strength at $\sim$ 12 Myrs (Origlia et al., 1993). In particular, *Starburst99* models the temporal evolution of two CO bandheads: CO 6-3 which occurs at 1.62μm, and CO 2-0 which occurs at 2.29μm. Both absorption features are the strongest CO bandheads in the H and K band, respectively.

EWs were measured for both bandheads in our cluster sample using *SPLAT-VO*. The CO 2-0 bandhead is the most common of the two absorption features in our star cluster sample appearing in the K band spectra of 14 star clusters, whilst the CO 6-3 bandhead appears in the H band spectra of 7 star clusters and is generally weaker than the CO 2-0 bandhead for star clusters showing both absorption features. Christopher (2008) note that both CO bandhead EWs can be reduced by non-stellar continuum emission from hot dust, but also state that contamination from dust emission in the Antennae clusters is quite small in the H and K bands. Therefore, the extracted EWs for both bandheads can be viewed as lower limits.

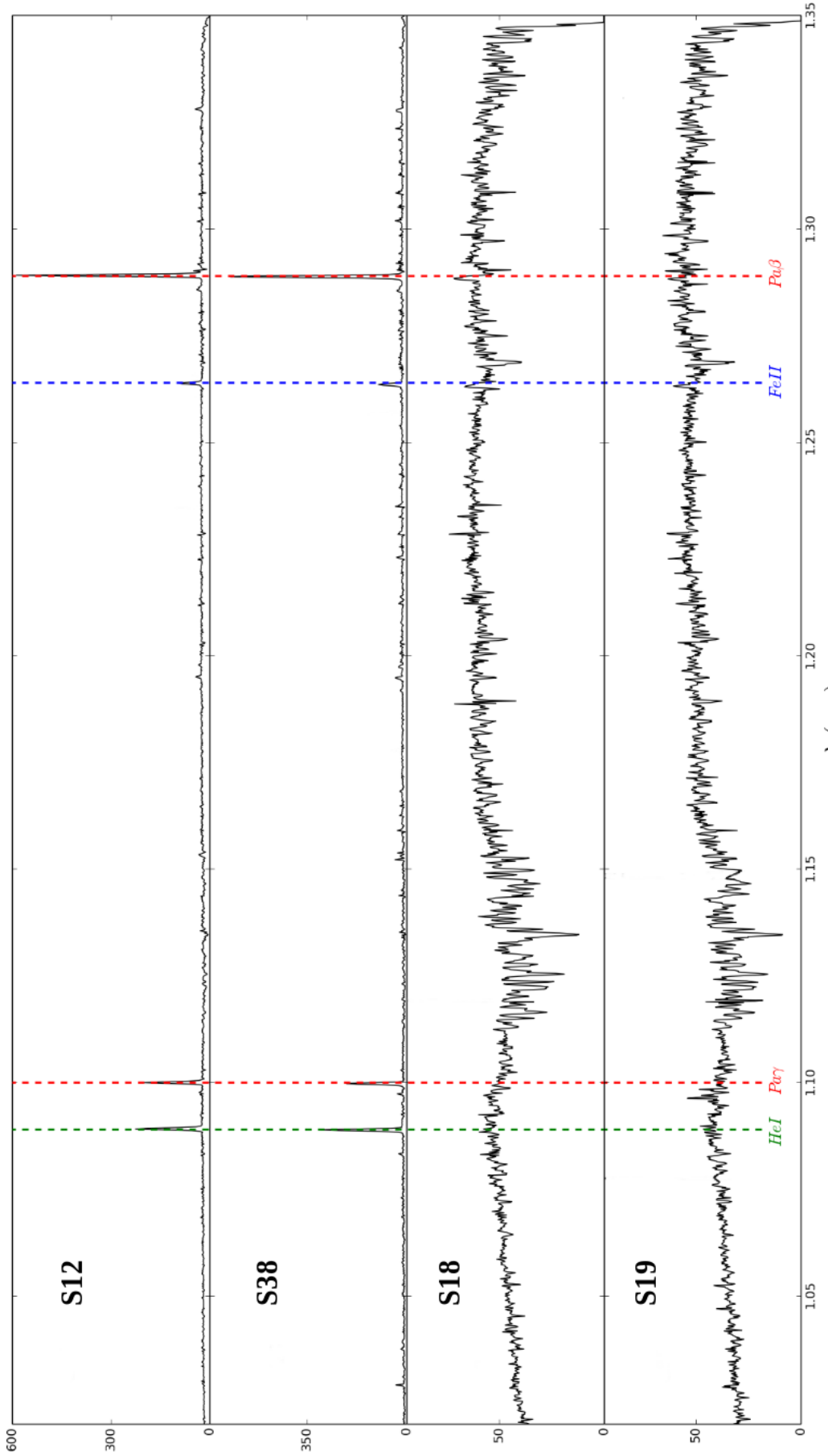

FIGURE 4.11: Comparison between spectra from the youngest and oldest star clusters in the YJ band. Clusters S12 and S38 both have ages of ~ 5 Myrs, and S18 and S19 have ages of ~ 8 Myrs. In contrast to the younger clusters, the older clusters show no emission lines in there spectra. This is likely due to the absence of massive OB stars in the older clusters, which are responsible for these emission lines.

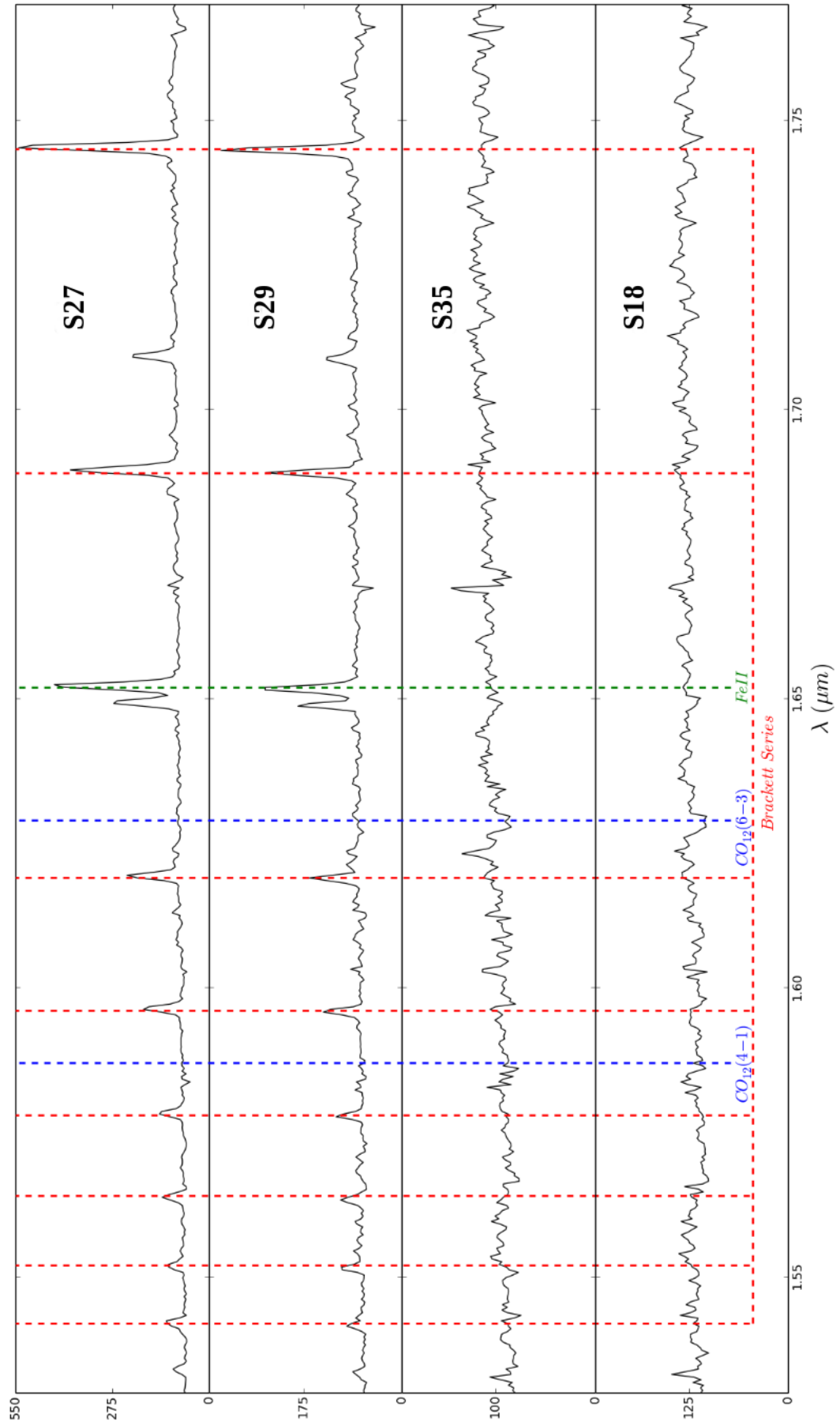

Figure 4.11 Continued. A comparison between spectra from the youngest and oldest star clusters in the H band is shown here. S27 and S29 have ages between 3 - 5 Myrs, and S18 and S35 have ages of $\sim$ 8 Myrs. The older star clusters show CO (6-3) absorption in their spectra. This bandhead is a tracer of RSGs, which begin to populate a star cluster $\sim$ 7 Myrs after it has formed (Gazak et al., 2013).

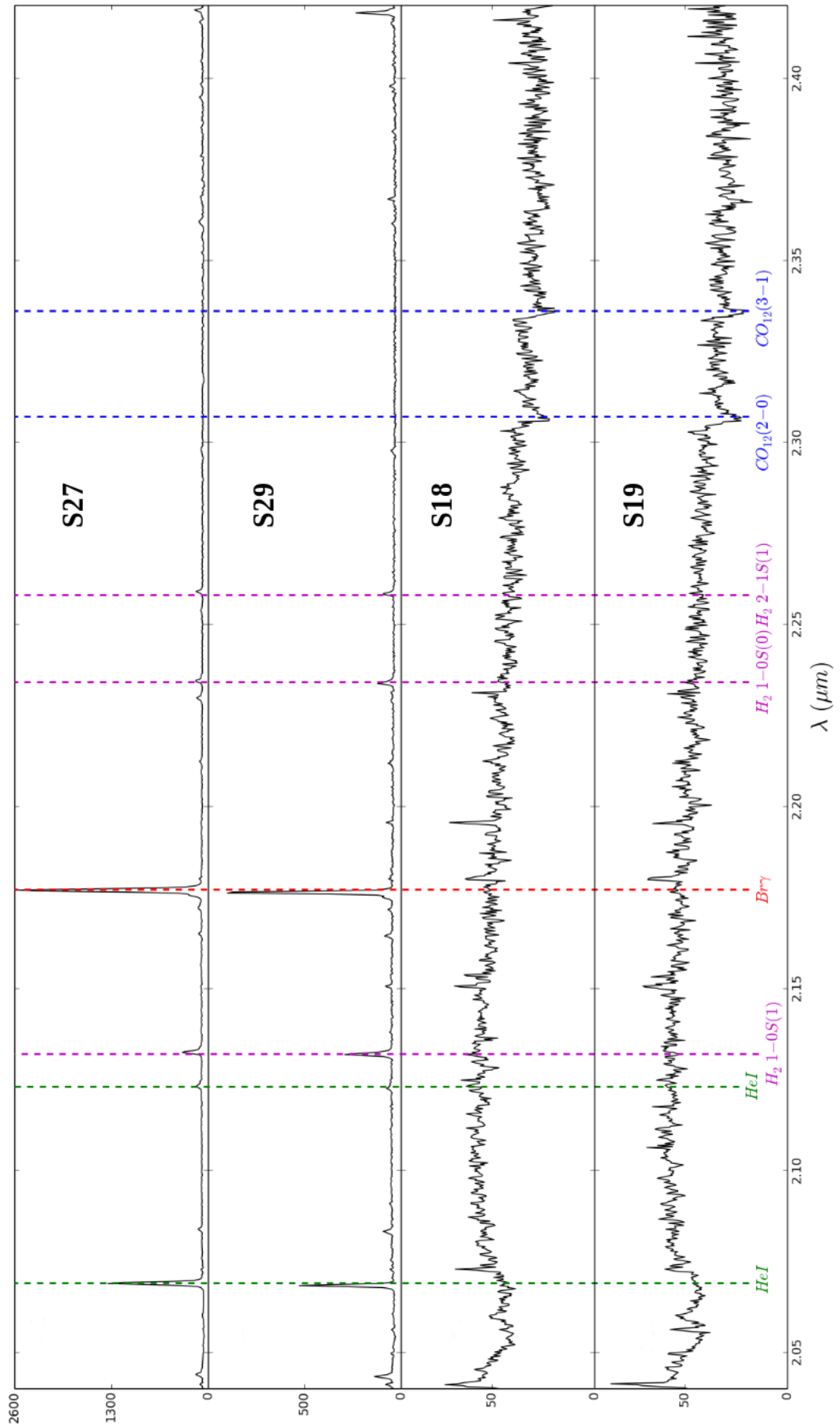

Figure 4.11 Continued. A comparison between spectra from the youngest and oldest star clusters in the K band is shown here. S27 and S29 are plotted here again, along with S18 and S19. Similar to the spectra from the YJ and H bands, the older clusters are devoid of emission lines in their spectra due to the absence of massive OB stars. They do show CO (2-0) absorption in their spectra, which like the CO (6-3) bandhead in the H band, is a tracer of RSGs.

4.3.3 Extinction Estimates

Varying densities of gas and dust around the Antennae are likely to have produced variable extinction across the entire system. Photometric work by Whitmore and Schweizer (1995) and Whitmore et al. (1999) compare colour-colour diagrams of Antennae star clusters to population synthesis models and estimate an optical extinction of $A_V = 0-3$ mag around the Antennae. They find the highest extinction occurs in the overlapping region between the two progenitor galaxies. Kassin et al. (2003) concur with this from their photometric surveys, and find a peak extinction of $A_V = 3$ mag around the overlap region and an average reddening of $A_V = 1$ throughout the Antennae.

However, both surveys were taken at optical wavelengths which is unlikely to penetrate the largest gas and dust concentrations in the overlap region. Near-infrared photometry was performed by Mengel et al. (2005) for star clusters around the Antennae, including star clusters in the overlap region that are obscured in the optical. They conclude the extinction varies between $A_V = 0 - 10$ around the Antennae, and the heaviest reddening occurs in the overlap region. Furthermore, they find that reddening drops with cluster age, which is consistent with the theory that star clusters form in very dense and dust-enshrouded cocoons which they blow free of after 8 - 10 Myrs. Near-infrared spectroscopic work by Gilbert and Graham (2007) derive $A_V = 10$ for the youngest star clusters in the overlap region, in agreement with the extinction results by Mengel et al. (2005).

The large spatial distribution of our star cluster sample provides the opportunity to further determine how extinction varies throughout the Antennae. Since our survey is taken in the near-infrared, we can also determine good measurements of extinction around the overlap region and other gas and dust-enshrouded regions around the Antennae.

In order to determine extinction using spectroscopy, it is necessary to identify emission lines with fixed intrinsic intensity ratios and compare the observed ratios from star clusters to these intrinsic line ratios. Any deviation of the observed ratio to the intrinsic line ratio will indicate the degree of extinction. The best line pair to use in our sample is Paβ and Paγ, which has an intrinsic line ratio of 1.80, assuming Case B recombination and an electron temperature of 10^4 K (Osterbrock, 1989). The Paβ and Brγ line pair is also useful in the near-infrared, and has a ratio of 5.89 over a wide range of physical conditions (Hummer and Storey

ID	Paβ/Paγ	Paβ/Brγ	FeII$_{1.26}$/FeII$_{1.64}$	A$_V$ (Mag)
S5	2.99			2.0
S6	2.63	2.15	3.34	1.9
S7	2.42			1.1
S8	2.53	1.48	1.89	1.5
S10	2.51			1.3
S11	2.34			1.0
S12	3.11			2.2
S13	2.64			1.5
S15	2.71			1.6
S17	2.62	2.57		1.4
S21	2.89	1.63	2.89	2.1
S22	3.83	1.45	2.02	1.8
S24	3.49			2.7
S25	2.50			2.7
S26	2.94			2.0
S30	2.79			1.8
S34	2.18			0.8
S37	2.71			1.6
S38	3.47			2.6
S39	2.64			1.5

TABLE 4.4: Extinction values for star clusters around the Antennae. Extinction measurements were determined by comparing Paβ/Paγ, Paβ/Brγ and FeII$_{1.26}$/FeII$_{1.64}$ line ratios observed from our star cluster sample to their intrinsic ratios. These lines have intrinsic line ratios of Paβ/Paγ = 1.80 (Osterbrock, 1989), Paβ/Brγ = 5.89 (Hummer and Storey 1987; Osterbrock 1989) , and FeII$_{1.26}$/FeII$_{1.64}$ = 1.36 (Nussbaumer and Storey, 1988).

1987; Osterbrock 1989). FeII emission can be used as an alternative to hydrogen recombination lines to measure extinction, particularly the FeII$_{1.26}$/FeII$_{1.64}$ ratio, where both FeII emission lines share the same upper level with an intrinsic ratio of 1.36 (Nussbaumer and Storey, 1988).

Extinction values were determined for 20 star clusters in our sample using Paβ/Paγ line ratios. Extinction values for 5 of these clusters were also calculated using Paβ/Brγ and FeII$_{1.26}$/FeII$_{1.64}$ line ratios. Derived extinctions for these star clusters are listed in Table 4.4. Extinction was calculated using the the empirical extinction relation determined by Calzetti et al. (1994):

$$A(\lambda) = \kappa(\lambda) E(B-V) \tag{4.1}$$

where $A(\lambda)$ is the extinction in magnitudes at wavelength λ, $\kappa(\lambda)$ is the value of the attenuation curve at wavelength λ, and $E(B-V)$ is the broadband colour excess which can be expressed as:

$$E(B-V) = \frac{2.5}{\kappa(\lambda_2) - \kappa(\lambda_1)} \times log_{10}\left[\frac{(F1/F2)_{obs}}{(F1/F2)_{int}}\right] \tag{4.2}$$

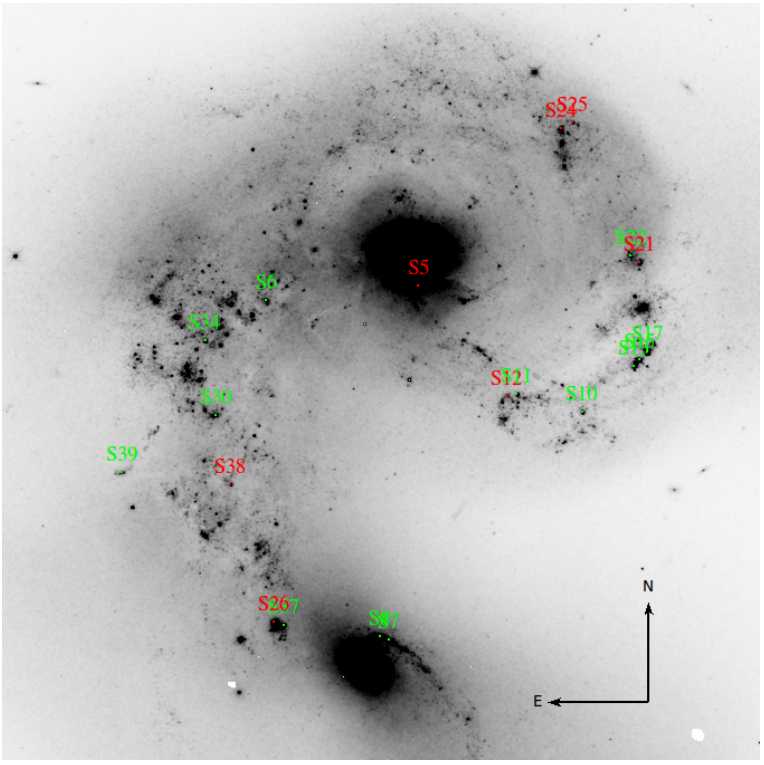

FIGURE 4.12: Variation of extinction around the Antennae. Extinction was calculated using Paβ/Paγ, Paβ/Brγ and FeII$_{1.26}$/FeII$_{1.64}$ line ratios. Green objects have $A_V < 2$ mag and red objects have $A_V > 2$ mag. The heaviest reddening is located in the overlap region and north-west of NGC 4038. Both regions have extinction values of $A_V \sim 2.5$ mag. The lowest extinction is located south-west of NGC 4038, which has an average extinction of $A_V \sim 1.5$ mag.

Here, $(F1/F2)_{obs}$ and $(F1/F2)_{int}$ denote the observed and intrinsic line ratios for wavelengths λ_1 and λ_2. The values for $\kappa(\lambda_1)$ and $\kappa(\lambda_2)$ are taken from the attenuation curve proposed by Calzetti (1997) and Calzetti et al. (2000). Once the broadband colour excess is determined, the optical extinction A_V can be calculated using Equation 4.1. Optical attenuation is most commonly determined at $\lambda_V = 0.55\mu$m in the literature, where $\kappa(V) = 4.05$ (Momcheva et al., 2013). Hence, optical extinction was calculated at $\lambda_V = 0.55\mu$m in our analysis.

Derived optical extinctions are listed in Table 4.4. The mean extinction of our sample is $A_V = 1.8$ mag with a maximum extinction of $A_V = 2.7$ mag. Figure 4.12 shows how extinction varies around the Antennae. The heaviest reddening is located in the overlapping region between NGC 4038/39 and the region north-west of NGC 4038. The lowest extinction is located in the region south-west to the centre of NGC 4038.

4.3.4 Star Cluster Ages

Determining the age distribution of the Antennae star clusters is crucial to understanding how star clusters formed and will evolve in a galaxy merger. Ages can be derived by comparing EW measurements from § 4.3.2 with synthetic EWs from *Starburst99* models. *Starburst99* provides synthetic EWs for Paβ and Brγ recombination lines as well as measurements of the CO 2-0 and CO 6-3 bandheads. Figure 4.13 show how these model EWs vary as a function of age. The strength of Paβ and Brγ emission lines decrease sharply with age until 10 Myrs, presumably due the decline of massive OB stars as a star cluster evolves. The CO bandheads behave in a more complex manner to the hydrogen recombination lines in that their EWs fluctuate as a function of age. Both CO bandheads show peaks in their EW at $\sim$ 7 Myrs and $\sim$ 10 Myrs and $\sim$ 140 Myrs. Therefore, a single CO bandhead EW value can represent more than one age in the model spectra.

Ages were derived by interpolating the measured EWs from the star cluster sample with model EWs from *Starburst99*. Determining ages for Paβ and Brγ emission lines was fairly straight forward as a single EW measurement corresponded to a single age. However, for the CO bandheads, the fluctuation of the model EW distribution with age meant that some EW measurements from the star clusters gave multiple ages. For these few cases, all possible ages were recorded. In several cases, the cluster age was determined using more than one line. In this case, the average age was taken between all derived ages. Ages derived from multiple lines typically differed by 1 Myr from each other.

Table 4.5 lists the ages determined from our star cluster sample. Ages were derived for 38 of the 47 star clusters in our sample. The remaining 9 star clusters have no absorption/emission features in their spectra, therefore ages could not be derived for these star clusters. Regarding the 38 star clusters that have absorption/emission features in their spectra, the age of 14 of these star clusters were derived using more than one absorption/emission line.

S27 has the youngest age in this sample with an age of 3.6 ± 0.1 Myrs, whilst the oldest age is estimated for S18 which has an age of 8.4 ± 0.4 Myrs. A comparison between the spectra of a few of the youngest and oldest star clusters in the Antennae sample are shown in Figure 4.11. The older ($>$ 8 Myr) clusters show an absence of strong recombination lines that are frequently seen in the younger clusters. This indicates the absence of massive OB stars in these star clusters,

which is expected since these stars have a lifetime of less than 6 Myrs (de Grijs et al. 2004; Kornei and McCrady 2009). Furthermore, the youngest (< 5 Myr) star clusters in this sample are absent of CO absorption in their spectra which indicates that RSGs have yet to populate these star clusters.

Figure 4.14 shows the age distribution of the star clusters throughout the Antennae. The youngest star clusters in this sample are concentrated in the overlapping region between the two galaxies, particularly in the southern part of the overlap region. The star clusters here are typically less than 6 Myrs old. The oldest star clusters are generally clumped in a region south-east of the core of NGC 4038. The ages here are in excess of 8 Myrs. There is not a large variation in age between the youngest and oldest star clusters, however the younger ages in the southern part of the overlap region suggests there is a higher rate of recent cluster formation present in that region.

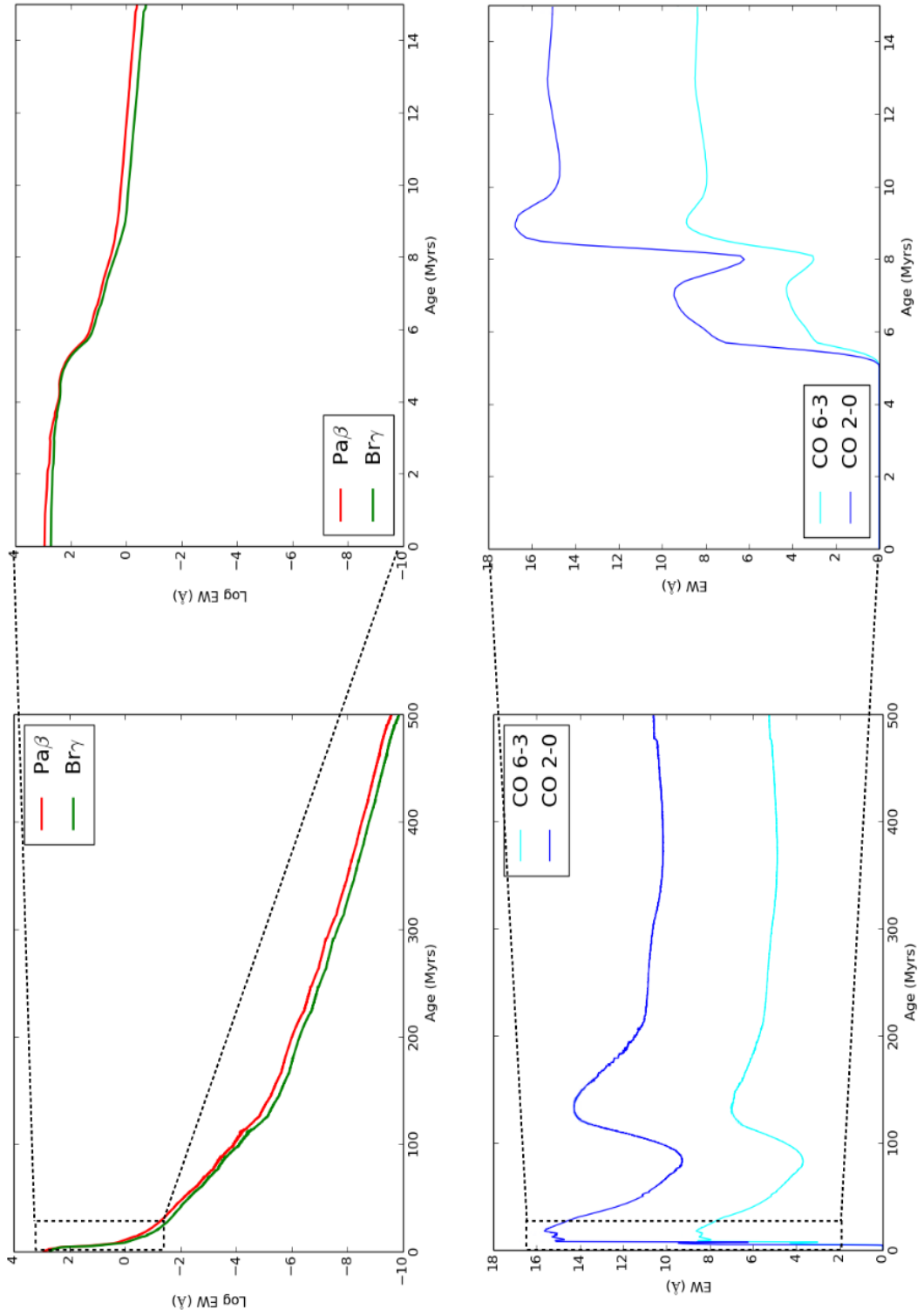

FIGURE 4.13: Evolution of model equivalent widths with age. *Top-Left:* Evolution of Paβ and Brγ hydrogen recombination lines with age. *Top-Right:* Closer inspection of the evolution of hydrogen recombination lines over the ages of our star cluster sample. *Bottom-Left:* Evolution of CO 6-3 and CO 2-0 bandheads with age. *Bottom-Right:* Closer inspection of the evolution of CO 6-3 and CO 2-0 bandheads over the ages of our star cluster sample. These model results are taken from *Starburst99* assuming an instantaneous burst, solar metallicity and a Kroupa IMF.

Target	Paβ (Myrs)	Brγ (Myrs)	CO 6-3 (Myrs)	CO 2-0 (Myrs)	Mean Age (Myrs)	Mass ($\times 10^5 \mathcal{M}_\odot$)	Literature Age (Myrs)	Literature Mass ($\times 10^5 \mathcal{M}_\odot$)
S1								
S2								
S3								
S4		6.2±0.3		5.5±0.1	5.9±0.3	1.1±0.1	3.2-6.8	0.8-3.2
S5	5.7±0.1				5.7±0.1	3.6±0.2	<6.8	2.5-10.0
S6	5.4±0.1	5.8±0.2			5.6±0.6	1.6±0.3	3.2-6.8	0.8-3.2
S7	6.5±0.3				6.5±0.3	7.8±0.2	9.0-10.3	2.3-3.2
S8	6.4±0.2	6.7±0.2		8.2±0.2	7.1±0.3	6.6±0.1	8.9-9.3	2.7-2.9
S9	7.7±0.6				7.7±0.6	5.7±1.0	8.9-9.3	2.7-3.0
S10	6.4±0.2				6.4±0.2	12.7±0.2	9.6-10.0	4.0-4.3
S11	7.0±0.5				7.0±0.5	8.5±0.5	9.2-9.7	3.1-3.4
S12	5.2±0.1				5.2±0.1	17.6±1.7	7.4-8.3	5.2-7.2
S13	5.4±0.1				5.4±0.1	31.1±3.1	8.4-8.8	8.8-10.0
S14		6.2±0.2			6.2±0.2	8.1±0.2	6.4-7.2	
S15	5.5±0.1				5.5±0.1	26.6±2.8	8.4-9.2	7.1-9.5
S16		6.1±0.2			6.1±0.2	8.1±0.3	8.0-8.8	3.6-5.0
S17	5.8±0.2	6.6±0.3	7.0±1.4	8.4±0.2	7.0±0.8	6.9±0.8	8.4-8.8	3.6-3.8
S18			8.5±0.4	8.3±0.2	8.4±0.4	14.0±1.9	4.7-6.6	5.1-5.7
S19				8.4±0.1	8.4±0.1	14.0±0.5	5.2-7.0	5.0-5.2
S20		7.7±0.8		8.2±1.4	7.9±1.6	14.0±3.7	8.6-9.0	7.8-8.8
S21	6.0±0.3	6.4±0.2			6.2±0.4	12.9±0.8	8.3-9.1	5.2-7.0
S22	5.8±0.2	6.0±0.2			5.9±0.3	11.2±1.5	8.7-9.2	4.1-4.7
S23			7.6±1.1	7.1±1.6	7.4±1.9	10.8±5.2	3.5-6.7	2.0-2.1
S24	7.3±0.2				7.3±0.2	22.6±0.7	8.7-9.6	3.4-4.4
S25	6.4±0.2	7.0±0.2	8.3±1.2	8.2±1.4	7.5±1.1	5.6±1.1	10.3-10.5	1.6-1.7
S26	5.3±0.1				5.3±0.1	54.4±5.4	3.4	50.0
S27		3.6±0.1			3.6±0.1	50.0±3.1	3.5	42.3
S28		5.5±0.2		7.1±1.4	6.3±1.4	16.1±3.6	5.7	41.3
S29		5.0±0.1			5.0±0.1	31.3±2.4	3.9	19.3
S30	6.6±0.2				6.6±0.2	10.8±0.2	6.8	4.1
S31		5.7±0.2			5.7±0.2	3.3±0.5	6.9	0.7
S32		5.5±0.2		7.0±1.4	6.3±1.4	10.1±2.6	6.6	6.5
S33		5.5±0.2			5.5±0.2	21.3±4.4	6.2	26.0
S34	8.0±0.5				8.0±0.5	6.2±1.1	6.5	7.4
S35			7.2±1.4	8.7±0.3	8.0±1.4	7.4±2.0	6.3	14.7
S36								
S37	6.0±0.1				6.0±0.1	4.0±0.1	47.9	12.0
S38	5.0±0.1				5.0±0.1	3.9±0.3	204.1	16.0
S39	5.8±0.1				5.8±0.1	1.7±0.1	5.8	1.1
S40				7.0±1.3	7.0±1.3	3.7±1.0	32.3	6.6
S41								
S42								
S43								
S44			7.4±1.3	7.6±1.4	7.5±1.9	3.3±1.4	102.3	9.4
S45				8.0±1.3	8.0±1.3	1.3±0.4	145.5	8.0
S46								
S47								

TABLE 4.5: Ages and masses derived for star clusters. Age estimates from more than one line were averaged. Mean ages were used to derive cluster masses using the procedure described in § 4.3.5. Measurements from the literature are shown for comparison. These literature measurements are taken from Gilbert and Graham (2007), Christopher (2008), Bastian et al. (2009), and Whitmore et al. (2010).

4.3.5 Star Cluster Masses

The cluster mass is a crucial parameter in determining whether a star cluster will evolve into a bound star cluster or dissolve into an open cluster. Generally star clusters with masses exceeding $10^5 \mathcal{M}_\odot$ tend to survive the numerous disruption mechanisms that occur during star cluster evolution and remain bound (Bastian et al. 2009; Portegies Zwart et al. 2010). However this depends heavily on the cluster environment and how intense tidal forces are (Lada and Lada 2003; Kruijssen et al. 2012).

The most direct method of measuring the mass of a star cluster is by determining its dynamical mass using the virial theorem (Spitzer, 1987):

$$M = 10 \frac{r_{hp} \sigma_r^2}{G} \tag{4.3}$$

Here r_{hp} is the projected half-light radius (in parsec), σ_r is 1D line-of-sight velocity (in kms^{-1}), and G is Newton's gravitational constant. Hence, the half-light radii and 1D velocity are the only observable quantities required to determine a star clusters dynamical mass.

At a distance of 19.2 Mpc for the Antennae galaxies, a typical star cluster size (half-light radius) of $r_{hp} = 5$ pc (Larsen 2004a; Gilbert and Graham 2007) corresponds to an angular size of $0\farcs05$. This angular size is just resolvable using high resolution images from the HST, such as those in Figure 4.3 and Figure 4.14.

Star clusters exhibit velocity dispersions ranging between $\sigma_r = 10$ - 30 kms^{-1}(Larsen et al. 2006; Gilbert and Graham 2007), which at the distance of the Antennae (19.2 Mpc) requires spectral resolutions of $\lambda/\delta\lambda \sim 7000$ or higher to resolve. KMOS provides intermediate spectral resolution ($\sim$ 2000 - 3800), which is insufficient to resolve the expected velocity dispersion from star clusters in the Antennae. Therefore, the virial theorem cannot be used to determine masses for our star cluster sample.

An alternative approach is to calculate photometric masses for our sample. This procedure requires the near-infrared magnitudes and age estimates of these star clusters, which are given in Table 4.1 and Table 4.5, respectively. These parameters can then be compared with the *Starburst99* models to estimate the masses for these star clusters.

As discussed in § 4.3.1.1, *Starburst99* has been used to model the temporal evolution of star clusters in the Antennae galaxies. These models assume a star cluster mass of $\mathcal{M}_{SB99} = 10^6 \mathcal{M}_{\odot}$. The cluster mass of an observed star cluster can then be determined using the relation:

$$\frac{L_{SC}}{L_{SB99}} = \frac{\mathcal{M}_{SC}}{\mathcal{M}_{SB99}} \tag{4.4}$$

where L_{SC} and $\mathcal{M}_{SC}$ are luminosity and mass of a star cluster, and L_{SB99} is the predicted luminosity from *Starburst99*. Converting Equation 4.4 to absolute magnitude and rearranging for observed star cluster mass gives:

$$M_{SC} - M_{SB99} = -2.5 log_{10}\Big(\frac{\mathcal{M}_{SC}}{\mathcal{M}_{SB99}}\Big) \tag{4.5}$$

$$\mathcal{M}_{SC} = \mathcal{M}_{SB99} \times 10^{-0.4((m_{SC}-DM)-M_{SB99})} \tag{4.6}$$

where M_{SC} and M_{SB99} are the absolute star cluster magnitude and the *Starburst99* model absolute magnitude respectively, m_{SC} is the apparent star cluster magnitude, and DM is the observed distance modulus of the Antennae galaxies, taken to be 31.41 (Whitmore et al., 1999).

Ages derived in § 4.3.4 were used to determine the predicted absolute K band magnitude of each star cluster in the sample. These values were then inserted into Equation 4.6 along with the observed apparent K band magnitudes of the cluster sample to determine the mass of each star cluster. Table 4.5 lists the derived masses. All 38 star clusters with derived ages have masses exceeding $10^5 \mathcal{M}_{\odot}$, and 17 of these have masses exceeding $10^6 \mathcal{M}_{\odot}$. The mass distribution of these star clusters is similar to their age distribution, in the sense that the most massive star clusters are located in the southern overlap region and the least massive star clusters are found south-east of the nucleus of NGC 4038 (see Figure 4.14).

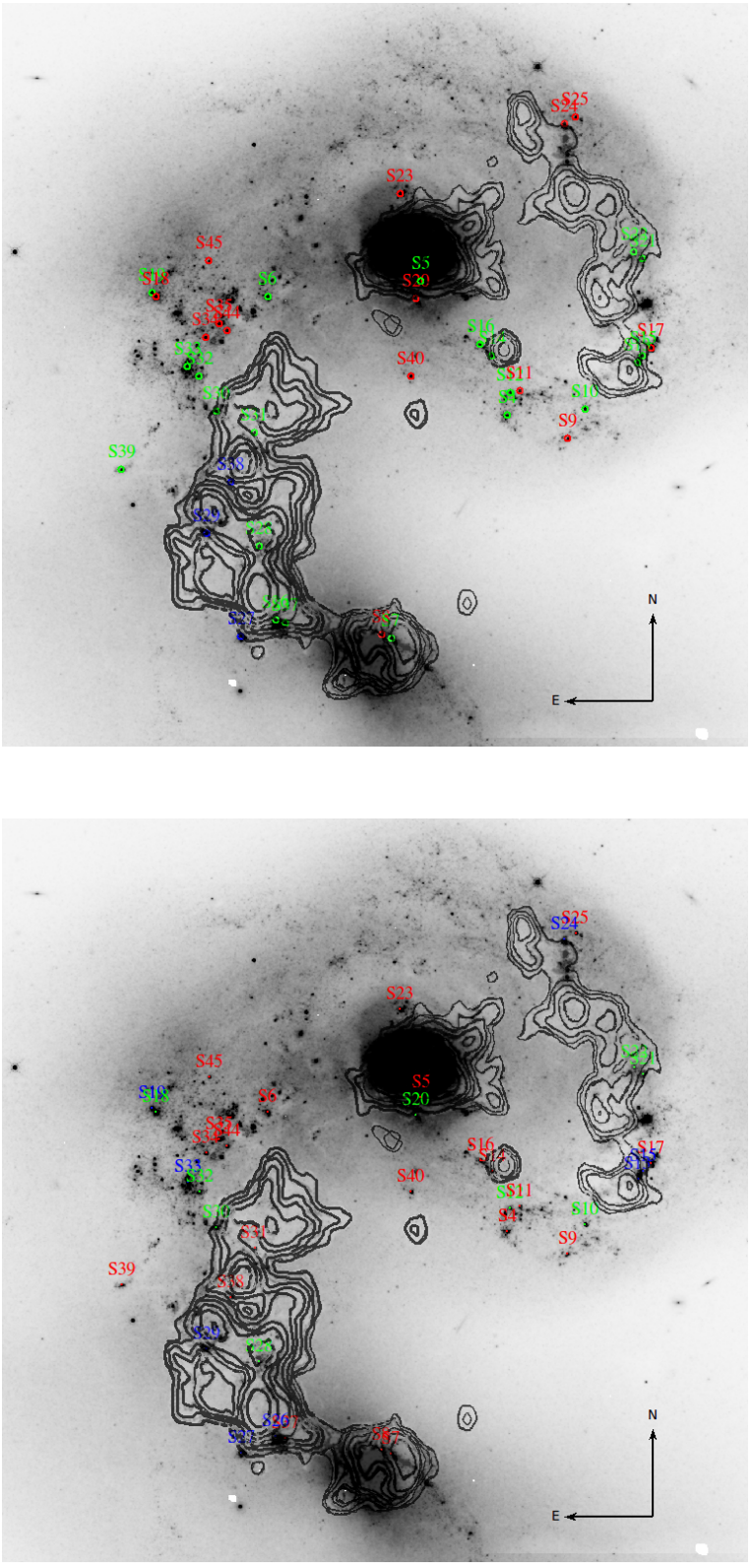

FIGURE 4.14: *Top*: Spatial distribution of star cluster sample with age. Blue objects have ages less than 5 Myrs, green objects have ages between 5 - 7 Myrs, and red objects have ages exceeding 7 Myrs. *Bottom*: Spatial distribution of the star cluster sample with mass. Star clusters labelled in red have masses $\leq 10^5 \mathcal{M}_\odot$, green star clusters have masses between $1 - 2 \times 10^6 \mathcal{M}_\odot$, and star clusters labelled in blue have masses exceeding $2 \times 10^6 \mathcal{M}_\odot$. Black contours represent a CO intensity map from Wilson et al. (2000).

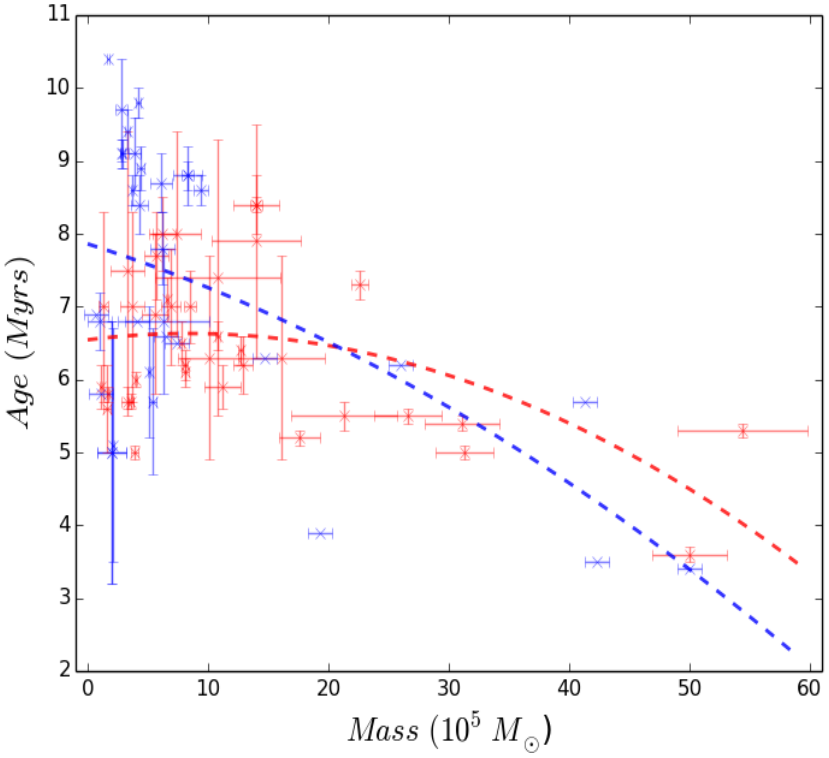

FIGURE 4.15: Comparison between derived ages and masses with those in the literature (see Table 4.5). The mass distribution of our sample as a function of age is plotted in red, and the same distribution from the literature is plotted in blue. The dashed lines represent best-fit lines to our distribution (red) and the literature distribution (blue). Clusters S7 - S25 have older ages in the literature due to different model parameters used by Christopher (2008), hence the older ages at lower masses for the literature distribution compared to our observed distribution. Both distributions show cluster mass decreasing with increasing age.

4.3.6 Metallicity Estimates

The analyses in § 4.3.4 and § 4.3.5 assume solar metallicities for the Antennae star cluster models. In this section we attempt to test this assumption by determining star cluster metallicities from metallic lines observed in the spectra of our star cluster sample.

Metallicity is closely linked to the effects of star formation in a galaxy, most notably the chemical enrichment of young stellar populations within a galaxy and its interstellar medium. Understanding variations in metallicity over ranges of galactic mass, redshifts and different environments is crucial in constraining theories of galaxy formation and chemical evolution. Metallicity investigations are mostly performed using spectroscopic observations. Emission lines from HII regions have often been used to estimate metallicity in star forming regions. Typical analysis methods use fluxes from the strongest forbidden lines relative to Hβ to produce empirical metallicity calibrations (Kewley and Ellison 2008; Bresolin et al. 2009). However, these calibrations are subject to systematic uncertainties due to variations in metallicity in selected HII region samples. This often leads to several commonly used empirical calibrations yielding varying and often conflicting metallicity measurements for the same sources (Kewley and Ellison 2008; Kudritzki 2010).

An alternative approach is to analyse the spectra from blue supergiants, which avoids the uncertain calibrations associated with the "strong line" HII region method. Blue supergiants have become particularly powerful tracers of chemical abundances out to distances of $\sim$ 7 Mpc via low resolution optical spectroscopy (Bresolin et al. 2006; Kudritzki et al. 2013). Blue supergiants are generally observed at optical wavelengths. However their descendants, red supergiants (RSGs), are extremely bright in the near-infrared, emitting luminosities of $\sim 10^6$ L/L$_\odot$ (Humphreys and Davidson, 1979). RSGs have very short lifetimes of $\sim$ 50 Myrs and dominate the near-infrared light in a star forming region $\sim$ 10 Myrs after the formation of the first massive stars.

Extracting chemical abundances from RSG spectra is rather challenging since their cool atmospheres contain molecular material that fill their spectra with literally thousands of strong molecular lines, many of which overlap and blend with metallic lines (Davies et al., 2010). Sufficiently high spectral resolution of $\lambda/\delta\lambda \sim$ 17,000 is required to separate molecular lines from metallic lines. This high resolution is very difficult to achieve with high S/N at 100 Mpc distances. However, molecular

lines from RSGs are considerably reduced in number and strength in the J band. Here, the most prominent features are metallic lines of FeI and the α-elements MgI, SiI and TiI. Therefore, considerably lower spectral resolutions of $\lambda/\delta\lambda \sim 1800$ can be used in the J band to extract chemical abundances from RSGs (Gazak et al., 2014).

Metallic lines from RSGs could in principle be used to find the chemical abundance of star clusters in the Antennae. Unfortunately, many of the star clusters in our sample have ages < 10 Myrs and while metallic lines are seen in 5 star clusters in the YJ band, their S/N is too low to extract chemical abundances. To bypass this issue, the YJ band spectra of all the star clusters with ages between 7 - 10 Myrs are combined to increase the S/N of the metallic lines. Figure 4.16 shows the resultant combined spectrum. The averaging procedure increased the S/N of the metallic lines to > 80 per resolution element, which is sufficient to derive chemical abundances using this method (B. Davies priv. comm.).

The technique proposed by Davies et al. (2010), which compares observed spectra to synthetic spectra, is adopted here to derive a metallicity for the average Antennae cluster spectra. Metallicity calculations were kindly performed by Ben Davies, whom we express our sincerest gratitude. Synthetic spectra with metallicities ranging between $-1.0 < [\mathrm{Z}] < 0.4$ were computed using 1D local thermal equilibrium (LTE) MARCS model atmospheres (Gustafsson et al., 2008), and were calculated in non-local thermal equilibrium (NLTE) for FeI, SiI and TiI using atomic models described by Bergemann et al. (2012, 2013). These lines are crucial in determining chemical abundances in the J band. MgI lines are ignored as sufficient atomic data for NLTE corrections are not available (B. Davies priv. comm.). Prior to fitting synthetic spectra to the observed spectrum, the spectral resolution of the synthetic spectra was degraded to the resolution of the observed spectrum using a gaussian convolution kernel.

Synthetic spectra with metallicities ranging between $-1.0 < [\mathrm{Z}] < 0.4$ were fitted to the observed spectrum and best-fit values for effective temperature (T_{eff}), surface gravity ($\log g$), and microturbulence (ξ) were derived. Synthetic spectra providing unphysical values of $\log g$ ($-0.5 < \log g > 0.5$) were eliminated. Reduced χ^2 values were determined for the remaining fits. The synthetic spectrum with the lowest reduced χ^2 was determined to be the best-fit spectrum, and is shown in Figure 4.16. Parameters derived from the best-fit spectrum are listed in Table 4.6. Figure

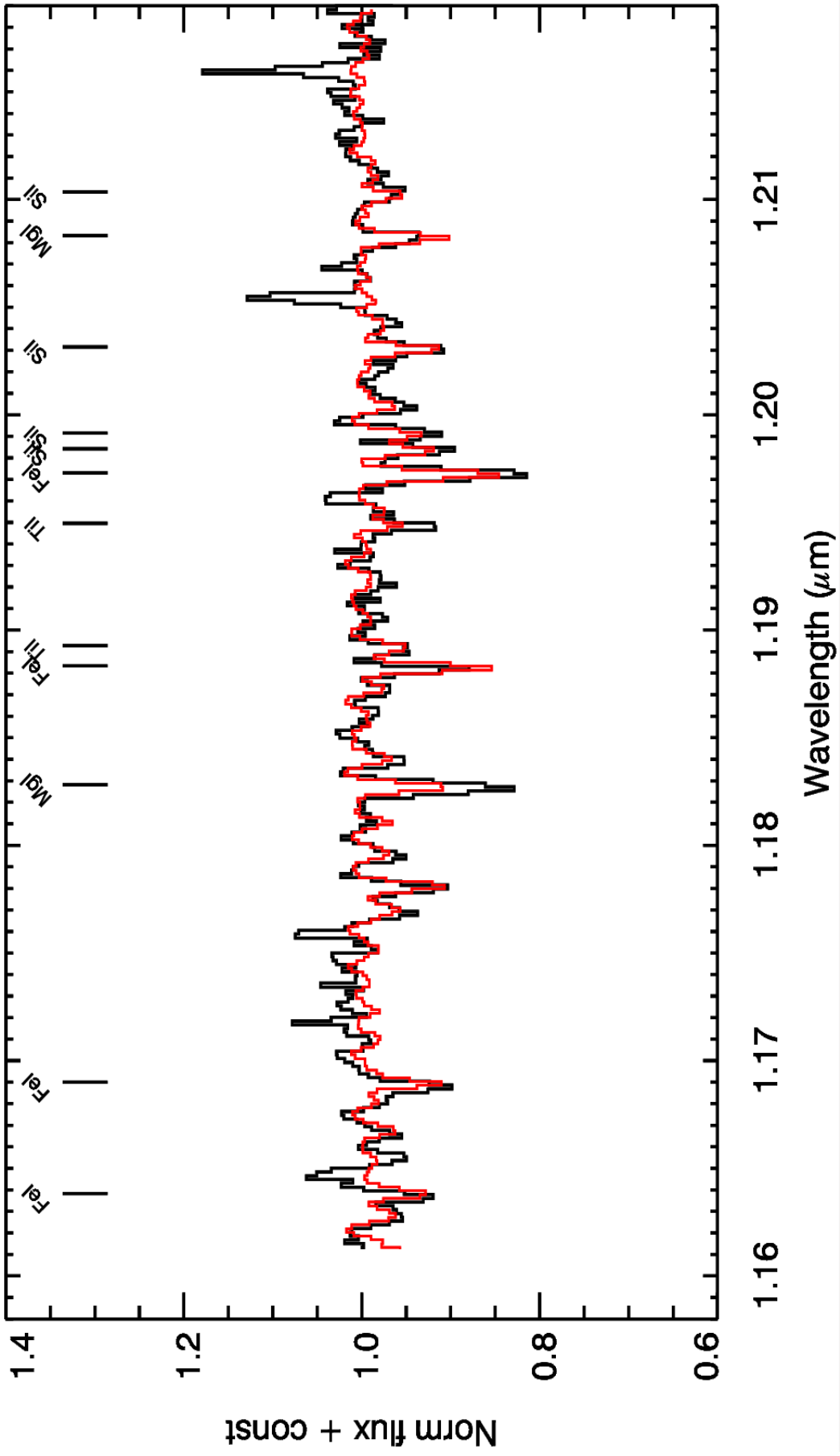

FIGURE 4.16: Best-fit of synthetic spectra from MARCS model atmospheres (*red*) to combined spectra of star clusters in our sample with ages between 7 - 10 Myrs (*black*). A metallicity of $[Z] = -0.14 \pm 0.20$, corrected for dilution of RSG spectral lines, was computed from this best-fit spectrum, and is consistent with solar metallicity.

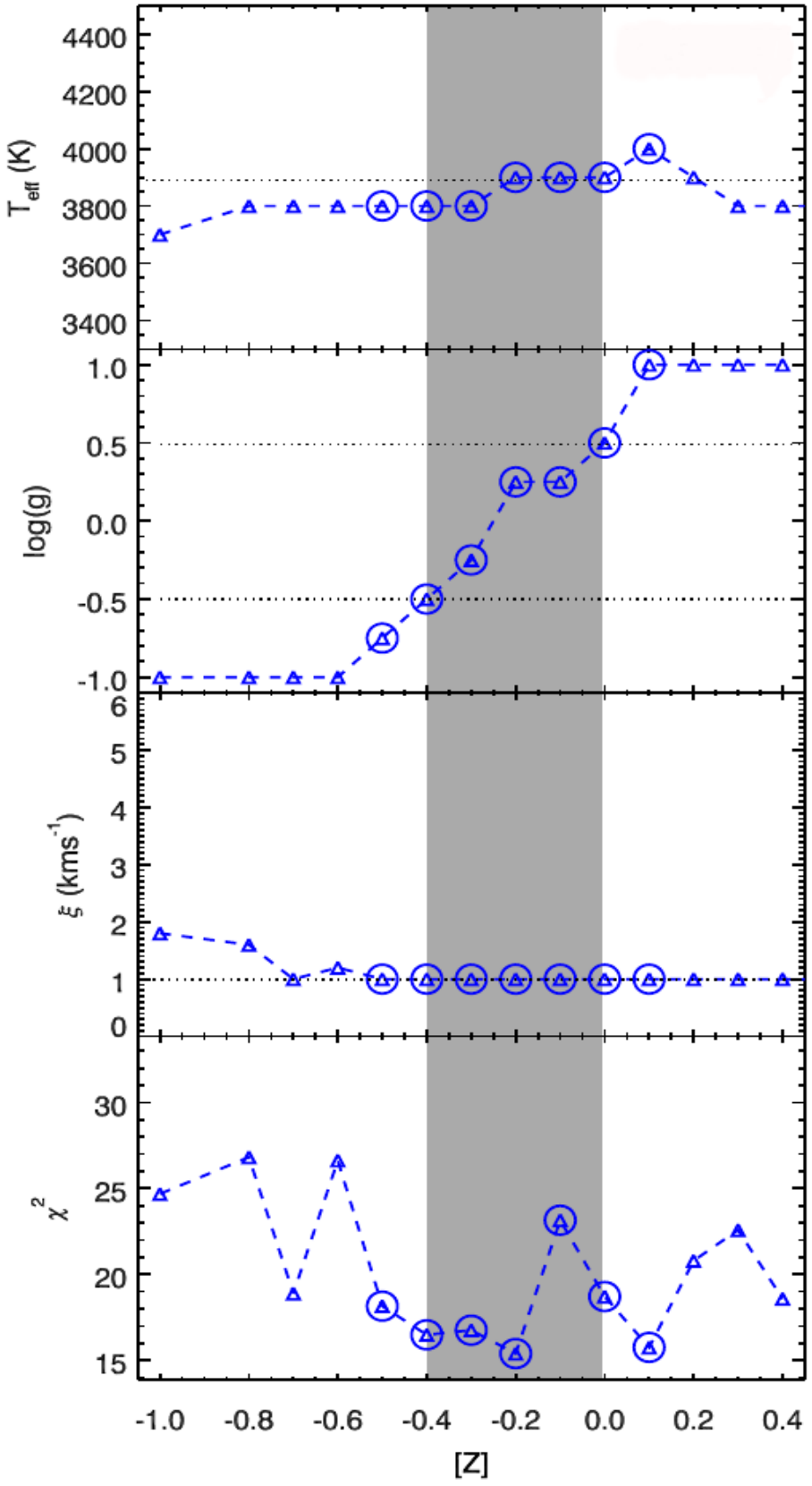

FIGURE 4.17: Best-fit model parameters (T_{eff}, log g, ξ) as a function of metallicity is shown here. Blue triangles represent derived model parameters. The bottom plot shows reduced χ^2 values for each fit, which are also represented by blue triangles. Synthetic spectra with unphysical values of surface gravity, outside the range -0.5 < log g < 0.5 (grey shaded region), were ignored. A metallicity of [Z] = -0.14 ± 0.20 was computed from the best-fit spectrum after correcting for dilution of RSG spectral lines.

T_{eff}	ΔT_{eff}	log g	Δlog g	ξ	$\Delta\ \xi$	Z	ΔZ	$\lambda/\delta\lambda$	$\Delta(\lambda/\delta\lambda)$
3890	80	0.17	0.59	1.0	0.5	-0.14	0.20	2893	130

TABLE 4.6: Derived parameters from best-fit spectrum. The derived metallicity was corrected by +0.05 dex to account for dilution of RSG spectral lines by the other stars in a star cluster. The degraded resolution of synthetic spectra is listed in the final two columns.

4.17 shows the best-fit model parameters (T_{eff}, log g, ξ) as a function of metallicity and a reduced χ^2 for each fit.

A metallicity of [Z] $= -0.19 \pm 0.20$ was computed from the best-fit spectrum. However, this required a correction of +0.05 dex for dilution of RSG spectral lines by the other stars in a star cluster (B. Davies priv. comm.). A corrected metallicity of [Z] $= -0.14 \pm 0.20$ was obtained for our combined spectrum, and is consistent with solar metallicity. The large error is due to the low S/N of the spectrum, even after combining several observed spectra. Earlier surveys have also found solar metallicities for star clusters in the Antennae (Mengel et al. 2005; Christopher 2008; Bastian et al. 2009). Therefore, the metallicity results from our star cluster sample are consistent with the literature. However, J band spectral surveys of Antennae star clusters with ages exceeding 10 Myrs are required to compute a more accurate metallicity for the Antennae star clusters.

4.3.7 Observed Line Intensities and Ratios

As discussed in § 4.3.2, several different mechanisms are responsible for the emission lines observed in our star cluster sample. Hence, these emission lines can be used as tracers of the physical conditions (temperature, density) of the interstellar medium. Figures 4.19 and 4.20 show intensity maps of star clusters with several bright emission lines in their spectra. In some cases the peak intensity of the observed emission lines vary in location from one another, indicating varying physical conditions within the star cluster. Peak intensities from the HeI emission lines correlate well with peak intensities of hydrogen recombination lines (see Figure 4.19 and Figure 4.20). These lines are generally produced from UV photoionisation of gas due to the presence of massive OB stars (Vanzi and Rieke 1997; Alonso-Herrero et al. 2003). Hence, these intensities map the location of the most massive stars in a star cluster.

Vibrationally excited H_2 emission arises from photoionisation of gas from massive stars or thermal shocks from SNe or stellar winds (Dale et al. 2004; Rosenberg et al. 2012). Unlike HeI or Brγ emission, H_2 emission does not originate in HII regions but in the surrounding molecular gas (Hanson et al., 2002). Clusters S17 and S28 show a variance in the location of H_2 emission compared to HeI and Brγ emission (see Figure 4.20), suggesting that H_2 emission occurs away from HII regions. However, this variance in location is not always observed in our sample as illustrated from intensity maps of S29, where H_2 emission occurs in the same location as HeI and Brγ emission. The location of H_2 emission does correlate somewhat with FeII emission (see Figure 4.20). FeII lines at 1.26μm and 1.64μm are also produced from strong thermal shocks associated with SNRs (de Grijs et al., 2004). Therefore, the correlation in location between the two emission types suggests that the H_2 emission may be produced from thermal shocks from SNRs.

Line ratios can give further information into the environment and star formation history of a star cluster. As mentioned earlier, FeII emission is thought to be due to SN activity and so is an indicator of past star formation. Whereas, Paβ and Brγ emission are produced from massive OB stars, and therefore primarily measure current star formation rates. Hence, [FeII/Paβ] and [FeII/Brγ] line ratios can be interpreted as indicators of the maturity of star clusters. Moreover, FeII - hydrogen line ratios and the [H_2/Brγ] line ratio can be used to determine whether the local environment is dominated by thermal shock excitation from SNRs or UV destruction (Larkin et al. 1998; de Grijs et al. 2004). These line ratios also have the advantage that they are relatively insensitive to extinction (Dale et al. 2004; Koo 2014).

Figure 4.18 shows how the measured line ratios vary with age of our star cluster sample. The [FeII/Paβ] and [FeII/Brγ] line ratios increase with age. This possibly indicates that star formation is decreasing with increasing age. Furthermore, these line ratios reach a maximum of [FeII/Paβ] = 0.4 and [FeII/Brγ] = 0.7. Low values like these have been observed in HII regions, such as Orion, where hydrogen recombination lines are much stronger than FeII emission lines (Mouri et al. 2000; Koo 2014). The [H_2/Brγ] line ratio also increases almost linearly with age. The maximum line ratio observed here is [H_2/Brγ] = 0.7, which is typical for HII regions (Larkin et al., 1998). However, the steady increase of all three line ratios with

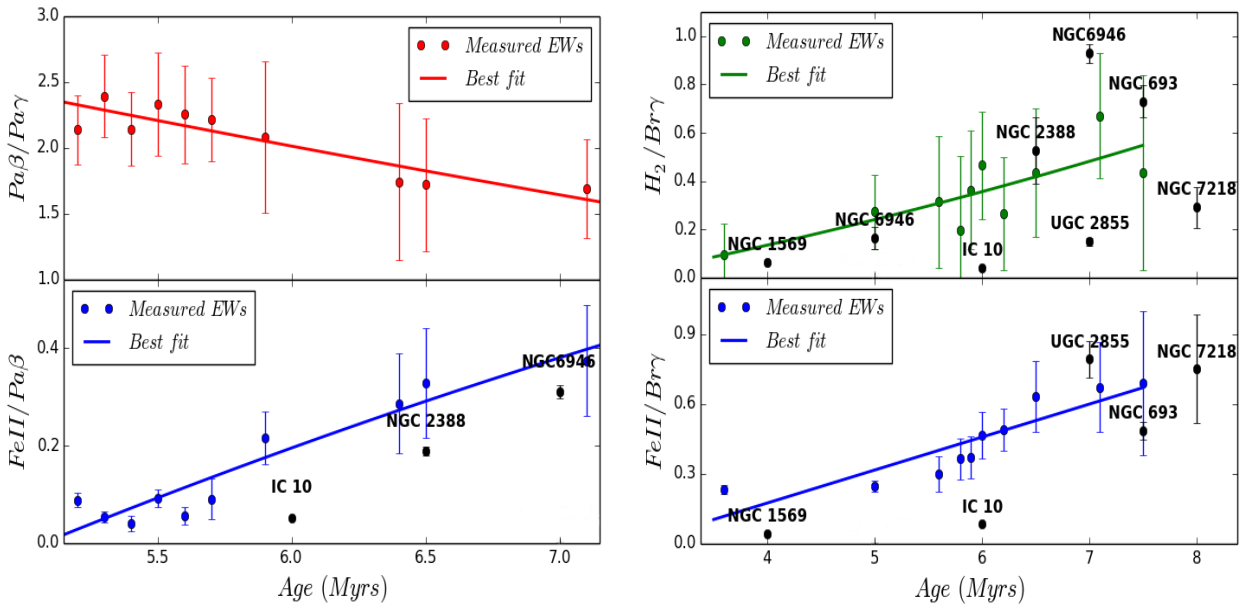

FIGURE 4.18: *Top-Left*: Dots represent [Paβ/Paγ] line ratios obtained from our star cluster sample in the YJ band. The red line represents the best fit to the observed ratios. *Bottom-Left*: Same as *top-left* but now for [FeII/Paβ] line ratios. *Top-Right*: Same layout as *top-left* but now for [H_2/Brγ] line ratios measured from star clusters in the K band. *Bottom-Right*: Same as *top-right* but now for [FeII/Brγ] line ratios, where FeII emission was measured in the H band. Line ratios from nuclear and HII regions in star forming galaxies, measured by Dale et al. (2004), are plotted in black for comparison. Errors for these line ratios are plotted where available.

age suggests that thermal shock excitation from SNRs is becoming increasingly important in ionising gas within a star cluster as it evolves.

In addition to these line ratios, Figure 4.18 shows how [Paβ/Paγ] line ratio varies as a function of age. Large [Paβ/Paγ] line ratios require high excitation temperatures, hence the observed linear decrease of this line ratio with age possibly represents a decrease in temperature within a star cluster as it evolves (Kwan and Fischer, 2011). Massive OB stars are responsible for ionising gas that produce strong hydrogen recombination lines. Therefore, this decrease in temperature is likely due to the decline of massive OB stars in star clusters as they evolve.

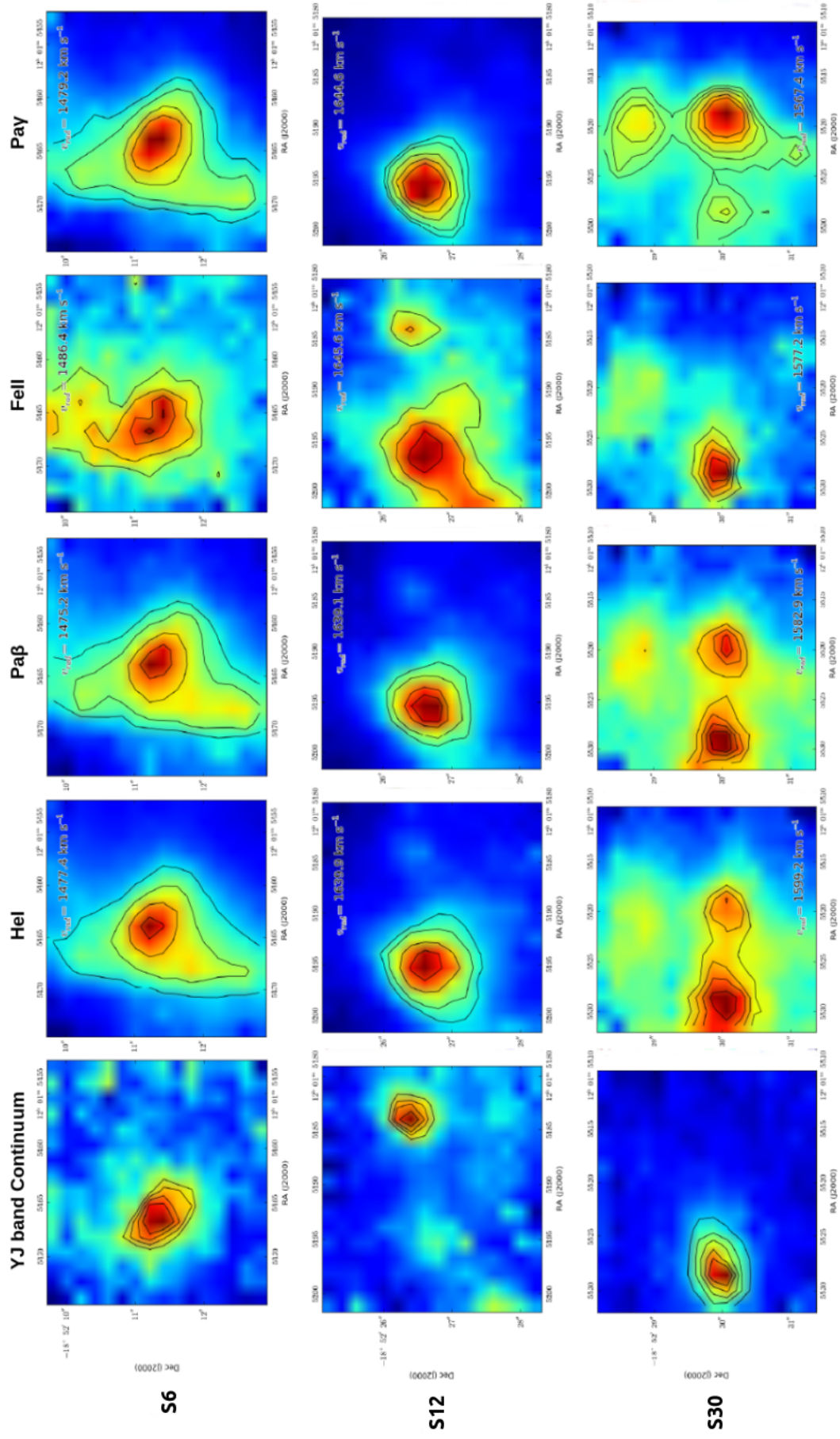

FIGURE 4.19: Intensity maps for $HeI_{1.08\mu m}$, Paγ, $FeII_{1.26\mu m}$, and Paβ emission lines are plotted along with YJ band continuum maps for star clusters S6, S12, and S30. The location of the peak intensity varies for each emission line, particularly for $FeII_{1.26\mu m}$ emission, due to the different mechanisms producing these emission lines. These maps show the physical conditions and excitation mechanisms within a star cluster. Radial velocities measured from each emission line are also labelled.

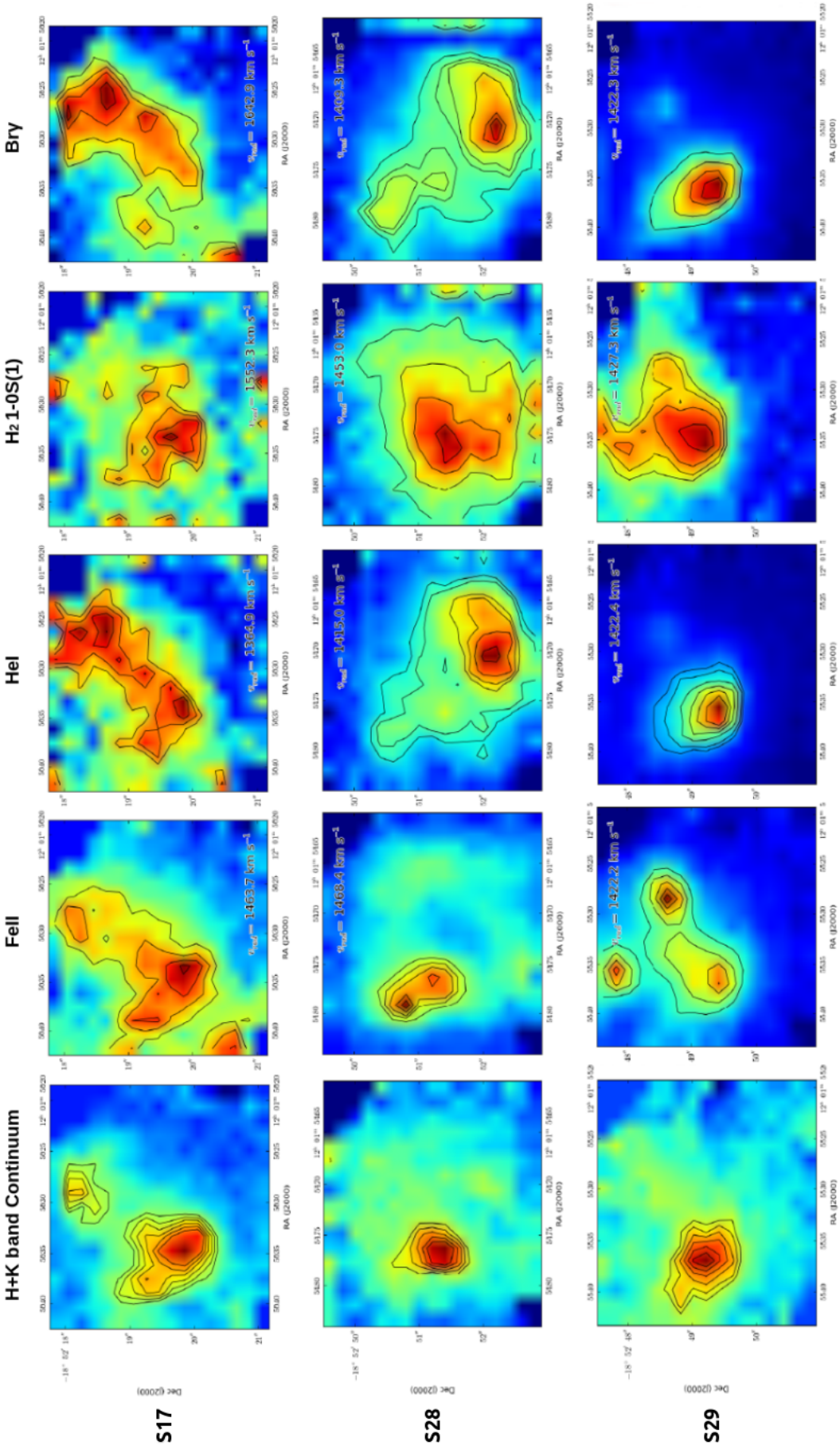

FIGURE 4.20: Intensity maps for $FeII_{1.64\mu m}$, $HeI_{2.06\mu m}$, H_2 1-0S(1), and Brγ emission lines are plotted along with HK band continuum maps for star clusters S17, S28, and S29. Here, the distribution of $FeII_{1.64\mu m}$ and H_2 1-0S(1) emission is seen to vary the most when compared to the other emission lines. Radial velocities measured from each emission line are also labelled.

4.3.8 Star Cluster Radial Velocities

Heliocentric corrected radial velocities were derived from the brightest emission lines in the spectra of our star cluster sample, which were usually the Paβ and Brγ hydrogen recombination lines. The centre of these emission lines were measured using *SPLAT-VO*. These were then compared to rest frame wavelengths to determine radial velocities for each of the star clusters. Velocity measurements are listed in Table 4.7. Star clusters in the southern overlap region are observed orbiting the Antennae with the lowest radial velocities. The highest radial velocities are observed near the cores of the progenitor disk galaxies.

Target	V_{Rad} kms^{-1}	V_{Rad}(HI) kms^{-1}	ΔV_{Rad} kms^{-1}
S4	1661±18	1690	-29
S5	1647±30	1640	7
S6	1621±16	1630	-9
S7	1697±24	1715	-18
S8	1659±36	1690	-31
S9	1671±18	1710	-39
S10	1687±26	1700	-13
S11	1662±18	1685	-23
S12	1664±27	1685	-21
S13	1663±23	1680	-17
S14	1680±17	1670	10
S15	1658±22	1675	-17
S16	1653±21	1665	-12
S17	1636±29	1675	-39
S20	1591±25	1605	-14
S21	1614±23	1630	-16
S22	1607±13	1630	-23
S24	1553±23	1565	-12
S25	1539±26	1560	-21
S26	1478±19	1490	-12
S27	1510±13	1490	20
S28	1411±13	1470	-59
S29	1424±18	1470	-46
S30	1566±30	1560	6
S31	1643±19	1620	23
S32	1596±21	1580	16
S33	1607±27	1580	27
S34	1624±24	1620	4
S37	1476±15	1490	-14
S38	1571±23	1560	11
S39*	1463±21	1515	-52

TABLE 4.7: Radial velocities of star clusters, corrected for the heliocentric motion of the Earth. Radial velocities were determined from Paβ and Brγ emission lines. HI velocities from Hibbard et al. (2001) are shown for comparison. Their measurements indicate that HI maps the rotation of the progenitor spirals. Many HI velocities are within 3σ of measured radial velocities for star clusters at the same location. This suggests that star clusters in our sample are associated with one of the progenitor disks. Asterisks represent clusters with no HI radial velocity measurements at the same location. HI radial velocities for these locations were determined by extrapolating from the nearest HI radial velocity measurement.

4.3.9 Supernova Rates

As discussed in § 4.3.2.4, the supernova rate can give insight into the star formation history of a galaxy. Supernovae (SNe) produce bright, compact FeII line emission in the near-infrared via thermal shock excitation of dust grains in large transition zones between HII and HI regions (Vanzi and Rieke 1997; de Grijs et al. 2004). This FeII emission can still be observed $\sim 10^4$ years after a SN explosion, making it a useful probe of supernova rates. Determining the supernova rate for each star cluster with FeII emission in its spectra will help understand how recent star formation varies throughout the Antennae galaxies.

FeII emission is detected in the spectra of 21 star clusters in our sample, 13 show FeII (1.26μm) emission and 11 show FeII (1.64μm) emission. In addition to this spectroscopic data, HST/WFC3 narrow band images centred at FeII (1.64μm) emission are available. Hence, both photometric and spectroscopic observations are used to determine supernova rates around the Antennae galaxies. Values recorded from either emission line are interchangeable as these lines share the same upper atomic level and have an intrinsic line ratio of FeII $\lambda 1.26/\lambda 1.64 = 1.36$ (Nussbaumer and Storey, 1988).

The relationship between supernova rate and FeII proposed by Rosenberg et al. (2012) is adopted for this study. Rosenberg et al. (2012) determined supernova rates for a dozen starburst galaxies by first measuring Brγ equivalent widths from their starburst galaxy sample. Equivalent width measurements were then input to the *Starburst99* model to determine supernova rates. Rosenberg et al. (2012) then attempted to determine a correlation between FeII (1.64μm) luminosities from these starburst galaxies and their supernova rates. From their pixel-pixel analysis of ESO/SINFONI data cubes of starburst galaxies, Rosenberg et al. (2012) found a strong linear relationship between the FeII (1.26μm) emission line and the supernova rate, which can be expressed in the form:

$$\log \frac{\mathrm{SNrate}}{\mathrm{yr^{-1}pc^{-2}}} = 1.01 \times \log \frac{\mathrm{FeII_{1.26}}}{\mathrm{ergs^{-1}pc^{-2}}} - 41.17 \tag{4.7}$$

where $\mathrm{FeII_{1.26}}$ is the FeII luminosity density per squared parsec, and the two constants are results from linear regression fits to supernova rate and FeII emission data from several galaxies.

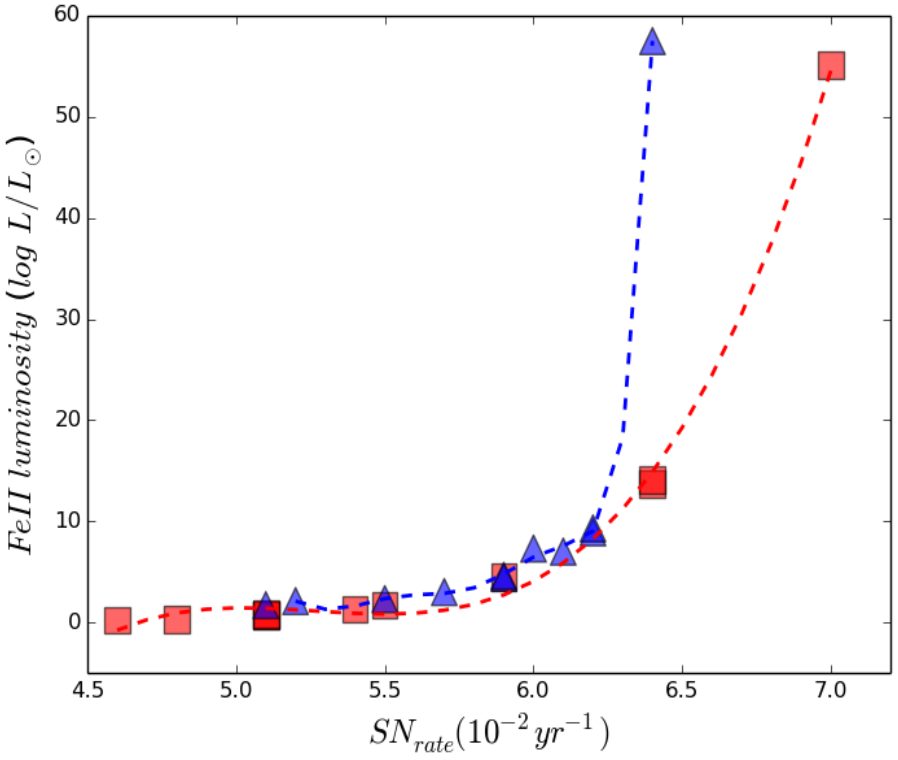

FIGURE 4.21: Comparison between photometric supernova rates (blue triangles) and spectroscopic supernova rates (red squares) for measured $FeII_{1.64}$ luminosities. 11 star clusters in our sample have both spectroscopic and photometric H band data, and enabled a direct comparison between FeII luminosity and supernova rate. Both photometric and spectroscopic supernova rates are seen to increase gradually with FeII luminosity, even if one excludes the most luminous cluster (S27) in the plot.

Spectroscopic and photometric luminosities were determined for star clusters with either $FeII_{1.26}$ or $FeII_{1.64}$ line emission in their spectra. Measurements were taken in a 0.5″ radius around each star cluster. Many of these star clusters were only observed in one of the two bands where FeII emission is present, hence the luminosity of only one FeII emission line was determined for these star clusters. Luminosities for the remaining FeII emission line was calculated using the conversion factor of FeII $\lambda 1.26/\lambda 1.64 = 1.36$ (Nussbaumer and Storey, 1988). The supernova rate of each star cluster was then calculated using Equation 4.7 and the measured photometric and spectroscopic luminosities.

Table 4.8 lists the calculated supernova rates and FeII luminosities and Figure 4.22 shows how the supernova rate varies throughout the Antennae galaxies. The highest supernova rates are generally located in the southern overlap region. Cluster

S27 in particular has the highest supernova rate in the entire star cluster sample with a supernova rate of ~ 0.6 yr^{-1} measured from spectroscopy. The lowest supernova rates are located south and south-east of the centre of NGC 4038. In these regions the supernova rate is generally on the order of 10^{-3} yr^{-1}.

Target	$log\ (L_{1.26}^{spec}/L_\odot)$	$log\ (L_{1.64}^{spec}/L_\odot)$	$log\ (L_{1.26}^{phot}/L_\odot)$	$log\ (L_{1.64}^{phot}/L_\odot)$	$SNR_{1.26}^{spec}$ $(10^{-2}yr^{-1})$	$SNR_{1.64}^{spec}$ $(10^{-2}yr^{-1})$	$SNR_{1.26}^{phot}$ $(10^{-2}yr^{-1})$	$SNR_{1.64}^{phot}$ $(10^{-2}yr^{-1})$
S5	5.9	5.8	6.5	6.4	5.1	3.8	18.9	13.9
S6	5.1	4.8	6.0	5.9	0.7	0.3	6.0	4.4
S7	5.2	5.1	6.5	6.4	0.9	0.7	18.6	13.6
S8	5.2	5.1	5.8	5.7	0.8	0.7	3.7	2.7
S10	5.4	5.3	6.6	6.5	1.4	1.0	23.8	17.4
S11	4.6	4.5	6.6	6.5	0.2	0.2	25.9	17.4
S12	5.9	5.7	6.1	6.0	4.4	3.3	7.8	5.7
S13	5.7	5.5	6.2	6.0	2.8	2.0	8.5	6.2
S14	5.2	5.1	6.1	6.0	0.9	0.7	7.2	5.3
S15	6.1	5.9	6.4	6.2	7.1	5.2	14.0	10.3
S16	5.3	5.1	6.0	5.9	1.1	0.8	6.2	4.6
S21	4.8	5.4	6.2	6.0	0.4	1.3	9.9	7.3
S22	5.7	5.5	5.8	5.7	2.9	1.7	4.1	3.0
S25	4.7	4.6	6.2	6.0	0.3	0.2	10.0	7.3
S26	6.1	5.9	6.9	6.7	6.7	4.9	44.9	32.9
S27	7.1	7.0	6.5	6.4	77.8	57.1	75.5	55.5
S28	6.5	6.4	6.3	6.2	19.2	14.1	12.1	8.9
S29	6.5	6.4	6.3	6.2	18.6	13.7	12.7	9.3
S32	6.0	5.9	6.2	6.1	6.2	4.5	9.6	7.0
S37	5.1	5.0	6.5	6.4	0.8	0.6	20.3	14.7
S38	6.0	5.9	6.3	6.1	6.2	4.5	11.3	8.3
S39	4.6	4.4	6.2	6.1	0.2	0.2	10.4	7.6

TABLE 4.8: Supernova rates of our star cluster sample. Luminosities were determined using spectral measurements of FeII emission in YJ band and H band, and photometrical measurements of FeII emission in the H band. The majority of star clusters were observed in one band, hence only one FeII line was observed from these star clusters. However, luminosities for the remaining FeII emission line were calculated using the knowledge that both emission lines share the same upper atomic level and have an intrinsic line ratio of $\lambda 1.26/\lambda 1.64 = 1.36$ (Nussbaumer and Storey, 1988).

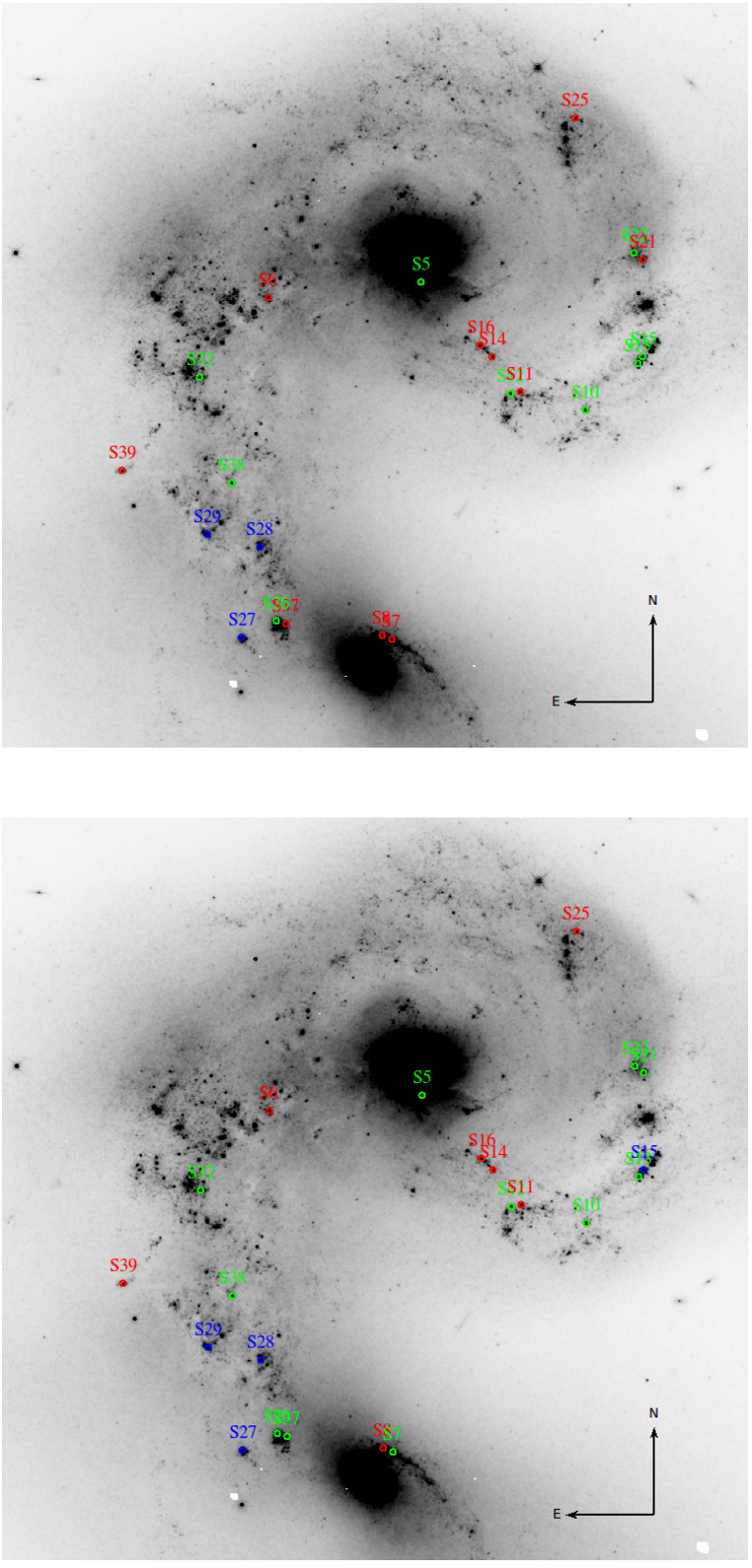

FIGURE 4.22: Variation of supernova rate across the Antennae. Supernova rates calculated from spectroscopy using the $FeII_{1.26}$ emission line are shown in the *top* diagram, and supernova rates calculated using the $FeII_{1.64}$ emission line are shown in the *bottom* diagram. Star clusters labelled in red have supernova rates of ~ 0.001 yr^{-1}, green star clusters have supernova rates ~ 0.01 yr^{-1}, and blue star clusters have supernova rates on the order of 0.1 yr^{-1}. The youngest and most massive star clusters in our sample have the highest supernova rates.

4.4 Discussion

4.4.1 Spatial Distribution of Antennae Star Clusters

As shown in § 4.3.4 and § 4.3.5, the ages and masses of star clusters in the Antennae system are observed to vary with position in the merger. An inverse correlation is found between age and mass in that the star cluster mass in our sample decreases with increasing age. Moreover, the most massive and youngest star clusters are located in the southern overlap region, and the oldest and least massive star clusters are located in the region south-east of the core of NGC 4038. Therefore, the local environment within the Antennae must vary, particularly between these two regions.

The young ages in the southern overlap region can be explained by the large concentration of molecular gas that occupies the same area. CO observations by Stanford et al. (1990) identified three large concentrations of molecular gas, one in each of the two nuclei and a third, more massive concentration in the overlap region (see Figure 4.14). Furthermore, over half of the total CO emission from the Antennae comes from this southern overlap region (Wilson et al., 2000). Strong [NeIII]/[NeII] ratios measured from the southern overlap region suggest that much of this molecular gas is likely being used to fuel star formation (Wilson et al. 2000; Wilson et al. 2003). This is apparent from the initial star cluster catalogue recorded from the Antennae by Whitmore and Schweizer (1995) where approximately 90% of the star clusters in this catalogue are located in the southern overlap region. Therefore, given the large abundance of molecular gas in the southern overlap region, new star clusters are likely to be continuously forming in this region, giving rise to the young ages observed there. Also, this large abundance of gas implies there is more material to form high mass ($\geq 10^5 \mathcal{M}_\odot$) star clusters.

In contrast to the southern overlap region, there is very little molecular gas associated with the region south-east of the core of NGC 4038, where the oldest and least massive star clusters are found. It is possible that all the molecular gas initially present in this region has already been used to form star clusters, hence there is insufficient gas available to produce a new generation of star clusters as young as those in the southern overlap region. The low mass of these star clusters suggests there was less molecular gas (or perhaps less dense) available to form from, compared to the southern overlap region.

In addition to hosting the youngest and most massive star clusters, the southern overlap region also has the highest supernova rate observed in the Antennae. The high supernova rate in this region is unsurprising given that many of the star clusters in this region have emission lines characteristic of massive OB stars. The abundance of massive OB stars here were likely formed from the large supply of molecular gas. As the supernova rate is an indicator of the star formation rate, the high supernova rate in the southern overlap region confirms that the star formation rate there is also very high. Stanford et al. (1990) speculate that the star formation rate in this region may be as high as $\sim 5\ \mathcal{M}_{\odot}\ \mathrm{yr}^{-1}$, implying that all the molecular gas in the southern overlap region ($\sim 1 \times 10^{9}\ \mathcal{M}_{\odot}$) will be exhausted in $\sim$ 200 Myrs.

The lowest supernova rates are observed in the regions south and south-east of the centre of NGC 4038. The low supernova rate observed south of NGC 4038 is surprising as this region shows strong CO emission and therefore is abundant in molecular gas (Wilson et al., 2000). Hence, this region should be an active site of star formation and SNe (Wilson et al., 2003). The low supernova rates observed could be due to the number of molecular gas clouds present in this region. Unlike the southern overlap region, where there are 4 - 5 giant molecular gas clouds in close proximity to one another, the region south of NGC 4038 has only one isolated molecular gas cloud. The gas clouds in the southern overlap region are possibly colliding with each other and producing massive OB stars in their boundary layers (Wilson et al., 2000), however no such collisions are taking place south of the centre of NGC 4038. Hence, this would reduce the star formation rate and supernova rate in this region.

4.4.2 Comparison with Previous Antennae Surveys

As mentioned in § 4.2.1, all star clusters observed in this survey have prior observations at optical or near-infrared wavelengths. Therefore, it is interesting to compare results from this study with those in the literature. The star clusters in our sample are relatively constrained in age (3 - 10 Myrs) compared with earlier surveys (e.g., Whitmore et al. 1999; Bastian et al. 2009). This is primarily due to a selection bias in our sample as star clusters that are bright in the K band were selected for this survey. The K band luminosity of star clusters generally peaks at ages less than 10 Myrs and there are few clusters with bright K band magnitudes

at older ages (Mengel et al., 2005), hence the young mean age of our star cluster sample.

Eight star clusters observed in this survey were also observed by Bastian et al. (2009) using optical spectroscopy. However, useful KMOS spectra were only available for 5 of these star clusters: S4, S5, S6, S7, and S21. The remaining star clusters, S1, S2 and S3, showed no absorption/emission features in their near-infrared spectra. Bastian et al. (2009) suggest S1 and S2 have ages between 80 - 250 Myrs, and S3 has an age of $\sim$ 20 Myrs. Given these ages, these star clusters will have no emission lines in their spectra. Furthermore, S1 and S2 are unlikely to have strong CO bandheads since these absorption lines peak at 12 Myrs due to the presence of RSGs, and will have likely become indistinguishable from the continuum at the ages of these star clusters (Gazak et al., 2013). B299 may have CO absorption bands in the H and K bands, however this cluster was only observed in the YJ band where no CO bandheads are present. Ages and masses derived for S4, S5, and S6 are in agreement with measurements from Bastian et al. (2009). Moreover, the presence of hydrogen recombination lines and helium lines in the spectra of these star clusters confirms the presence of massive OB stars.

Based on the age distribution of our sample (shown in Figure 4.14), star clusters in the Antennae do not form in isolation, but rather as parts of extended star-forming regions. This is in agreement with Zhang et al. (2001) and Bastian et al. (2006) who suggest that star clusters do not form stochastically, but are part of an extended hierarchy of star formation. An example of an extended star forming region is the southern overlap region, which harbours the youngest star clusters in our sample. The star clusters observed in this region were also observed by Gilbert and Graham (2007) using high resolution spectroscopy in the K band. Their calculated ages and masses are in general agreement with those from this survey, although they derive somewhat younger ages for S26 and S29 (see Table 4.5).

S26 (Figure 4.23) has also been observed by Greissl et al. (2010) and is a particularly interesting target due to the absorption and emission in its near-infrared spectra. Greissl et al. (2010) found CO absorption bands in the H and K band spectra of S26 along with strong hydrogen recombination lines. This is unusual since CO bandheads appear in star clusters $\sim$ 7 - 12 Myrs old and are due to RSGs, whereas hydrogen recombination lines are from OB stars and indicate an age less than 6 Myrs for a star cluster. Greissl et al. (2010) conclude that S26 is

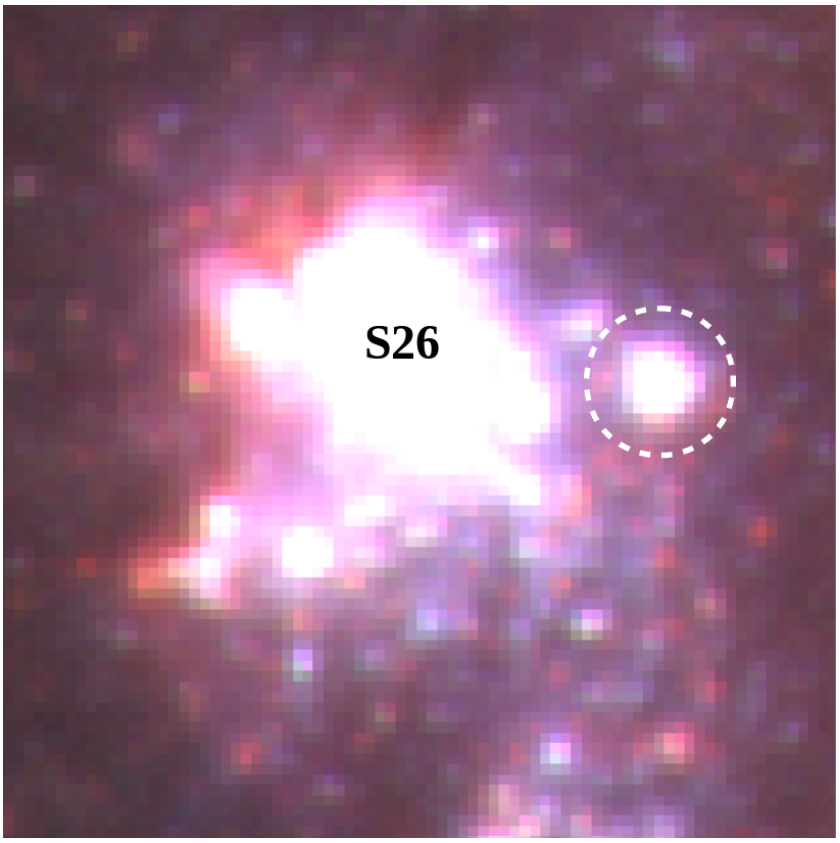

FIGURE 4.23: Cluster S26 has shown spectral features consistent with two stellar age groups. Spectra of this cluster shows hydrogen recombination lines that are produced from OB stars (< 6 Myrs old) and CO bandheads produced from RSGs (which appear ∼ 7 - 12 Myrs after the birth of a cluster). Greissl et al. (2010) suggest that S26 is a cluster of clusters as it is surrounded by fainter sources. They conclude that S26 is at least two separate clusters with an age spread of 6 - 18 Myrs and mass ratio $\mathcal{M}_{old}/\mathcal{M}_{young} < 0.2$. One of the surrounding sources is S37 (white dashed circle) which may have branched away from S26 at an earlier time.

in fact two separate star clusters with an age spread of 6 - 18 Myrs and mass ratio $\mathcal{M}_{old}/\mathcal{M}_{young} < 0.2$. Furthermore, Gilbert and Graham (2007) suggest that S26 may actually be a cluster of clusters as it is surrounded by fainter sources. S26 is known to have a neighbouring star cluster, S37. Given the similar age between these two star clusters, it is possible that S37 branched away from S26 during its early stages of evolution. Unfortunately, S26 was only observed in the YJ band in this study, hence CO bandheads were not detected. However, several star clusters in this survey have absorption and emission lines in their spectra, the brightest of which is S28. Similar to S26, this star cluster is also surrounded by fainter objects, and therefore may also be a cluster of clusters. However, if S28 is indeed a single cluster then the presence of both hydrogen recombination lines and CO

bandheads may indicate that star formation within this cluster is ongoing rather than a single burst.

A number of theories have tried to explain the presence of both these spectral features using the scenario of multiple star formation episodes within a star cluster (e.g., D'Ercole et al. 2008; Conroy and Spergel 2011). However, these theories require sufficiently high masses ($> 10^6$ $\mathcal{M}_\odot$) for star clusters after formation, and a sufficient gas abundance to fuel multiple episodes of star formation. Neither of these parameters are observed in Galactic and extragalactic young massive clusters, implying that multiple star formation theories have some drawbacks. Bastian et al. (2013b) have proposed an alternative theory that invokes binary stars. They suggest that the high stellar densities of young GCs imply that Wolf-Rayet stars in binary systems would have a longer lifetime and inhabit a star cluster during the same periods as RSGs. Such a star cluster will therefore consist of both hydrogen recombination lines and CO bandheads. Studies of Westerlund 1, a young massive cluster in the Galaxy, are in agreement with this theory. The model proposed by Bastian et al. (2013b) will need further verifications in future work, but for now illustrates that star cluster formation may have proceeded in a way that is consistent with the known physics of young massive cluster formation.

4.4.3 Comparison with Star Clusters in other Major Mergers

The results from our Antennae sample can be compared to star clusters in other major mergers. NGC 3256 is classified as an intermediate-stage merger in Toomre's list of nearby merging systems (Toomre, 1977) and is in a more advanced merger state than the Antennae galaxies (Trancho et al., 2007b). Photometric surveys by Zepf et al. (1999) indicate the presence of 1000 possible star clusters. The brightest of these have been observed spectroscopically by Trancho et al. (2007a) and several cluster parameters have been derived. Given that star clusters in the Antennae sample presented here were also selected based on their brightness, a comparison can be made between the brightest star clusters in these two galaxy mergers. Both mergers consist of star clusters with masses exceeding $10^6 \mathcal{M}_\odot$, and the average star cluster mass in both samples is $1 \times 10^6 \mathcal{M}_\odot$. The most massive star cluster in each galaxy is also very similar, having masses of $\sim 5 \times 10^6 \mathcal{M}_\odot$.

The similarity in cluster mass between these two mergers is quite remarkable considering NGC 3256 has significantly more molecular gas than the Antennae ($2 \times 10^{10} \mathcal{M}_{\odot}$ compared to $5 \times 10^{9} \mathcal{M}_{\odot}$: Casoli et al. 1991; Zepf et al. 1999; Wilson et al. 2000) and a higher star formation rate (33 $\mathcal{M}_{\odot}$ yr^{-1} compared to 20 $\mathcal{M}_{\odot}$ yr^{-1}: Zhang et al. 2001; Knierman et al. 2003). Moreover, the star formation rate in the Antennae is likely to increase substantially as the nuclei of NGC 4038/39 merge (Cox et al. 2006; Hopkins et al. 2009). Considering there is a tight relation between the most massive star cluster in a galaxy and its star formation rate (Larsen, 2004b), an increase in star formation may well lead to the Antennae producing star clusters with masses exceeding $10^{7} \mathcal{M}_{\odot}$, such as those found in NGC 7252 where the nuclei of the progenitor galaxies have merged (Schweizer and Seitzer, 1998). The same increase in cluster mass is also likely to occur in NGC 3256, however the larger abundance of molecular gas in NGC 3256 may fuel the formation of more massive star clusters than the Antennae will produce.

Currently there are no supernova rates from individual star clusters in mergers available for comparison. However, supernova rates recorded from the Antennae galaxies can be compared to supernova rates from the large sample of starburst galaxies observed by Rosenberg et al. (2012). Based on measurements of Brγ emission, star forming regions around the centre of these starburst galaxies have ages between 6 - 7 Myrs and so are comparable to the ages of the Antennae star clusters. Furthermore, their sample includes star forming regions in NGC 520 which is thought to be a galaxy merger between a gas-rich spiral and a gas-poor spiral that began merging $\sim$ 300 Myrs ago (Stanford and Balcells, 1991). Therefore, the age of this merger is comparable to the age of the Antennae merger.

The supernova rates measured by Rosenberg et al. (2012) are listed in Table 4.9. From our sample, 14 star clusters with measured supernova rates have ages between 6 - 7 Myrs. With the exception of S28, which has a supernova rate of ~ 0.1 yr^{-1}, the remaining star clusters have supernova rates between $10^{-2} - 10^{-3}$ yr^{-1}. All of these supernova rates are similar to rates measured for half of the starburst galaxy sample studied by Rosenberg et al. (2012). The supernova rate of S28 in particular is comparable to the supernova rate of NGC 520, which has a supernova rate of ~ 0.3 yr^{-1}. Furthermore, the Antennae star clusters younger than 6 Myrs have supernova rates between 0.1 - 0.6 yr^{-1}, which is comparable to the highest supernova rates recorded from this starburst galaxy sample. Considering that the supernova rate correlates with star formation rate, the supernova rates from the

Galaxy	Age (Myr)	SNrate (10^{-2}yr^{-1})
Arp 220	6.8	70
NGC 520	6.6	30
NGC 1084	7.3	0.9
NGC 1614	6.4	90
NGC 1792	7.9	0.7
NGC 1808	6.9	6
NGC 3628	6.9	1
NGC 4536	6.7	30
NGC 6240	7.7	360
NGC 7552	6.7	30
NGC 7632	7.0	3

TABLE 4.9: Supernova Rates measured from nearby starburst galaxies by Rosenberg et al. (2012). Ages are measured from high star forming regions within these starburst galaxies.

Antennae star clusters indicate that the star formation rate in this merger is very high compared to many starburst galaxies.

4.4.4 Are Star Clusters associated with the Antennae Galaxy Disks?

Radial velocities for our star cluster sample were calculated in section § 4.3.8. These can be compared to HI observations of the Antennae galaxies by Hibbard et al. (2001). In their survey they derived velocity maps for extended regions around the Antennae galaxies. These HI maps clearly show the rotation of the progenitor spirals. Therefore, any significant difference between the star cluster radial velocities and the HI velocities at a particular location may indicate that the star clusters are not associated with the galactic disks. Bastian et al. (2009) found three star clusters in their sample have radial velocities significantly different to the HI velocity maps, indicating that there are some Antennae star clusters that are not associated with either disks.

Figure 4.24 and Table 4.7 show a comparison between radial velocities of our star cluster sample, measured using either Paβ or Brγ emission, and the HI velocities measured by Hibbard et al. (2001). All star clusters in our sample follow the HI rotation, and are therefore associated with one of the progenitor disks. S39 does not have any HI radial velocity measurements for comparison. However, its radial

velocity is similar to the radial velocities of the surrounding star clusters in our sample, which are all likely associated with the progenitor disks. Therefore, S39 is also likely associated with one of the progenitor disks.

This result is unsurprising given the ages of the star clusters in our sample. Star clusters only a few Myrs old are generally found forming within the progenitor disks of galaxy mergers (e.g., Trancho et al. 2007a). However, star clusters may become part of the halo cluster population of the merger remnant as they evolve. This has been observed by Bastian et al. (2009) for some of the older ($\sim$ few hundred Myrs) star clusters in the Antennae. Moreover, this is observed for older merger remnants like NGC 3921 (Schweizer et al., 2004) and NGC 7252 (Schweizer and Seitzer, 1998) where the progenitor disks have been completely disrupted. The orbits of star clusters in these galaxy mergers are dominated by random motions rather than disk rotation. Therefore, while the star clusters in our sample are currently associated with the progenitor disks of the Antennae, they may form the halo cluster population of this merger as it evolves.

4.4.5 Outflows from Star Clusters

Gas outflows are often observed from massive ($10^6 \mathcal{M}_\odot$) star clusters that are a few Myrs old (Hodapp and Davis 2002; Eislöffel et al. 2003). These outflows are due to stellar winds from massive OB stars and SN explosions that accelerate the local gas to high enough velocities to escape the star cluster volume (Tenorio-Tagle et al., 2005). There is reason to believe that some of the star clusters in the Antennae galaxies may also have outflows. Gilbert and Graham (2007) find that several clusters in their sample have HII velocity dispersions exceeding the escape velocity of the star cluster, suggesting the gas within these star clusters has adequate energy to escape the cluster's potential well.

Outflows can often be traced by shock-excited H_2 emission as they leave the dense cores of star clusters (Hodapp and Davis, 2002). A particularly useful emission line is the H_2 1-0S(1) line occurring at 2.12μm (Eislöffel et al., 2003). Thirteen star clusters in our sample have this emission line in their spectra (see Table 4.3). Furthermore, intensity maps of these clusters show H_2 1-0S(1) emission lines structured as lobes and filaments that are located away from the centre of the star cluster where the HII regions are present. However, it is unknown whether the observed H_2 emission is shock excited or excited by UV florescence. Excitation

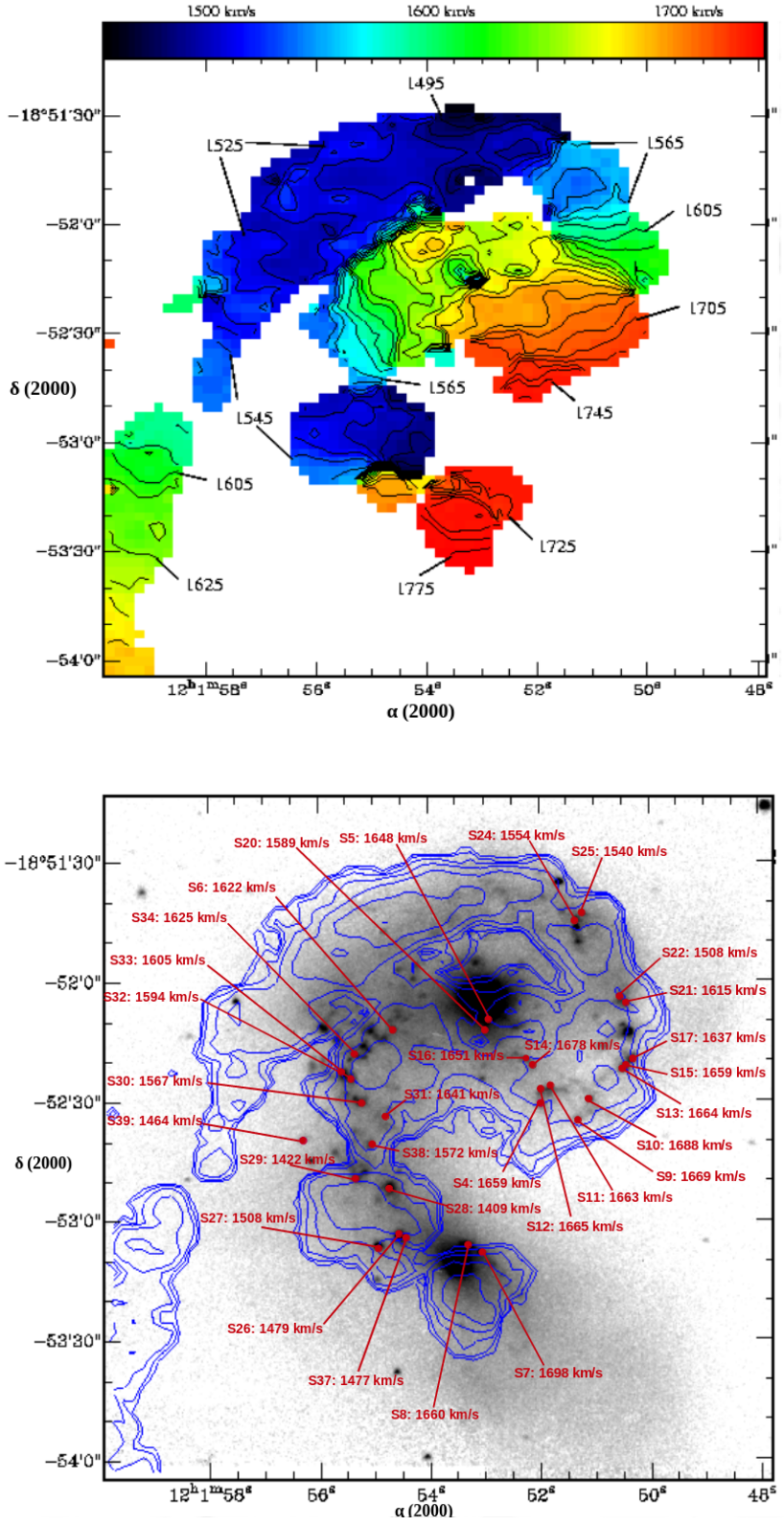

FIGURE 4.24: *Top*: HI maps of the Antennae produced by Hibbard et al. (2001). The variation in colour around the Antennae represents the variation in radial velocity of HI. *Bottom*: HI contours superimposed on a K band image (Hibbard et al. 2001; Figure 9) and overplotted with radial velocities measured from star clusters in our sample.

by the latter process does not trace outflows. Therefore, it is unclear if these star clusters have outflows. Fortunately, H_2 line ratios can be used to differentiate between excitation by thermal shocks and UV photoionisation (Hanson et al., 2002). Four star clusters in our sample have strong H_2 1-0S(0) emission at 2.22μm along with H_2 1-0S(1) emission. These are S27, S28, S29, and S31, all of which have been observed by Gilbert and Graham (2007) and are suggested to have outflows.

H_2 1-0S(0)/ H_2 1-0S(1) line ratios from these stars clusters range between 0.4 - 0.5. This range is typically observed from photodissociation regions (PDRs) formed by UV photons (Hanson et al., 2002). Shock excited H_2 emission have lower values, generally between 0.1 - 0.2. Therefore, these star clusters may not have outflows. However, VLT/SINFONI surveys show that S28 and S29 are located near deeply embedded H_2 sources (Herrera et al., 2012). H_2 line ratios from these sources range between 0.1 - 0.2, indicating H_2 emission is being powered by shock excitation. Therefore, these sources may be newly formed star clusters that have outflows that are breaking through the dense cores of these clusters and shock-exciting the surrounding molecular gas.

4.5 Conclusion

Near-infrared spectra of star clusters in the Antennae galaxies have been observed using the KMOS Multi-object Integral Field Spectrometer of the ESO VLT. Bright (M_k < -12) star clusters with near-infrared spectroscopic data or optical photometric/spectroscopic data were selected for this survey. A total sample of 47 star clusters were observed: 26 star clusters were observed in the H, K, and HK bands, and 30 were observed in the YJ band.

- The clusters in this survey generally have ages between 3 - 10 Myrs. These are very young compared to some clusters found in the Antennae that have typical ages of $\sim$ 200 Myrs. However, our sample is biased to the brightest clusters in the near-infrared, and therefore contains some of the youngest clusters in the Antennae. The derived ages are in agreement with earlier optical and near-infrared measurements for the same clusters.

- The youngest star clusters are located in the southern overlap region. This is also the same location where the most massive star clusters in our sample are found. The southern overlap region is also abundant in molecular gas (mass $\sim 10^9 \mathcal{M}_{\odot}$) which is thought to be fuelling the formation of massive star clusters. The high supernova rate calculated for the star clusters located in this region confirms that the southern overlap region is a hotbed for star formation in the Antennae. Given the abundance of molecular gas available for star formation, the southern overlap region may continue to host the youngest and most massive star clusters in the Antennae for the next few hundred Myrs.

- The metallicity of the star clusters, derived from red supergiant dominated spectral features, is consistent with solar abundance to within $\pm$ 0.2 dex. This is in agreement with metallicities derived from earlier surveys. However, further observations of these features are required to better constrain the metallicity of star clusters around the Antennae. Given the photometric masses estimated for these star clusters, many of them may survive past the current early, violent periods of star cluster evolution and evolve into old (Gyr) star clusters.

- The kinematics of all the star clusters in our sample suggest an association with one of the two disk galaxies involved in the merger. A similar result is found for the merger NGC 3256, which is similar in age to the Antennae although at a more advanced stage of merging. However, older mergers like NGC 7252 are dominated by clusters orbiting in a random motion rather than disk rotation. This implies that galaxy mergers form the majority of their star clusters in disks, and their orbits become randomized as the merger evolves.

- Several star clusters in our sample contain spectral features expected from both massive OB stars and RSGs, the brightest of which is cluster S28. Based on our results, it is unclear whether S28 is a single star cluster or a group of clusters. If S28 is indeed a single star cluster then the peculiar spectral features may be explained by invoking longer lifetimes of Wolf-Rayet stars in stellar binaries, as suggested by Bastian et al. (2013b).

- Based on the above results, we suggest three points for future surveys of the Antennae star clusters. Firstly, star clusters with ages $\sim$ 12 Myrs should be

observed in the YJ band. Not only will this give a better constraint on the metallicity than what we have provided, it may also indicate how metallicity varies throughout the Antennae star cluster population, particularly if there is any difference in metallicity between the southern overlap region and other regions of the Antennae. Secondly, radial velocities of star clusters with ages closer to the time of the last pericentre passage ($\sim$ 200 Myrs ago) should be investigated. Given that we have established that the youngest star clusters prominently form in the disks, it will be interesting to see if the older star clusters have evolved to form part of the halo cluster population of the merger. Finally, given that at least two star clusters in our sample (S26 and S28) may be multiple clusters, it would be interesting to compare these to other similar star clusters in the Antennae to better understand how they form and evolve. Star cluster #79 from Christopher (2008) (knot S in Whitmore et al. 2010) is an ideal target to observe for comparison as high resolution HST images show it has an unusually large size and morphology compared to other star clusters in the Antennae and may well be a complex of clusters.

Chapter 5

NGC 1487

5.1 Introduction

NGC 1487 is described as a peculiar late-type galaxy (Sersic 1968; Agüero 1971). The main features of this galaxy are characterised by four bright condensations in the central region (see Figure 5.1) and two faint asymmetric tails extending out to $\sim$ 13 kpc from the galactic centre. These bright condensations have spectral characteristics typical of HII regions (Aguero and Paolantonio, 1997), which suggest the presence of massive OB stars and relatively recent ($\sim$ 5 Myrs) star formation in these condensations. Equivalent width measurements from emission lines in these condensations indicate star formation rates higher than typically found in galaxy mergers, and the morphological structure of NGC 1487 suggests this galaxy is the product of a merger process between two late-type galaxies (Aguero and Paolantonio, 1997).

All four condensations are further examined by Lee and Lee (2005), who identify more than 500 star cluster candidates in their two-colour photometric analysis of NGC 1487 using HST/WFPC2 data. They conclude that these star cluster candidates are likely to have been produced from tidal interactions occurring between the two late-type galaxies involved in this merger. Furthermore, from their photometric analysis they propose that the merging process may have occurred $\sim$ 500 Myrs ago. The brightest 3 star cluster candidates in the catalogue produced by Lee and Lee (2005) have been further investigated by Mengel et al. (2008) using

NGC 1487	
$\alpha_{\rm J2000}$	$03^{\rm h}55^{\rm m}46{\rm s}$
$\delta_{\rm J2000}$	$-42°22'05''$
M_V	-18.32
$cz_{\rm hel}$	711 ± 15 kms^{-1}
D	10.0 ± 0.2 Mpc
Scale	46 pc arcsec^{-1}

TABLE 5.1: Basic parameters of NGC 1487 taken from Aguero and Paolantonio (1997). Hubble constant is taken as $H_0 = 71$ kms^{-1}Mpc^{-1}.

near-infrared spectroscopy surveys with VLT/ISAAC. They confirm these candidates are bona fide star clusters and find absorption features typically observed from red supergiants (RSGs) in all three star clusters, which implies an age of $\approx$ 10 Myrs. This young age also implies that these star clusters may have survived the early, violent phases of star cluster evolution, where stellar winds from massive OB stars and supernova explosions are continually removing gas from the star cluster and causing it to dissolve (Portegies Zwart et al., 2010). The magnitudes of these star clusters are generally quite faint when compared to those in other mergers like the Antennae (Whitmore et al., 2010). Furthermore, NGC 1487 is quite a faint galaxy merger, having a total magnitude of $M_K = -20.4$ which is comparable to the LMC (Micheva et al., 2013).

Given the large abundance of star cluster candidates, NGC 1487 presents an opportunity to expand our understanding of star cluster formation and evolution in merging galaxies. In this study, we present photometric and spectroscopic analysis of the brightest star clusters in NGC 1487. The star cluster sample observed in this survey is introduced in § 5.2 along with the photometric and spectroscopic data used. Properties derived for these star clusters are presented in § 5.3. Implications of our findings are discussed in § 5.4 and conclusions from our survey are presented in § 5.5.

5.2 Data Reduction

5.2.1 Photometric Data

HST Wide Field Planetary Camera 2 (WFPC2) and Advanced Camera for Surveys/High Resolution Channel (ACS/HRC) images of NGC 1487 were acquired

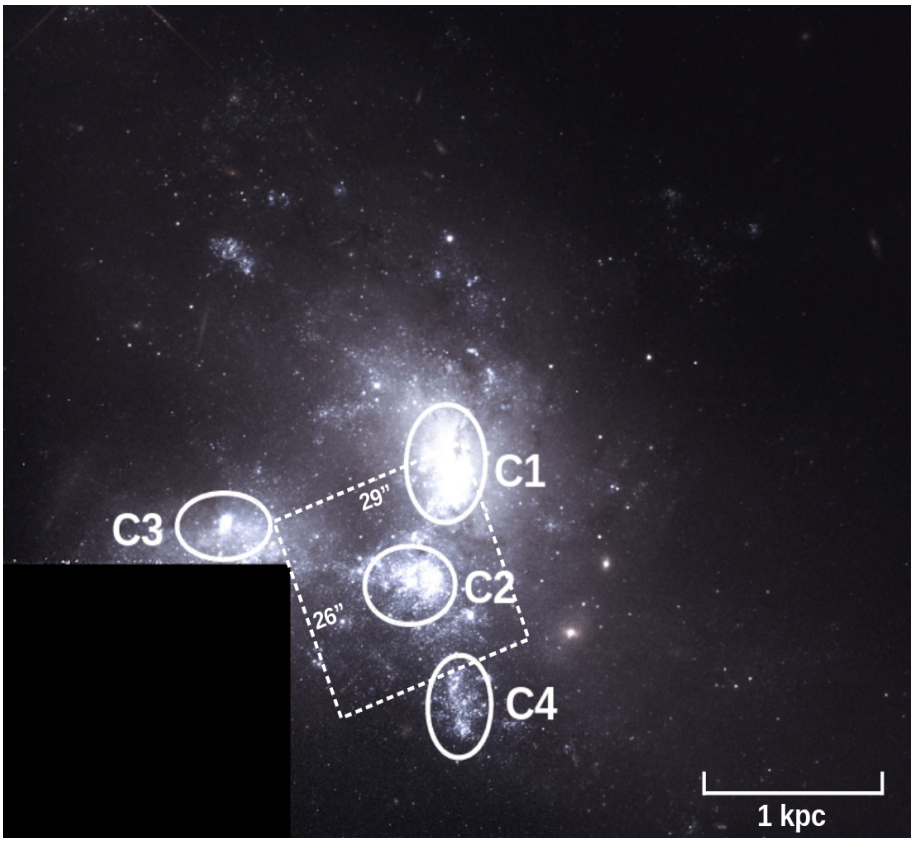

FIGURE 5.1: HST/WFPC2 mosaic of the central region of NGC 1487. The size of this image is $2.0' \times 1.7'$. Each of the four condensations discussed in § 5.1 are labelled here. Condensations are numbered according to the catalogue produced by Aguero and Paolantonio (1997). The dashed box represents the field of view ($29'' \times 26''$) of the ACS/HRC frame used for this work.

as part of Proposal-ID 5396 (PI: S. Zepf) and 9473 (PI:W. Vacca), respectively. WFPC2 frames were taken in the F450W and F814W filters, and HRC frames were taken in the F435W band. Reduced images from the HST pipeline are used for both sets of data. WFPC2 frames are centred at $\alpha_{\rm J2000} = 03^{\rm h}55^{\rm m}45\overset{\rm s}{.}3$, $\delta_{\rm J2000} = -42°22'10''$ and the HRC frames are centred at $\alpha_{\rm J2000} = 03^{\rm h}55^{\rm m}45\overset{\rm s}{.}2$, $\delta_{\rm J2000} = -42°22'15''$. The spatial resolution of the WFPC2 frames and HRC frames are $0.1''$/pixel and $0.03''$/pixel, respectively. At the adopted distance of 10.0 ± 0.2 Mpc for NGC 1487 (Lee and Lee, 2005), 1 parsec corresponds to an angular size of $0''.02$. Given that massive star clusters have an average size of $\sim$ 5 pc (Schweizer et al. 1996; Bastian et al. 2013c), the spatial resolution of both frames should be sufficient to resolve the star cluster population in NGC 1487. Galactic reddening values of A_{F435W} and $A_{F450W} = 0.043$, and $A_{F814W} = 0.018$ were used throughout this investigation (Schlafly and Finkbeiner, 2011). Total integration times for each HST frame are listed in Table 5.2.

5.2.2 Spectroscopic Data

Spectroscopic surveys were taken in the near-infrared in order to penetrate through dense clouds that enshroud star clusters at young ($\sim$ few Myr) ages. Spectroscopy was performed with KMOS at VLT-ANTU on 16/11/13. Observations were taken in the HK bandpass at a spectral resolution of $\lambda/\delta\lambda \sim 2000$. The total wavelength coverage in the HK band is 1.5 - 2.4μm. KMOS arms were allocated to individual targets using the KMOS Arm Allocator software (*KARMA*) (Wegner and Muschielok, 2008). The observing pattern was set to object-sky-object-sky, and the observing mode was set to *Free-dither*. Three IFUs (one for each KMOS detector) were fixed on regions devoid of star clusters and bright objects while 19 IFUs observed star cluster targets. The three sky observing IFUs were used to improve sky subtraction. IFUs #2 and #13 were unavailable for use. Raw frames from both science and calibration observations were processed using recipes from the ESO *SPARK* data reduction kit (Davies et al., 2013). Reduced science data cubes for each star cluster target were produced using the standard monolithic pipeline available in *SPARK*. The total exposure time for each target is listed in Table 5.2 and a mosaic of the collapsed cubes is shown in Figure 5.3.

5.2.3 Star Cluster Catalogue

Few surveys have been made of star clusters in NGC 1487. From the limited studies in the literature, Lee and Lee (2005) have used HST/WFPC2 images of NGC 1487 to detect 560 star cluster candidates around the system over an apparent magnitude range of $18.5 < B < 24$. Furthermore, three of these candidates are confirmed as bona fide star clusters through near-infrared spectroscopy (Mengel et al., 2008). The brightest star cluster candidates ($B < 22$ mag) from the catalogue produced by Lee and Lee (2005) are selected for this survey. The catalogue produced by Lee and Lee (2005) is generally confined to the centre of NGC 1487, and primarily focus on the four condensations. Star clusters may exist outside this central region and possibly in the tidal tails as seen in other galaxy mergers (e.g., Whitmore et al. 1999; Trancho et al. 2007b). Therefore, HST frames presented in § 5.2.1 were used in our survey to identify additional star cluster candidates beyond $\sim 1'$ from the centre of NGC 1487. *SExtractor* (Bertin and Arnouts, 1996) was used to identify star cluster candidates based on colour, magnitude and ellipticity values. Objects with colours B-I < 0.5, magnitudes of $B < 22$ mag, and ellipticity

Target	Other Names	α_{J2000}	δ_{J2000}	KMOS Integration time/s	HST Integration time/s		
					F435W	F450W	F814W
SC1	4	$03^h55^m45\overset{s}{.}23$	$-42°22'12\overset{''}{.}56$	300	1540	3600	3200
SC2	14	$03^h55^m45\overset{s}{.}37$	$-42°22'13\overset{''}{.}06$	300	1540	3600	3200
SC3	24	$03^h55^m45\overset{s}{.}26$	$-42°22'13\overset{''}{.}96$	300	1540	3600	3200
SC4	54	$03^h55^m46\overset{s}{.}19$	$-42°22'17\overset{''}{.}76$	300	1540	3600	3200
SC5	80	$03^h55^m44\overset{s}{.}67$	$-42°22'02\overset{''}{.}66$	300	1540	3600	3200
SC6	135	$03^h55^m42\overset{s}{.}56$	$-42°21'52\overset{''}{.}66$	300	1540	3600	3200
SC7	149	$03^h55^m44\overset{s}{.}33$	$-42°21'49\overset{''}{.}06$	300	1540	3600	3200
SC8	157	$03^h55^m44\overset{s}{.}41$	$-42°21'35\overset{''}{.}06$	300	1540	3600	3200
SC9	435/436	$03^h55^m47\overset{s}{.}25$	$-42°22'04\overset{''}{.}36$	300	1540	3600	3200

TABLE 5.2: Coordinates and integration times for star clusters observed in NGC 1487. The second column represents the IDs used in Lee and Lee (2005).

values $\epsilon < 0.4$ were deemed as possible star cluster candidates. These constraints are based on properties of star clusters in several merging galaxies (e.g., Whitmore et al. 1999; Goudfrooij et al. 2001a; Rejkuba 2001).

The brightest star cluster candidates catalogued by Lee and Lee (2005) are concentrated in two condensations, both $\sim 3'' \times 3''$ in size, near the centre of NGC 1487 (see Figure 5.1). Generally, star cluster candidates in these regions are separated by $\sim 0.5''$ from each other. This level of crowding is problematic when performing spectroscopy. KMOS IFUs have a spatial coverage of $2.8'' \times 2.8''$, which is comparable in size to either of these concentrated regions. Therefore, to prevent collision between pick-off arms, only one IFU arm can be allocated to any of these regions. This implies that the allocated IFUs will sample multiple star cluster candidates (see Figure 5.3 for example), however not all star cluster candidates in these regions will be observed.

The final star cluster catalogue used for photometry and spectroscopy is listed in Table 5.2. As shown in Figure 5.2, this sample is biased towards the brightest star cluster candidates in NGC 1487. 10 of the 19 star cluster candidates observed using KMOS proved too faint to observe and were not analysed in this survey. Furthermore, star cluster candidates detected using *SExtractor* are generally two magnitudes fainter than the brightest candidates around the centre of NGC 1487. Therefore, star cluster candidates located at galactocentric distances beyond $\sim 1'$ were not observed in this preliminary survey.

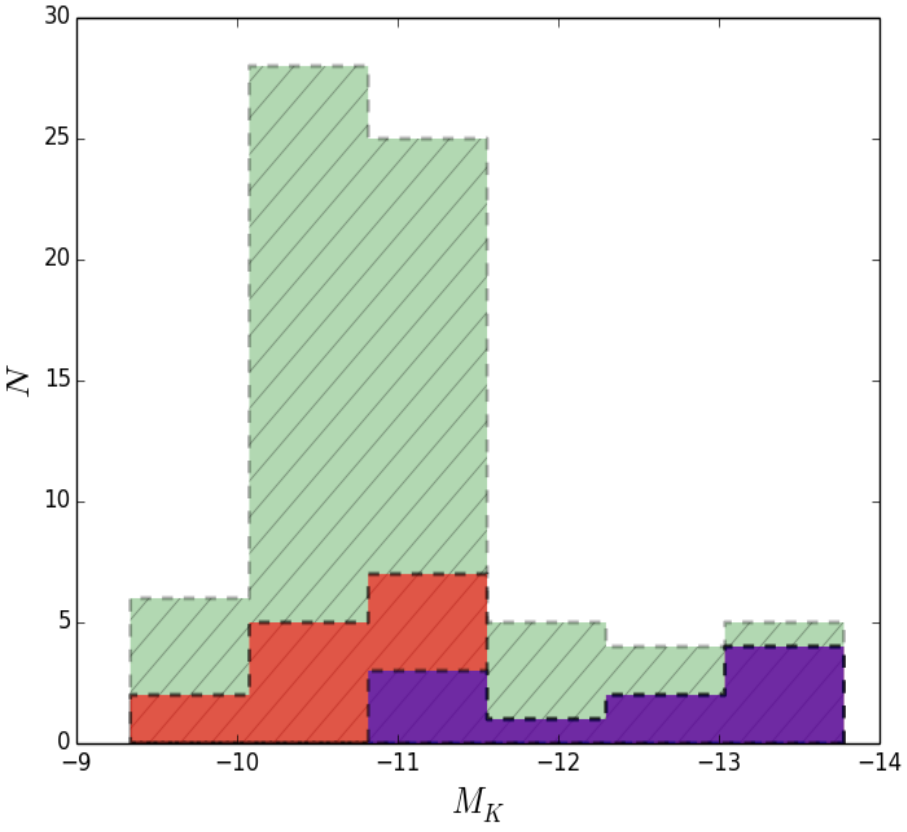

FIGURE 5.2: Luminosity function of star clusters in NGC 1487. The green histogram represents absolute magnitudes from the sample of star cluster candidates catalogued by Lee and Lee (2005) and candidates identified from our survey using *SExtractor*. Apparent magnitudes from these two samples were converted to the K band using spectral model fits from *Starburst99* stellar population synthesis models, assuming solar metallicity with an instantaneous burst and a Kroupa IMF. The red histogram represents star cluster candidates that were selected for spectroscopy from our initial star cluster sample. The purple histogram represents star clusters that showed absorption/emission features in their spectra, and were therefore analysed in this chapter.

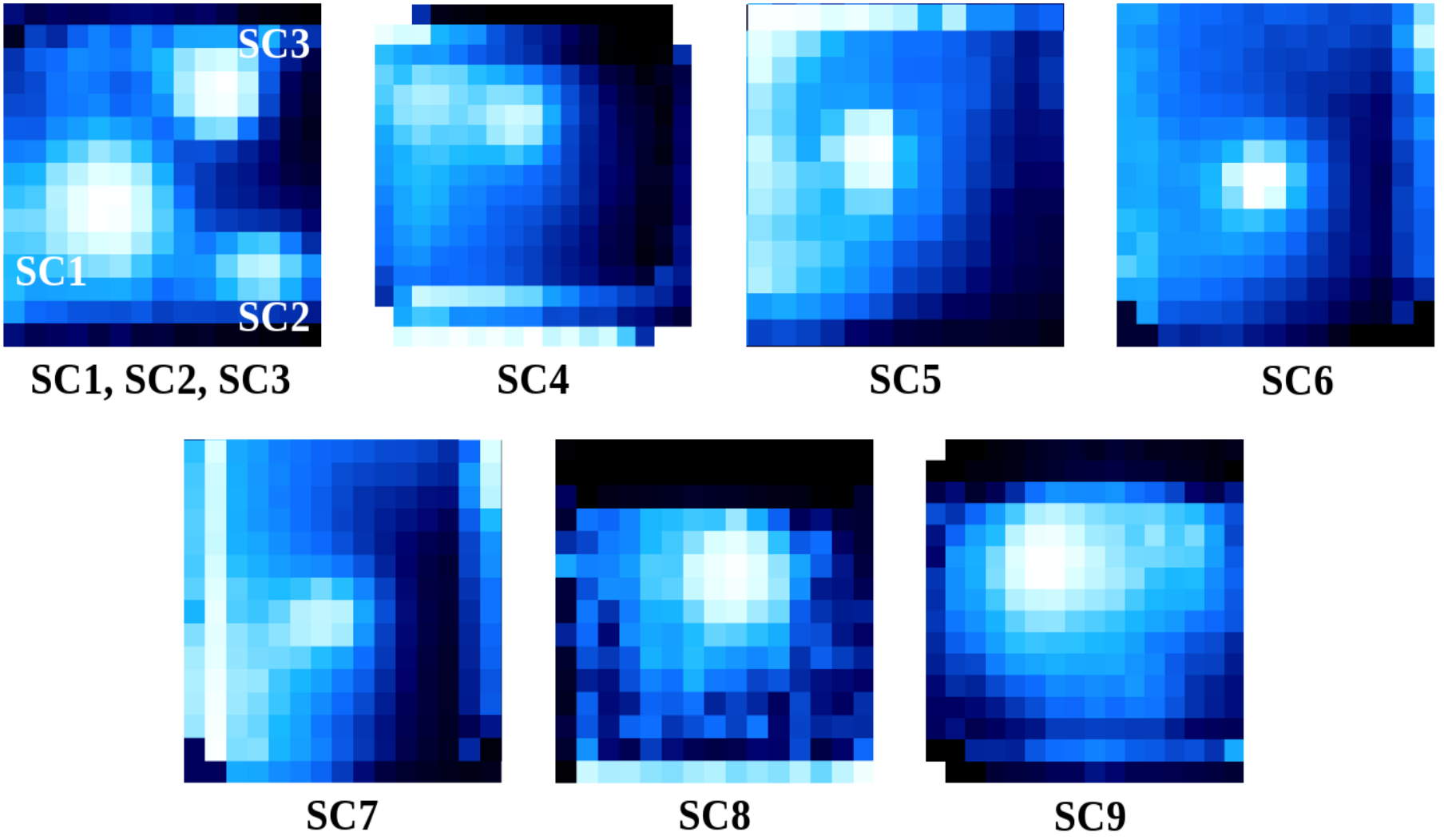

FIGURE 5.3: Collapsed continuum cubes of our star cluster sample. Emission and absorption features were avoided when producing these images using the *kmo_make_image* recipe from the ESO *SPARK* data reduction package (Davies et al., 2013). SC1, SC2 and SC3 were all observed with the same IFU due to their close proximity with each other. Hence, they all appear in a single cube.

5.3 Results

5.3.1 Ages

Star cluster ages in NGC 1487 can be used to trace the star formation activity associated with this galaxy merger. Ages were derived for the star cluster sample in Table 5.2 by comparing observed CO 2-0 bandhead equivalent widths to synthetic equivalent widths from *Starburst99* models (Leitherer et al., 1999) for a variety of ages. The CO 2-0 bandhead is a characteristic feature in the spectra of red supergiants, which first appear in star clusters with ages exceeding $\sim$ 7 Myrs (Davies et al. 2010; Gazak et al. 2013). Stellar population synthesis models show that the strength of the CO 2-0 bandhead peaks around 12 Myrs after the formation of a star cluster, and then gradually declines over the next 100 Myrs (Origlia et al., 1993). However, it is worth noting that CO bandhead equivalent widths can be reduced by non-stellar continuum emission from hot dust. Therefore, the extracted equivalent widths for the CO 2-0 bandheads can be viewed as lower limits.

In addition to the CO 2-0 bandhead, 4 star clusters have Brγ emission lines in their spectra. Figure 5.4 shows typical output spectra from our star cluster sample. Equivalent widths from these observed emission lines were also compared with synthetic equivalent widths from *Starburst99* models to determine ages for these 4 star clusters.

Solar metallicity and a Kroupa IMF were adopted for *Starburst99* models. These parameters have typically been used for other galaxy mergers such as the Antennae galaxies (Larsen 2004b; Christopher 2008). Furthermore, the star formation profile was set to an instantaneous burst of star formation. Star clusters are typically very small (R_{eff} $\sim$ few parsec) and very concentrated, hence star formation is effectively instantaneous across a star cluster (Mengel et al. 2005; Bastian et al. 2009).

Table 5.3 lists the ages determined for our star cluster sample. With the exceptions of SC5 and SC8, the age range of our sample is tightly constrained around $\sim$ 7 Myrs, suggesting the majority of star clusters in our sample formed around the same time. The age distribution of these star clusters around NGC 1487 is shown in Figure 5.5. Excluding SC5 and SC8, there is no significant variance of cluster

Target	Brγ Age (Myrs)	CO 2-0 Age (Myrs)	Mean Age (Myrs)	Mass ($\times 10^6 \mathcal{M}_\odot$)	R_{EFF} (pc)	R_{King} (pc)	ϵ	$cz_{\rm hel}$ kms^{-1}	M_K
SC1	6.0±0.3	9.0±0.8	7.5±0.7	0.6±0.1	1.2±0.4	1.1±0.3	0.8	696±16	-12.8
SC2		9.0±0.8	9.0±0.8	0.7±0.1	2.1±0.2	1.8±0.6	0.8	882±140	-13.1
SC3	6.3±0.4	7.7±1.3	7.0±1.2	1.5±0.5	2.9±0.4	2.8±0.2	0.7	848±44	-13.8
SC4		7.0±1.2	7.0±1.2	0.3±0.1	1.7±0.3	1.7±0.5	0.3	988±38	-11.1
SC5		16.7±8.6	16.7±8.6	0.4±0.1	2.4±0.2	2.1±0.4	0.8	697±99	-12.0
SC6		6.9±1.4	6.9±1.4	0.2±0.1	2.3±0.3	1.9±0.4	0.7	863±147	-10.9
SC7	5.6±0.1	7.5±1.4	6.6±1.2	0.2±0.1	1.6±0.4	1.2±0.3	0.8	693±40	-11.2
SC8		103.4±97.8	103.4±97.8	3.6±2.6	3.8±0.3	3.5±1.0	0.8	964±113	-12.9
SC9	5.7±0.1	7.5±1.5	6.6±1.3	0.7±0.2	5.7±1.0	5.4±0.8	0.9	811±13	-13.1

TABLE 5.3: Ages, masses, and radial velocities calculated for our sample using Brγ and CO 2-0 lines are presented here. The size and ellipticity of each star cluster was determined using the ISHAPE routine in the data reduction package BAOLAB (Larsen, 1999). Magnitudes were taken from Lee and Lee (2005) and Mengel et al. (2008), and assume a distance modulus of $m - M = 30$ and a foreground reddening of $A_K = 0.004$ (Schlafly and Finkbeiner, 2011).

age with location in NGC 1487. Star clusters located in the condensation regions show similar ages to those in less dense regions. Given the large errors of SC5 and SC8, both these clusters may be of similar age to the rest of our sample.

5.3.2 Masses

Derived ages from § 5.3.1 were used in tandem with stellar population synthesis models to estimate the photometric masses of star clusters in our sample. *Starburst99* models were used here. Model parameters were set to an instantaneous burst, Kroupa IMF, solar metallicity and age limit of 500 Myrs. Ages from § 5.3.1 were used to determine the expected K band magnitudes for our star cluster sample. These were then compared to the observed K band magnitudes to determine photometric masses. *Starburst99* models assume a star cluster mass of $\mathcal{M}_{SB99} = 10^6\ \mathcal{M}_\odot$. Photometric masses for our star cluster sample were determined by scaling this model mass to the ratio of the observed and expected K band magnitudes.

The derived masses are listed in Table 5.3, and Figure 5.5 shows how star cluster mass varies across NGC 1487. Unlike the age distribution, there is some correlation of star cluster mass with location in NGC 1487. The most massive star clusters are generally located near the condensation regions. The exception to this is SC5, which has a relatively low mass of $\sim 3 \times 10^5\ \mathcal{M}_\odot$ and is located in condensation C1 (see Figure 5.1). The largest star clusters in our sample are SC3 and SC8, with masses of $\sim 2 \times 10^6\ \mathcal{M}_\odot$ and $\sim 4 \times 10^6\ \mathcal{M}_\odot$ respectively. Unlike SC3, SC8 is located in an isolated region away from any condensation region. From Table

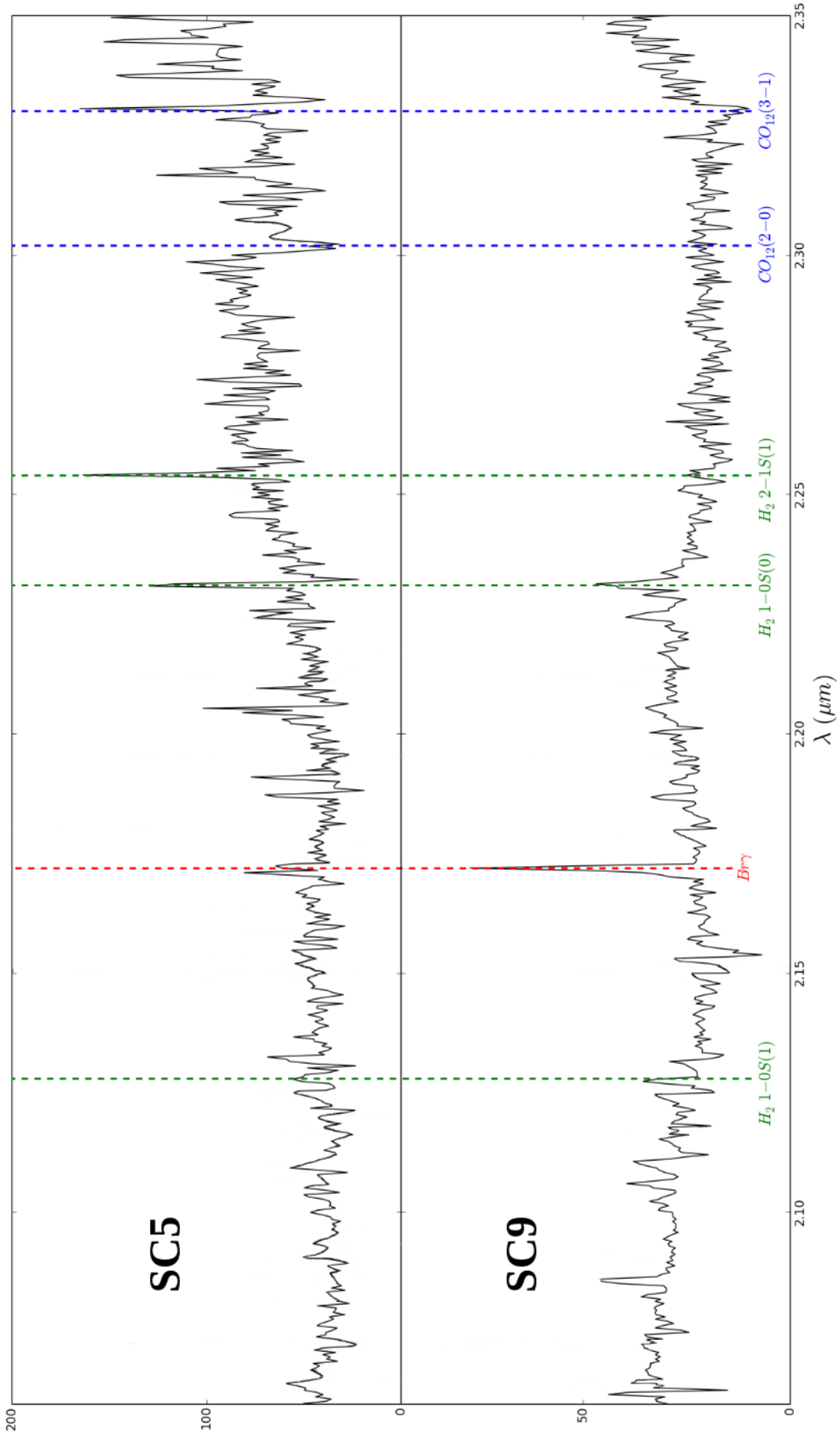

FIGURE 5.4: Typical output spectra from our star cluster sample showing Brγ and CO 2-0 lines. Brγ emission implies an age less than 6 Myrs, and CO bandheads are observed when the first RSGs form in a star cluster, typically around 7 Myrs after the formation of the star cluster (Kornei and McCrady 2009; Gazak et al. 2013). Strong Brγ emission and weak CO 2-0 absorption from SC9 suggests it is younger than SC5 which has no Brγ emission in its spectrum.

5.3 and Figure 5.5, one can see that star clusters evolving in isolated regions tend to have low masses of $\sim 3 \times 10^5$ $\mathcal{M}_\odot$. This suggests that possibly more gas was available to form SC8 than for other isolated star clusters. However, HI or CO observations of NGC 1487 are required to understand the gas distribution around the merger and confirm this hypothesis.

Inspection of the HST frames available suggest that SC2 and SC9 in our sample may be blended sources. Both star clusters are in close proximity to a neighbouring star cluster. SC9 in particular cannot be distinguished into two separate clusters in the WFPC2 frames, but has been suggested in earlier surveys to consist of two separate star clusters in close proximity Lee and Lee (2005). Given the blending effects of these clusters, the ages and masses derived from SC2 and SC9 may represent average values between multiple star clusters.

5.3.3 Radial Velocities

Table 5.3 lists radial velocities for our star cluster sample, corrected for the heliocentric motion of the Earth. These were derived using the CO 2-0 bandhead, which appears in the spectra of all observed star clusters, and Brγ emission lines where available. *SPLAT-VO* (Castro-Neves and Draper, 2014) was used to measure the centre of these features in the spectra of each star cluster. These central values were then compared to the rest frame wavelengths of CO 2-0 and Brγ respectively, to determine radial velocities. The difference between radial velocities measured for a star cluster using both CO 2-0 and Brγ features was typically between 50 - 100 kms^{-1}.

Figure 5.5 shows the radial velocity distribution of these star clusters. Our sample shows no systematic rotation velocity around NGC 1487, in agreement with Aguero and Paolantonio (1997) from their radial velocity measurements. Furthermore, the radial velocity of several star clusters in our sample suggest they may no longer be associated with this merger. The radial velocity of NGC 1487, as listed in Table 5.1, is $\sim$ 711 $\pm$ 15 kms^{-1}(Aguero and Paolantonio, 1997). Several star clusters in our sample have radial velocities that are offset by approximately a hundred kms^{-1}from the mean radial velocity of NGC 1487. Whether these radial velocity offsets are sufficient to escape NGC 1487 or not can be determined by comparing with the escape velocity of NGC 1487. The total mass of NGC 1487 is 2×10^{10} $\mathcal{M}_\odot$ and the size of the merger is R_{hp} $\sim$ 4 kpc (Vorontsov-Vel'Yaminov 1987;

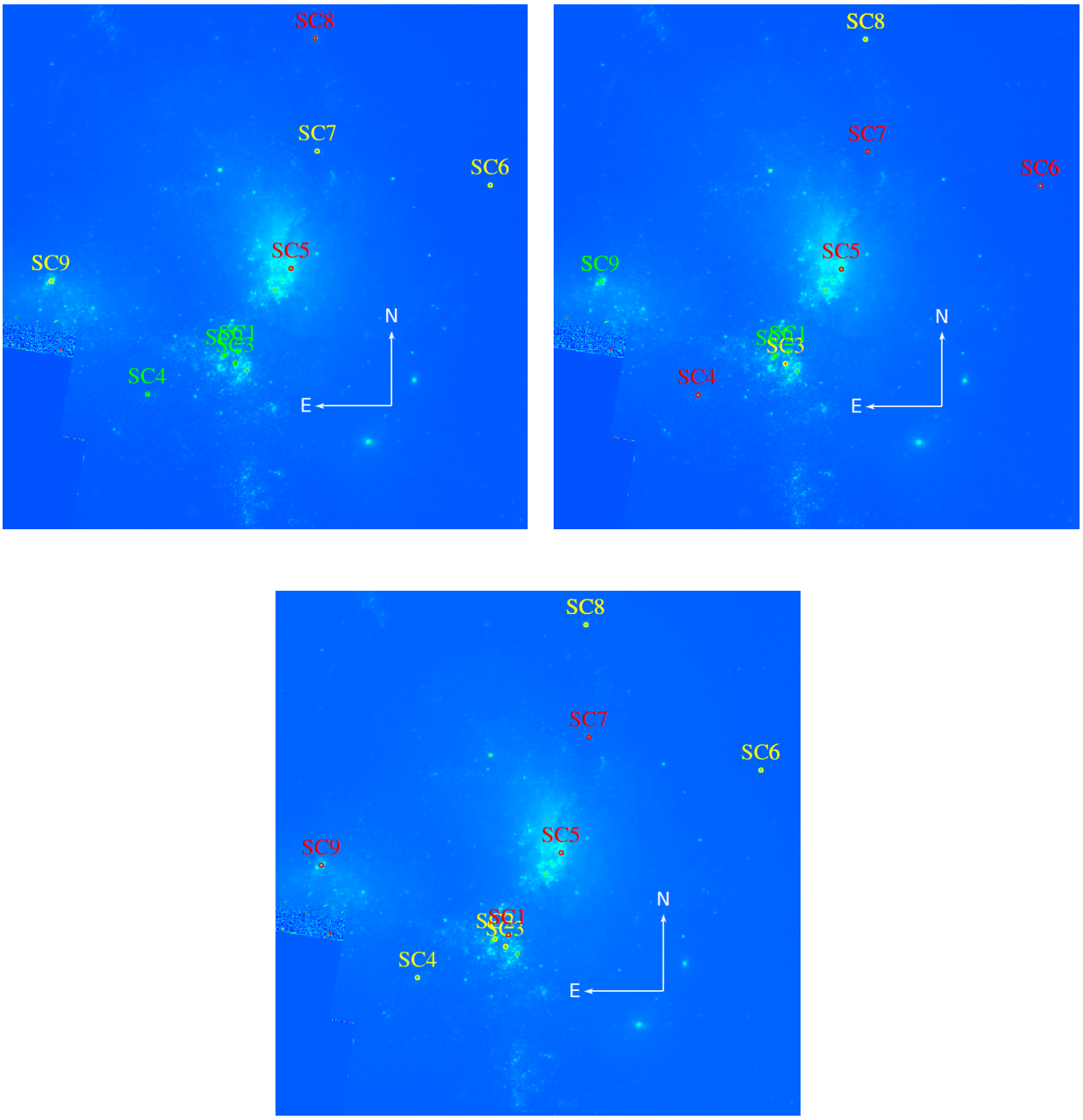

FIGURE 5.5: *Top-Left*: Age distribution of star cluster sample in NGC 1487. Yellow objects have ages less than 7 Myrs, green objects have ages between 7 - 8 Myrs, and red objects have ages exceeding 8 Myrs. *Top-Right*: Mass distribution of the star cluster sample in NGC 1487. Star clusters labelled in red have masses less than $0.5 \times 10^6 \mathcal{M}_\odot$, green star clusters have masses between $0.5 - 1.0 \times 10^6 \mathcal{M}_\odot$, and star clusters labelled in yellow have masses exceeding $1 \times 10^6 \mathcal{M}_\odot$. *Bottom*: Radial velocity distribution of our star cluster sample, corrected for the heliocentric motion of the Earth. NGC 1487 has a measured radial velocity of $\sim 711 \pm 15$ kms^{-1}(Aguero and Paolantonio, 1997). Red represents star clusters with $cz_{\rm hel}<$ 850 kms^{-1}and yellow represents star clusters with $cz_{\rm hel}>$ 850 kms^{-1}.

Aguero and Paolantonio 1997; Micheva et al. 2013). These two parameters give an escape velocity of $\nu_{esc} \sim 200$ kms^{-1}from the centre of NGC 1487. However, the star clusters in our sample are generally located around 0.5′ from the centre. Taking this distance into account gives an escape velocity of $\nu_{esc} \sim 150$ kms^{-1}. Some star clusters, such as SC4 and SC8, have radial velocity offsets that exceed this escape velocity. Therefore, it is possible that some star clusters may no longer be bound to NGC 1487.

5.3.4 Sizes and Ellipticities

Star cluster sizes and ellipticities were measured from the ACS/HRC frame and WFPC2 frames. Given the higher spatial resolution of the ACS/HRC frames, WFPC2 frames were only used for star clusters that were not covered by the ACS/HRC field of view. These parameters were determined using the ISHAPE routine, which is implemented in the data reduction package BAOLAB (Larsen, 1999). ISHAPE convolves a user provided PSF with an analytic elliptical profile for a range of sizes until the best fit between the observed light profile and model profile is obtained. Standard PSF files were generated using the *PSF* task in the *DAOPHOT* package and stellar objects in the ACS/HRC and WFPC2 frames.

Best fits were obtained using both an Elson, Fall, and Freeman (EFF) profile (Elson et al., 1987) and King profile (King, 1962). A power-law index of 2.5 and concentration parameter of 30 were adopted for the EFF profile and King profile, respectively. These parameters were used in earlier surveys of NGC 1487 and for star clusters in other galaxy mergers (Mengel et al. 2008; Bastian et al. 2009), and therefore provide a direct comparison between results.

Derived sizes and ellipticities for our star cluster sample using both profile fits are listed in Table 5.3. Figure 5.6 shows a comparison between sizes obtained for EFF profile fits and King profile fits. These profile fits generally give values consistent with one another, although the King profile tends to provide slightly smaller effective radii than the EFF profile fits. Our sample has a size range of $R_{hp} = 1$ - 6 pc, which is typical for young star clusters (Larsen 2004a; Lee et al. 2005). Star clusters located in the condensation regions are slightly larger (by $\sim$ 1 pc) than those in isolated regions. SC9 is the largest star cluster in our sample, with a size of $R_{hp} \sim 6$ pc. However, this target has been proposed to be two star clusters in close contact by Lee and Lee (2005), which may explain the large

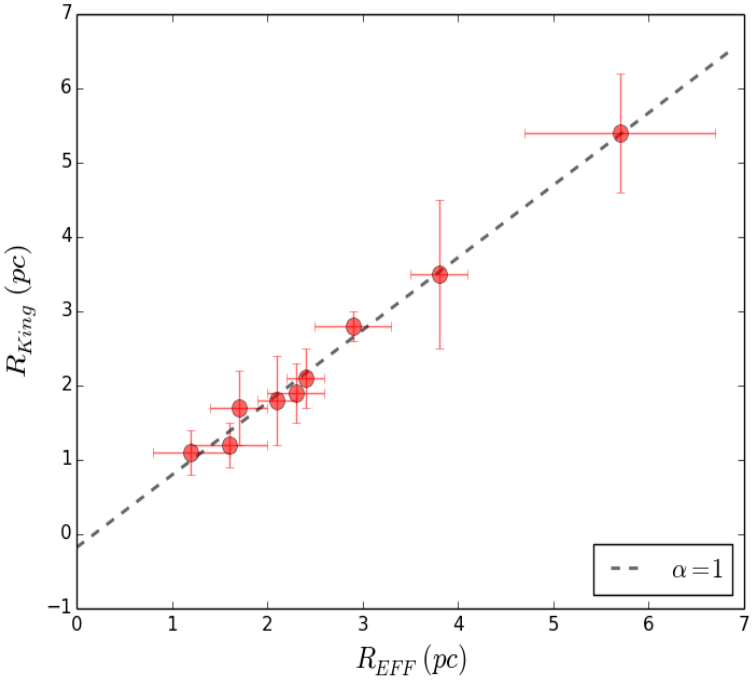

FIGURE 5.6: Comparison between sizes obtained for EFF profile fits and King profile fits for our star cluster sample. Both profiles give similar sizes to each other. Black dashes represent the best fit line to this plot, and has a gradient of $\alpha = 1$.

size of this object. There is no significant difference between the ellipticity of star clusters in condensation regions and isolated regions. Both locations consist of star clusters with ellipticities ranging between $0.7 < \epsilon < 0.8$.

5.4 Discussion

5.4.1 Spatial Distribution around NGC 1487

Ages and masses of our NGC 1487 star cluster sample were determined in § 5.3.1 and § 5.3.2, respectively. These results imply that while most of the star clusters in our sample have an age of ~ 7 Myrs, there is a variation of star cluster mass around NGC 1487, particularly between the condensation regions and isolated regions. Generally star clusters in these condensations are at least twice as massive as those in isolated regions. The larger star cluster masses observed in the condensations is expected due to the abundance of gas available in these regions. Aguero and Paolantonio (1997) note that each condensation has spectral features characteristic

of HII regions, which is likely produced from many of the star cluster candidates observed by Lee and Lee (2005). However, it is surprising that these condensations do not harbour younger populations of star clusters compared to the isolated regions. Given there is an abundant supply of gas available in these condensations to produce star clusters with masses $\sim 10^6 \mathcal{M}_{\odot}$, one would expect a higher star formation rate in these regions compared to isolated regions as observed in other mergers such as the Antennae (Wilson et al. 2000; Zhang et al. 2001; Gilbert and Graham 2007). A higher star formation rate would imply that star clusters in these condensations should be younger than those in regions of lower density if star formation around NGC 1487 is continuous rather than the product of a single burst of star formation. However, in the case of a single burst of star formation throughout NGC 1487, the star formation rate will not affect the age of a star cluster as all star clusters around NGC 1487 would have formed at roughly the same time. The fact that there is no age difference between most star clusters in the condensation and isolated regions implies that a single burst of star formation occurred throughout NGC 1487 around 7 Myrs ago.

Our results also show a range of ages and masses of star clusters in each condensation, particularly when comparing C1 to the other condensations. SC5, the only star cluster observed in condensation C1, is approximately half the mass and twice the age of star clusters in the other condensations. Considering our observations were biased to the brightest star clusters in NGC 1487, SC5 is likely the most massive star cluster in C1 (Elmegreen and Efremov 1997; Larsen 2002). The older age of SC5 compared to star clusters in other condensations may imply that C1 was the first condensation to form. Furthermore, considering that star cluster surveys in the literature often show a correlation between star cluster mass and environmental gas density (Jog and Solomon 1992; Elmegreen and Efremov 1997), the low mass of SC5 suggests that C1 is less dense than the other condensations.

5.4.2 Comparison with Previous Surveys in NGC 1487

The results presented in § 5.3 confirm the presence of star clusters in the three brightest condensation regions as proposed by Aguero and Paolantonio (1997). However, star clusters are not located only in these regions but are spread around NGC 1487. Mengel et al. (2008) made spectral observations in the K band of two star clusters in our sample, SC2 and SC3. Both surveys detect CO 2-0 bandheads

	Our Survey				Mengel et al. (2008)			
Target	Age (Myrs)	$M_{phot}(10^6\mathcal{M}_\odot)$	R_{hp} (pc)	ϵ	Age (Myrs)	$M_{dyn}(10^6\mathcal{M}_\odot)$	R_{hp} (pc)	ϵ
SC2	9.0±0.8	0.7±0.1	2.0±0.2	0.8	8.5±0.5	0.6±0.2	2.1±0.2	0.8
SC3	7.0±1.2	1.5±0.5	2.9±0.5	0.7	8.4±0.5	1.2±0.6	2.8±0.5	0.8

TABLE 5.4: Comparison between star cluster properties determined in our survey and Mengel et al. (2008). SC2 and SC3 were observed in both surveys. Ages, masses, sizes and ellipticities obtained from both surveys are in agreement with each other.

in the spectra of these star clusters. The derived ages and masses for these star clusters from both surveys are in agreement with one another (see Table 5.4). Similarly, the observed sizes for these star clusters from both surveys are in agreement with each other.

5.4.3 Star Cluster SC8

A star cluster that has been neglected thus far, but is particularly interesting, is SC8. This object is comfortably the most massive star cluster in our sample, with a mass $\sim 4 \times 10^6 \mathcal{M}_\odot$. Given our selection bias of observing the brightest star clusters in NGC 1487 and the luminosity-mass relation, SC8 is possibly the most massive star cluster in NGC 1487. It is also the largest star cluster in our sample, with a size of $R_{hp} \sim 4$ pc. The age of this star cluster suggests it has survived the early violent periods of star cluster evolution and may evolve to become a globular cluster (Portegies Zwart et al. 2010; Longmore et al. 2014). Furthermore, it is likely that SC8 formed as a result tidal interactions from the galaxy merger, as its age is less than the 500 Myr age of NGC 1487 (Lee and Lee, 2005). The large mass of SC8 along with its relatively isolated location in NGC 1487 increase the probability of this star cluster remaining bound as it evolves (Lada and Lada 2003; Kruijssen et al. 2012). Given that this target has a radial velocity offset exceeding the escape velocity of NGC 1487, SC8 may no longer be bound to the merger.

SC8 is comparable in mass to the brightest star clusters in the Antennae (Gilbert and Graham 2007; Christopher 2008). The Antennae hosts $\sim$ 8000 star clusters, the brightest of which have masses between $10^6 - 10^7 \mathcal{M}_\odot$. However, these star clusters are also quite young ($<$ 10 Myrs) and it is unclear whether they will remain bound as they evolve. Given the larger error in its age, SC8 may be a young ($<$ 10 Myrs) star cluster or a star cluster in a more advanced stage of evolution. Regardless, its relatively isolated location and large mass increase the likelihood

of SC8 remaining bound, and therefore an interesting target for observing and understanding the evolution of young massive star clusters into old (several Gyr) globular clusters.

5.4.4 Comparison with other Galaxy Mergers

The merger between the two late-type spiral galaxies in NGC 1487 is thought to have taken place $\sim$ 500 Myrs ago, and the system is therefore in an early stage of evolution (Aguero and Paolantonio, 1997). The Antennae and NGC 3256 are galaxy mergers of similar age to NGC 1487 and host well over 1000 star clusters each that can be compared to star clusters around NGC 1487 (Whitmore et al. 1999; Trancho et al. 2007b). Our star cluster sample has masses comparable to star clusters found in both the Antennae and NGC 3256, which range between $10^5 - 10^7 \mathcal{M}_\odot$ (Gilbert and Graham 2007; Trancho et al. 2007a). However, the sizes of star clusters observed in NGC 1487 are smaller than those of the same luminosity in either NGC 3256 or the Antennae, which typically show sizes of $R_{hp} \sim 7$ pc (Zepf et al. 1999; Bastian et al. 2009). Furthermore, NGC 3256 and the Antennae host star clusters that are up to three orders of magnitude brighter than those found in NGC 1487 (Zepf et al. 1999; Christopher 2008). The smaller sizes and fainter magnitudes of star clusters in NGC 1487 suggests there is less gas available to produce star clusters here than in the Antennae and NGC 3256. This implies that the proposed late-type spiral progenitors of NGC 1487 may have had a lower gas content than NGC 3256 and the Antennae.

Further evidence for the lower abundance of gas in NGC 1487 compared to the other two mergers can be seen from a comparison between the masses of star clusters in all three galaxy mergers. The majority of star clusters in our NGC 1487 sample have an age $\sim$ 7 Myrs and mass $\sim 10^5$ $\mathcal{M}_\odot$. However, star clusters of the same age in both the Antennae galaxies and NGC 3256 have masses of the order of $\sim 10^6$ $\mathcal{M}_\odot$ (Trancho et al. 2007a; Christopher 2008). The difference in observed cluster mass may be due to a low star formation rate in NGC 1487 compared to the Antennae galaxies and NGC 3256. This lower star formation rate may likely result from a low gas content in NGC 1487. This star formation rate is expected to increase as NGC 1487 evolves (Cox et al. 2006; Hopkins et al. 2009). Therefore, NGC 1487 may produce more massive star clusters as it completes the merging process. However, if NGC 1487 does indeed have a lower gas content than

NGC 3256 or the Antennae, it is unlikely to produce more massive star clusters than either of these two mergers.

5.5 Conclusion

Star clusters in the galaxy merger NGC 1487 have been studied using a near-infrared spectral survey from KMOS and a photometric survey with HST/ACS. A total of 9 star clusters were observed and analysed in our investigation.

- The age distribution of star clusters around NGC 1487 is fairly uniform and suggests an instantaneous burst of star formation occurred in the past 10 Myrs. Masses derived for our sample are comparable to masses of star clusters in other major mergers of similar age, and also show a correlation with the densest regions of NGC 1487, such that the most massive star clusters are located in the densest regions. This is typically what is observed in other galaxy mergers, such as the Antennae, and is further evidence that the most massive star clusters form in dense, highly pressurised environments (Jog and Solomon 1992; Elmegreen and Efremov 1997).

- Radial velocity measurements suggest that most of the star clusters in our sample are likely bound to NGC 1487. However, some star clusters such as SC4 and SC8 have velocities exceeding the escape velocity of NGC 1487. Therefore these star clusters may no longer be bound to this merger, suggesting that NGC 1487 may have insufficient mass to retain star clusters produced after merging commenced. However, this scenario is uncertain given the large errors of our radial velocity measurements. Our star cluster sample shows no systematic circular motion consistent with either disk of the proposed spiral progenitors. It is unclear whether star clusters at larger radii from the galactic centre are forming the halo population of NGC 1487, as is currently occurring in other mergers such as the Antennae and NGC 3256 (see Chapter 4).

- Star cluster SC8 is a particularly interesting target for further investigation. Its age suggests that it may have been one of the earliest star clusters to form as a result of the galaxy merger and may have survived the early chaotic period of star cluster evolution. It is also one of the largest and brightest

star clusters in NGC 1487 and therefore easily identifiable. This star cluster can be studied in more detail and compared to other star clusters of similar ages, such as those in NGC 7252, to better understand how star clusters produced from tidal interactions in merging galaxies may evolve to several Gyr-old globular clusters.

- The star clusters in our sample generally have a median size of $R_{hp} \sim 2$ pc, while those in NGC 3256 and the Antennae have sizes ~ 7 pc. The larger star cluster sizes in the latter galaxy mergers compared to those in NGC 1487 may be due to a greater abundance of gas in NGC 3256 and the Antennae. An abundant gas supply has likely fuelled the formation of larger star clusters in NGC 3256 and the Antennae than those observed in NGC 1487. This may be indicative of a more general correlation between star cluster size and the abundance of gas to fuel star formation. Further surveys of the gas content and distribution around NGC 1487 and other galaxy mergers of varying size are required to verify this theory.

Chapter 6

Conclusion

6.1 Summary of Surveys

In this thesis we have analysed star clusters formed in galaxy mergers for a range of evolutionary states using both photometric and spectroscopic observations. In Chapter 2 and Chapter 3 we use HST photometric observations to analyse star cluster candidates in HCG 90 and NGC 5128. We identified star cluster candidates that are a few hundred Myrs old and have likely survived the early chaotic periods of star cluster formation (Lada and Lada 2003; Kruijssen 2012). If these candidates are indeed star clusters, they are likely to remain bound and evolve into Gyr-old globular clusters. Furthermore, star cluster candidates younger than 10 Myrs were identified in both HCG 90 and NGC 5128. This suggests that a burst of star formation has recently occurred in both systems. Whether these star cluster candidates remain bound as they evolve is unclear as they are still in the 'infant mortality' stage of star cluster evolution. We find a deficit in the cluster population of HCG 90 and attribute this to stripping of star clusters from their host galaxies due to ongoing tidal interactions. We observe no deficit in the cluster population of NGC 5128. Neither observation shows agreement with galaxy merger simulations by Kruijssen et al. (2012) which suggest tidal interactions in galaxy mergers destroy more star clusters than they form.

In Chapter 4 and Chapter 5 we use near-infrared spectroscopic observations from the recently commissioned KMOS instrument on board the VLT to analyse star clusters around the Antennae and NGC 1487. Both systems are major mergers

between two spiral galaxies. Nearly all star clusters observed in either galaxy merger are less than 10 Myrs old, with some star clusters having ages less than 5 Myrs. Unlike the majority of star cluster candidates discussed in Chapter 2 and Chapter 3 , our sample of star clusters in the Antennae and NGC 1487 have not evolved past the turbulent 'infant mortality' stage of star cluster evolution, hence it is unclear if they will remain bound as they evolve. Furthermore, the young ages of these star clusters suggest that both the Antennae and NGC 1487 have had a relatively recent burst of star formation.

The following sections will discuss the major findings from these observations and their implications. This chapter will then conclude with suggestions for possible future work that may lead on from the studies presented in this thesis.

6.2 Cluster Formation *vs* Destruction in Galaxy Mergers

In Chapter 2 and Chapter 3 we observed the cluster population around NGC 7174/76 and NGC 5128, and compared them to calculated values of the expected cluster population for both systems. We estimate a deficit in the number of clusters observed in NGC 7174/76 compared to what is expected, based on cluster specific frequency values. The lower cluster population observed in NGC 7174/76 could be due to the tidal interactions occurring around the merger. Kruijssen et al. (2012) suggest that tidal interactions around galaxy mergers may disrupt more star clusters than they produce. Their simulations show that the dynamical heating of star clusters by tidal shocks, which are about an order of magnitude stronger in merging galaxies than in isolated galaxies, is sufficient to destroy star clusters at a higher rate than new clusters are being formed. This could explain the low cluster population in NGC 7174/76. However, there is an alternative and simpler scenario to explain the observed cluster population. A bright diffuse intragroup light is apparent around HCG 90, which is likely the product of tidal stripping from the extended halos of the central three interacting galaxies (White et al., 2003). Given that globular clusters have spatially extended distributions around these galaxy types (Brodie and Strader, 2006), it is possible that many globular clusters were also stripped from their parent galaxies to form the intragroup light. This would then result in parent galaxies with a low cluster population, as is observed

for NGC 7174/76, and an intragroup light with a high cluster population. Based on the specific frequency of the intragroup light, this scenario provides a more likely explanation for the low cluster population in NGC 7174/76 than the cluster disruption scenario. Moreover, our observations of the cluster population in NGC 5128 are in disagreement with the Kruijssen et al. (2012) merger simulations. We find no deficit in the observed cluster population at the centre of NGC 5128, suggesting that tidal interactions have not destroyed more clusters than produced.

However, the simulations by Kruijssen et al. (2012) model major mergers between gas-rich spiral galaxies, similar to the Antennae. Both NGC 7174/76 and NGC 5128 consist of tidal interactions between a spiral and elliptical galaxy. Furthermore, NGC 5128 is only a minor merger. Gas-rich spiral-spiral collisions like the Antennae or NGC 3256 are likely to have stronger tidal interactions than observed in NGC 7174/76 and NGC 5128. Therefore, perhaps tidal interactions are more disruptive in gas-rich major mergers and produce a lower cluster population than expected. Observations of the entire cluster population in a major merger between two gas-rich spiral galaxies are required to determine if this is indeed the case.

6.3 Star Clusters Forming the Merger Halo

From their spectral observations of the Antennae, Bastian et al. (2009) observed three star clusters that have radial velocities significantly offset from disk rotation of either progenitor spiral. They determined this difference by comparing radial velocities of star clusters with HI velocities in the same location. These HI radial velocities map the rotation of the progenitor spirals in the Antennae. The velocity offsets of these three star clusters suggests that they may be forming the halo cluster population of the Antennae. These three star clusters are typically a few hundred Myrs old, and were probably formed after the first pericentre passage between the two progenitor galaxies. In Chapter 4 we compared radial velocities from our Antennae star cluster sample to HI velocities to determine if they were still associated with either of the progenitor disks. Our sample of Antennae star clusters are a few Myrs old. We determined that our cluster sample is likely still associated with the disks of the progenitor galaxies. Our results, combined with Bastian et al. (2009), suggest that the Antennae star clusters are experiencing an evolutionary process whereby they are initially located in gas-rich environments such as the progenitor disks and then gradually evolve away from the disks to form

the halo cluster population of the merger (assuming these clusters remain bound). This is expected if young massive star clusters do indeed evolve into old globular clusters.

This is observed in older merger remnants like NGC 3921 (Schweizer et al., 2004) and NGC 7252 (Schweizer and Seitzer, 1998) where star clusters formed from these galaxy mergers have orbits dominated by random motion rather than disk rotation. Unlike the Antennae, NGC 3921 and NGC 7252 have likely evolved enough to fully disrupt their progenitor disks and merge the progenitor nuclei. Therefore, given that there is no longer a disk for star clusters to orbit, it is natural for star clusters to acquire random orbital motions around these merger remnants. In the case of the Antennae however, the progenitor disks are still relatively intact. The fact that some star clusters are showing 'halo kinematics' in the Antennae suggests that the halo cluster population of a merger remnant may begin to form before the progenitor nuclei coalesce. It is unclear if star clusters in NGC 1487 are also populating the halo. Clusters SC4 and SC8 from our NGC 1487 sample have radial velocities exceeding the escape velocity of NGC 1487. However, velocity maps of the gas around NGC 1487 are required to determine if our sample of star clusters are associated with either progenitor disk. Nevertheless, further surveys of star clusters with ages closer to the time of the last pericentre passage of their host merger are required to determine how and when star clusters begin forming the halo cluster population of their host merger remnant.

6.4 Correlation between Cluster Size and Gas Abundance

In Chapter 3 and Chapter 5 we observed star cluster sizes (r_{eff}) that are smaller than those observed in other mergers but comparable to sizes observed for GCs in the Galaxy. Star clusters that likely formed from tidal interactions in NGC 5128 and NGC 1487 have an average size of $r_{eff} \sim 3$ pc in both systems. This is similar to the median 3 pc size observed for GCs in the Milky Way (Djorgovski, 1993). However, mergers like NGC 3921 and NGC 7252 have considerably larger clusters with sizes between 5 - 7 pc (Schweizer et al. 1996; Bastian et al. 2013c). Also, clusters in the Antennae have an average size of $r_{eff} \sim 6$ pc (Mengel et al. 2008; Bastian et al. 2009). Given that the clusters observed in NGC 5128 have similar

ages to those in NGC 3921 and NGC 7252, it is unlikely that the difference in size is related to age. Clusters observed in NGC 1487 and the Antennae also have similar ages but different effective radii. Moreover, we find no correlation between cluster mass and cluster size. Both the Antennae and NGC 1487 have different average cluster sizes for a given mass. In Chapter 3 and Chapter 5 we concluded the smaller observed cluster sizes in these mergers compared to other mergers was due to a difference in gas abundance. However, while the gas mass of NGC 1487 is unknown, NGC 5128, NGC 7252 and the Antennae each have gas masses around 10^9 $\mathcal{M}_\odot$ (Israel 1998; Hibbard et al. 1994; Wilson et al. 2000). This suggests that gas abundance is unlikely to be responsible for the varying cluster size between these mergers. Murray (2009) extensively studied young star cluster sizes for a range of masses. They find no correlation between cluster size and mass between $10^4 - 10^6$ $\mathcal{M}_\odot$. However, they do find an increase in cluster size with mass for star clusters with masses $\geq 10^6$ $\mathcal{M}_\odot$. They contribute this to a balance between accretion powered radiation pressure and gravity when the clusters formed, and determine a mass-radius relation of $r_{cl} \sim M_{cl}^{3/5}$. Bastian et al. (2013c) also find evidence supporting a mass-radius relation for clusters $\geq 10^6$ $\mathcal{M}_\odot$ in their NGC 7252 sample. Nevertheless, studies of young star clusters with masses between $10^4 - 10^6$ $\mathcal{M}_\odot$ are required to understand why no mass-radius relation is observed for these masses.

6.5 Clusters Forming within Clusters

Several star clusters in our Antennae sample have spectral features consistent with the presence of both OB stars and RSG stars. OB stars evolve rapidly and are typically present in star clusters less than ~ 6 Myrs old. RSGs begin to dominate the near-infrared spectra of star clusters older than ~ 7 Myrs. The fact that both stellar types are observed in several Antennae clusters suggests two possibilities: (1) these clusters exhibit multiple episodes of star formation, as suggested for many Galactic GCs; (2) these clusters have formed from the merger of at least two star clusters, both of which have different ages to each other.

Multiple bursts of star formation in young (< 1 Gyr) massive star clusters has been suggested as an explanation for chemical abundance variations observed within Galactic GCs. A number of theories have been proposed to explain the chemical

and photometric anomalies observed in Galactic GCs, albeit under the assumption of sufficiently high masses ($> 10^6$ $\mathcal{M}_\odot$) for the clusters after formation (e.g., Decressin et al. 2007; D'Ercole et al. 2008; de Mink et al. 2009). These theories predict that a second epoch of star formation should occur within a cluster between 5 - 500 Myrs after the first generation forms. Therefore, the spectra of star clusters younger than 500 Myrs should have a combination of features expected from both young and old stellar populations. However, Bastian et al. (2013a) find no evidence of ongoing star formation in their cluster sample. They observed spectra and colour-magnitude diagrams of 130 Galactic and extragalactic young (10 - 1000 Myrs) massive clusters and rule out the possibility of ongoing star formation lasting hundreds of Myrs within a cluster, and state that a near instantaneous formation of a secondary population within an existing first generation is unlikely. Nevertheless, our Antennae cluster sample does agree with some predictions from multiple population models, as they have masses exceeding 10^6 $\mathcal{M}_\odot$ and consist of at least two stellar age groups. However, the time between the first and second generation of stars in these clusters is $\sim$ 1 Myr which is much shorter than the 5 Myr lower limit time period predicted by these models.

An alternative theory to explain the stellar population observed in our Antennae clusters is the merging between two star clusters of different ages. Binary star clusters have been observed in the Antennae (Peacock et al., 2013) and NGC 3256 (Bastian et al., 2013a). Cluster S1 from our Antennae sample was studied in detail at optical wavelengths by Peacock et al. (2013). From their GMOS spectra, Peacock et al. (2013) determined that S1 harbours two stellar populations with ages of 8 Myrs and 80 Myrs, respectively. However, upon closer inspection with high resolution HST images, they determined S1 is composed of an 80 Myr old cluster and a nearby HII region which is 8 Myrs old. These sources were simply indistinguishable in the GMOS spectra. Furthermore, Peacock et al. (2013) suggest that the small velocity difference between the two sources implies they will coalesce in the near future. This coalescence could produce a cluster with multiple stellar populations similar to Galactic GCs. Cluster T661 (Trancho et al., 2007a) in the ongoing galactic merger NGC 3256 shows a similar spectrum at optical wavelengths to S1 and may also be a binary cluster (Bastian et al., 2013a). Given the locations (southern overlap region) and unusual morphologies of the Antennae star clusters in our sample that show multiple stellar populations, it is likely they are the product of binary star clusters. High resolution images in the near-infrared are desirable to determine whether these clusters can be separated into

more clusters, as optical HST images suffer from high extinction in these regions.

6.6 Future Work

The discovery of young massive star clusters in galaxy mergers as well as quiescent galaxies over the last few dacades has led to the conclusion that a significant fraction of star formation in the local universe occurs in clustered environments. Therefore, studying the formation and evolution of star clusters, including the dynamical processes they encounter, is of critical importance in both stellar and galactic astrophysics. Observing star clusters during the first few hundred Myrs of their lifetime is vital in understanding why the vast majority of star clusters disperse in the early stages of their evolution, and what conditions are required for young star clusters to evolve into bound Gyr-old globular clusters. Merging and interacting systems often host large numbers of recently formed star clusters and are ideal targets to study and understand the properties of massive star clusters. In this thesis, we observed four merging systems at various evolutionary states and attempted to contribute more knowledge on the formation and evolution of star clusters in merging galaxies. Having drawn conclusions from each of these surveys we list here future work that can be performed in these merging systems as well as other galaxy mergers that may help better understand the formation and evolution of star clusters.

- Entire star cluster populations in gas-rich galaxy mergers must be investigated to determine if tidal shocks during galaxy mergers destroy more star clusters than they produce. Simulations by Kruijssen et al. (2012) suggest this is the case. However, observations of spiral and elliptical mergers in this thesis disagree with their simulations. Further surveys of the total cluster populations in other galaxy mergers are required to determine if simulations by Kruijssen et al. (2012) provide an accurate representation of star formation in merging galaxies.

- One conclusion drawn from our spectral survey of star clusters in the Antennae is that some star clusters may be the product of merging between multiple clusters. Several young star clusters in other galaxy mergers agree with this scenario. Other star clusters in the Antennae, such as star cluster #79 from Christopher (2008) (knot S in Whitmore et al. 2010) may shed

more light on this topic. Star cluster #79 has an unusually large size and morphology compared to other star clusters in the Antennae and may well be a complex of clusters. Moreover, it is located in a region of relatively low extinction compared to other regions around the Antennae, and can be observed at optical wavelengths as well as in the near-infrared.

- Future surveys of galaxy mergers should study the radii of star clusters with masses between $10^4 - 10^6$ $\mathcal{M}_\odot$. Murray (2009) and Bastian et al. (2013c) find a mass-radius relation for clusters exceeding 1×10^6 $\mathcal{M}_\odot$. Remarkably, no mass-radius relation is observed for clusters less than 10^6 $\mathcal{M}_\odot$. Given that most star clusters observed in galaxy mergers have masses between $10^4 - 10^6$ $\mathcal{M}_\odot$, it is vital to understand why no relation is observed for these masses.

- We recommend observations of star clusters with ages closer to the time of the last pericentre passage of their host merger. Radial velocity measurements of star clusters in the Antennae suggest that some star clusters may be forming the halo cluster population of the galaxy merger (Bastian et al., 2009). This may also be the case for some star clusters in NGC 1487, which is of similar age to the Antennae. Observations of NGC 3256, a merger of similar age to the Antennae and NGC 1487, also show some star clusters no longer associated with the disks of either galaxy involved in the merger remnant. Moreover, most star clusters in older galaxy mergers like NGC 3921 (Schweizer et al., 2004) and NGC 7252 (Schweizer and Seitzer, 1998), have no orbital motion associated with disk rotation. Therefore, it is clear that star clusters formed from a galaxy merger begin to form the halo cluster population of a merger as it evolves. Understanding how and when this occurs may require observations of star clusters formed around the last pericentre passage of their host merger. Depending on the age of the merger, some of these star clusters may have evolved off the disks of either parent galaxy, as seen for some star clusters in the Antennae and NGC 3256.

Bibliography

Aarseth, S. J. and Heggie, D. C. Basic N-body modelling of the evolution of globular clusters - I. Time scaling. *MNRAS*, 297:794–806, July 1998. doi: 10.1046/j.1365-8711.1998.01521.x.

Agüero, E. L. A List of Interesting Southern Galaxies. *P.A.S.P.*, 83:310, June 1971. doi: 10.1086/129127.

Aguero, E. L. and Paolantonio, S. The Peculiar Galaxy NGC 1487. *AJ*, 114:102, July 1997. doi: 10.1086/118456.

Akiyama, K. Time variation of ellipticity of globular clusters in the Large Magellanic Cloud. *Earth Moon and Planets*, 54:203–239, September 1991. doi: 10.1007/BF00056321.

Allam, S.; Assendorp, R.; Longo, G.; Braun, M., and Richter, G. Far infrared properties of Hickson compact groups of galaxies. I. High resolution IRAS maps and fluxes. *AAPS*, 117:39–82, May 1996.

Alonso-Herrero, A.; Rieke, G. H.; Rieke, M. J., and Kelly, D. M. The [Fe II] 1.644 Micron Emission in M82 and NGC 253: Is It a Measure of the Supernova Rate? *AJ*, 125:1210–1225, March 2003. doi: 10.1086/367790.

Arimoto, N. and Yoshii, Y. Chemical and photometric properties of a galactic wind model for elliptical galaxies. *AAP*, 173:23–38, February 1987.

Armand, C.; Baluteau, J.-P.; Joubert, M.; Gry, C., and Cox, P. The near-infrared spectrum of ultracompact HII regions. *AAP*, 306:593, February 1996.

Ashman, K. M. and Zepf, S. E. The formation of globular clusters in merging and interacting galaxies. *ApJ*, 384:50–61, January 1992. doi: 10.1086/170850.

Ashman, K. M. and Zepf, S. E. Some Constraints on the Formation of Globular Clusters. *AJ*, 122:1888–1895, October 2001. doi: 10.1086/323133.

Baldwin, J. A.; Ferland, G. J.; Korista, K. T.; Hamann, F., and LaCluyzé, A. The Origin of Fe II Emission in Active Galactic Nuclei. *ApJ*, 615:610–624, November 2004. doi: 10.1086/424683.

Barkhouse, W. A.; West, M. J., and Bothun, G. D. Globular Cluster Population of Hickson Compact Group 22a and 90c. *ApJ*, 562:679–688, December 2001. doi: 10.1086/323771.

Barnes, J. E. Encounters of disk/halo galaxies. *ApJ*, 331:699–717, August 1988. doi: 10.1086/166593.

Barnes, J. E. and Hernquist, L. Dynamics of interacting galaxies. *ARA&A*, 30: 705–742, 1992. doi: 10.1146/annurev.aa.30.090192.003421.

Bastian, N. On the star formation rate - brightest cluster relation: estimating the peak star formation rate in post-merger galaxies. *MNRAS*, 390:759–768, October 2008. doi: 10.1111/j.1365-2966.2008.13775.x.

Bastian, N.; Emsellem, E.; Kissler-Patig, M., and Maraston, C. Young star cluster complexes in NGC 4038/39. Integral field spectroscopy using VIMOS-VLT. *AAP*, 445:471–483, January 2006. doi: 10.1051/0004-6361:20053793.

Bastian, N.; Gieles, M.; Goodwin, S. P.; Trancho, G.; Smith, L. J.; Konstantopoulos, I., and Efremov, Y. The early expansion of cluster cores. *MNRAS*, 389: 223–230, September 2008. doi: 10.1111/j.1365-2966.2008.13547.x.

Bastian, N.; Trancho, G.; Konstantopoulos, I. S., and Miller, B. W. Gemini Spectroscopic Survey of Young Star Clusters in Merging/Interacting Galaxies. III. The Antennae. *ApJ*, 701:607–619, August 2009. doi: 10.1088/0004-637X/701/1/607.

Bastian, N.; Adamo, A.; Gieles, M.; Silva-Villa, E.; Lamers, H. J. G. L. M.; Larsen, S. S.; Smith, L. J.; Konstantopoulos, I. S., and Zackrisson, E. Stellar clusters in M83: formation, evolution, disruption and the influence of the environment. *MNRAS*, 419:2606–2622, January 2012. doi: 10.1111/j.1365-2966.2011.19909.x.

Bastian, N.; Cabrera-Ziri, I.; Davies, B., and Larsen, S. S. Constraining globular cluster formation through studies of young massive clusters - I. A lack of ongoing

star formation within young clusters. *MNRAS*, 436:2852–2863, December 2013a. doi: 10.1093/mnras/stt1779.

Bastian, N.; Lamers, H. J. G. L. M.; de Mink, S. E.; Longmore, S. N.; Goodwin, S. P., and Gieles, M. Early disc accretion as the origin of abundance anomalies in globular clusters. *MNRAS*, 436:2398–2411, December 2013b. doi: 10.1093/mnras/stt1745.

Bastian, N.; Schweizer, F.; Goudfrooij, P.; Larsen, S. S., and Kissler-Patig, M. Luminosity profiles and sizes of massive star clusters in NGC 7252. *MNRAS*, 431:1252–1263, May 2013c. doi: 10.1093/mnras/stt253.

Bergemann, M.; Kudritzki, R.-P.; Plez, B.; Davies, B.; Lind, K., and Gazak, Z. Red Supergiant Stars as Cosmic Abundance Probes: NLTE Effects in J-band Iron and Titanium Lines. *ApJ*, 751:156, June 2012. doi: 10.1088/0004-637X/751/2/156.

Bergemann, M.; Kudritzki, R.-P.; Würl, M.; Plez, B.; Davies, B., and Gazak, Z. Red Supergiant Stars as Cosmic Abundance Probes. II. NLTE Effects in J-band Silicon Lines. *ApJ*, 764:115, February 2013. doi: 10.1088/0004-637X/764/2/115.

Bertin, E. and Arnouts, S. SExtractor: Software for source extraction. *AAPS*, 117:393–404, June 1996.

Bik, A.; Lamers, H. J. G. L. M.; Bastian, N.; Panagia, N., and Romaniello, M. Clusters in the inner spiral arms of M 51: The cluster IMF and the formation history. *AAP*, 397:473–486, January 2003. doi: 10.1051/0004-6361:20021384.

Blaauw, A. The O Associations in the Solar Neighborhood. *ARA&A*, 2:213, 1964. doi: 10.1146/annurev.aa.02.090164.001241.

Boily, C. M. and Kroupa, P. The impact of mass loss on star cluster formation - I. Analytical results. *MNRAS*, 338:665–672, January 2003. doi: 10.1046/j.1365-8711.2003.06076.x.

Borgman, J.; Koornneef, J., and Slingerland, J. Infra-red photometry of a heavily reddened cluster in Ara. *AAP*, 4:248–252, February 1970.

Brandl, B. R.; Clark, D. M.; Eikenberry, S. S.; Wilson, J. C.; Henderson, C. P.; Barry, D. J.; Houck, J. R.; Carson, J. C., and Hayward, T. L. Deep Near-Infrared Imaging and Photometry of the Antennae Galaxies with WIRC. *ApJ*, 635:280–289, December 2005. doi: 10.1086/497357.

Brandner, W.; Grebel, E. K.; Chu, Y.-H.; Dottori, H.; Brandl, B.; Richling, S.; Yorke, H. W.; Points, S. D., and Zinnecker, H. HST/WFPC2 and VLT/ISAAC Observations of Proplyds in the Giant H II Region NGC 3603. *AJ*, 119:292–301, January 2000. doi: 10.1086/301192.

Brandner, W.; Clark, J. S.; Stolte, A.; Waters, R.; Negueruela, I., and Goodwin, S. P. Intermediate to low-mass stellar content of Westerlund 1. *AAP*, 478: 137–149, January 2008. doi: 10.1051/0004-6361:20077579.

Bresolin, F.; Pietrzyński, G.; Urbaneja, M. A.; Gieren, W.; Kudritzki, R.-P., and Venn, K. A. The Araucaria Project: VLT Spectra of Blue Supergiants in WLM-Classification and First Abundances. *ApJ*, 648:1007–1019, September 2006. doi: 10.1086/506200.

Bresolin, F.; Gieren, W.; Kudritzki, R.-P.; Pietrzyński, G.; Urbaneja, M. A., and Carraro, G. Extragalactic Chemical Abundances: Do H II Regions and Young Stars Tell the Same Story? The Case of the Spiral Galaxy NGC 300. *ApJ*, 700: 309–330, July 2009. doi: 10.1088/0004-637X/700/1/309.

Brodie, J. P. and Strader, J. Extragalactic Globular Clusters and Galaxy Formation. *ARA&A*, 44:193–267, September 2006. doi: 10.1146/annurev.astro.44.051905.092441.

Bruzual, G. and Charlot, S. Stellar population synthesis at the resolution of 2003. *MNRAS*, 344:1000–1028, October 2003. doi: 10.1046/j.1365-8711.2003.06897.x.

Calzetti, D. UV opacity in nearby galaxies and application to distant galaxies. In Waller, W. H., editor, *American Institute of Physics Conference Series*, volume 408 of *American Institute of Physics Conference Series*, pages 403–412, May 1997. doi: 10.1063/1.53764.

Calzetti, D.; Kinney, A. L., and Storchi-Bergmann, T. Dust extinction of the stellar continua in starburst galaxies: The ultraviolet and optical extinction law. *ApJ*, 429:582–601, July 1994. doi: 10.1086/174346.

Calzetti, D.; Armus, L.; Bohlin, R. C.; Kinney, A. L.; Koornneef, J., and Storchi-Bergmann, T. The Dust Content and Opacity of Actively Star-forming Galaxies. *ApJ*, 533:682–695, April 2000. doi: 10.1086/308692.

Carlberg, R. G. Dissipative formation of an elliptical galaxy. *ApJ*, 286:403–415, November 1984. doi: 10.1086/162615.

Casoli, F.; Dupraz, C.; Combes, F., and Kazes, I. CO in mergers. III - NGC 1614 and NGC 3256. *AAP*, 251:1–10, November 1991.

Castro-Neves, M. and Draper, P. W. SPLAT-VO: Spectral Analysis Tool for the Virtual Observatory, February 2014. Astrophysics Source Code Library.

Chapelon, S.; Buat, V.; Burgarella, D., and Kissler-Patig, M. The globular cluster system around the low-luminosity S0 galaxy NGC 7457. *AAP*, 346:721–730, June 1999.

Chattopadhyay, A. K.; Chattopadhyay, T.; Davoust, E.; Mondal, S., and Sharina, M. Study of NGC 5128 Globular Clusters Under Multivariate Statistical Paradigm. *ApJ*, 705:1533–1547, November 2009. doi: 10.1088/0004-637X/705/2/1533.

Chies-Santos, A. L.; Pastoriza, M. G.; Santiago, B. X., and Forbes, D. A. The globular cluster system of NGC 5846 revisited: colours, sizes and X-ray counterparts. *AAP*, 455:453–459, August 2006. doi: 10.1051/0004-6361:20054212.

Cho, J.; Sharples, R. M.; Blakeslee, J. P.; Zepf, S. E.; Kundu, A.; Kim, H.-S., and Yoon, S.-J. Globular cluster systems of early-type galaxies in low-density environments. *MNRAS*, 422:3591–3610, June 2012. doi: 10.1111/j.1365-2966.2012.20873.x.

Chomiuk, L. and Povich, M. S. Toward a Unification of Star Formation Rate Determinations in the Milky Way and Other Galaxies. *AJ*, 142:197, December 2011. doi: 10.1088/0004-6256/142/6/197.

Christopher, M. H. *Young, massive star clusters in the antennae*. PhD thesis, California Institute of Technology, December 2008.

Cidale, L.; Zorec, J.; Maillard, J. P., and Morrell, N. Paschen and Brackett Lines in Be stars. In Smith, M. A.; Henrichs, H. F., and Fabregat, J., editors, *IAU Colloq. 175: The Be Phenomenon in Early-Type Stars*, volume 214 of *Astronomical Society of the Pacific Conference Series*, page 472, 2000.

Clark, D. M.; Eikenberry, S. S.; Raines, S. N.; Gruel, N.; Elston, R.; Guzman, R.; Boreman, G., and Glenn, P. E. Probing the super star cluster environment of NGC 1569 using FISICA. *MNRAS*, 428:2290–2294, January 2013. doi: 10.1093/mnras/sts200.

Clark, J. S.; Fender, R. P.; Waters, L. B. F. M.; Dougherty, S. M.; Koornneef, J.; Steele, I. A., and van Blokland, A. Discovery of extended radio emission in the young cluster Wd1. *MNRAS*, 299:L43–L47, October 1998. doi: 10.1046/j.1365-8711.1998.02038.x.

Clark, J. S.; Negueruela, I.; Crowther, P. A., and Goodwin, S. P. On the massive stellar population of the super star cluster ¡ASTROBJ¿Westerlund 1¡/ASTROBJ¿. *AAP*, 434:949–969, May 2005. doi: 10.1051/0004-6361:20042413.

Cohn, H. and Hut, P. Is there life after core collapse in globular clusters? *ApJ Lett.*, 277:L45–L48, February 1984. doi: 10.1086/184199.

Conroy, C. and Spergel, D. N. On the Formation of Multiple Stellar Populations in Globular Clusters. *ApJ*, 726:36, January 2011. doi: 10.1088/0004-637X/726/1/36.

Cote, P.; Marzke, R. O., and West, M. J. The Formation of Giant Elliptical Galaxies and Their Globular Cluster Systems. *ApJ*, 501:554, July 1998. doi: 10.1086/305838.

Cote, S.; Freeman, K. C.; Carignan, C., and Quinn, P. J. Discovery of Numerous Dwarf Galaxies in the Two Nearest Groups of Galaxies. *AJ*, 114:1313, October 1997. doi: 10.1086/118565.

Cox, T. J.; Jonsson, P.; Primack, J. R., and Somerville, R. S. Feedback in simulations of disc-galaxy major mergers. *MNRAS*, 373:1013–1038, December 2006. doi: 10.1111/j.1365-2966.2006.11107.x.

Dale, D. A.; Roussel, H.; Contursi, A.; Helou, G.; Dinerstein, H. L.; Hunter, D. A.; Hollenbach, D. J.; Egami, E.; Matthews, K.; Jr.Murphy, T. W.; Lafon, C. E., and Rubin, R. H. Near-Infrared Integral Field Spectroscopy of Star-forming Galaxies. *ApJ*, 601:813–830, February 2004. doi: 10.1086/380753.

Davies, B.; Kudritzki, R.-P., and Figer, D. F. The potential of red supergiants as extragalactic abundance probes at low spectral resolution. *MNRAS*, 407:1203–1211, September 2010. doi: 10.1111/j.1365-2966.2010.16965.x.

Davies, R. I. A method to remove residual OH emission from near-infrared spectra. *MNRAS*, 375:1099–1105, March 2007. doi: 10.1111/j.1365-2966.2006.11383.x.

Davies, R. I.; Agudo Berbel, A.; Wiezorrek, E.; Cirasuolo, M.; Förster Schreiber, N. M.; Jung, Y.; Muschielok, B.; Ott, T.; Ramsay, S.; Schlichter, J.; Sharples, R., and Wegner, M. The Software Package for Astronomical Reductions with KMOS: SPARK. *AAP*, 558:A56, October 2013. doi: 10.1051/0004-6361/201322282.

de Carvalho, R. R.; Ribeiro, A. L. B.; Capelato, H. V., and Zepf, S. E. Redshift Survey of Galaxies around a Selected Sample of Compact Groups. *ApJS*, 110: 1, May 1997. doi: 10.1086/312992.

de Grijs, R.; Gilmore, G. F.; Mackey, A. D.; Wilkinson, M. I.; Beaulieu, S. F.; Johnson, R. A., and Santiago, B. X. Mass segregation in young compact clusters in the Large Magellanic Cloud - III. Implications for the initial mass function. *MNRAS*, 337:597–608, December 2002. doi: 10.1046/j.1365-8711.2002.05954.x.

de Grijs, R.; Smith, L. J.; Bunker, A.; Sharp, R. G.; Gallagher, J. S.; Anders, P.; Lançon, A.; O'Connell, R. W., and Parry, I. R. CIRPASS near-infrared integral-field spectroscopy of massive star clusters in the starburst galaxy NGC 1140. *MNRAS*, 352:263–276, July 2004. doi: 10.1111/j.1365-2966.2004.07932.x.

de Mink, S. E.; Pols, O. R.; Langer, N., and Izzard, R. G. Massive binaries as the source of abundance anomalies in globular clusters. *AAP*, 507:L1–L4, November 2009. doi: 10.1051/0004-6361/200913205.

de Pree, C. G.; Nysewander, M. C., and Goss, W. M. NGC 3576 and NGC 3603: Two Luminous Southern H II Regions Observed at High Resolution with the Australia Telescope Compact Array. *AJ*, 117:2902–2918, June 1999. doi: 10.1086/300892.

de Wit, W. J.; Testi, L.; Palla, F., and Zinnecker, H. The origin of massive O-type field stars: II. Field O stars as runaways. *AAP*, 437:247–255, July 2005. doi: 10.1051/0004-6361:20042489.

Decressin, T.; Meynet, G.; Charbonnel, C.; Prantzos, N., and Ekström, S. Fast rotating massive stars and the origin of the abundance patterns in galactic globular clusters. *AAP*, 464:1029–1044, March 2007. doi: 10.1051/0004-6361:20066013.

D'Ercole, A.; Vesperini, E.; D'Antona, F.; McMillan, S. L. W., and Recchi, S. Formation and dynamical evolution of multiple stellar generations in globular

clusters. *MNRAS*, 391:825–843, December 2008. doi: 10.1111/j.1365-2966.2008.13915.x.

Djorgovski, S. Physical Parameters of Galactic Globular Clusters. In Djorgovski, S. G. and Meylan, G., editors, *Structure and Dynamics of Globular Clusters*, volume 50 of *Astronomical Society of the Pacific Conference Series*, page 373, January 1993.

Dufour, R. J.; Harvel, C. A.; Martins, D. M.; IIISchiffer, F. H.; Talent, D. L.; Wells, D. C.; van den Bergh, S., and Jr.Talbot, R. J. Picture processing analysis of the optical structure of NGC 5128 /Centaurus A/. *AJ*, 84:284–301, March 1979. doi: 10.1086/112421.

Eckart, A.; Cameron, M.; Rothermel, H.; Wild, W.; Zinnecker, H.; Rydbeck, G.; Olberg, M., and Wiklind, T. Observations of CO isotopic emission and the far-infrared continuum of Centaurus A. *ApJ*, 363:451–463, November 1990. doi: 10.1086/169357.

Eggleton, Peter. *Evolutionary processes in binary and multiple stars*, volume 40. Cambridge University Press, 2006.

Eislöffel, J.; Froebrich, D.; Stanke, T., and McCaughrean, M. J. Molecular Outflows in the Young Open Cluster IC 348. *ApJ*, 595:259–265, September 2003. doi: 10.1086/377216.

Elmegreen, B. G. On the Rapid Collapse and Evolution of Molecular Clouds. *ApJ*, 668:1064–1082, October 2007. doi: 10.1086/521327.

Elmegreen, B. G. and Efremov, Y. N. A Universal Formation Mechanism for Open and Globular Clusters in Turbulent Gas. *ApJ*, 480:235, May 1997. doi: 10.1086/303966.

Elmegreen, B. G. and Efremov, Y. N. Hierarchy of Interstellar and Stellar Structures and the Case of the Orion Star-Forming Region. *ArXiv Astrophysics e-prints*, January 1998.

Elmegreen, B. G. and Hunter, D. A. On the Disruption of Star Clusters in a Hierarchical Interstellar Medium. *ApJ*, 712:604–623, March 2010. doi: 10.1088/0004-637X/712/1/604.

Elson, R. A. W.; Fall, S. M., and Freeman, K. C. The structure of young star clusters in the Large Magellanic Cloud. *ApJ*, 323:54–78, December 1987. doi: 10.1086/165807.

Elson, R. A. W.; Freeman, K. C., and Lauer, T. R. Core expansion in young star clusters in the Large Magellanic Cloud. *ApJ Lett.*, 347:L69–L71, December 1989. doi: 10.1086/185610.

Fabbiano, G.; Krauss, M.; Zezas, A.; Rots, A., and Neff, S. The Multicolored Hot Interstellar Medium of "the Antennae" Galaxies (NGC 4038/4039). *ApJ*, 598: 272–287, November 2003. doi: 10.1086/378791.

Faber, S. M.; Wegner, G.; Burstein, D.; Davies, R. L.; Dressler, A.; Lynden-Bell, D., and Terlevich, R. J. Spectroscopy and photometry of elliptical galaxies. VI - Sample selection and data summary. *ApJS*, 69:763–808, April 1989. doi: 10.1086/191327.

Faber, S. M.; Willmer, C. N. A.; Wolf, C.; Koo, D. C.; Weiner, B. J.; Newman, J. A.; Im, M.; Coil, A. L.; Conroy, C.; Cooper, M. C.; Davis, M.; Finkbeiner, D. P.; Gerke, B. F.; Gebhardt, K.; Groth, E. J.; Guhathakurta, P.; Harker, J.; Kaiser, N.; Kassin, S.; Kleinheinrich, M.; Konidaris, N. P.; Kron, R. G.; Lin, L.; Luppino, G.; Madgwick, D. S.; Meisenheimer, K.; Noeske, K. G.; Phillips, A. C.; Sarajedini, V. L.; Schiavon, R. P.; Simard, L.; Szalay, A. S.; Vogt, N. P., and Yan, R. Galaxy Luminosity Functions to z˜1 from DEEP2 and COMBO-17: Implications for Red Galaxy Formation. *ApJ*, 665:265–294, August 2007. doi: 10.1086/519294.

Fall, S. M. and Zhang, Q. Dynamical Evolution of the Mass Function of Globular Star Clusters. *ApJ*, 561:751–765, November 2001. doi: 10.1086/323358.

Figer, D. F. Young Massive Clusters in the Galactic Center. In Lamers, H. J. G. L. M.; Smith, L. J., and Nota, A., editors, *The Formation and Evolution of Massive Young Star Clusters*, volume 322 of *Astronomical Society of the Pacific Conference Series*, page 49, December 2004.

Figer, D. F.; McLean, I. S., and Najarro, F. A K-Band Spectral Atlas of Wolf-Rayet Stars. *ApJ*, 486:420–434, September 1997.

Figer, D. F.; McLean, I. S., and Morris, M. Massive Stars in the Quintuplet Cluster. *ApJ*, 514:202–220, March 1999. doi: 10.1086/306931.

Figer, D. F.; Najarro, F.; Gilmore, D.; Morris, M.; Kim, S. S.; Serabyn, E.; McLean, I. S.; Gilbert, A. M.; Graham, J. R.; Larkin, J. E.; Levenson, N. A., and Teplitz, H. I. Massive Stars in the Arches Cluster. *ApJ*, 581:258–275, December 2002. doi: 10.1086/344154.

Fleming, D. E. B.; Harris, W. E.; Pritchet, C. J., and Hanes, D. A. CCD photometry of the globular cluster systems in NGC 4494 and NGC 4565. *AJ*, 109: 1044–1054, March 1995. doi: 10.1086/117340.

Forbes, D. A.; Brodie, J. P., and Grillmair, C. J. On the Origin of Globular Clusters in Elliptical and cD Galaxies. *AJ*, 113:1652, May 1997. doi: 10.1086/118382.

Freedman, Roger; Geller, Robert, and Kaufmann, William J. *Universe*. W.H. Freeman and Company, 2010.

Gallagher, J. S. and Smith, L. J. Environments of Super Star Clusters. In Lamers, H. J. G. L. M.; Smith, L. J., and Nota, A., editors, *The Formation and Evolution of Massive Young Star Clusters*, volume 322 of *Astronomical Society of the Pacific Conference Series*, page 149, December 2004.

Gazak, J. Z.; Bastian, N.; Kudritzki, R.-P.; Adamo, A.; Davies, B.; Plez, B., and Urbaneja, M. A. Age dating stellar populations in the near infrared: an absolute age indicator from the presence/absence of red supergiants. *MNRAS*, 430:L35–L39, March 2013. doi: 10.1093/mnrasl/sls043.

Gazak, J. Z.; Davies, B.; Bastian, N.; Kudritzki, R.; Bergemann, M.; Plez, B.; Evans, C.; Patrick, L.; Bresolin, F., and Schinnerer, E. A New Method for Measuring Metallicities of Young Super Star Clusters. *ApJ*, 787:142, June 2014. doi: 10.1088/0004-637X/787/2/142.

Geisler, D.; Gómez, M.; Harris, W. E.; Woodley, K.; Harris, G. L.; Puzia, T., and Hempel, M. The Globular Cluster System of NGC 5128. In Vazdekis, A. and Peletier, R., editors, *IAU Symposium*, volume 241 of *IAU Symposium*, pages 440–444, August 2007. doi: 10.1017/S174392130700871X.

Geisler, D.; Gómez, M.; Woodley, K. A.; Harris, W. E., and Harris, G. L. H. Sizes of Confirmed NGC 5128 Globular Clusters. In Vesperini, E.; Giersz, M., and Sills, A., editors, *IAU Symposium*, volume 246 of *IAU Symposium*, pages 425–426, May 2008. doi: 10.1017/S1743921308016098.

Gieles, M. The early evolution of the star cluster mass function. *MNRAS*, 394: 2113–2126, April 2009. doi: 10.1111/j.1365-2966.2009.14473.x.

Gieles, M.; Larsen, S. S.; Bastian, N., and Stein, I. T. The luminosity function of young star clusters: implications for the maximum mass and luminosity of clusters. *AAP*, 450:129–145, April 2006a. doi: 10.1051/0004-6361:20053589.

Gieles, M.; Larsen, S. S.; Scheepmaker, R. A.; Bastian, N.; Haas, M. R., and Lamers, H. J. G. L. M. Observational evidence for a truncation of the star cluster initial mass function at the high mass end. *AAP*, 446:L9–L12, February 2006b. doi: 10.1051/0004-6361:200500224.

Gieles, M.; Portegies Zwart, S. F.; Baumgardt, H.; Athanassoula, E.; Lamers, H. J. G. L. M.; Sipior, M., and Leenaarts, J. Star cluster disruption by giant molecular clouds. *MNRAS*, 371:793–804, September 2006c. doi: 10.1111/j.1365-2966.2006.10711.x.

Gies, D. R. The kinematical and binary properties of association and field O stars. *ApJS*, 64:545–563, July 1987. doi: 10.1086/191208.

Gil de Paz, A.; Boissier, S.; Madore, B. F.; Seibert, M.; Joe, Y. H.; Boselli, A.; Wyder, T. K.; Thilker, D.; Bianchi, L.; Rey, S.-C.; Rich, R. M.; Barlow, T. A.; Conrow, T.; Forster, K.; Friedman, P. G.; Martin, D. C.; Morrissey, P.; Neff, S. G.; Schiminovich, D.; Small, T.; Donas, J.; Heckman, T. M.; Lee, Y.-W.; Milliard, B.; Szalay, A. S., and Yi, S. The GALEX Ultraviolet Atlas of Nearby Galaxies. *ApJS*, 173:185–255, December 2007. doi: 10.1086/516636.

Gilbert, A. M. and Graham, J. R. Feedback in the Antennae Galaxies (NGC 4038/9). I. High-Resolution Infrared Spectroscopy of Winds from Super Star Clusters. *ApJ*, 668:168–181, October 2007. doi: 10.1086/520910.

Gómez, M. and Woodley, K. A. Sizes of Confirmed Globular Clusters in NGC 5128: A Wide-Field High-Resolution Study. *ApJ Lett.*, 670:L105–L108, December 2007. doi: 10.1086/524223.

Goudfrooij, P.; Alonso, M. V.; Maraston, C., and Minniti, D. The star cluster system of the 3-Gyr-old merger remnant NGC 1316: clues from optical and near-infrared photometry. *MNRAS*, 328:237–256, November 2001a. doi: 10.1046/j.1365-8711.2001.04860.x.

Goudfrooij, P.; Mack, J.; Kissler-Patig, M.; Meylan, G., and Minniti, D. Kinematics, ages and metallicities of star clusters in NGC 1316: a 3-Gyr-old merger remnant. *MNRAS*, 322:643–657, April 2001b. doi: 10.1046/j.1365-8711.2001.04154.x.

Greissl, J.; Meyer, M. R.; Christopher, M. H., and Scoville, N. Z. Star Formation History of a Young Super-Star Cluster in NGC 4038/39: Direct Detection of Low-Mass Pre-Main Sequence Stars. *ApJ*, 710:1746–1754, February 2010. doi: 10.1088/0004-637X/710/2/1746.

Gustafsson, B.; Edvardsson, B.; Eriksson, K.; Jørgensen, U. G.; Nordlund, Å., and Plez, B. A grid of MARCS model atmospheres for late-type stars. I. Methods and general properties. *AAP*, 486:951–970, August 2008. doi: 10.1051/0004-6361:200809724.

Hanson, M. M.; Luhman, K. L., and Rieke, G. H. A Near-Infrared Survey of Radio-selected Ultracompact H II Regions. *ApJS*, 138:35–61, January 2002. doi: 10.1086/324073.

Harris, G. L. H. NGC 5128: The Giant Beneath. *PASA*, 27:475–481, October 2010. doi: 10.1071/AS09063.

Harris, G. L. H.; Harris, W. E., and Geisler, D. Wide-Field Washington Photometry of the NGC 5128 Globular Cluster System. II. Large-Scale Properties of the System. *AJ*, 128:723–735, August 2004. doi: 10.1086/421848.

Harris, G. L. H.; Rejkuba, M., and Harris, W. E. The Distance to NGC 5128 (Centaurus A). *PASA*, 27:457–462, October 2010. doi: 10.1071/AS09061.

Harris, G. L. H.; Gómez, M.; Harris, W. E.; Johnston, K.; Kazemzadeh, F.; Kerzendorf, W.; Geisler, D., and Woodley, K. A. Eight Hundred New Candidates for Globular Clusters in NGC 5128 (Centaurus A). *AJ*, 143:84, April 2012. doi: 10.1088/0004-6256/143/4/84.

Harris, W. E. Globular cluster systems in galaxies beyond the Local Group. *ARA&A*, 29:543–579, 1991. doi: 10.1146/annurev.aa.29.090191.002551.

Harris, W. E. Photometric Properties of Globular Cluster Systems in Large Galaxies. In Smith, G. H. and Brodie, J. P., editors, *The Globular Cluster-Galaxy Connection*, volume 48 of *Astronomical Society of the Pacific Conference Series*, page 472, January 1993.

Harris, W. E. and van den Bergh, S. Globular clusters in galaxies beyond the local group. I - New cluster systems in selected northern ellipticals. *AJ*, 86: 1627–1642, November 1981. doi: 10.1086/113047.

Harris, W. E.; Harris, G. L. H.; Barmby, P.; McLaughlin, D. E., and Forbes, D. A. Structural Parameters for Globular Clusters in NGC 5128. II. Hubble Space Telescope ACS Imaging and New Clusters. *AJ*, 132:2187–2197, November 2006. doi: 10.1086/507579.

Harris, William E. Globular cluster systems. In *Star clusters*, pages 223–408. Springer, 2001.

Herrera, C. N.; Boulanger, F.; Nesvadba, N. P. H., and Falgarone, E. ALMA CO and VLT/SINFONI H_2 observations of the Antennae overlap region: mass and energy dissipation. *AAP*, 538:L9, February 2012. doi: 10.1051/0004-6361/201118317.

Hibbard, J. E.; Guhathakurta, P.; van Gorkom, J. H., and Schweizer, F. Cold, warm, and hot gas in the late-stage merger NGC 7252. *AJ*, 107:67–89, January 1994. doi: 10.1086/116835.

Hibbard, J. E.; van der Hulst, J. M.; Barnes, J. E., and Rich, R. M. High-Resolution H I Mapping of NGC 4038/39 ("The Antennae") and Its Tidal Dwarf Galaxy Candidates. *AJ*, 122:2969–2992, December 2001. doi: 10.1086/324102.

Hibbard, J. E.; Bianchi, L.; Thilker, D. A.; Rich, R. M.; Schiminovich, D.; Xu, C. K.; Neff, S. G.; Seibert, M.; Lauger, S.; Burgarella, D.; Barlow, T. A.; Byun, Y.-I.; Donas, J.; Forster, K.; Friedman, P. G.; Heckman, T. M.; Jelinsky, P. N.; Lee, Y.-W.; Madore, B. F.; Malina, R. F.; Martin, D. C.; Milliard, B.; Morrissey, P.; Siegmund, O. H. W.; Small, T.; Szalay, A. S.; Welsh, B. Y., and Wyder, T. K. Ultraviolet Morphology and Star Formation in the Tidal Tails of NGC 4038/39. *ApJ Lett.*, 619:L87–L90, January 2005. doi: 10.1086/423244.

Hickson, P. Systematic properties of compact groups of galaxies. *ApJ*, 255:382–391, April 1982. doi: 10.1086/159838.

Hickson, P.; Mendes de Oliveira, C.; Huchra, J. P., and Palumbo, G. G. Dynamical properties of compact groups of galaxies. *ApJ*, 399:353–367, November 1992. doi: 10.1086/171932.

Hills, J. G. The effect of mass loss on the dynamical evolution of a stellar system - Analytic approximations. *ApJ*, 235:986–991, February 1980. doi: 10.1086/157703.

Hodapp, K. W. and Davis, C. J. Molecular Hydrogen Outflows in W51. *ApJ*, 575: 291–305, August 2002. doi: 10.1086/341217.

Hodge, P. W. and Jr.Kennicutt, R. C. An atlas of H II regions in 125 galaxies. *AJ*, 88:296–328, March 1983. doi: 10.1086/113318.

Homeier, N. L.; Blum, R. D.; Pasquali, A.; Conti, P. S., and Damineli, A. Results from a near infrared search for emission-line stars in the Inner Galaxy: Spectra of new Wolf-Rayet stars. *AAP*, 408:153–159, September 2003. doi: 10.1051/0004-6361:20030989.

Hopkins, P. F.; Cox, T. J.; Younger, J. D., and Hernquist, L. How do Disks Survive Mergers? *ApJ*, 691:1168–1201, February 2009. doi: 10.1088/0004-637X/691/2/1168.

Hummer, D. G. and Storey, P. J. Recombination-line intensities for hydrogenic ions. I - Case B calculations for H I and He II. *MNRAS*, 224:801–820, February 1987.

Humphreys, R. M. and Davidson, K. Studies of luminous stars in nearby galaxies. III - Comments on the evolution of the most massive stars in the Milky Way and the Large Magellanic Cloud. *ApJ*, 232:409–420, September 1979. doi: 10.1086/157301.

Irwin, J. A. Arcs and bridges in the interacting galaxies NGC 5775/NGC 5774. *ApJ*, 429:618–633, July 1994. doi: 10.1086/174349.

Israel, F. P. Centaurus A - NGC 5128. *A&AR*, 8:237–278, 1998. doi: 10.1007/s001590050011.

Jog, C. J. and Solomon, P. M. A triggering mechanism for enhanced star formation in colliding galaxies. *ApJ*, 387:152–161, March 1992. doi: 10.1086/171067.

Jordán, A.; Côté, P.; Blakeslee, J. P.; Ferrarese, L.; McLaughlin, D. E.; Mei, S.; Peng, E. W.; Tonry, J. L.; Merritt, D.; Milosavljević, M.; Sarazin, C. L.; Sivakoff, G. R., and West, M. J. The ACS Virgo Cluster Survey. X. Half-Light

Radii of Globular Clusters in Early-Type Galaxies: Environmental Dependencies and a Standard Ruler for Distance Estimation. *ApJ*, 634:1002–1019, December 2005. doi: 10.1086/497092.

Jordán, A.; McLaughlin, D. E.; Côté, P.; Ferrarese, L.; Peng, E. W.; Mei, S.; Villegas, D.; Merritt, D.; Tonry, J. L., and West, M. J. The ACS Virgo Cluster Survey. XII. The Luminosity Function of Globular Clusters in Early-Type Galaxies. *ApJS*, 171:101–145, July 2007. doi: 10.1086/516840.

Kainulainen, J. T.; Alves, J. F.; Beletsky, Y.; Ascenso, J.; Kainulainen, J. M.; Amorim, A.; Lima, J.; Marques, R.; Moitinho, A.; Pinhão, J.; Rebordão, J., and Santos, F. D. Uncovering the kiloparsec-scale stellar ring of NGC 5128. *AAP*, 502:L5–L8, August 2009. doi: 10.1051/0004-6361/200912624.

Kaisler, D.; Harris, W. E.; Crabtree, D. R., and Richer, H. B. Globular Clusters in NGC 1275. *AJ*, 111:2224, June 1996. doi: 10.1086/117956.

Kassin, S. A.; Frogel, J. A.; Pogge, R. W.; Tiede, G. P., and Sellgren, K. Stellar Populations in NGC 4038/39 (the Antennae): Exploring a Galaxy Merger Pixel by Pixel. *AJ*, 126:1276–1285, September 2003. doi: 10.1086/377520.

Kewley, L. J. and Ellison, S. L. Metallicity Calibrations and the Mass-Metallicity Relation for Star-forming Galaxies. *ApJ*, 681:1183–1204, July 2008. doi: 10.1086/587500.

King, I. The structure of star clusters. I. an empirical density law. *AJ*, 67:471, October 1962. doi: 10.1086/108756.

Kleinmann, S. G. and Hall, D. N. B. Spectra of late-type standard stars in the region 2.0-2.5 microns. *ApJS*, 62:501–517, November 1986. doi: 10.1086/191149.

Knierman, K. A.; Gallagher, S. C.; Charlton, J. C.; Hunsberger, S. D.; Whitmore, B.; Kundu, A.; Hibbard, J. E., and Zaritsky, D. From Globular Clusters to Tidal Dwarfs: Structure Formation in the Tidal Tails of Merging Galaxies. *AJ*, 126:1227–1244, September 2003. doi: 10.1086/377481.

Kontizas, E.; Kontizas, M.; Sedmak, G., and Smareglia, R. Ellipticities at R(h) of LMC star clusters. *AJ*, 98:590–595, August 1989. doi: 10.1086/115159.

Koo, B.-C. Infrared [Fe II] and Dust Emissions from Supernova Remnants. In Ray, A. and McCray, R. A., editors, *IAU Symposium*, volume 296 of *IAU Symposium*, pages 214–221, January 2014. doi: 10.1017/S1743921313009496.

Kornei, K. A. and McCrady, N. A Young Super Star Cluster in the Nuclear Region of NGC 253. *ApJ*, 697:1180–1186, June 2009. doi: 10.1088/0004-637X/697/2/1180.

Kruijssen, J. M. D. On the fraction of star formation occurring in bound stellar clusters. *MNRAS*, 426:3008–3040, November 2012. doi: 10.1111/j.1365-2966.2012.21923.x.

Kruijssen, J. M. D.; Pelupessy, F. I.; Lamers, H. J. G. L. M.; Portegies Zwart, S. F., and Icke, V. Modelling the formation and evolution of star cluster populations in galaxy simulations. *MNRAS*, 414:1339–1364, June 2011. doi: 10.1111/j.1365-2966.2011.18467.x.

Kruijssen, J. M. D.; Pelupessy, F. I.; Lamers, H. J. G. L. M.; Portegies Zwart, S. F.; Bastian, N., and Icke, V. Formation versus destruction: the evolution of the star cluster population in galaxy mergers. *MNRAS*, 421:1927–1941, April 2012. doi: 10.1111/j.1365-2966.2012.20322.x.

Krumholz, M. R.; Klein, R. I.; McKee, C. F.; Offner, S. S. R., and Cunningham, A. J. The Formation of Massive Star Systems by Accretion. *Science*, 323:754–, February 2009. doi: 10.1126/science.1165857.

Kudritzki, R.-P. Dissecting galaxies with quantitative spectroscopy of the brightest stars in the Universe. *Astronomische Nachrichten*, 331:459, May 2010. doi: 10.1002/asna.200911342.

Kudritzki, R.-P.; Urbaneja, M. A.; Gazak, Z.; Macri, L.; Jr.Hosek, M. W.; Bresolin, F., and Przybilla, N. A Direct Stellar Metallicity Determination in the Disk of the Maser Galaxy NGC 4258. *ApJ Lett.*, 779:L20, December 2013. doi: 10.1088/2041-8205/779/2/L20.

Kundu, A. and Whitmore, B. C. New Insights from HST Studies of Globular Cluster Systems. I. Colors, Distances, and Specific Frequencies of 28 Elliptical Galaxies. *AJ*, 121:2950–2973, June 2001. doi: 10.1086/321073.

Kundu, A. and Zepf, S. E. Bimodal Infrared Colors of the M87 Globular Cluster System: Peaks in the Metallicity Distribution. *ApJ Lett.*, 660:L109–L112, May 2007. doi: 10.1086/518214.

Kundu, A.; Whitmore, B. C.; Sparks, W. B.; Macchetto, F. D.; Zepf, S. E., and Ashman, K. M. The Globular Cluster System in the Inner Region of M87. *ApJ*, 513:733–751, March 1999. doi: 10.1086/306865.

Kwan, J. and Fischer, W. Origins of the H, He I and Ca II line emission in classical T Tauri stars. *MNRAS*, 411:2383–2425, March 2011. doi: 10.1111/j.1365-2966.2010.17863.x.

Lada, C. J. Star formation - From OB associations to protostars. In Peimbert, M. and Jugaku, J., editors, *Star Forming Regions*, volume 115 of *IAU Symposium*, pages 1–17, 1987.

Lada, C. J. and Lada, E. A. Embedded Clusters in Molecular Clouds. *ARA&A*, 41:57–115, 2003. doi: 10.1146/annurev.astro.41.011802.094844.

Lamers, H. J. G. L. M.; Gieles, M.; Bastian, N.; Baumgardt, H.; Kharchenko, N. V., and Portegies Zwart, S. An analytical description of the disruption of star clusters in tidal fields with an application to Galactic open clusters. *AAP*, 441:117–129, October 2005. doi: 10.1051/0004-6361:20042241.

Larkin, J. E.; Armus, L.; Knop, R. A.; Soifer, B. T., and Matthews, K. A Near-Infrared Spectroscopic Survey of LINER Galaxies. *ApJS*, 114:59–72, January 1998. doi: 10.1086/313063.

Larsen, S. S. Young massive star clusters in nearby galaxies. II. Software tools, data reductions and cluster sizes. *AAPS*, 139:393–415, October 1999. doi: 10.1051/aas:1999509.

Larsen, S. S. The Luminosity Function of Star Clusters in Spiral Galaxies. *AJ*, 124:1393–1409, September 2002. doi: 10.1086/342381.

Larsen, S. S. The structure and environment of young stellar clusters in spiral galaxies. *AAP*, 416:537–553, March 2004a. doi: 10.1051/0004-6361:20034533.

Larsen, S. S. Star Formation in Clusters. *ArXiv Astrophysics e-prints*, August 2004b.

Larsen, S. S. The mass function of young star clusters in spiral galaxies. *AAP*, 494:539–551, February 2009. doi: 10.1051/0004-6361:200811212.

Larsen, S. S.; Forbes, D. A., and Brodie, J. P. Hubble Space Telescope photometry of globular clusters in the Sombrero galaxy. *MNRAS*, 327:1116–1126, November 2001. doi: 10.1046/j.1365-8711.2001.04797.x.

Larsen, S. S.; Origlia, L.; Brodie, J. P., and Gallagher, J. S. Near-infrared spectroscopy of a young super-star cluster in NGC 6946: chemical abundances and abundance patterns*. *MNRAS*, 368:L10–L14, May 2006. doi: 10.1111/j.1745-3933.2006.00148.x.

Larson, R. B. Models for the formation of elliptical galaxies. *MNRAS*, 173:671–699, December 1975.

Lauberts, A. and Valentijn, E. A. *The surface photometry catalogue of the ESO-Uppsala galaxies*. European Southern Observatory, 1989.

Lee, H. J. and Lee, M. G. The Star Cluster System of the Merging Galaxy NGC 1487. *Journal of Korean Astronomical Society*, 38:345–355, September 2005.

Lee, M. G.; Chandar, R., and Whitmore, B. C. Properties of Resolved Star Clusters in M51. *AJ*, 130:2128–2139, November 2005. doi: 10.1086/491786.

Leitherer, C. Time Scales in Starbursts. In von Hippel, T.; Simpson, C., and Manset, N., editors, *Astrophysical Ages and Times Scales*, volume 245 of *Astronomical Society of the Pacific Conference Series*, page 390, 2001.

Leitherer, C.; Schaerer, D.; Goldader, J. D.; Delgado, R. M. G.; Robert, C.; Kune, D. F.; de Mello, D. F.; Devost, D., and Heckman, T. M. Starburst99: Synthesis Models for Galaxies with Active Star Formation. *ApJS*, 123:3–40, July 1999. doi: 10.1086/313233.

Lejeune, T.; Cuisinier, F., and Buser, R. Standard stellar library for evolutionary synthesis. I. Calibration of theoretical spectra. *AAPS*, 125:229–246, October 1997. doi: 10.1051/aas:1997373.

Lin, L. Interaction-Triggered Star Formation in Distant Galaxies and the Role of Mergers in Galaxy Evolution. In Smith, B.; Higdon, J.; Higdon, S., and Bastian, N., editors, *Galaxy Wars: Stellar Populations and Star Formation in Interacting Galaxies*, volume 423 of *Astronomical Society of the Pacific Conference Series*, page 329, June 2010.

Lockwood, G. W. Stellar Energy Distributions in an Infrared Cluster in ARA. *ApJ*, 193:103–108, October 1974. doi: 10.1086/153133.

Longmore, S. N.; Rathborne, J.; Bastian, N.; Alves, J.; Ascenso, J.; Bally, J.; Testi, L.; Longmore, A.; Battersby, C.; Bressert, E.; Purcell, C.; Walsh, A.; Jackson, J.; Foster, J.; Molinari, S.; Meingast, S.; Amorim, A.; Lima, J.; Marques, R.; Moitinho, A.; Pinhao, J.; Rebordao, J., and Santos, F. D. G0.253 + 0.016: A Molecular Cloud Progenitor of an Arches-like Cluster. *ApJ*, 746:117, February 2012. doi: 10.1088/0004-637X/746/2/117.

Longmore, S. N.; Kruijssen, J. M. D.; Bastian, N.; Bally, J.; Rathborne, J.; Testi, L.; Stolte, A.; Dale, J.; Bressert, E., and Alves, J. The Formation and Early Evolution of Young Massive Clusters. *ArXiv e-prints*, January 2014.

Longo, G.; Grimaldi, A., and Richter, G. Discovery of an excess of blue star clusters around Hickson 90. *AAP*, 299:L45, July 1995.

Lumsden, S. L. and Puxley, P. J. Forbidden Feˆ+ emission from supernova remnants in M33. *MNRAS*, 276:723–733, October 1995.

Lumsden, S. L. and Puxley, P. J. Near-infrared spectroscopy of the ultracompact HII region G45.12+0.13. *MNRAS*, 281:493–508, July 1996.

Makino, J. Postcollapse Evolution of Globular Clusters. *ApJ*, 471:796, November 1996. doi: 10.1086/178007.

Malin, D. F.; Quinn, P. J., and Graham, J. A. Shell structure in NGC 5128. *ApJ Lett.*, 272:L5–L7, September 1983. doi: 10.1086/184106.

Maraston, C. Stellar Population Models. In Combes, F. and Palouš, J., editors, *IAU Symposium*, volume 235 of *IAU Symposium*, pages 52–56, May 2007. doi: 10.1017/S1743921306005047.

McLaughlin, D. E. The Efficiency of Globular Cluster Formation. *AJ*, 117:2398–2427, May 1999. doi: 10.1086/300836.

McLaughlin, D. E.; Barmby, P.; Harris, W. E.; Forbes, D. A., and Harris, G. L. H. Structural parameters for globular clusters in NGC 5128 - III. ACS surface brightness profiles and model fits. *MNRAS*, 384:563–590, February 2008. doi: 10.1111/j.1365-2966.2007.12566.x.

Mengel, S.; Lehnert, M. D.; Thatte, N., and Genzel, R. Star-formation in NGC 4038/4039 from broad and narrow band photometry: cluster destruction? *AAP*, 443:41–60, November 2005. doi: 10.1051/0004-6361:20052908.

Mengel, S.; Lehnert, M. D.; Thatte, N. A.; Vacca, W. D.; Whitmore, B., and Chandar, R. Young star clusters in interacting galaxies - NGC 1487 and NGC 4038/4039. *AAP*, 489:1091–1105, October 2008. doi: 10.1051/0004-6361:200809649.

Meylan, G. Mass Segregation in Star Clusters. In Lançon, A. and Boily, C. M., editors, *Massive Stellar Clusters*, volume 211 of *Astronomical Society of the Pacific Conference Series*, page 215, 2000.

Meylan, G. and Heggie, D. C. Internal dynamics of globular clusters. *A&AR*, 8: 1–143, 1997. doi: 10.1007/s001590050008.

Micheva, G.; Östlin, G.; Bergvall, N.; Zackrisson, E.; Masegosa, J.; Marquez, I.; Marquart, T., and Durret, F. Deep multiband surface photometry on a sample of 24 blue compact galaxies - I. *MNRAS*, 431:102–144, May 2013. doi: 10.1093/mnras/stt146.

Mihos, J. C.; Bothun, G. D., and Richstone, D. O. Modeling the Spatial Distribution of Star Formation in Interacting Disk Galaxies. *ApJ*, 418:82, November 1993. doi: 10.1086/173373.

Miller, B. W.; Whitmore, B. C.; Schweizer, F., and Fall, S. M. The Star Cluster System of the Merger Remnant NGC 7252. *AJ*, 114:2381, December 1997. doi: 10.1086/118655.

Miller, B. W.; Lotz, J. M.; Ferguson, H. C.; Stiavelli, M., and Whitmore, B. C. The Specific Globular Cluster Frequencies of Dwarf Elliptical Galaxiesfrom the Hubble Space Telescope. *ApJ Lett.*, 508:L133–L137, December 1998. doi: 10.1086/311739.

Milone, A. P.; Bedin, L. R.; Piotto, G., and Anderson, J. Multiple stellar populations in Magellanic Cloud clusters. I. An ordinary feature for intermediate age globulars in the LMC? *AAP*, 497:755–771, April 2009. doi: 10.1051/0004-6361/200810870.

Minniti, D.; Rejkuba, M.; Funes, J. G., and Jr.Kennicutt, R. C. The Most Exciting Massive Binary Cluster in NGC 5128: Clues to the Formation of Globular Clusters. *ApJ*, 612:215–221, September 2004. doi: 10.1086/422546.

Momcheva, I. G.; Lee, J. C.; Ly, C.; Salim, S.; Dale, D. A.; Ouchi, M.; Finn, R., and Ono, Y. Nebular Attenuation in Hα-selected Star-forming Galaxies at

z = 0.8 from the NewHα Survey. *AJ*, 145:47, February 2013. doi: 10.1088/0004-6256/145/2/47.

Morel, T.; Doyon, R., and St-Louis, N. Near-infrared [Fe II] emission from supernova remnants and the supernova rate of starburst galaxies. *MNRAS*, 329: 398–410, January 2002. doi: 10.1046/j.1365-8711.2002.05026.x.

Morganti, R. The Many Faces of the Gas in Centaurus A (NGC 5128). *PASA*, 27:463–474, October 2010. doi: 10.1071/AS09076.

Mouri, H.; Kawara, K., and Taniguchi, Y. Excitation Mechanism of Near-Infrared [Fe II] Emission in Seyfert and Starburst Galaxies. *ApJ*, 528:186–200, January 2000. doi: 10.1086/308142.

Murphy, B. W.; Cohn, H. N., and Hut, P. Realistic models for evolving globular clusters. II - POST core collapse with a mass spectrum. *MNRAS*, 245:335–349, July 1990.

Murray, N. The Sizes and Luminosities of Massive Star Clusters. *ApJ*, 691:946–962, February 2009. doi: 10.1088/0004-637X/691/2/946.

Jr.Neilsen, E. H.; Tsvetanov, Z. I., and Ford, H. C. The Surface Brightness Fluctuations and Globular Cluster Population of NGC 4478. *ApJ*, 483:745, July 1997. doi: 10.1086/304267.

Nussbaumer, H. and Storey, P. J. Transition probabilities for forbidden Fe II infrared lines. *AAP*, 193:327–333, March 1988.

Oliva, E.; Moorwood, A. F. M., and Danziger, I. J. Infrared spectroscopy of supernova remnants. *AAP*, 214:307–320, April 1989.

Oosterloo, T. and Iovino, A. HI observations of compact groups of galaxies. *PASA*, 14:48–51, April 1997. doi: 10.1071/AS97048.

Origlia, L.; Moorwood, A. F. M., and Oliva, E. The 1.5-1.7 micrometer spectrum of cool stars: Line identifications, indices for spectral classification and the stellar content of the Seyfert galaxy NGC 1068. *AAP*, 280:536–550, December 1993.

Osmond, J. P. F. and Ponman, T. J. The GEMS project: X-ray analysis and statistical properties of the group sample. *MNRAS*, 350:1511–1535, June 2004. doi: 10.1111/j.1365-2966.2004.07742.x.

Osterbrock, D. E. *Astrophysics of gaseous nebulae and active galactic nuclei*. W.H. Freeman and Company, 1989.

Ostrov, P.; Geisler, D., and Forte, J. C. The metallicity gradient and distribution function of globular clusters around NGC 1399. *AJ*, 105:1762–1778, May 1993. doi: 10.1086/116553.

Pandey, A. K.; Nilakshi, N.; Ogura, K.; Sagar, R., and Tarusawa, K. NGC 7654: An interesting cluster to study star formation history. *AAP*, 374:504–522, August 2001. doi: 10.1051/0004-6361:20010642.

Parker, R. J. and Goodwin, S. P. Do O-stars form in isolation? *MNRAS*, 380: 1271–1275, September 2007. doi: 10.1111/j.1365-2966.2007.12179.x.

Peacock, M. B.; Zepf, S. E., and Finzell, T. Signatures of Multiple Stellar Populations in Unresolved Extragalactic Globular/Young Massive Star Clusters. *ApJ*, 769:126, June 2013. doi: 10.1088/0004-637X/769/2/126.

Peng, E. W.; Ford, H. C.; Freeman, K. C., and White, R. L. A Young Blue Tidal Stream in NGC 5128. *AJ*, 124:3144–3156, December 2002. doi: 10.1086/344308.

Peng, E. W.; Jordán, A.; Côté, P.; Takamiya, M.; West, M. J.; Blakeslee, J. P.; Chen, C.-W.; Ferrarese, L.; Mei, S.; Tonry, J. L., and West, A. A. The ACS Virgo Cluster Survey. XV. The Formation Efficiencies of Globular Clusters in Early-Type Galaxies: The Effects of Mass and Environment. *ApJ*, 681:197–224, July 2008. doi: 10.1086/587951.

Piatti, A. E.; Bica, E., and Claria, J. J. Fundamental parameters of the highly reddened young open clusters Westerlund 1 and 2. *AAPS*, 127:423–432, February 1998. doi: 10.1051/aas:1998111.

Plana, H.; Mendes de Oliveira, C.; Amram, P., and Boulesteix, J. The Kinematics of the Warm Gas in the Interacting Hickson Compact Group of Galaxies HCG 90. *AJ*, 116:2123–2135, November 1998. doi: 10.1086/300621.

Ponman, T. J.; Bourner, P. D. J.; Ebeling, H., and Böhringer, H. A ROSAT survey of Hickson's compact galaxy groups. *MNRAS*, 283:690–708, December 1996.

Portegies Zwart, S. F.; McMillan, S. L. W., and Gieles, M. Young Massive Star Clusters. *ARA&A*, 48:431–493, September 2010. doi: 10.1146/annurev-astro-081309-130834.

Price, D. J. and Bate, M. R. Inefficient star formation: the combined effects of magnetic fields and radiative feedback. *MNRAS*, 398:33–46, September 2009. doi: 10.1111/j.1365-2966.2009.14969.x.

Quillen, A. C.; de Zeeuw, P. T.; Phinney, E. S., and Phillips, T. G. The kinematics of the molecular gas in Centaurus A. *ApJ*, 391:121–136, May 1992. doi: 10.1086/171329.

Quillen, A. C.; Graham, J. R., and Frogel, J. A. The warped disk of Centaurus A in the near-infrared. *ApJ*, 412:550–567, August 1993. doi: 10.1086/172943.

Rejkuba, M. Deep VLT search for globular clusters in NGC 5128: Color-magnitude diagrams and globular cluster luminosity function. *AAP*, 369:812–825, April 2001. doi: 10.1051/0004-6361:20010180.

Rejkuba, M. Globular cluster luminosity function as distance indicator. *APSS*, 341:195–206, September 2012. doi: 10.1007/s10509-012-0986-9.

Rejkuba, M.; Dubath, P.; Minniti, D., and Meylan, G. Masses and M/L Ratios of Bright Globular Clusters in NGC 5128. In Vesperini, E.; Giersz, M., and Sills, A., editors, *IAU Symposium*, volume 246 of *IAU Symposium*, pages 418–422, May 2008. doi: 10.1017/S1743921308016074.

Rejkuba, M.; Harris, W. E.; Greggio, L., and Harris, G. L. H. How old are the stars in the halo of NGC 5128 (Centaurus A)? *AAP*, 526:A123, February 2011. doi: 10.1051/0004-6361/201015640.

Renaud, F. *Dynamics of the Tidal Fields and Formation of Star Clusters in Galaxy Mergers*. PhD thesis, PhD Thesis, 281 pages, 121 figures, 2010, 2010.

Renzini, A. Origin of multiple stellar populations in globular clusters and their helium enrichment. *MNRAS*, 391:354–362, November 2008. doi: 10.1111/j.1365-2966.2008.13892.x.

Ribeiro, A. L. B.; de Carvalho, R. R.; Capelato, H. V., and Zepf, S. E. Structural and Dynamical Analysis of the Hickson Compact Groups. *ApJ*, 497:72, April 1998a. doi: 10.1086/305442.

Ribeiro, A. L. B.; de Carvalho, R. R.; Capelato, H. V., and Zepf, S. E. Structural and Dynamical Analysis of the Hickson Compact Groups. *ApJ*, 497:72, April 1998b. doi: 10.1086/305442.

Rose, J. A. A survey of compact groups of galaxies. *ApJ*, 211:311–318, January 1977. doi: 10.1086/154936.

Rosenberg, M. J. F.; van der Werf, P. P., and Israel, F. P. [FeII] as a tracer of supernova rate in nearby starburst galaxies. *AAP*, 540:A116, April 2012. doi: 10.1051/0004-6361/201218772.

Samurovic, S. Globular Clusters and Planetary Nebulae Kinematics and X-Ray Emission in the Early-Type Galaxy NGC 5128. *Serbian Astronomical Journal*, 173:35, December 2006. doi: 10.2298/SAJ0673035S.

Saviane, I.; Momany, Y.; da Costa, G. S.; Rich, R. M., and Hibbard, J. E. A New Red Giant-based Distance Modulus of 13.3 Mpc to the Antennae Galaxies and Its Consequences. *ApJ*, 678:179–186, May 2008. doi: 10.1086/533408.

Schaerer, D.; Meynet, G.; Maeder, A., and Schaller, G. Grids of stellar models. II - From 0.8 to 120 solar masses at Z = 0.008. *AAPS*, 98:523–527, May 1993.

Schechter, P. An analytic expression for the luminosity function for galaxies. *ApJ*, 203:297–306, January 1976. doi: 10.1086/154079.

Schlafly, E. and Finkbeiner, D. P. Recalibrating SFD Using SDSS Spectroscopy And Photometry. In *American Astronomical Society Meeting Abstracts #218*, page 318, May 2011.

Schlegel, D.; Finkbeiner, D., and Davis, M. Application of SFD Dust Maps to Galaxy Counts and CMB Experiments. In Colombi, S.; Mellier, Y., and Raban, B., editors, *Wide Field Surveys in Cosmology*, page 297, 1998.

Schreier, E. J.; Capetti, A.; Macchetto, F.; Sparks, W. B., and Ford, H. J. Hubble Space Telescope Imaging and Polarimetry of NGC 5128 (Centaurus A). *ApJ*, 459:535, March 1996. doi: 10.1086/176917.

Schweizer, F. Colliding and merging galaxies. I - Evidence for the recent merging of two disk galaxies in NGC 7252. *ApJ*, 252:455–460, January 1982. doi: 10.1086/159573.

Schweizer, F. and Seitzer, P. Ages and Metallicities of Young Globular Clusters in the Merger Remnant NGC 7252. *AJ*, 116:2206–2219, November 1998. doi: 10.1086/300616.

Schweizer, F.; Miller, B. W.; Whitmore, B. C., and Fall, S. M. Hubble Space Telescope Observations of Candidate Young Globular Clusters and Stellar Associations in the Recent Merger Remnant NGC 3921. *AJ*, 112:1839, November 1996. doi: 10.1086/118146.

Schweizer, F.; Seitzer, P., and Brodie, J. P. Keck Spectroscopy of Two Young Globular Clusters in the Merger Remnant NGC 3921. *AJ*, 128:202–210, July 2004. doi: 10.1086/421851.

Schweizer, F.; Burns, C. R.; Madore, B. F.; Mager, V. A.; Phillips, M. M.; Freedman, W. L.; Boldt, L.; Contreras, C.; Folatelli, G.; González, S.; Hamuy, M.; Krzeminski, W.; Morrell, N. I.; Persson, S. E.; Roth, M. R., and Stritzinger, M. D. a New Distance to the Antennae Galaxies (ngc 4038/39) Based on the Type ia Supernova 2007sr. *AJ*, 136:1482–1489, October 2008. doi: 10.1088/0004-6256/136/4/1482.

Scoville, N. Z.; Polletta, M.; Ewald, S.; Stolovy, S. R.; Thompson, R., and Rieke, M. High-Mass, OB Star Formation in M51: Hubble Space Telescope Hα and Paα Imaging. *AJ*, 122:3017–3045, December 2001. doi: 10.1086/323445.

Seale, J. P.; Looney, L. W.; Wong, T.; Ott, J.; Klein, U., and Pineda, J. L. The Life and Death of Dense Molecular Clumps in the Large Magellanic Cloud. *ApJ*, 751:42, May 2012. doi: 10.1088/0004-637X/751/1/42.

Sellgren, K. and Smith, R. G. The 3 micron spectrum of the classical Be star Beta Monocerotis A. *ApJ*, 388:178–183, March 1992. doi: 10.1086/171140.

Sersic, Jose Luis. Atlas de galaxias australes. *Cordoba, Argentina: Observatorio Astronomico, 1968*, 1, 1968.

Sharples, R.; Bender, R.; Agudo Berbel, A.; Bennett, R.; Bezawada, N.; Bouché, N.; Bramall, D.; Casali, M.; Cirasuolo, M.; Clark, P.; Cliffe, M.; Davies, R.; Davies, R.; Drory, N.; Dubbeldam, M.; Fairley, A.; Finger, G.; Genzel, R.; Haefner, R.; Hess, A.; Jeffers, P.; Lewis, I.; Montgomery, D.; Murray, J.; Muschielok, B.; Förster Schreiber, N.; Pirard, J.; Ramsey-Howat, S.; Rees, P.; Richter, J.; Robertson, D.; Robson, I.; Rolt, S.; Saglia, R.; Schlichter, J.; Tecza, M.; Todd, S.; Wegner, M., and Wiezorrek, E. Recent Progress on the KMOS Multi-object Integral Field Spectrometer. *The Messenger*, 139:24–27, March 2010.

Sharples, R.; Bender, R.; Agudo Berbel, A.; Bezawada, N.; Castillo, R.; Cirasuolo, M.; Davidson, G.; Davies, R.; Dubbeldam, M.; Fairley, A.; Finger, G.; Förster Schreiber, N.; Gonte, F.; Hess, A.; Jung, I.; Lewis, I.; Lizon, J.-L.; Muschielok, B.; Pasquini, L.; Pirard, J.; Popovic, D.; Ramsay, S.; Rees, P.; Richter, J.; Riquelme, M.; Rodrigues, M.; Saviane, I.; Schlichter, J.; Schmidtobreick, L.; Segovia, A.; Smette, A.; Szeifert, T.; van Kesteren, A.; Wegner, M., and Wiezorrek, E. First Light for the KMOS Multi-Object Integral-Field Spectrometer. *The Messenger*, 151:21–23, March 2013.

Simpson, C. and Meadows, V. The Nuclear Spectrum of the Radio Galaxy NGC 5128 (Centaurus A). *ApJ Lett.*, 505:L99–L102, October 1998. doi: 10.1086/311616.

Sirianni, M.; Jee, M. J.; Benítez, N.; Blakeslee, J. P.; Martel, A. R.; Meurer, G.; Clampin, M.; De Marchi, G.; Ford, H. C.; Gilliland, R.; Hartig, G. F.; Illingworth, G. D.; Mack, J., and McCann, W. J. The Photometric Performance and Calibration of the Hubble Space Telescope Advanced Camera for Surveys. *P.A.S.P.*, 117:1049–1112, October 2005. doi: 10.1086/444553.

Snijders, L.; van der Werf, P. P.; Brandl, B. R.; Mengel, S.; Schaerer, D., and Wang, Z. Subarcsecond Resolution Mid-Infrared Observations of Super Star Clusters in the Antennae (NGC 4038/4039). *ApJ Lett.*, 648:L25–L28, September 2006. doi: 10.1086/507424.

Sparke, L. S. A Dynamical Model for the Twisted Gas Disk in Centaurus A. *ApJ*, 473:810, December 1996. doi: 10.1086/178193.

Jr.Spitzer, L. Distribution of Galactic Clusters. *ApJ*, 127:17, January 1958. doi: 10.1086/146435.

Jr.Spitzer, L. and Shull, J. M. Random gravitational encounters and the evolution of spherical systems. VII - Systems with several mass groups. *ApJ*, 201:773–782, November 1975. doi: 10.1086/153943.

Jr.Spitzer, L. and Thuan, T. X. Random Gravitational Encounters and the Evolution of Spherical Systems. IV Isolated Systems of Identical Stars. *ApJ*, 175:31, July 1972. doi: 10.1086/151537.

Spitzer, Lyman. Dynamical evolution of globular clusters. *Princeton, NJ, Princeton University Press, 1987, 191 p.*, 1, 1987.

Staneva, A.; Spassova, N., and Golev, V. The ellipticities of globular clusters in the Andromeda galaxy. *AAPS*, 116:447–461, May 1996.

Stanford, S. A. and Balcells, M. Dynamical simulations of the interacting galaxies in the NGC 520/UGC 957 system. *ApJ*, 370:118–129, March 1991. doi: 10.1086/169796.

Stanford, S. A.; Sargent, A. I.; Sanders, D. B., and Scoville, N. Z. CO aperture synthesis of NGC 4038/39 (ARP 244). *ApJ*, 349:492–496, February 1990. doi: 10.1086/168334.

Tan, J. C. and McKee, C. F. The Genesis of Super Star Clusters as Self-Gravitating HII Regions. In Tacconi, L. and Lutz, D., editors, *Starburst Galaxies: Near and Far*, page 188, 2001.

Tenorio-Tagle, G.; Silich, S.; Rodríguez-González, A., and Muñoz-Tuñón, C. On the Extreme Stationary Outflows from Super Star Clusters: From Superwinds to Supernebulae and Further Massive Star Formation. *ApJ*, 620:217–222, February 2005. doi: 10.1086/426962.

Thompson, R. I. High-resolution near-infrared spectra of NGC 4151: Line and continuum analysis. *ApJ*, 445:700–711, June 1995. doi: 10.1086/175732.

Toomre, A. Mergers and Some Consequences. In Tinsley, B. M. and D. CampbellLarson, R. B. G., editors, *Evolution of Galaxies and Stellar Populations*, page 401, 1977.

Trancho, G.; Bastian, N.; Miller, B. W., and Schweizer, F. Gemini Spectroscopic Survey of Young Star Clusters in Merging/Interacting Galaxies. II. NGC 3256 Clusters. *ApJ*, 664:284–295, July 2007a. doi: 10.1086/518886.

Trancho, G.; Bastian, N.; Schweizer, F., and Miller, B. W. Gemini Spectroscopic Survey of Young Star Clusters in Merging/Interacting Galaxies. I. NGC 3256 Tidal Tail Clusters. *ApJ*, 658:993–998, April 2007b. doi: 10.1086/511735.

Treister, E.; Castander, F. J.; Maccarone, T. J.; Gawiser, E.; Coppi, P. S.; Urry, C. M.; Maza, J.; Herrera, D.; Gonzalez, V.; Montoya, C., and Pineda, P. The Calán-Yale Deep Extragalactic Research (CYDER) Survey: Optical Properties and Deep Spectroscopy of Serendipitous X-Ray Sources. *ApJ*, 621:104–122, March 2005. doi: 10.1086/427471.

van den Bergh, S. Some Constraints on Galaxy Evolution Imposed by the Specific Frequency of Globular Clusters. *AJ*, 110:2700, December 1995. doi: 10.1086/117723.

van den Bergh, S. The Flattening of Globular Clusters. *AJ*, 135:1731–1737, May 2008. doi: 10.1088/0004-6256/135/5/1731.

van den Bergh, S. and Harris, W. E. Globular clusters in galaxies beyond the local group. II - The edge-on spirals NGC 891 and NGC 4565. *AJ*, 87:494–499, March 1982. doi: 10.1086/113122.

Vansevičius, V.; Kodaira, K.; Narbutis, D.; Stonkutė, R.; Bridžius, A.; Deveikis, V., and Semionov, D. Compact Star Clusters in the M31 Disk. *ApJ*, 703: 1872–1883, October 2009. doi: 10.1088/0004-637X/703/2/1872.

Vanzi, L. and Rieke, G. H. Infrared Spectroscopy of Blue Dwarf Galaxies. *ApJ*, 479:694–701, April 1997.

Vázquez, G. A. and Leitherer, C. Optimization of Starburst99 for Intermediate-Age and Old Stellar Populations. *ApJ*, 621:695–717, March 2005. doi: 10.1086/427866.

Vesperini, E. Evolution of globular cluster systems in elliptical galaxies - II. Power-law initial mass function. *MNRAS*, 322:247–256, April 2001. doi: 10.1046/j.1365-8711.2001.04072.x.

Villegas, D.; Minniti, D., and Funes, J. G. HST photometry of the binary globular cluster Sersic 13N-S in NGC 5128. *AAP*, 442:437–442, November 2005. doi: 10.1051/0004-6361:20042359.

Villegas, D.; Jordán, A.; Peng, E. W.; Blakeslee, J. P.; Côté, P.; Ferrarese, L.; Kissler-Patig, M.; Mei, S.; Infante, L.; Tonry, J. L., and West, M. J. The ACS Fornax Cluster Survey. VIII. The Luminosity Function of Globular Clusters in Virgo and Fornax Early-type Galaxies and Its Use as a Distance Indicator. *ApJ*, 717:603–616, July 2010. doi: 10.1088/0004-637X/717/2/603.

Vorontsov-Vel'Yaminov, B. A. *Extragalactic astronomy*. Harwood Academic Publishers, 1987.

Walborn, N. R.; Howarth, I. D.; Lennon, D. J.; Massey, P.; Oey, M. S.; Moffat, A. F. J.; Skalkowski, G.; Morrell, N. I.; Drissen, L., and Parker, J. W. A New

Spectral Classification System for the Earliest O Stars: Definition of Type O2. *AJ*, 123:2754–2771, May 2002. doi: 10.1086/339831.

Wang, Z.; Fazio, G. G.; Ashby, M. L. N.; Huang, J.-S.; Pahre, M. A.; Smith, H. A.; Willner, S. P.; Forrest, W. J.; Pipher, J. L., and Surace, J. A. The Off-Nuclear Starbursts in NGC 4038/4039 (The Antennae Galaxies). *ApJS*, 154:193–198, September 2004. doi: 10.1086/423205.

Wegner, M. and Muschielok, B. KARMA: the observation preparation tool for KMOS. In *Society of Photo-Optical Instrumentation Engineers (SPIE) Conference Series*, volume 7019 of *Society of Photo-Optical Instrumentation Engineers (SPIE) Conference Series*, August 2008. doi: 10.1117/12.787190.

West, M. J.; Cote, P.; Jones, C.; Forman, W., and Marzke, R. O. Intracluster Globular Clusters. *ApJ Lett.*, 453:L77, November 1995. doi: 10.1086/309748.

Westerlund, B. A Heavily Reddened Cluster in ARA. *P.A.S.P.*, 73:51, February 1961. doi: 10.1086/127618.

Westerlund, B. E. Photometry and spectroscopy of stars in the region of a highly reddened cluster in ARA. *AAPS*, 70:311–324, September 1987.

White, P. M.; Bothun, G.; Guerrero, M. A.; West, M. J., and Barkhouse, W. A. Extraordinary Diffuse Light in Hickson Compact Group 90. *ApJ*, 585:739–749, March 2003. doi: 10.1086/346075.

Whitmore, B. The Formation of Globular Clusters in the Local Universe. In Kissler-Patig, M., editor, *Extragalactic Globular Cluster Systems*, page 336, 2003. doi: 10.1007/10857603_51.

Whitmore, B. C. The Formation of Star Clusters. *ArXiv Astrophysics e-prints*, December 2000.

Whitmore, B. C. and Schweizer, F. Hubble space telescope observations of young star clusters in NGC-4038/4039, 'the antennae' galaxies. *AJ*, 109:960–980, March 1995. doi: 10.1086/117334.

Whitmore, B. C.; Zhang, Q.; Leitherer, C.; Fall, S. M.; Schweizer, F., and Miller, B. W. The Luminosity Function of Young Star Clusters in "the Antennae" Galaxies (NGC 4038-4039). *AJ*, 118:1551–1576, October 1999. doi: 10.1086/301041.

Whitmore, B. C.; Chandar, R.; Schweizer, F.; Rothberg, B.; Leitherer, C.; Rieke, M.; Rieke, G.; Blair, W. P.; Mengel, S., and Alonso-Herrero, A. The Antennae Galaxies (NGC 4038/4039) Revisited: Advanced Camera for Surveys and NICMOS Observations of a Prototypical Merger. *AJ*, 140:75–109, July 2010. doi: 10.1088/0004-6256/140/1/75.

Wilson, C. D.; Scoville, N.; Madden, S. C., and Charmandaris, V. High-Resolution Imaging of Molecular Gas and Dust in the Antennae (NGC 4038/39): Super Giant Molecular Complexes. *ApJ*, 542:120–127, October 2000. doi: 10.1086/309504.

Wilson, C. D.; Scoville, N.; Madden, S. C., and Charmandaris, V. The Mass Function of Supergiant Molecular Complexes and Implications for Forming Young Massive Star Clusters in the Antennae (NGC 4038/4039). *ApJ*, 599:1049–1066, December 2003. doi: 10.1086/379344.

Woodley, K.; Harris, W.; Gomez, M.; Puzia, T.; Harris, G., and Geisler, D. The Metallicities, Ages, and Alpha Element Enhancements of Globular Clusters in the Elliptical Galaxy, NGC 5128: A Homogeneous Spectroscopic Study with Gemini/GMOS. In *American Astronomical Society Meeting Abstracts #213*, volume 213 of *American Astronomical Society Meeting Abstracts*, pages 605–609, December 2009.

Woodley, K. A. and Gómez, M. The Globular Cluster System of NGC 5128: Ages, Metallicities, Kinematics and Structural Parameters. *PASA*, 27:379–389, October 2010. doi: 10.1071/AS09059.

Woodley, K. A.; Harris, W. E., and Harris, G. L. H. Radial Velocities of Newly Discovered Globular Clusters in NGC 5128. *AJ*, 129:2654–2662, June 2005. doi: 10.1086/430189.

Woodley, K. A.; Gómez, M.; Harris, W. E.; Geisler, D., and Harris, G. L. H. The Kinematics of the Globular Cluster System of NGC 5128 with a New Large Sample of Radial Velocity Measurements. *AJ*, 139:1871–1888, May 2010. doi: 10.1088/0004-6256/139/5/1871.

Woodworth, S. C. and Harris, W. E. The Globular Cluster Systems in the Coma Ellipticals. III. The Unique Case of IC 4051. *AJ*, 119:2699–2710, June 2000. doi: 10.1086/301400.

Zabludoff, A. I. and Mulchaey, J. S. The Properties of Poor Groups of Galaxies. I. Spectroscopic Survey and Results. *ApJ*, 496:39, March 1998. doi: 10.1086/305355.

Zepf, S. E. and Ashman, K. M. Globular Cluster Systems Formed in Galaxy Mergers. *MNRAS*, 264:611, October 1993.

Zepf, S. E.; Ashman, K. M.; English, J.; Freeman, K. C., and Sharples, R. M. The Formation and Evolution of Candidate Young Globular Clusters in NGC 3256. *AJ*, 118:752–764, August 1999. doi: 10.1086/300961.

Zepf, S. E.; Beasley, M. A.; Bridges, T. J.; Hanes, D. A.; Sharples, R. M.; Ashman, K. M., and Geisler, D. Dynamical Constraints on the Formation of NGC 4472 and Its Globular Clusters. *AJ*, 120:2928–2937, December 2000. doi: 10.1086/316850.

Zhang, Q. and Fall, S. M. The Mass Function of Young Star Clusters in the "Antennae" Galaxies. *ApJ Lett.*, 527:L81–L84, December 1999. doi: 10.1086/312412.

Zhang, Q.; Fall, S. M., and Whitmore, B. C. A Multiwavelength Study of the Young Star Clusters and Interstellar Medium in the Antennae Galaxies. *ApJ*, 561:727–750, November 2001. doi: 10.1086/322278.